

**DEVELOPMENT AND OPTIMIZATION OF HIGH
BRIGHTNESS NANO-APERTURE ION SOURCE
FOR PROTON BEAM WRITING APPLICATIONS**

XU XINXIN

NATIONAL UNIVERSITY OF SINGAPORE

2017

**DEVELOPMENT AND OPTIMIZATION OF HIGH
BRIGHTNESS NANO-APERTURE ION SOURCE
FOR PROTON BEAM WRITING APPLICATIONS**

XU XINXIN

(B.Sc., Lanzhou University)

**A THESIS SUBMITTED FOR THE DEGREE OF
DOCTOR OF PHILOSOPHY
DEPARTMENT OF PHYSICS
NATIONAL UNIVERSITY OF SINGAPORE**

2017

Supervisor:
Associate Professor Jeroen Anton van Kan

Examiners:
Associate Professor Thomas Osipowicz
Professor Mark B. H. Breese
Dr. Andreas Markwitz, GNS Science, New Zealand

DECLARATION

I hereby declare that this thesis is my original work and it has been written by me in its entirety. I have duly acknowledged all the sources of information which have been used in the thesis.

This thesis has also not been submitted for any degree in any university previously.



XU Xinxin

23 August 2017

Acknowledgements

It has been my great fortune to work with my supervisor, Assoc. Prof. Jeroen Anton van Kan, who gives a lot of advice and guidance to my Ph.D project. Jeroen is not only a creative scientist but also a skilled engineer. His continuous support and immense knowledge always inspire me to think more in the research, and helping me realize the thesis.

I want to express my gratitude to Dr. Pattabiraman Santhana Raman. Dr. Raman is always patient and helpful. He provides excellent perspective to view a problem, explains it clearly and offers key insights towards solving it. In the period of writing this thesis, Dr. Raman has read through it and given many constructive suggestions.

Thanks to my senior Dr. Liu Nannan who mentored and trained me to start the project. Thanks to our lab technologist Mr. Rajasekaran Mariappan who has given continuous technical support. I appreciate Dr. Saumitra Vajandar and Dr. Shuvan Prashant Turaga who have helped me to correct the thesis. Special thanks to Dr. Chan Taw Kuei who taught me about RBS and ERDA techniques.

Thanks to Assoc. Prof. Anjam Khursheed, Prof. Frank Watt, Assoc. Prof. Thomas Osipowicz, Assoc. Prof. Andrew Bettoli, and Prof. Mark Breese for their encouragement, valuable suggestions and insightful comments.

I'm also very grateful to our "Friday dinner group" including Dr. Saumitra, Dr. Prashant, Dr. Tanmoy Basu, Mr. Rajasekaran, Mr. Tan Huei Ming, Ms. Tao Ye, and Mr. Balaji Vengatachalam. With you guys, we have a lot of fun and enjoyment.

I acknowledge the help and encouragement rendered by CIBA members and friends, Mr. Choo Theam Fook, Dr. Ren Minqin, Dr. Chen Ce-Belle, Dr. Liu Fan, Dr. Mi Zhaozhong (Mike), Dr. Liang Haidong, Mr. Sarfraz Qureshi, Mr. Pang Rudy, Mr. Tan Hong Qi, Ms. Shi Yi, Mr. Jin Huining (Kim), and Mr. Gong Jintao.

This thesis is dedicated to my parents.

For their endless love, support, and encouragement.

最后，我要感谢我的父母，他们的付出、支持和鼓励是我最坚强的后盾。特别是我的父亲，他是我心目中永远的英雄！

XU Xinxin

许新鑫

Table of Contents

Acknowledgements	i
Summary	vi
List of Tables	viii
List of Figures	ix
List of abbreviations	xvi
Chapter 1. Introduction	1
1.1 Characteristics of an ion source	3
1.1.1 Liouville's theorem.....	3
1.1.2 Emittance and brightness	5
1.1.3 Beam intrinsic energy and energy spread	10
1.1.4 Coulomb effects	12
1.2 Proton beam writing (PBW)	18
1.2.1 PBW facility at CIBA, NUS	18
1.2.2 Charged particle-matter interaction	20
1.2.3 Applications of PBW	26
1.3 Ion sources	29
1.3.1 Radio frequency (RF) ion source	29
1.3.2 Liquid metal ion source (LMIS)	32
1.3.3 Gas field ion source (GFIS)	34
1.3.4 Laser-cooled ion source	35
1.4 Scope of this thesis.....	37
References.....	40
Chapter 2. Nano-aperture ion source (NAIS)	50
2.1 The Concept of NAIS	51
2.1.1 Electron ionization process	51
2.1.2 The configuration of NAIS	52

2.1.3	Operational condition of NAIS	54
2.2	Theoretical NAIS source performance	57
2.2.1	Theoretical NAIS reduced brightness	57
2.2.2	Energy spread.....	61
2.3	The influence of Coulomb effect	63
2.3.1	Space charge effect	63
2.3.2	Statistical Coulomb effects	66
2.4	Summary	68
	Reference	69
Chapter 3. Simulated performance of nano-aperture ion source (NAIS).....		71
3.1	Introduction.....	71
3.2	Gas distributions	73
3.2.1	Consideration of the NAIS geometry relationship.....	73
3.2.2	Gas distributions of desired NAIS geometries.....	76
3.3	Simulated performance of NAIS.....	83
3.3.1	Initial condition of NAIS	83
3.3.2	Emittance, reduced brightness and energy spread	86
3.4	Coulomb effects of the NAIS	96
3.5	Summary	101
	References.....	102
Chapter 4. NAIS fabrication and performance		103
4.1	Introduction.....	103
4.2	Performance test of the NAIS with metal spacer	104
4.3	NAIS with recessed Si ₃ N ₄	112
4.3.1	Fabrication of NAIS with recessed Si ₃ N ₄	112
4.3.2	Brightness measurement of NAIS with recessed Si ₃ N ₄	116
4.4	Second-generation NAIS	121
4.4.1	Approach to high brightness NAIS	121

4.4.2	NAIS with internal electrodes	126
4.5	Summary	129
	References.....	131
Chapter 5.	Evaluation and design for a low energy proton microscope and a compact PBW (c-PBW) system	132
5.1	Low energy proton microscopy	133
5.1.1	Introduction.....	133
5.1.2	Advantage of low energy proton microscopy	134
5.1.3	Miniaturized Einzel lens	136
5.2	Design of c-PBW system	142
5.2.1	Introduction.....	142
5.2.2	Layout of the c-PBW system	145
5.2.3	Evaluation of c-PBW system	147
5.3	Summary	153
	References.....	155
Chapter 6.	Conclusion.....	158
Appendix 1.	Lens aberrations	160
1.1	Ideal lens optics.....	160
1.2	Chromatic aberration	162
1.3	Spherical aberration	164
1.4	Diffraction aberration.....	166
1.5	Other aberrations.....	167
	References.....	169
Appendix 2.	Relationship between electron probe current and probe size for different electron emitters.....	170
	References.....	175
List of Publications		176

Summary

Proton beam writing (PBW) is a direct-write lithographic technique developed in the Centre for Ion Beam Applications, National University of Singapore, which employs focused protons for fabricating three-dimensional nano-structures. In comparison to electron beam lithography (EBL), the advantage of PBW arises from the fact that a proton is ~1800 times heavier than an electron. Due to its heavier mass, a proton transfers lesser energy to secondary electrons and penetrates straighter into the material with low straggling, thereby depositing a constant energy along its path in resist. This linear energy loss profile makes PBW a unique technique to fabricate nano-structures without proximity effects. Currently, the performance of PBW in terms of spot size and throughput is limited by low brightness $\sim 20 \text{ A}/(\text{m}^2\text{srV})$ of the radio frequency ion source, employed in PBW systems. Nano-aperture ion source (NAIS) is a potential candidate to be an integral part of next generation PBW system with sub-10 nm resolution. The mechanism of NAIS is to generate ions by electron-gas collisions within a sub-micron ionization chamber. To evaluate the performance of NAIS, simulations were carried out for different geometries. The result predicts that a brightness of $> 10^6$ and $10^8 \text{ A}/(\text{m}^2\text{srV})$ for proton and H_2^+ respectively can be delivered by NAIS, thus making it suitable for sub-10 PBW system. Meanwhile, two different kinds of NAIS (NAIS with metal spacer and recessed Si_3N_4 NAIS) were designed and successfully fabricated using microelectromechanical systems technique. Experiments to measure source brightness were conducted inside different scanning electron microscopes. The maximum reduced brightness from the recessed Si_3N_4 NAIS was obtained to be $\sim 0.9_{-0.1}^{+1.0} \times 10^4 \text{ A}/(\text{m}^2\text{srV})$ for an Ar^+ beam. For further improvement of NAIS performance, a new NAIS design with internal electrodes is proposed, evaluated and simulated, aiming for higher brightness and lower energy spread. As an application, a low energy proton microscope equipped with NAIS is proposed and theoretically

evaluated. A compact PBW system with single digit nanometer resolution for fast writing is designed and evaluated. This system is expected to have a sub-10 nm lithographic resolution along with a writing speed comparable to that of EBL.

List of Tables

Table. 1- 1 Summary of characteristics for different kinds of ion source.....	38
Table. 2- 1 First ionization energy E_i for different gases [7], [8].	51
Table. 2- 2 Debye length λ_D and SCL beam current density J and current I for different ion species, at 1 μm characteristic length equipped with 1 keV tungsten SEM.	64
Table. 2- 3 Debye length λ_D and SCL beam current density J and current I for different ion pieces, at 100 nm characteristic length equipped with 1 keV Schottky SEM.....	65
Table. 2- 4 Reduced brightness calculated, where space charge effect is negligible for NAIS equipped with Schottky SEM with a characteristic length of 100 nm.....	65
Table. 2- 5 Effective transverse-longitudinal temperature relaxation time τ_{eef} and the ion flight time in NAIS, equipped with tungsten SEM with a characteristic length of 1 μm	66
Table. 2- 6 Effective transverse-longitudinal temperature relaxation time τ_{eef} and the ion flight time in NAIS, equipped with Schottky SEM with a characteristic length of 100 nm.	67
Table. 3- 1 NAIS performance for hydrogen gas with different injected electron beam diameters at characteristic length of 100 nm equipped with a Schottky SEM, and characteristic length of 1 μm equipped with a tungsten SEM, respectively.	95
Table. 4- 1 Experimentally measured reduced brightness and energy spread of NAISs with metal spacer and recessed Si_3N_4 , with comparison to the predicted NAIS with internal electrodes.	129
Table. 5- 1 Scaling down of lens for constant field and constant potential modes ($k < 1$).....	138
Table. 5- 2 Parameters obtained from PBO Lab with the Russian quadruplet and Oxford triplet configurations.	149
Table. 5- 3 Summary of 200 kV c-PBW with different lens configurations, to write a $10 \mu\text{m} \times 10 \mu\text{m}$ square on PMMA, comparing with current PBW and EBL. (Required doses for proton and electron are $10 \mu\text{C}/\text{cm}^2$ [37] and $1000 \mu\text{C}/\text{cm}^2$ [38], respectively).	152
Table. 6- 1 Experimentally measured reduced brightness and energy spread of NAISs with metal spacer and recessed Si_3N_4	158

List of Figures

Figure. 1- 1 Description of emittance ε_x . The emittance is equal to the area $A_{xx'}$, in phase space occupied by beam particles divided by π	6
Figure. 1- 2 Charged particles are emitted from a virtual source with an area of A (the smallest area when tracing back the beam trajectory), and accelerated to the potential of U with a solid angle Ω . For small angle, $\Omega \sim \pi \alpha_0^2$	8
Figure. 1- 3 Proton beam writing (PBW) facility at CIBA, NUS, comprised of RF ion source, acceleration column, 90° analyzing magnet, object silts, switching magnet, collimator slits and quadrupole lenses.	19
Figure. 1- 4 Beam trajectories of different beams: fast proton beam (2 MeV), slow heavy gallium beam (50 keV), electron beam (50 keV), and electromagnetic radiation (X-rays and EUV). Adapted from Ref [55].	21
Figure. 1- 5 Monte Carlo simulation of energy deposited in a 500 nm thick PMMA using protons and electrons. (a-c) 3000 keV, 1000 keV, and 500 keV protons. (d-f) 100 keV, 25 keV, and 10 keV electrons. Adapted from Ref [60].....	22
Figure. 1- 6 Different ion beam trajectories and sputter yields (SY) of H ⁺ , He ⁺ , Ne ⁺ , and Ga ⁺ at top) 100 keV, and bottom) 200 keV, in 200 nm thick PMMA. The incident ions (100 ions) are shown in black, and the dislocated atoms are shown in color. The total sputter yields are presented by summing the yields of hydrogen, carbon and oxygen atmos. Simulated using Monte Carlo simulation program SRIM [68].	24
Figure. 1- 7 Nano-structures fabricated by PBW, a) Scanning electron microscopy (SEM) image of parallel lines in a 350 nm thick PMMA layer [6]. b) SEM image of 22 nm wide line in 850 nm thick HSQ [91]. c) SEM image of 60 nm walls on 10 μm thick SU-8, aspect ratio of ~167. d) Microsized copy of Stonehenge in UK fabricated on SU-8 [5].....	26
Figure. 1- 8 Schematics, and photo taken from Ion Source Test Bench at CIBA, NUS of capacitively coupled RF ion source.....	30
Figure. 1- 9 A thonemann type RF ion source, also named as Helicon RF [133], [134].	31
Figure. 1- 10 Schematic diagram of multicusp ion source [145].	32
Figure. 1- 11 Needle type liquid metal ion source used in Focused Ion Beam machines. (a) Liquid metal ion source. (b) Ion emission process.	34
Figure. 1- 12 LMIS with a pyramidal tip, terminated with three atoms at apex. Helium atoms get ionized only in the vicinity of apex where the electric field is enhanced [157].	35

Figure. 1- 13 Schematics of Laser-cooled ion source [178].	36
Figure. 2- 1 Electron ionization process to generate ions.	51
Figure. 2- 2 Experimentally measured ionization cross sections of different ions as a function of incident electron energies. Data is extracted from Ref [10], [11].	52
Figure. 2- 3 Schematic of NAIS configuration and its dimensions.	54
Figure. 2- 4 Knudsen number K_n regimes.	54
Figure. 2- 5 Knudsen number K_n for hydrogen, helium, and argon as a function of characteristic length L for various gas pressures at room temperature (293 K).....	55
Figure. 2- 6 Electron probe current density J_e and current I_e as a function of electron probe size d_p for tungsten, LaB ₆ and Schottky emitters for 1 keV electron.....	58
Figure. 2- 7 Ion current I_i and reduced brightness B_r as a function of characteristic length L for tungsten SEM with 1 keV injected electron beam.	60
Figure. 2- 8 Ion current I_i and reduced brightness B_r as a function of characteristic length L for LaB ₆ SEM with 1 keV injected electron beam.	60
Figure. 2- 9 Ion current I_i and reduced brightness B_r as a function of characteristic length L for Schottky SEM with 1 keV injected electron beam.	61
Figure. 3- 1 NAIS simulation flow chart.	72
Figure. 3- 2 Gas pressure contour of the ionization chamber, simulated by COMSOL.	74
Figure. 3- 3 A rotationally symmetric simplified ionization chamber model for COMSOL simulation.	74
Figure. 3- 4 Hydrogen gas pressure distribution (simulated by COMSOL) for 100 nm spacing, 100 nm membranes, and 100 nm double-aperture configuration at 10 bar inlet gas pressure.....	75
Figure. 3- 5 Axial normalized hydrogen gas pressure distributions (normalized to the inlet hydrogen gas pressure, data extracted from COMSOL) for various L_a corresponding to a fixed spacing, L_s , of a) 100 nm, b) 200 nm, c) 500 nm, and d) 1 μm . In all above simulations $L_m = L_s$	76
Figure. 3- 6 Hydrogen gas pressure distribution (simulated by COMSOL) for 100 nm spacing, 100 nm membranes, and 100 nm double-aperture configuration at 10 bar inlet gas pressure. Right top: Axial normalized hydrogen gas pressure distribution. Left bottom: Radial normalized hydrogen gas pressure distribution.....	77

Figure. 3- 7 Hydrogen gas flow velocity (simulated by COMSOL) for 100 nm spacing, 100 nm membranes, and 100 nm double-aperture configuration. Top: hydrogen inlet gas pressure at 10 bar. Bottom: hydrogen inlet gas pressure at 1 bar. 79

Figure. 3- 8 Hydrogen gas pressure distribution (simulated by COMSOL) for 1 μm spacing, 1 μm membranes, and 1 μm double-aperture configuration at 10 bar inlet gas pressure. Right top: Axial normalized hydrogen gas pressure distribution. Left bottom: Radial normalized hydrogen gas pressure distribution. 80

Figure. 3- 9 Hydrogen gas flow velocity (simulated by COMSOL) for 1 μm spacing, 1 μm membranes, and 1 μm double-aperture configuration. Top: hydrogen inlet gas pressure at 1 bar. Bottom: hydrogen inlet gas pressure at 0.1 bar. 81

Figure. 3- 10 Schematic of the NAIS setup to simulate its performance. Initial proton beam is represented by light yellow circles. Ionization only happens at the double-aperture region, with a well confined gas distribution. The initial ion beam in NAIS is uniform in radial direction, and has a Gaussian distribution along the z-axis. 83

Figure. 3- 11 Electric field distributions with cylindrical symmetry (simulated by Poisson/ Superfish code). Top: For the NAIS chip with an extractor having an electric field of 10^6 V/m (Si_3N_4 membranes and metal electrodes are not visible due to the small size). Bottom: Close view of the double-aperture region with an electric field of 10^7 V/m 84

Figure. 3- 12 Initial beam parameters for characteristic lengths of 100 nm. a) Normalized energy distribution, satisfying the Maxwell-Boltzmann distribution at room temperature. b) Normalized z-axis distribution. c) Normalized velocity distribution in the transverse plane, satisfying a Gaussian distribution (where c is the speed of light). d) Beam in the transverse plane with a uniform distribution. e) Beam distribution at the z-x plane. f) Phase space with a Gaussian distribution of velocity in the transverse plane, where c is speed of light. 85

Figure. 3- 13 Proton beam trajectory simulation for characteristic lengths of 100 nm (simulated by GPT) a) Proton beam trajectory in large scale. b) Proton beam energy as a function of beam path z . c) Proton beam trajectory in NAIS region. d) Proton beam rms emittance in x direction as a function of beam path z 88

Figure. 3- 14 Proton beam characteristics at $z = 4 \text{ mm}$ plane for a characteristic length of 100 nm (simulated by GPT) a) Transverse beam distribution. b) Transverse phase space distribution. c) Beam energy spread distribution, satisfying a Gaussian distribution with a standard deviation of 1.1 eV. 89

Figure. 3- 15 Normalized rms emittance and reduced brightness as a function of extraction field. Emittance is normalized to extractor potential for comparison. 90

Figure. 3- 16 NAIS source performances as a function of the NAIS electric field at a fixed extractor potential of -1 keV for a characteristic length of 100 nm. a) rms emittance vs NAIS electric field. b) Extracted proton current vs NAIS field. c) Reduced brightness vs NAIS field. d) Energy spread vs NAIS field. e) Virtual source size vs NAIS field. 92

Figure. 3- 17 NAIS source performances as a function of the NAIS electric field at a fixed extractor potential of -1 keV for a characteristic length of 1 μm . a) rms emittance vs NAIS electric field. b) Extracted proton current vs NAIS field. c) Reduced brightness vs NAIS field. d) Energy vs NAIS field. e) Virtual source size vs NAIS field.93

Figure. 3- 18 NAIS emittance as a function of extracted beam current at a fixed extractor potential of -1 keV. NAIS electric fields are 10^7 V/m and 10^6 V/m for characteristic length of 100 nm and 1 μm , respectively. a) For H_2^+ with 100 nm. b) For H^+ with 100 nm. c) For H_2^+ with 1 μm . d) For H^+ with 1 μm97

Figure. 3- 19 NAIS rms energy spread as a function of extracted beam current at a fixed extractor potential of -1 keV. NAIS electric fields are 10^7 V/m and 10^6 V/m for characteristic length of 100 nm and 1 μm . a) For H_2^+ with 100 nm. b) For H^+ with 100 nm. c) For H_2^+ with 1 μm . d) For H^+ with 1 μm98

Figure. 3- 20 NAIS reduced brightness as a function of extracted beam current at a fixed extractor potential of -1 keV. NAIS electric fields are 10^7 V/m and 10^6 V/m for characteristic length of 100 nm and 1 μm , respectively. a) For H_2^+ with 100 nm. b) For H^+ with 100 nm. c) For H_2^+ with 1 μm . d) For H^+ with 1 μm99

Figure. 4- 1 NAIS reduced brightness measurement, carried out inside a Philips XL30 ESEM. a) Schematic. b) The actual setup inside the ESME.....105

Figure. 4- 2 Total Ar ion current as a function of extraction voltage. The inlet argon gas pressure was maintained at 700 mbar and chip bias was fixed at 9 V. Reproduced from Ref. [7].....107

Figure. 4- 3 Total Ar ion current as a function of chip bias. A 700 mbar inlet argon gas pressure and -1.55 kV extraction voltage were used. Reproduced from Ref. [7]....108

Figure. 4- 4 Total Ar ion current as a function of chip bias. A 700 mbar inlet argon gas pressure and -1.55 kV extraction voltage were used. Reproduced from Figure. 4-25(b) in Ref. [7].....109

Figure. 4- 5 Simulated virtual source size as a function of chip bias by GPT.110

Figure. 4- 6 Reduced brightness as a function of chip bias.....111

Figure. 4- 7 Depiction of NAIS with recessed Si_3N_4 chip fabrication process: a) DRIE to create gas inlet and double-aperture windows on silicon nitride. b) KOH etching to reach the bottom side of silicon nitride membrane. c) 10 nm Cr + 20 nm Au deposited by magnetron sputtering for electrode. d) 150 nm depth ionization spacer created by DRIE. e) NAIS chip bonded with two individual chips and FIB-milled for creating gas inlet aperture and double-aperture. The diameter of the double-aperture is 500 nm. (f) A fabricated NAIS chip with a $300 \mu\text{m} \times 300 \mu\text{m}$ gas inlet and $50 \mu\text{m} \times 50 \mu\text{m}$ double-aperture windows, the double-aperture is ~500 nm diameter.114

Figure. 4- 8 Schematics of NAIS chip holder. a) 3D view of NAIS chip holder. b) Sectional view of NAIS chip holder. c) Reverse 3D view of NAIS chip holder.....115

Figure. 4- 9 JEOL JSM-5600 W SEM at Department of Physics, NUS.....116

Figure. 4- 10 SEM image (taken by field emission SEM, FEI Verios 460) of the double-aperture after being used.....117

Figure. 4- 11 Reduced brightness measurement of NAIS with recessed Si₃N₄, carried out inside a JEOL JSM-5600 W SEM. a) Schematic of brightness measurement set-up. b) The actual setup inside the W SME.....118

Figure. 4- 12 Detailed schematic setup of NAIS and the brightness measurement. 120

Figure. 4- 13 Double-aperture window model (not at scale) for COMSOL simulation. The gray slab represents the silicon nitride with the double aperture in the middle. 122

Figure. 4- 14 Deformation of the Si₃N₄ membranes for different areas of double-aperture window for characteristic length of 1 μm. The gap between lines is the double-aperture window's diameter.....123

Figure. 4- 15 Deformation of the Si₃N₄ membranes for different sizes of double-aperture window for characteristic length of 100 nm. The gap between lines is the double-aperture124

Figure. 4- 16 Schematic for a general geometry for the proposed NAIS used for COMSOL Multiphysics simulation. The blue slab represents the silicon nitride with the double aperture in the middle, and the supporting silicon grid structure, on the silicon nitride, is shown in grey.125

Figure. 4- 17 Deflection of the Si₃N₄ membrane with silicon supporting grid structure.126

Figure. 4- 18 A top view of NAIS chip with internal electrodes.127

Figure. 5- 1 Trajectories and backscattered yield (BY) of protons (200 protons) for different incident energies (100 eV, 1 keV and 10 keV) in silicon. Simulated using Monte Carlo simulation program SRIM [16].135

Figure. 5- 2 Schematic of three-aperture Einzel lens. It consists of three apertures with first (entrance) and third (exit) apertures at same electric potential. The potential of the middle aperture is used to adjust the focus of the beam.137

Figure. 5- 3 Illustration of miniaturized Einzel lens, consisting of a collimator aperture (top aperture) and three-aperture focus lens.138

Figure. 5- 4 Proton probe size as function of probe current for different three-aperture sizes for acceleration-declaration (A-D) and deceleration-acceleration (D-A) modes with 100 eV protons.....141

Figure. 5- 5 Proton probe size as function of probe current for different three-aperture sizes for acceleration-declaration (A-D) and deceleration-acceleration (D-A) modes with 1 keV protons.....141

Figure. 5- 6 Proton beam lateral spread radii in PMMA for 100 keV, 200 keV and 500 keV, calculated from SRIM. These plots were obtained by accounting for 90 % of the total incoming protons.144

Figure. 5- 7 Schematic of a proposed c-PBW system for sub-10 nm lithography with 200 kV terminal voltage, integrated with a NAIS. (a) Electron injector, (b) NAIS, (c) Extractor, (d) Condenser lens, (e) Acceleration tube, (f) Electrostatic scanner, (g) Focusing lenses, (h) Sample stage.146

Figure. 5- 8 Layout of focusing lens configurations. (a) Russian quadruplet configuration with 4 lenses and (b) Spaced Oxford triplet configuration with 3 lenses.147

Figure. 5- 9 Proton beam FW50 widths in X and Y directions for (a) proton beam widths in X and Y directions with the variation of beam current and (b) proton beam divergence a with the variation of beam current, for Russian quadruplet lens configuration, (c) proton beam widths in X and Y directions with the variation of beam current and (d) proton beam divergence a with the variation of beam current, for spaced Oxford triplet lens configuration.150

Figure. 5- 10 Achievable smallest proton beam FW50 widths in X and Y directions as a function of overall system energy spread with > 0.2 pA beam current for (a) Russian quadruplet lens configuration, and (b) spaced Oxford triplet lens configuration.151

Figure. 5- 11 Proton beam widths in X and Y directions as a function of scan size, (a) Russian quadruplet lens configuration, (b) Spaced Oxford triplet lens configuration.152

Figure. A1- 1 Ideal lens: A beam passing the lens at distance r_0 from the optical axis is deflected by an angle $\Delta\alpha = a_1 r_0$160

Figure. A1- 2 An image d_i of an object d_o in an ideal lens.....161

Figure. A1- 3 Chromatic aberration showing parallel beam having different energies are focused at two different points. F is the focal point for beam with energy E_0 ..162

Figure. A1- 4 Chromatic aberration with magnification M . Different energy beams are focused onto different points. F is the focal point for parallel beam with energy E_0164

Figure. A1- 5 Schematic showing spherical aberration. The parallel beams far away from optical axis are deflected more strongly, creating a disc in the Gaussian image plane. F is the focal point.165

Figure. A1- 6 Schematic showing spherical aberration with magnification of M . The blue dash line represents the beam ray for ideal lens.....166

Figure. A1- 7 Schematic showing diffraction aberration, where a point is blurred to an Airy disc in the Gaussian image plane with a small convergence semi-angle α_i167

Figure. A2- 1 Minimal probe size d_p as a function of probe current I_p for different electron emitters and lens conditions for 1 keV electron beam. The individual contributions to the total probe size from a demagnified virtual source size d_I at image plane, chromatic aberration d_C , spherical aberration d_S , and diffraction aberration d_A are shown. a) Tungsten emitter ($\Delta E = 1$ eV) with a pinhole lens ($C_C = 10$ mm, $C_S = 20$ mm). b) LaB₆ emitter ($\Delta E = 1$ eV) with a pinhole lens ($C_C = 10$ mm, $C_S = 20$ mm). c) Schottky emitter ($\Delta E = 0.3$ eV) with a snorkel lens ($C_C = 3$ mm, $C_S = 3$ mm). d) Cold field emitter ($\Delta E = 0.2$ eV) with a snorkel lens ($C_C = 3$ mm, $C_S = 3$ mm).....172

Figure. A2- 2 Minimal probe size d_p as a function of probe current I_p for tungsten, LaB₆, Schottky, and cold field emitters for 1 keV electron beam, data compiled from Figure. A2-1.....173

List of abbreviations

1D	One-Dimensional
2D	Two-Dimensional
3D	Three-Dimensional
4D	Four-Dimensional
6D	Six-Dimensional
C-PBW	Compact-Proton Beam Writing
DRIE	Deep Reactive Ion Etching
DI Water	Deionized Water
EBL	Electron Beam Lithography
EI	Electron Ionization
ESEM	Environmental Scanning Electron Microscope
EUV	Extreme Ultraviolet
FIB	Focused Ion Beam
FW50	Full Width 50%
GSIF	Gas Field Ion Source
HIM	Helium Ion Microscope
HSQ	Hydrogen Silsesquioxane
IBL	Ion Beam Lithography
ISS	Ion Scattering Spectroscopy
K-V	Kapchinskij-Vladimirskij
KOH	Potassium Hydroxide
LEEM	Low Energy Electron Microscopy
LEIS	Low Energy Ion Scattering
LMIS	Liquid Metal Ion Source
LPCVD	Low-Pressure Chemical Vapor Deposition
MEMS	Microelectromechanical Systems
NAIS	Nano-Aperture Ion Source
PBW	Proton Beam Writing
PMMA	Polymethyl Methacrylate
RF	Radio-Frequency
SCL	Space Charge Limited
SEM	Scanning Electron Microscope
Si₃N₄	Silicon Nitride
STIM	Scanning transmission microscopy
UV	Ultraviolet

Chapter 1. Introduction

Ion sources have spurred development in scientific, industrial and medical fields, including nuclear physics, mass spectroscopy, particle accelerator, imaging, lithography, ion etching, ion implantation, ion engine, radiation therapy, etc. Generally, plasma generator and extractor are the critical components in ion sources. Plasma generator produces a fundamental state of matter, plasma [1], and serves as an ion reservoir [2]. The development of ion sources spans many disciplines, which depend on the different mechanisms to generate plasma, the so-called ionization process. The ionization process has various approaches, namely, field ionization, thermal ionization, photoionization, electron impact ionization, chemical ionization, etc. [2], [3]. Both positive and negative ions can be generated through an ionization process. The extractor is employed to guide, shape and accelerate the beam, and/or remove unwanted charged particles. The extraction system transfers the beam from plasma generator to next beam transport system for further study or usage.

Ion sources have been extensively studied for over a century, but the research is still continuing to grow drastically due to the emergence of new fields. Till date, more than a hundred principal types of sources have been developed and these new sources are being exploited for different applications [4]. In our laboratory, Centre for Ion Beam Applications (CIBA), National University of Singapore (NUS), we have developed a new technique, Proton Beam Writing (PBW) [5]–[7], which uses focused MeV protons/ H_2^+ to pattern three-dimensional (3D) nanostructures on photoresists. However, the current low brightness $\sim 20 \text{ A}/(\text{m}^2\text{srV})$ radio-frequency (RF) ion source, employed in the PBW system [8]–[10], restricts the resolution and throughput of PBW. At the same time, the footprint of such system is very large, all of which limit widespread applications of the technique. High writing speed and sub-10 nanometer resolution require high beam brightness and low energy spread of the ion source. This chapter

servers as an introduction and review of different ion sources and PBW technique. The characteristics of a charged particle beam are also described within this chapter. Finally, the motivation and an outline of this thesis are presented.

1.1 Characteristics of an ion source

The resolution and current density of a charged particle beam at the image plane are determined by ion source, beam transport system, and Coulomb interactions [11]. The two intrinsic parameters of an ion source, namely, brightness and energy spread determine the ultimate spot size and probe current in an ion beam system.

1.1.1 Liouville's theorem

Liouville's theorem states that the phase-space distribution function of a charged particle beam is constant along its path. A six-dimensional (6D) conceptual Euclidean space is constructed, using Cartesian coordinates q_i and its conjugate momenta p_i , in which every particle's status can be represented as a point $\mathbf{U} = \{q_i, p_i\}$ ($i = x, y, z$). All the particles occupy a volume in the hyperspace, so called phase space, with a density distribution ρ . ρ is a function of q_i, p_i and time t , which can be described by \mathbf{U} and t . A velocity vector $\mathbf{W} = \dot{\mathbf{U}} = \frac{d\mathbf{U}}{dt} = (\dot{q}_i, \dot{p}_i)$ can be employed to describe the motion of system acted upon by different forces. This velocity vector is equivalent to the “law of motion” in the phase space.

Assuming the system is a conservative system, the Hamiltonian $H(q_i, p_i, t)$ of the system can be described as

$$\begin{cases} \frac{\partial H}{\partial p_i} = \dot{q}_i \\ \frac{\partial H}{\partial q_i} = -\dot{p}_i \end{cases} \quad (i = x, y, z) \quad (1.1)$$

As a result,

$$\nabla \cdot \mathbf{W} = \frac{\partial \dot{q}_i}{\partial q_i} + \frac{\partial \dot{p}_i}{\partial p_i} = \frac{\partial^2 H}{\partial p_i \partial q_i} - \frac{\partial^2 H}{\partial q_i \partial p_i} = 0 \quad (1.2)$$

This shows that no source or sink (divergence-free) exists in the velocity vector.

Since charged particles cannot be generated or extinguished in the beam transport system, the number of corresponding points in the phase space remains constant and therefore the continuity equation is given as

$$\begin{aligned}\frac{\partial \rho}{\partial t} + \nabla \cdot (\rho \mathbf{W}) &= \frac{\partial \rho}{\partial t} + \nabla \rho \cdot \mathbf{W} + \rho (\nabla \cdot \mathbf{W}) \\ &= \frac{\partial \rho}{\partial t} + \left(\frac{\partial \rho}{\partial q_i} \dot{q}_i + \frac{\partial \rho}{\partial p_i} \dot{p}_i \right) = 0\end{aligned}\tag{1.3}$$

Because

$$\frac{d\rho}{dt} = \frac{\partial \rho}{\partial t} + \left(\frac{\partial \rho}{\partial q_i} \dot{q}_i + \frac{\partial \rho}{\partial p_i} \dot{p}_i \right)\tag{1.4}$$

So

$$\frac{d\rho}{dt} = \frac{\partial \rho}{\partial t} + \left(\frac{\partial \rho}{\partial q_i} \dot{q}_i + \frac{\partial \rho}{\partial p_i} \dot{p}_i \right) = 0\tag{1.5}$$

This is defined as Liouville's theorem which indicates that the density of ensemble of particles is constant in the phase space.

In the above discussion, we know that the number of points in the phase space remains constant, and can be expressed as

$$\frac{d(\delta N)}{dt} = \frac{d(\rho \delta V)}{dt} = \frac{d\rho}{dt} \delta V + \rho \frac{d(\delta V)}{dt} = 0\tag{1.6}$$

where N and V are the number and volume of points in the phase space respectively.

From Eq. 1.5,

$$\frac{d(\delta V)}{dt} = \frac{d}{dt} \int d^3 q_i d^3 p_i = 0\tag{1.7}$$

This is an alternative expression of Liouville's theorem showing that the volume of points in the phase space is time-invariant. It also can be stated as

$$\int d^3q_i d^3p_i = \text{const} \quad (1.8)$$

Generally, the shape changes when the points move.

If there is no coupling between x , y and z directions, the Liouville's theorem can be projected to two-dimensional (2D) phase space as the phase-space area remains constant,

$$\int dq_x dp_x = \text{const} \quad (1.9)$$

Strictly speaking, Liouville's theorem is deduced based on the hypothesis of conservative force system. However, Liouville's theorem is still valid, as long as the interaction between neighboring particles (statistical effects) is negligible when compared with the interaction between the individual particle and the average collective field generated by the ensemble of particles (so-called space charge effect) [12], [13].

1.1.2 Emittance and brightness

A charged particle beam from an ion source always possesses a spread in its kinetic energy [12]. Therefore a quantitative parameter called emittance ε , is introduced to describe this intrinsic spread, and to characterize the beam quality. For the following discussion, z -direction is the longitudinal direction, whereas (x, y) is the transverse plane of the beam.

The emittance in transverse plane (x, x') , also named as the effective emittance, is expressed as [14], [15] (shown in Figure. 1-1)

$$\varepsilon_x = \frac{1}{\pi} \iint dx dx' = \frac{A_{xx'}}{\pi} \quad (1.10)$$

In which x is the transverse trajectory and x' is defined as $x' = \frac{dx}{dz} = \frac{\dot{x}}{\dot{z}} \approx \frac{P_x}{P}$, $A_{xx'}$ is the area of the beam occupied in the phase space. P and P_x are the beam overall momentum

and momentum component in x direction, respectively. The normalized emittance is introduced as [15]

$$\varepsilon_{nx} = \beta\gamma\varepsilon_x \quad (1.11)$$

Where $\beta = v/c$ and γ is Lorentz factor. v and c are beam velocity and speed of light, respectively. If there is no coupling between x , y and z motion, when the beam is subjected to a linear focus force, and when the Coulomb effects are negligible, the normalized emittance is conserved according to Liouville's theorem.

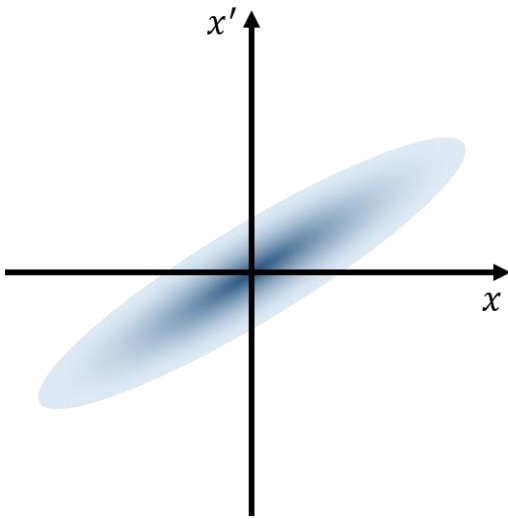


Figure. 1- 1 Description of emittance ε_x . The emittance is equal to the area A_{xx} , in phase space occupied by beam particles divided by π .

In reality, it is not convenient to define the phase space area because of fuzzy edges. To avoid this effect, the root-mean-squared (*rms*) emittance in subspace is used as [16], [17]

$$\varepsilon_{x rms} = \sqrt{\langle x^2 \rangle \langle x'^2 \rangle - \langle x^2 x'^2 \rangle} \quad (1.12)$$

Here $\langle \rangle$ indicate the average over the distribution of charge particle beams.

While emittance is used to only characterize the beam quality, brightness B is used to describe the beam quality as well as useful beam current. This brightness depends on both current I emitting from a virtual source area A (also called as virtual/effective source size) and solid angle Ω subtended, as in Figure. 1-2 [18]–[21],

$$B = \frac{d^2I}{d\Omega dA} = \frac{d^4I}{dx dx' dy dy'} \quad (1.13)$$

The average brightness can be described as

$$\bar{B} = \frac{I}{\iint d\Omega dA} = \frac{I}{V_4} \quad (1.14)$$

where $V_4 = \iint d\Omega dA$ is the integral of the occupied volume in the four-dimensional (4D) phase space for the transverse plane. Generally, a hyperellipsoid distribution in the 4D phase space can be formulated as [12]

$$\frac{x^2}{a^2} + \left(\frac{ax'}{\epsilon_x}\right)^2 + \frac{y^2}{b^2} + \left(\frac{by'}{\epsilon_y}\right)^2 = 1 \quad (1.15)$$

The integral of the occupied volume $V_4 = \iint d\Omega dA = (\pi^2/2)\epsilon_x\epsilon_y$. As a result, the average brightness is given by

$$\bar{B} = \frac{I}{V_4} = \frac{2I}{\pi^2\epsilon_x\epsilon_y} \quad (1.16)$$

This average brightness can be expressed in the situation where different amounts fractions of the beam are included, such as 100%, 90%, 50%, etc.

According to normalized emittance, the reduced brightness is introduced to eliminate the influence of beam energy or moment,

$$B_n = \frac{B}{\beta^2\gamma^2} \quad (1.17)$$

Noticing that the conventional definition of normalized emittance (as illustrated in Figure. 1-2) is given by

$$B_n = \frac{d^2I}{Ud\Omega dA} \approx \frac{I}{U\pi\alpha_0^2 A} \quad (1.18)$$

Where U is the longitudinal potential, Ω is the solid angle, A is the virtual source area, and α_0 is the beam half angle. For a proper comparison to conventional definition, the reduced brightness is multiplied by a constant factor of $\frac{2e}{mc^2}$ from definition of Eq. 1.17,

$$B_n = \frac{2eB}{mc^2\beta^2\gamma^2} \quad (1.19)$$

where e is elementary charge and m is the ion rest mass.

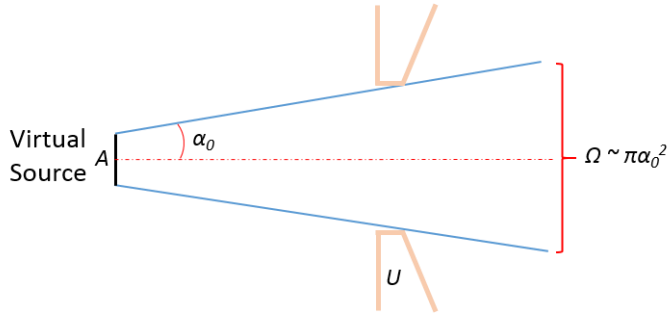


Figure. 1- 2 Charged particles are emitted from a virtual source with an area of A (the smallest area when tracing back the beam trajectory), and accelerated to the potential of U with a solid angle Ω . For small angle, $\Omega \sim \pi\alpha_0^2$.

A simple and clear example of a hyperellipsoid distribution is waterbag model formed by a uniformly filled ellipsoid in the 4D phase space. Due to the uniformity of the hyperellipsoid, the average brightness and peak brightness are the same [15]. The projection into the 2D subspace is still an ellipse, but with a parabolic density distribution, decreasing from the center to edge [22]. The effective emittance is

$$\epsilon_x = 6\epsilon_{x rms} \quad (1.20)$$

The average brightness \bar{B} and peak brightness \hat{B} are

$$\bar{B} = \hat{B} = \frac{2I}{\pi^2\epsilon_x\epsilon_y} = \frac{I}{18\pi^2\epsilon_{x rms}\epsilon_{y rms}} \quad (1.21)$$

The other example is the beam with 4D uniform ellipsoidal shell distribution, named as Kapchinskij-Vladimirskij (K-V) distribution [14]. In this scenario, any projected 2D plane (e.g. (x, y) , (x, x')) produces a uniform ellipse distribution. For the initial beam

or in the beam waist, the phase space ellipse is upright and the effective emittance is, by symmetry,

$$\epsilon_x = 4\epsilon_{x rms} \quad (1.22)$$

The average brightness \bar{B} is

$$\bar{B} = \frac{2I}{\pi^2 \epsilon_x \epsilon_y} = \frac{I}{8\pi^2 \epsilon_{x rms} \epsilon_{y rms}} \quad (1.23)$$

Because the reduced emittance, $\epsilon_{nx} = \beta\gamma\epsilon_x = 4\beta\gamma\epsilon_{x rms} = 4\beta\gamma x_{rms} x'_{rms}$, in which x_{rms} and x'_{rms} are the rms width $\sqrt{\langle x^2 \rangle}$ and divergence $\sqrt{\langle x'^2 \rangle}$. Then the average reduced brightness is expressed as

$$\bar{B}_n = \frac{4eI}{mc^2 \pi^2 \epsilon_{nx} \epsilon_{ny}} = \frac{eI}{4mc^2 \pi^2 \epsilon_{x rms} \epsilon_{y rms}} \quad (1.24)$$

Assume an initial beam with round uniform distribution in transverse plane, radius a and transverse velocity defined by Maxwell-Boltzmann distribution in 2D space as

$\exp[-m \frac{(v_x^2 + v_y^2)}{2kT}]$. Then the *rms* emittance is

$$\epsilon_{nx} = \frac{4}{c} x_{rms} v_{th rms} = 2a \sqrt{\frac{kT}{mc^2}} \quad (1.25)$$

where $v_{th rms}$ is the transverse *rms* velocity, *rms* width $x_{rms} = \frac{r_{rms}}{\sqrt{2}} = \frac{a}{2}$ and transverse *rms* velocity $v_{x rms} = \sqrt{\frac{kT}{m}}$.

From Eq. 1.24, the average reduced brightness is

$$\bar{B}_n = \frac{Ie}{\pi^2 a^2 kT} \quad (1.26)$$

which is corresponding to thermionic planar emitter brightness $B_n = \frac{Je}{\pi kT}$ with uniform current density $J = \frac{I}{\pi a^2}$ [23]. It shows that the reduced brightness is governed by

environmental temperature, beam current and virtual source size. The environment temperature determines the beam initial energy, resulting in intrinsic angular spread of beam.

Another interesting and more realistic model is Gaussian distribution in 4D phase space.

The effective emittance is [24]

$$\epsilon_x = n^2 \epsilon_{x rms} \quad (1.27)$$

where the beam envelope is truncated at $n\delta$ ($n \geq 4$) and δ is the standard deviation of the Gaussian distribution.

The peak brightness is [15]

$$\hat{B} = \frac{I}{4\pi^2 \epsilon_{x rms} \epsilon_{y rms}} \quad (1.28)$$

And the average brightness \bar{B} can be approximated from Eq. 1.16 as

$$\bar{B} = \frac{2I}{\pi^2 \epsilon_x \epsilon_y} = \frac{2I}{n^2 \pi^2 \epsilon_{x rms} \epsilon_{y rms}}, (n \geq 4) \quad (1.29)$$

For an ideal beam transport system, the reduced emittance and brightness remain constant according to Liouville's theorem. But in the real laboratory beams, a lot of factors, such as external effects (e.g. nonlinear applied force and aberrations) and internal effects (Coulomb effects) increase the reduced emittance (emittance growth). The internal Coulomb effects originate from the beam itself and will be discussed in a later section.

1.1.3 Beam intrinsic energy and energy spread

In most situations, ions will inherit their original gas's thermal energy with Maxwell-Boltzmann distribution. This intrinsic thermal energy will contribute to the initial angular spread of the beam, defining the emittance in the transverse plane. The velocity distribution function is given by

$$(v_x, v_y, v_z) = \left(\frac{m}{2\pi kT}\right)^{3/2} \exp\left[-\frac{m(v_x^2 + v_y^2 + v_z^2)}{2kT}\right] \quad (1.30)$$

where m is the charged particle mass and k is the Boltzmann constant. The three-dimensional Maxwell-Boltzmann velocity distribution is the product of the distributions for three independent directions $f(v_x, v_y, v_z) = f(v_x)f(v_y)f(v_z)$, where one-dimensional (1D) velocity distribution is

$$f(v_i) = \left(\frac{m}{2\pi kT}\right)^{1/2} \exp\left[-\frac{m(v_i^2)}{2kT}\right], (i = x, y, z) \quad (1.31)$$

which is a normal distribution with a mean velocity $\bar{v}_i = 0$.

The speed distribution is obtained from $dv_x dv_y dv_z = v^2 \sin\theta dv d\theta d\phi$, given as

$$F(v) = 4\pi v^2 \left(\frac{m}{2\pi kT}\right)^{3/2} \exp\left(-\frac{mv^2}{2kT}\right) \quad (1.32)$$

and the energy distribution is

$$f(E) = F(v) \frac{dv}{dE} = 2 \sqrt{\frac{E}{\pi}} \left(\frac{1}{kT}\right)^{3/2} \exp\left(-\frac{E}{kT}\right) \quad (1.33)$$

The mean kinetic energy $\bar{E} = \frac{3}{2}kT$, and the three independent one-dimensional mean kinetic energies $\bar{E}_i = \frac{1}{2}kT$, will determine the initial beam angular spread and emittance. To achieve a high brightness ion beam, one approach is to reduce the operational temperature for low angular spread, while the other approach is to increase the beam current density.

For a charged beam, it usually has the longitudinal energy distribution ($E \pm \Delta E$). This plays a crucial role in characterizing the beam property and consequently affects the resolution of focused beam. This energy spread ΔE introduces chromatic aberration in the beam transport system, thereby results in a broadened beam (elaborated in Appendix 1). Generally, there are three factors contributing to the longitudinal energy

spread. First, the intrinsic energy spread originates from the initial thermal energy. The longitudinal beam energy spread is an inherent beam energy spread related to the operational temperature of the ion source, named as *rms* energy spread as kT . The second contribution to the longitudinal energy spread is caused by the different ion generation positions resided in different electric potentials of the ion source. This energy spread can be reduced by generating ions in a small source region with a desired electric field. Whereas, the third contributor for energy spread is attributed to the Coulomb effects among the ions, including Boersch effect [25] and trajectory displacement effect [26], which will be discussed in the following section.

1.1.4 Coulomb effects

According to Liouville's theorem, the reduced emittance of a beam stays constant with the assumption of the conservative force. But in reality, there also exists particle-particle interactions, attributed to Coulomb effects. Generally, Coulomb effects consist of three different types: space charge effect, Boersch effect, and trajectory displacement effect [12]. The space charge effect is deflection of a charged particle via the self-generated field from the beam. The Boersch effect and trajectory displacement effect are classed as statistical effects, stemming from individual pairs of particle-particle interaction. Here, an important factor to clarify the influence of Coulomb effects is Debye length λ_D , which will be introduced first.

Debye length λ_D is given by the combination of electron and ion Debye lengths λ_{D_e} and λ_{D_i} [27],

$$\frac{1}{\lambda_D^2} = \frac{1}{\lambda_{D_e}^2} + \frac{1}{\lambda_{D_i}^2} = \frac{q_e^2 n_e}{\varepsilon_0 k T_e} + \frac{q_i^2 n_i}{\varepsilon_0 k T_i} \quad (1.34)$$

where $q_e(q_i)$ are the electron (ion) charges; $n_e(n_i)$ are the electron (ion) densities; $T_e(T_i)$ are the temperatures of the electrons (ions) respectively, ε_0 is the electric constant. If the dimension of plasma is much larger than the Debye length λ_D , the plasma will

have a shielding effect that limits the maximum plasma density (same for beam current density), known as “Debye shielding”. This Debye shielding comes from space charge effect caused by the self-generated field. One remarkable point should be noticed is that most literature only employs the electron Debye length ($\lambda_D \rightarrow \lambda_{D_e}$) as an approximation, with an assumption that ions move much slower than electrons due to the heavy mass. But, the key determinant is ion temperature rather than mass, which means the approximation ($\lambda_D \rightarrow \lambda_{D_e}$) only happens when $T_e \gg T_i$ in a neutralizing background of plasma. The ion Debye length must be taken into consideration in case of non-neutralizing background of plasma, similar electron and ion densities, and the different charge state of ions.

For the scenario where the beam dimension is much larger than the Debye length λ_D , the self-generated field will function and collective effects will be important. The space charge limited (SCL) current located across two parallel electrodes can be described by Child-Langmuir law [28], [29].

For two-dimensional Child-Langmuir Law, the SCL current density $J(2)$ is given by [30]

$$J(2) \cong J(1) \left(1 + \frac{D}{\pi L_a}\right) = \frac{4\epsilon_0}{9D^2} \left(\frac{2e}{m}\right)^{1/2} V^{3/2} \left(1 + \frac{D}{\pi L_a}\right) \quad (1.35)$$

where $J(1)$ is the SCL current density in 1D model, D is the separation between two parallel electrodes, V is the potential across these electrodes, e and m are the charge and mass of charged particles, respectively, and L_a is the emitting width of the source. This SCL current density is the upper limit of current density, which is of fundamental importance for ion sources.

The influence of statistical effects caused by individual pairs of particle-particle interaction can be estimated by the mean free path l , given roughly as [31]

$$l \sim (n_i \lambda_{D_i}^3) \lambda_{D_i} \quad (1.36)$$

Roughly speaking, collisions can be ignored when the mean free path is much larger than beam size. Meanwhile, this particle-particle collision is to compare the beam radius (or inter particle-particle distance) with Debye length [12]. If the Debye length is much larger than beam radius ($\lambda_D \gg a$), the single-particle will dominate, meaning the Liouville's theorem will still hold. Otherwise, the inter particle-particle collision will dominate and degrade the emittance and increase the energy spread of the beam.

Boersch effect [25] is the phenomenon wherein the longitudinal energy gets broadened towards the thermodynamic equilibrium with the exchange of transverse energy, resulting in the increase of longitudinal temperature with the decrease of transverse temperature. As discussed in the previous part, the ion beam has an initial (intrinsic) energy following a Maxwell-Boltzmann distribution at the state of thermodynamic equilibrium, with transverse energy spread (defined as standard deviation, *rms* energy spread) $\overline{\Delta E}_{\perp i} = 2kT_{\perp i}$, and the longitudinal energy spread $\overline{\Delta E}_{\parallel i} = kT_{\parallel i}$, ($T_{\perp i} = T_{\parallel i} = T_i$). When the ion beam is generated in the source region, an extraction system extracts and accelerates the beam subsequently to the potential of V . The temperature in beam's longitudinal direction will be [12]

$$kT_{\parallel a} = \frac{(kT_{\parallel i})^2}{2qV} \quad (1.37)$$

One should be cautious about that the temperature here, as it is not the same as described in Debye length part. In case of Debye length, the overall average beam energy is referred to as the electron/ion temperature. Whereas in this case, the temperature is defined by the energy spread distribution which corresponds to the thermal distribution, also known as local temperature. As seen from Eq. 1.37, the longitudinal beam temperature $T_{\parallel a}$ reduces dramatically due to the acceleration ($T_{\parallel a} \ll T_{\parallel i}$), known as “cooling effect” from the acceleration. But in the transverse plane, no

acceleration/deceleration happens for the beam, the transverse beam temperature $T_{\perp a}$ remains constant as initial temperature $T_{\perp i}$. Due to the non-equilibrium state of energy spread between transverse plane and longitudinal direction, the “hot” temperature in transverse plane tends to transfer to longitudinal direction for a 3D thermodynamic equilibrium state, according to Coulomb collision and other processes. As a result, the energy spread and emittance in transverse plane will decrease while the longitudinal energy spread increases. The decreased transverse emittance has a positive effect and increases the brightness. However, the increased longitudinal energy spread will introduce more chromatic aberration, causing the degradation of the beam focus resolution.

The temperature relaxation is expressed in exponential functions as [12]

$$T_{\perp a} = \frac{2}{3} T_i (1 + \frac{1}{2} e^{-3t/\tau_{eff}}) \quad (1.38)$$

and

$$T_{\parallel a} = \frac{2}{3} T_i (1 - e^{-3t/\tau_{eff}}) \quad (1.39)$$

where the effective transverse-longitudinal temperature relaxation time τ_{eff} is described as

$$\tau_{eff} = \frac{15(4\pi\epsilon_0)^2 m^{1/2} (kT_{eff})^{3/2}}{8\pi^{1/2} n q^4 \ln \Lambda} \quad (1.40)$$

Here n is the beam current density $\frac{I}{qa^2\pi v}$, T_{eff} is the effective temperature, and $\ln \Lambda$ is the Coulomb logarithm,

For Debye length λ_D less than beam size,

$$\ln \Lambda = \ln \frac{3}{2\sqrt{\pi}} \frac{(kT_{eff}/mc^2)^{3/2}}{r_c^{3/2} n^{1/2}} \quad (1.41)$$

For Debye length λ_D larger than beam size,

$$\ln \Lambda = \ln \frac{3akT_{eff}}{r_c mc^2} \quad (1.42)$$

in which, I , a and v are the beam current, beam radius, and beam velocity, respectively,

r_c is the classical particle radius as $\frac{q^2}{4\pi\epsilon_0 mc^2}$. The energy spread in longitudinal direction

is

$$\Delta E_a = (2qV k T_{||a})^{1/2} \quad (1.43)$$

The final transverse and longitudinal temperatures at equilibrium state will be $T_{\perp f} =$

$T_{||f} = \frac{2}{3} T_i$. However, in general situation, the Boersch effect doesn't have enough time to achieve thermodynamic equilibrium, because the transverse-longitudinal temperature relaxation time is much longer than typical beam transporting time.

Particle-particle interaction does not only contribute to the Boersch effect, but also contributes to stochastic transverse trajectory displacements, known as trajectory displacement effect [26]. The change in transverse trajectory causes broadening of the virtual source size, resulting in deterioration of beam reduced brightness. The broadening of virtual source radius is proportional to the beam current density, given as [32]

$$r_{BR} \propto \frac{r^2 J^{2/3}}{V^{7/6}} \quad (1.44)$$

where J is the beam current density, r is the virtual source radius and V is the beam potential. This broadening in virtual source size results in a reduced brightness

$$B'_r = B_r \frac{r^2}{r^2 + r_{BR}^2} \quad (1.45)$$

Usually, the longitudinal displacement can be reduced when a strong electric field is applied to shorten the interaction time.

The space charge effect imposes an upper limit to the beam current. For a uniform round beam, this effect is linear to the transverse distance of the charged particle to the axis, causing a defocusing effect. Therefore, the system resolution will not be affected by the space charge effect since this effect can be compensated by external focus lens. But for a non-uniform beam, this effect should be taken into consideration. For Boersch effect and the trajectory displacement effect, these statistical Coulomb effects introduce the deterioration of beam quality. Statistical Coulomb effects become more significant at large beam current density and longer interaction time (low energy), which cannot be corrected by any external lens. This implies that low-energy equipment is restricted by these statistical effects [33]–[35]. An intermediate component to accelerate and then deaccelerate the beam is usually employed to minimise these effects. Generally speaking, at source region, the velocity of charged particles is slow and the current density is high, so the statistical Coulomb effects play a role and have to be considered more carefully in this region.

1.2 Proton beam writing (PBW)

Proton beams have been used in masked lithography since 1979 [36]. In early experiments, Adesida [37] and Brenner et al. [38] used 200 keV energy reproducing features in PMMA resist down to 50 nm in line width and 8 MeV energy proton beams respectively for masked irradiation of PMMA.

Proton beam writing (PBW) is a direct write 3D lithographic technique that utilizes fast and focused MeV proton or H_2^+ beams to pattern photoresists (e.g. hydrogen silsesquioxane (HSQ), SU-8, AR-P, and polymethyl methacrylate (PMMA)) and form sub-100 nm features in layers up to 10 μm thick [39], [40]. Focused MeV proton lithography was then demonstrated at Oxford University in 1993 [41] and further optimized at CIBA, NUS, with the world's first and dedicated PBW system with sub 100 nm writing capability [6]. This technique is also available at several other ion microprobe laboratories worldwide (Leipzig [42], Lund [43], Ljubljana [44], Debrecen [45], Guildford [46], Rez [47], Takasaki [48], Tokyo [49], etc.).

1.2.1 PBW facility at CIBA, NUS

The current PBW facility at CIBA, NUS as illustrated in Figure. 1-3, is the second generation PBW system. This PBW system employs a radio frequency (RF) ion source [8] within a 3.5 MV High Voltage Engineering Europa SingletronTM accelerator [50], [51]. This accelerator has the capacity to deliver different ions, such as H_2^+ , H^+ , He^+ , He^{2+} , O^+ , etc. These high-energy ion beams are being used at 6 different beamlines, at CIBA, NUS, where multi-disciplinary research activities are carried out. H_2^+ and proton are generated in the RF ion source, and then extracted and accelerated to about 1-2 MeV with a total beam current of $\sim 10s \mu A$. The desired ion beam (H_2^+ /proton, typical \sim few μA) is selected by the double focusing 90° analyzing magnet. The opening size of the object slits is very crucial as it is the object size for the quadrupole focus lens system, and is typically set at $7 \times 3 \mu m^2$. Next, the switching magnet steers the beam

in the PBW beamline. The beam exiting the object slit drifts for about 7.5 m before being collimated using a collimator. Prior to the focusing system, an electrostatic scanner is utilized to scan the beam of in an area up to $150 \mu\text{m} \times 150 \mu\text{m}$ in the focal plane. The focusing system consists of three magnetic quadrupole lenses (Oxford Microbeams OM52) operated in a spaced Oxford triplet configuration with an $857 \times (-130)$ demagnification at X and Y directions [10]. The image distance is 30 mm, and the beam spot size is measured using an on/off-axis scanning transmission ion microscopy (STIM) and an ion-induced secondary electrons detector. With an image current of 0.013 pA, a $9.3 \times 32 \text{ nm}^2$ beam spot size for 2 MeV proton was achieved, which is the smallest beam size ever achieved for MeV protons [52]. The RF ion source in this current PBW system has a reduced source brightness, B_r , of $\sim 20 \text{ A}/(\text{m}^2\text{srV})$ [10], [50], restricting the beam resolution and throughput of PBW. Therefore a high brightness ion source is the key to further improve the performance of PBW system.

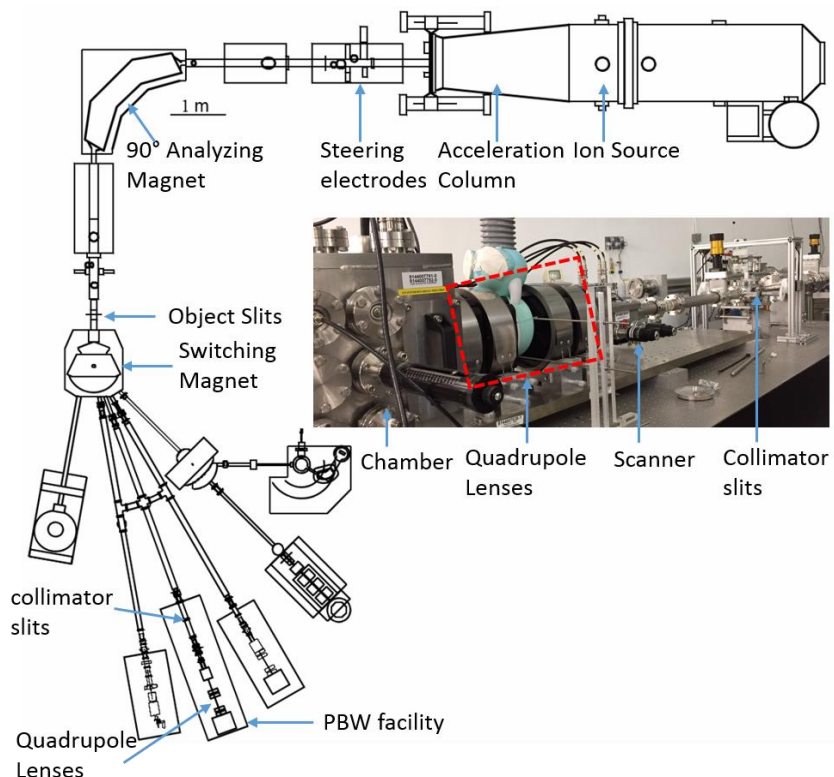


Figure. 1- 3 Proton beam writing (PBW) facility at CIBA, NUS, comprised of RF ion source, acceleration column, 90° analyzing magnet, object slits, switching magnet, collimator slits and quadrupole lenses.

1.2.2 Charged particle-matter interaction

To evaluate PBW, it is necessary to understand the behavior of charged particle-matter interactions. When an energetic charged particle beam is incident on the sample, several processes happen, causing the charged particles to slow down while they interact with the sample material. In total, the four different interaction processes occur described as follows [53], [54],

- (1) Inelastic interaction between incident charged particles and bound electrons in the matter.
- (2) Elastic interaction between incident charged particles and bound electrons in the matter.
- (3) Elastic interaction between incident charged particles and nuclei in the matter.
- (4) Inelastic interaction between incident charged particles and nuclei in the matter.

All the above interaction processes are caused by Coulomb field generated by electrons and nuclei. The incident charged particles can also penetrate the Coulomb field to trigger nuclear reaction, but this process has a very small cross section and can, therefore, be neglected here.

The inelastic interaction between charged particles and electrons, causes ionization or excitation of the bound electrons, resulting in generation of secondary electrons. This process is referred as electronic stopping. The elastic interaction between incident charged particles and nuclei is known as nuclear stopping power, forming displacement of atoms (defect) and surface sputtering. These two processes are the two primary energy loss mechanisms for incident charged particles. Therefore, the electronic and nuclear stoppings are the main interaction mechanisms, resulting in secondary electrons, backscattered ions, sputtered matter atoms and defect formation. For different species of charged particles, the different phenomena are triggered, based mainly on the mass and energy, as shown in Figure. 1-4.

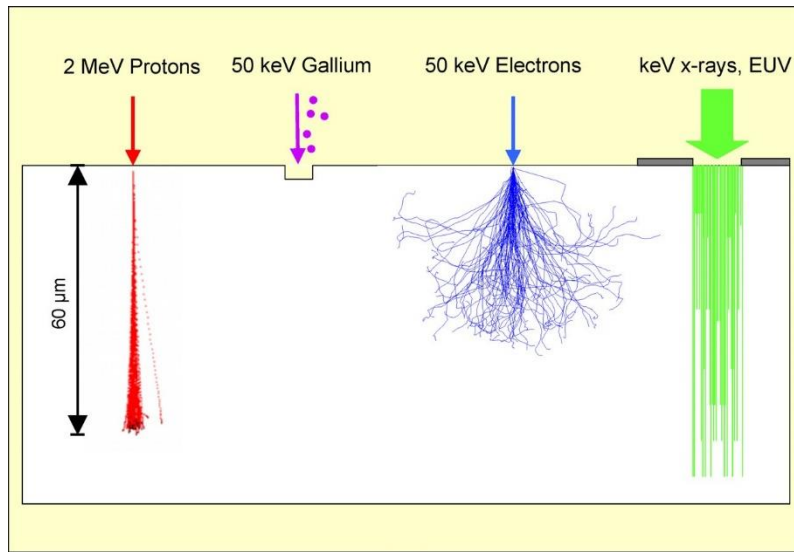


Figure. 1- 4 Beam trajectories of different beams: fast proton beam (2 MeV), slow heavy gallium beam (50 keV), electron beam (50 keV), and electromagnetic radiation (X-rays and EUV). Adapted from Ref [55].

For patterning structures on the photoresist, electron beam lithography (EBL) uses finely focused electrons to eliminate the diffraction effects in optical lithography. During electron exposure, the inelastic collision between incident electrons and bound electrons of the photoresist, is the primary interaction, causing the ionization to generate secondary electrons, as shown in Figure. 1-4. These secondary electrons will further cascade to create more secondary electrons, as the energy transfer is relatively large. All these electrons orchestrate distinct chemical chain-scission (positive tone) or cross-linking (negative tone) in lithography and ultimately create the contrast between the exposed area and the rest. Usually, the dissociation and cross-linking energy are several eV's for photoresists, e.g. dissociation energy of C-C bonds in the organic photoresists is 3.6 eV [56]. A low energy (<15 eV) secondary electron can effectively dissociate or cross-link the organic molecules [57]. However, the energy of secondary electrons (> 100 eV [58]) generated by primary electrons (~ few keV – ~ 150 keV) in a common EBL system. Such high energy secondary electrons make photoresists suffer from proximity effects which lead to unwanted resist exposure around the beam tracks and loss of resolution, due to electrons forming neighboring tracks (as shown in Figure. 1-5) [59].

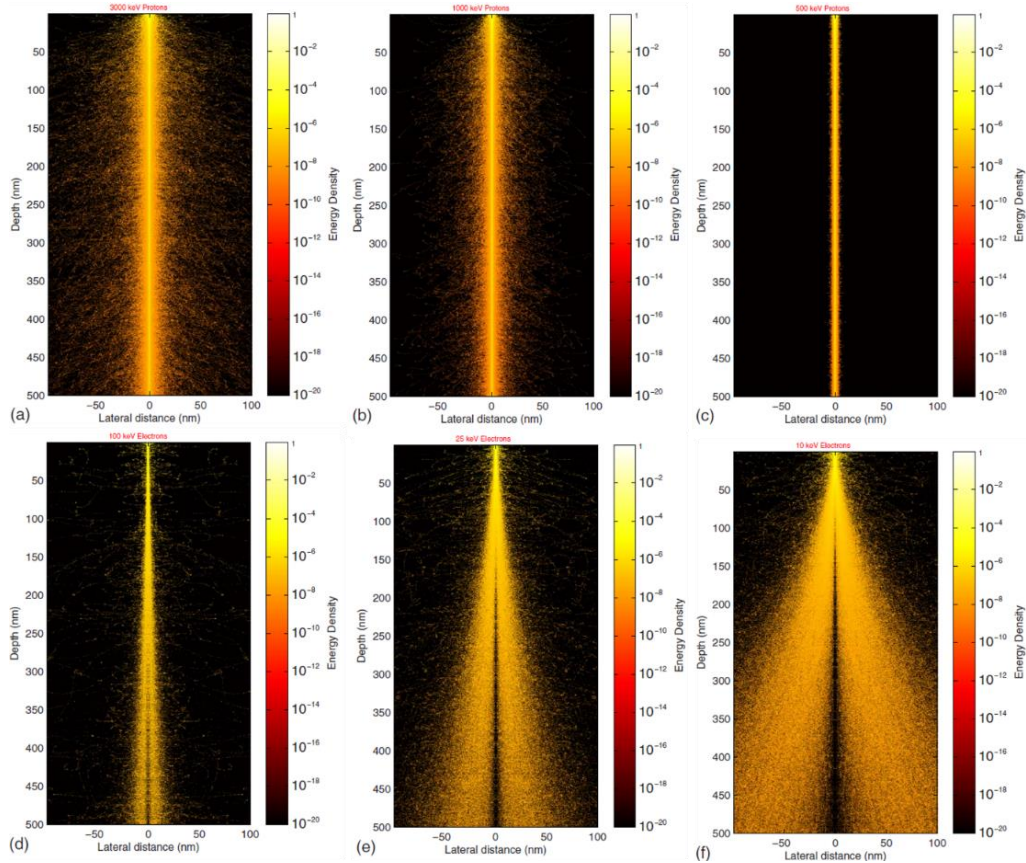


Figure. 1- 5 Monte Carlo simulation of energy deposited in a 500 nm thick PMMA using protons and electrons. (a-c) 3000 keV, 1000 keV, and 500 keV protons. (d-f) 100 keV, 25 keV, and 10 keV electrons. Adapted from Ref [60].

Proximity effects are the dominant reason that limit the resolution in EBL [61], despite electron spot sizes down to 50 pm. Currently, 10 nm lines have been achieved in 60 nm thick HSQ using EBL [62]. A thicker resist layer introduces higher electron beam forward scattering and therefore generates more secondary electrons in the resist, resulting in a broadening effect of the structures [63]. Obviously, thinner photoresists are easier, more applicable, and practical for achieving fine structures through EBL. Sub-5 nm lines have been fabricated at 25 nm thick HSQ with EBL [64]. Also, 2 nm wide isolated features and 10 nm periodic dot arrays were succeeded at 10 nm thick HSQ [65]. Similarly in PMMA, 5 to 7 nm grating lines were successfully patterned at a pitch of 30 nm in a 40 nm thick resist layer [66]. Unprecedented feature size of 1.7 nm has been produced on PMMA through aberration-corrected EBL with 200 keV

energy [67]. For EBL, the proximity effects introduced by high-energy secondary electrons restrict the patterned structure size, especially in thick photoresists.

An alternative lithographic technique to EBL is ion beam lithography (IBL) [55], here diffraction effects are negligible (much smaller de Broglie wavelength compared to EBL of the same energy), but most importantly a minimal proximity effect (as shown in Figure. 1-5). The interaction mechanisms between ion and matter, as in the previous discussion, are dominated by inelastic collision with bound electrons (generating secondary electrons) and elastic collision with nuclei (creating defects and causing sputtering). However, distinct differences emerge in the patterning process since the sputter yields (sputtered atoms per incident ion) differ for various incident ions, as illustrated in Figure. 1-4 and Figure. 1-6. Figure. 1-6 shows the penetration of ions generated by several ion sources (proton H^+ , helium He^+ , neon Ne^+ , and gallium Ga^+) striking 200 nm thick PMMA with a fixed incident energy of 100 keV and 200 keV, modeled using the Monte Carlo simulation program SRIM [68]. It is clearly illustrated that low mass ions penetrate deep and straight into material with a relatively low sputter yield, because at the same energy, light incident ions have a higher velocity and less interaction time, resulting in less energy transfer. As shown in Figure. 1-6, heavy ions, such as Ga^+ , have higher sputtering yield and are usually employed for sputtering or milling applications. Heavy ions can also be used for imaging, but must operate at relatively low beam current or short time to minimize the material damage.

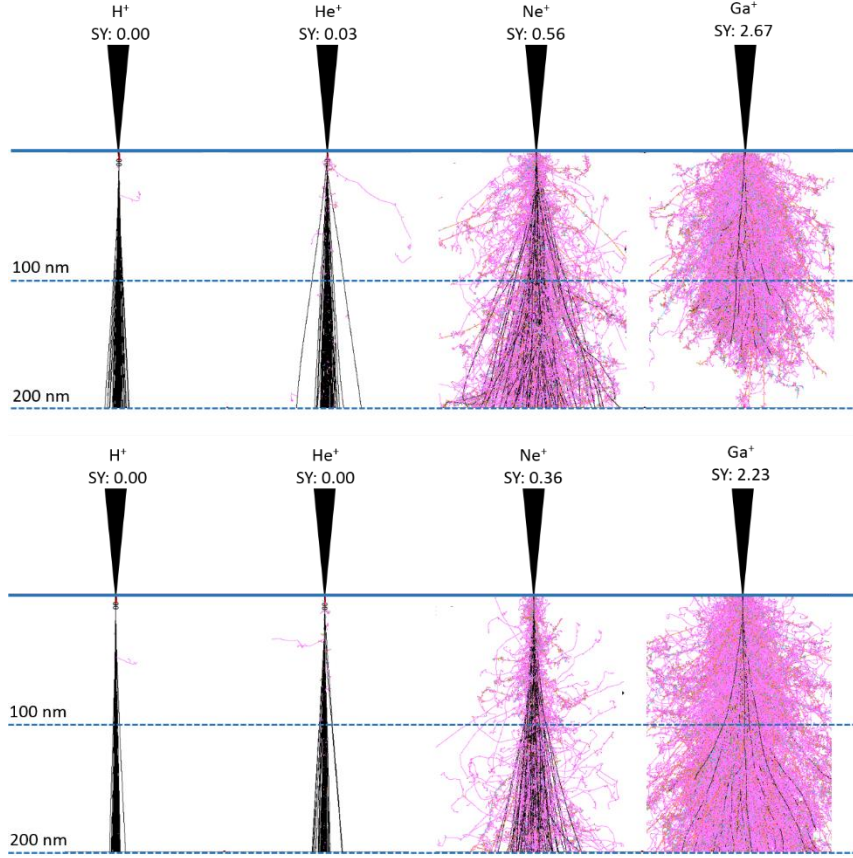


Figure. 1- 6 Different ion beam trajectories and sputter yields (SY) of H^+ , He^+ , Ne^+ , and Ga^+ at top) 100 keV, and bottom) 200 keV, in 200 nm thick PMMA. The incident ions (100 ions) are shown in black, and the dislocated atoms are shown in color. The total sputter yields are presented by summing the yields of hydrogen, carbon and oxygen atoms. Simulated using Monte Carlo simulation program SRIM [68].

An ion beam transfers energy to secondary electrons along the beam path. The energy deposition increases slowly with the depth where electronic stopping dominates. At the end of range, the energy deposition rapidly increases where the nuclear stopping becomes more prominent. The benefit of using light ions is that they greatly reduce the material damage (sputtering and defect) and are therefore more suitable for photolithography compared to the heavy ions. In the current PBW system, MeV protons mainly transfer less than 100 eV energy to secondary electrons, due to the higher mass of the proton, when compared to the electron (~1800 times). These secondary electrons are localized close to the beam trajectory, whereas the secondary electrons generated in EBL typically have energy of more than 100 eV [58], and travel long distances as shown in Figure. 1-5. As a result, there is limited scattering of protons

and minimal lateral spread of secondary electrons in photoresists (e.g. less than 2 nm within 5 μm thick PMMA [60]), resulting in minimal proximity effects coupled with a straight and deep proton trajectory, enabling the fabrication of high aspect ratio 3D nano-structures.

For a practical and convenient use, a 30 keV – 500 keV PBW system is better suited than a MeV system [37]. This energy range includes the recently developed helium ion microscope (HIM) of up to 40 keV energy [69]. As shown in Figure. 1-6, a proton beam travels more straight and deeper in material compared to the same energy helium ion beam. For 30 keV – 500 keV, both proton and helium ions transfer very low energy to secondary electrons ($< 10 \text{ eV}$) [70]–[73], which is just enough to alter the chemical property of photoresists [56], [57] with greatly reduced proximity effects compared to EBL. For 500 keV protons, 90% of energy deposited due to secondary electrons is still within 1 nm radial distance from the original proton track [60]. For a lower energy, the secondary electrons are limited to even smaller volume. Both proton and helium ions have higher energy deposition along the beam track because of the small amount of transferred energy to secondary electrons than in EBL, resulting in a more efficient dose sensitivity. For EBL, the typical required dose ranges from few 100s $\mu\text{C}/\text{cm}^2$ – few mC/cm^2 [74]–[81], while for proton and helium ions, the typical dose required is few $\mu\text{C}/\text{cm}^2$ – few 10s $\mu\text{C}/\text{cm}^2$ [82]–[86], 1-2 orders of magnitude higher sensitivity than that in EBL.

Both proton beam and helium ion beam are capable of fabricating nano-structures with less proximity effects. HIM has been commercially available in the market since 2007 by Carl Zeiss, Inc. [87], due to the development of a high brightness helium ion source, gas field ion source (GFIS) [88]. However, one drawback of using helium ions in lithography is the production of helium bubbles in the sample [89], [90]. Currently, PBW systems around the world operate only in MeV range. keV proton beam lithography is not available yet, restricted by the low proton beam brightness (e.g. ~ 20

$\text{A}/(\text{m}^2\text{srV})$ [10], [50]). At low energies, the energy spread significantly affects the focus ability, due to the chromatic aberration. According to our knowledge, stable high brightness proton sources ($>10^4 \text{ A}/(\text{m}^2\text{srV})$) have not been reported.

1.2.3 Applications of PBW

The characteristics of PBW are summarized as follows, according to the interaction between protons and matter,

- (1) Protons travel along relatively straight path.
- (2) Protons transfer less energy to secondary electrons as compared to electrons.
- (3) Protons generate more secondary electrons along the beam track as compared to electrons.
- (4) Protons deposits energy at near constant rate along the beam track, except at the end of range.
- (5) Nuclear collisions mostly happen near the end of range.
- (6) Low sputtering effect is caused by protons.

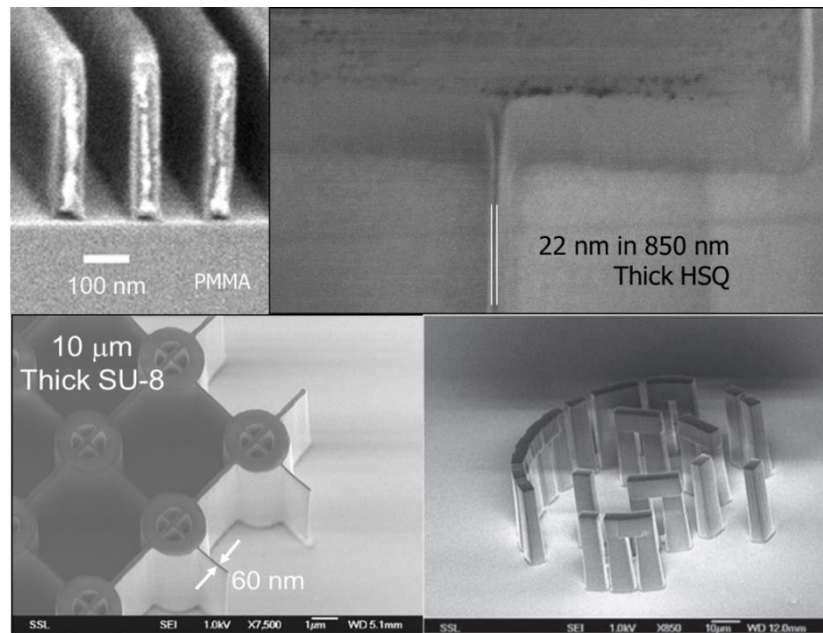


Figure. 1- 7 Nano-structures fabricated by PBW, a) Scanning electron microscopy (SEM) image of parallel lines in a 350 nm thick PMMA layer [6]. b) SEM image of 22 nm wide line in 850 nm thick HSQ [91]. c) SEM image of 60 nm walls on 10 μm thick SU-8, aspect ratio of ~167. d) Micro-sized copy of Stonehenge in UK fabricated on SU-8 [5].

All these characteristics make PBW more sensitive to photoresists, capable of fabricating high aspect ratio and high density 3D nano-structures. The even energy deposited along the beam track makes it possible to fabricate structures with smooth side walls. Moreover, the energy of PBW is tunable, making it possible to fabricate multilevel structures in one layer of photoresist. Figure. 1-7 shows structures fabricated by PBW. The applications of PBW are described below, arising from these unique features.

(1) Nano-imprinting

PBW, as well as EBL, as a direct write lithography cannot reach the throughput required in state of art extreme ultraviolet (EUV) lithographic technique. However, when coupled with nano-imprinting technique, direct write processes offer a low-cost, high-throughput, and rapid mass production technique [92]. PBW is a flexible technique to fabricate high aspect ratio molds and stamps with smooth side walls [93], [94]. Usually, the photoresist materials are not strong enough. Some alternative materials are employed as molds or stamps. Combined with Ni electroplating, 3D metallic stamps are successfully produced for mass production [93]–[95]. Recently, an OrmoStamp (Micro Resist Technology GmbH) mold was also demonstrated using PBW [96].

(2) Micro/Nano-fluidic devices

Micro/Nano-fluidic devices are used in medicine, chemistry, biology, and life sciences. The key point of these devices is to fabricate well-defined networks of nano-channels [97]. PBW is a promising candidate to fabricate vertical and smooth sidewalls in deep nano-channels [98], [99].

(3) Photonics

To fabricate photonics devices, two types of fabrication methods were developed. One involves direct fabrication of polymers for desired components, like waveguides, lens

arrays, and gratings. These polymers generally have a higher refractive index, and are coated on lower refractive substrates [100], [101]. The other one involves a direct writing modification in bulk polymer or fused silica, using the nuclear collision at the end of range without any development step for samples. In this process, a buried region with higher density and therefore higher refractive index is created at the end of range. [102], [103].

(4) Silicon micro-machining

Proton irradiation prior to electrochemical etching (hydrogen fluoride) and followed with potassium hydroxide (KOH) etching is capable to create 3D structures in bulk silicon. The mechanism of proton irradiation process is to build vacancies resulting in higher resistivity, and functioning as the electrochemical etch stop for the formation of porous silicon. High aspect ratio silicon needles and free-standing multilevel structures have been demonstrated [104]–[107]. In addition, PBW is adopted to produce porous silicon-based colored displays. They are achieved using selective proton beam patterning of silicon followed by electrochemical anodization to form porous silicon based multilayer Bragg stacks with different resonant reflected wavelengths. These displays can reflect all colors in visible spectrum and have high resolution due to the use of focused ion beam [108]–[110].

The applications of fast proton beams are not only limited to PBW, but also can be used in other domains, such as ion imaging for the whole cell [111], and micro particle-induced X-ray [112]. All these applications are based on the unique characteristics of proton beam and small focused beam size.

1.3 Ion sources

An ion source is one of the essential parts of accelerators. For different application purposes, different ion sources are employed. The following section will briefly discuss about various high brightness ion sources.

1.3.1 Radio frequency (RF) ion source

The construction of RF ion source was started in the 1940s [113]–[116], and they are widely used in accelerators because of high beam current, easy operation, wide range of ions, clean plasma, and long lifetime (> 1000 h). The mechanism of RF ion source is to form an RF discharge in a vacuum vessel filled with the gas of interest. The gas discharge is excited to create plasma by RF voltage which is either capacitively or inductively coupled.

Capacitively coupled RF ion source

As shown in Figure. 1-8, the RF ion source operated at CIBA, NUS employs a capacitively coupled mode by an oscillating RF voltage (~ 100 MHz) through two external ring electrodes exciting gas inside the quartz bottle. Plasma is generated through the discharge process, and confined by the axial magnetic field generated by four cylindrical permanent magnets seated symmetrically around the quartz tube. This axial magnetic field also helps electrons to travel in a helical path, resulting in higher electron-gas interactions, towards the tungsten probe (maintained at a positive bias ~ 1 kV). Ions are extracted from the quartz bottle through a 2 mm diameter extractor canal with a current density of ~ 1 mA/cm² [2], [117], with a negative voltage (~ -10 s kV), and then enter into the acceleration column. This capacitively coupled RF ion source, at our lab, usually operates at MV terminal, delivering a total current of \sim few 10s μ A, with $\sim 75\%$ proton yield and the rest of H₂⁺, 20 – 100 eV energy spread with and an emittance lower than 1.2π mm mrad MeV^{1/2} [8], [50], [51], [117]. The reduced

brightness for proton beam is \sim few $10s \text{ A}/(\text{m}^2\text{srV})$ [9], [118], with the reported highest as $74 \text{ A}/(\text{m}^2\text{srV})$ at CIBA, NUS [51].

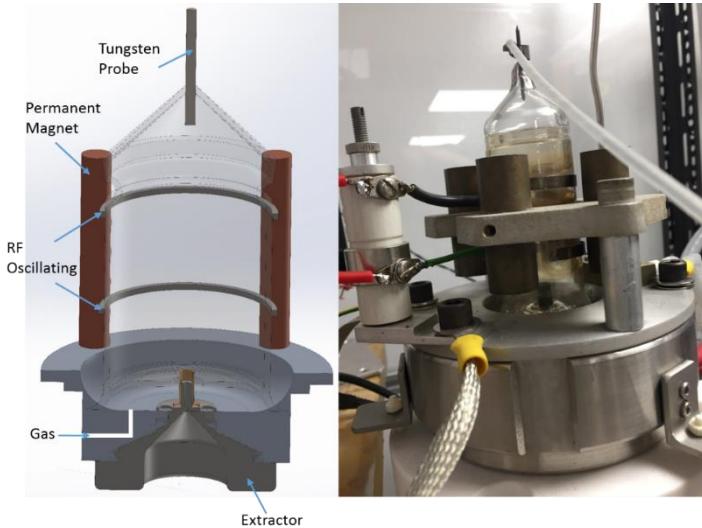


Figure. 1- 8 Schematics, and photo taken from Ion Source Test Bench at CIBA, NUS of capacitively coupled RF ion source.

Inductively coupled RF ion source

Inductively coupled RF ion source, employs helical induction coil or RF antenna and circular permanent magnet. The alternating magnetic field generated by RF voltage produces an azimuthal electric field to excite electrons into oscillation for ionizing the gas. This discharge process doesn't depend on large voltages to drive displacement current through the powered RF sheaths, leading to relatively low plasma energy ($< 10 \text{ eV}$), and higher power efficiency, capable of operating in low gas pressure [119]. The circular permanent magnet compresses the plasma more tightly than in the capacitively coupled mode. All these effects result in an ion beam with dense current density and high brightness. In this inductively coupled mode, the antenna coil is capable of being arranged either inside or outside the source chamber, as helicon RF ion source or multicusp ion source.

(1) Helicon RF ion source

Helicon RF is an inductively coupled source operated with an external RF antenna as shown in Figure. 1-9. Typically, this kind of ion source can generate plasma with densities as high as $\sim 10^{11} - 10^{12} \text{ /cm}^3$, with ion current density of $\sim 10 - 100 \text{ mA/cm}^2$ extracted from mm size region (total extracted current $\sim 100\text{s } \mu\text{A}$), $< 30 \text{ eV}$ energy spread, and $\sim 100 \text{ A/(m}^2\text{srV)}$ reduced brightness [120]–[122]. The hydrogen and helium reduced brightness was reported as $\sim 50 \text{ A/(m}^2\text{srV)}$ and $\sim 100 \text{ A/(m}^2\text{srV)}$, respectively [123]–[125]. An enhanced helicon RF ion source has shown an exciting reduced brightness operated for Ar^+ and Xe^+ with a small extracted aperture of $200 \mu\text{m}$ diameter. The reduced brightness for Ar^+ is $5400 \text{ A/(m}^2\text{srV)}$ emitted from $15.3 \mu\text{m}$ diameter virtual source, with an energy spread of 10 eV . While for Xe^+ it is $9100 \text{ A/(m}^2\text{srV)}$ emitted from $7.2 \mu\text{m}$ diameter virtual source with 7 eV energy spread [126]. This improvement in brightness is attributed to small source emitting size. The Xe FIB has been successfully and commercially developed for fast ($> 20x$ faster than Ga-FIB) and large volume material removal with micron-resolution [127]–[130]. Oregon Physics has released the Hyperion I positive ion source, which claimed to have reduced brightness up to $10^4 \text{ A/(m}^2\text{srV)}$ with Xe^+ , $6.7 \times 10^3 \text{ A/(m}^2\text{srV)}$ with helium He^+ , $4.5 \times 10^3 \text{ A/(m}^2\text{srV)}$ with oxygen O_2^+ and $\sim 10^3 \text{ A/(m}^2\text{srV)}$ with hydrogen H_3^+ [131], [132].

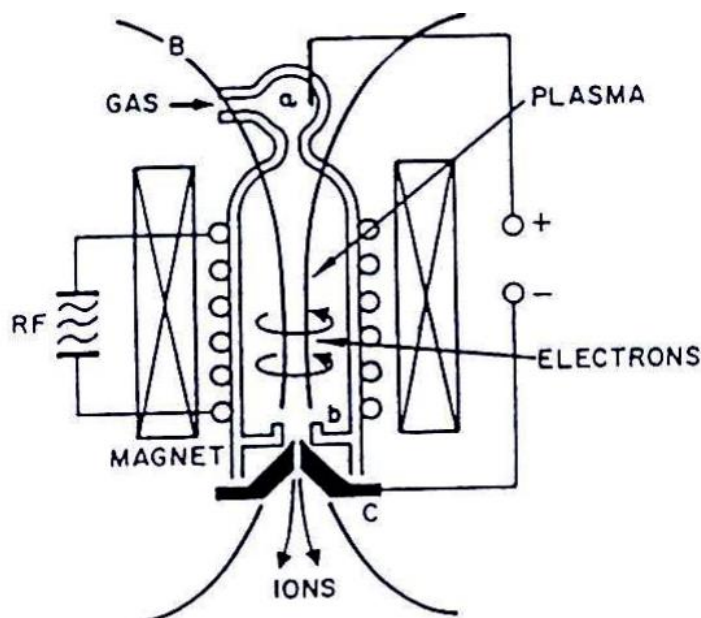


Figure. 1- 9 A thonemann type RF ion source, also named as Helicon RF [133], [134].

(2) Multicusp ion source

A multicusp ion source is an inductively coupled source operated with an internal RF antenna or dc filament as shown in Figure. 1-10, which is widely employed for both positive and negative ion beams. The RF antenna or dc filament is used for discharge and creating plasma. A magnetic filter is used to limit the production of undesired ion species, which also reduces the longitudinal energy spread and improves the beam quality. The alternating polarities of samarium-cobalt magnets generate the longitudinal line-cusp configuration remote from the RF antenna or dc filament, located in a magnetic field-free region of the source chamber centre, to constrain the quiescent plasma ($> 10^{12} /cm^3$ [135]). A uniform high beam density ($\sim 10 - 100s \text{ mA/cm}^2$), and low energy spread ($< 3 \text{ eV}$) ion beam can be extracted from this source [136]–[139]. The reduced brightness of proton and helium is typically $10 - 100 \text{ A/(m}^2\text{srV)}$ [118], [140]–[143]. The highest reported reduced brightness for helium is $2200 \text{ A/(m}^2\text{srV)}$ achieved at Lawrence Berkeley National Laboratory [144].

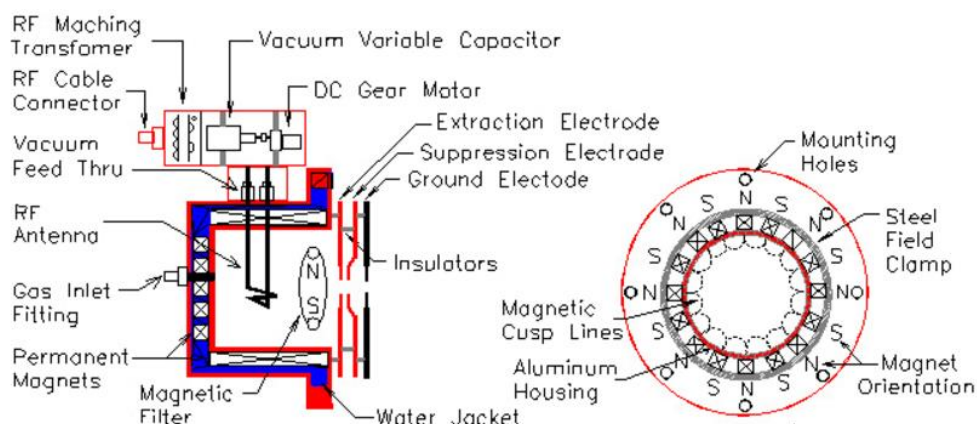


Figure. 1- 10 Schematic diagram of multicusp ion source [145].

1.3.2 Liquid metal ion source (LMIS)

Liquid metal ion source (LMIS) is one of the most widely used high brightness ion source, developed from the late 1960s and early 1970s, and commercialized in the early 1980s [146]. As shown in Figure. 1-11, LMIS comprises a sharp emitting tip coated with a metal film which has a high surface tension and low vapor pressure. When in

operation, the emitting tip is heated to melt the metal film into a liquid state, functioning as a liquid metal reservoir [146]–[149]. A strong electric field (10^{10} V/m by applying a ~ 10 kV potential) is used to pull the liquid metal to a sharp electrospray cone, known as Taylor cone [150]. Meanwhile, this strong electric field also generates ions at the tip of the Taylor cone by field evaporation. The most common LMIS is Ga-LMIS due to its low melting point (29.76 °C) and low vapor pressure ($< 10^{-7}$ mbar at melting point [151]), but several other metals (e.g. Al, In, Sn, Cs, Bi, Au), as well as alloy metals (Au-Si, Au-Ge, Si-Be-Au, Ni-B-Pt), are also used [146]. For Ga-LMIS, although the tip end is about 10 μm size, the end of Taylor cone is only ~ 5 nm in size, acting as the ion emitter [146]. The emitting current from a Taylor cone is \sim few μA with the current density as high as $> 10^6$ A/cm² [146], [152], [153], causing ion beam trajectory perturbations near the apex of Taylor and increasing the energy spread due to the Coulomb effects. Therefore, the typical virtual source size of Ga-LMIS is larger than emitting size, of about 50 nm with an angular current intensity of ~ 10 s μA/sr, and the reduced brightness is about 10^6 A/(m²srV) with a typical energy spread of around 5 eV [146], [152]. Due to the relatively low angular current, only part of the extracted ion beam is employed for focusing, restricted by spherical aberration. Hence the beam current on the sample is about few pA at high-resolution mode (< 10 nm), and > 50 nA current can be obtained at the sample at large beam size [146], [152]. The lifetime for LMIS is generally more than 1000 hours [154]. The typical LMIS provides relatively heavy ions, which is suitable for milling, and can only be used for imaging at very low current mode for a short time. However, the choice of ions from the LMIS is limited to metallic ions which introduce metallic contamination of the sample, and the energy spread results in high chromatic aberration, limiting the resolution to about 5 – 10 nm [146].

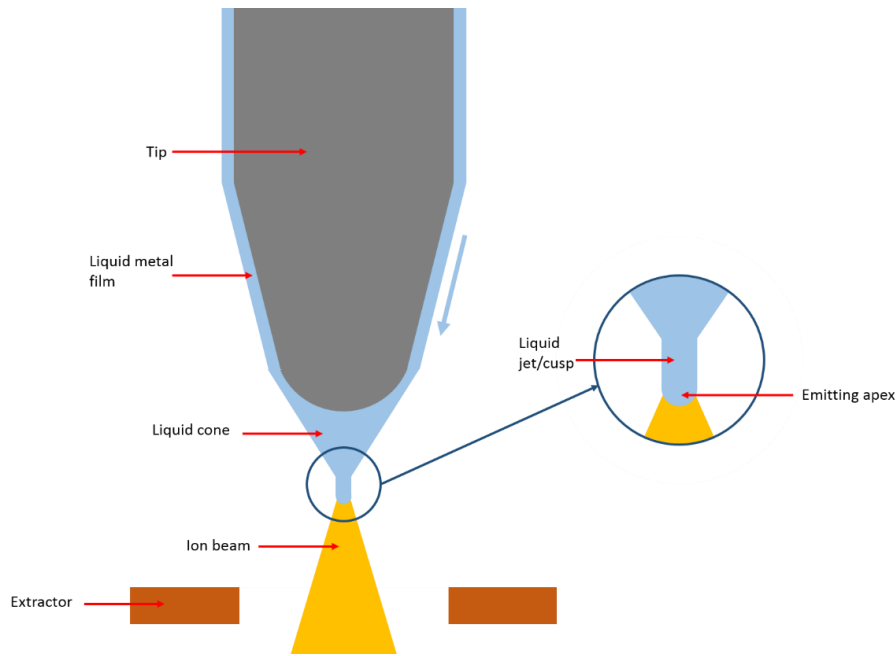


Figure. 1- 11 Needle type liquid metal ion source used in Focused Ion Beam machines. (a) Liquid metal ion source. (b) Ion emission process.

1.3.3 Gas field ion source (GFIS)

The ionization of gas field ion source (GFIS) is generated by applying a strong electric field (10^{10} V/m) [155]–[157], similar to LMIS. This ionization process is based on a gas field ionization source invented by Müller since 1951 [158]–[160]. Although GFIS has been developed for more than half a century, it has only emerged as a credible choice to work consistently for high brightness ion source by ALIS Corporation (acquired by Carl Zeiss, Inc. in 2006), commercially available as part of HIM since 2007 by Carl Zeiss, Inc. [87]. As shown in Figure. 1-12, a strong electric field is concentrated at the apex of a pyramidal tip, which terminates with three atoms. Gas molecules are drawn to the apex of the tip by polarization force with thermal accommodation, and ionized by the strong electric field due to the electron tunnelling [13], [146]. GFIS has been mostly used for generating He and Ne ions [157], [161] because helium and neon require the highest ionization energies and have low polarizabilities among all gasses [162], [163]. For helium, a 4 V/ \AA field strength (3.5 V/ \AA for neon) is required, which only exists in the vicinity of three protruding atoms, resulting in ionization occurring only in a very small region. A parallel beam can be

obtained which emits from a small area with small transverse energy. The extracted current is 10s pA to \sim 100 pA with angular current intensity varied from \sim few $\mu\text{A}/\text{sr}$ to 10s $\mu\text{A}/\text{sr}$ depending on the operational pressure, from a small virtual source size (\sim 0.3 nm), and the reduced brightness can reach as high as $> 10^9 \text{ A}/(\text{m}^2\text{srV})$ with a $< 1 \text{ eV}$ energy spread [146], [156], [157], [164], [165]. The small virtual source size, due to the three-atom terminated tip, coupled with low transverse energy, results in this high brightness. A probe current of 20 pA was operated at probe size of 2 – 3 nm achieved for helium [156]. Because of the high brightness and small energy spread, a small probe size of 0.25 nm has been achieved [166]. The lifetime for He-GFIS is many months of a long term usage, for Ne-GFIS is more than 10 hours [157], [167], [168]. While the GFIS can deliver an extremely high brightness ion beam, it is limited to He and Ne.

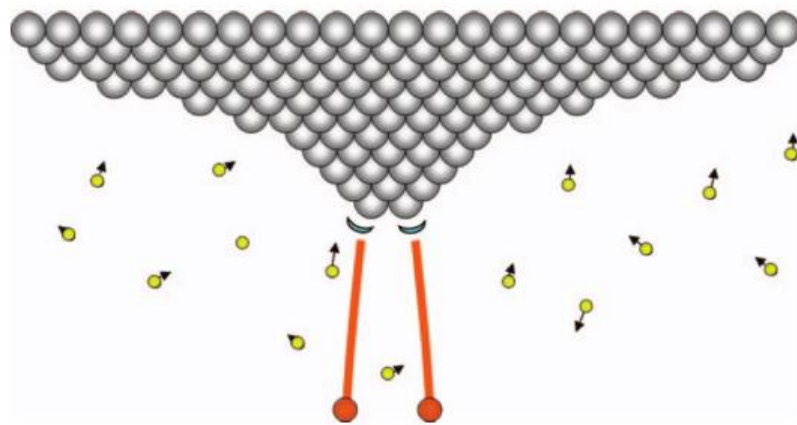


Figure. 1- 12 LMIS with a pyramidal tip, terminated with three atoms at apex. Helium atoms get ionized only in the vicinity of apex where the electric field is enhanced [157].

1.3.4 Laser-cooled ion source

Laser-cooled ion source, also called as ultra-cold ion source, acquires a high brightness and low energy spread through reducing the operational temperature of the source, resulting in a low beam angular spread. As shown in Figure. 1-13, laser beams are used to cool and trap the gas atoms into a magneto-optical trap created between the two electrodes at less than \sim 100 μK [169]–[172]. The ultra-cold gas atoms are near the threshold of photon ionization, and are ionized by an extra ionization laser to generate

desired ions. These ion sources can extract a few 100 pA current from 10s μm to few mm region, having a theoretical reduced brightness of around $10^7 \text{ A}/(\text{m}^2\text{srV})$, with $< 0.5 \text{ eV}$ energy spread [170], [172]–[175]. Using laser-cooled Cr, Li and Rb atoms, beams with reduced brightness of $2.25 \times 10^4 \text{ A}/(\text{m}^2\text{srV})$ [176], $6 \times 10^3 \text{ A}/(\text{m}^2\text{srV})$ [171] and $6 \times 10^6 \text{ A}/(\text{m}^2\text{srV})$ [177] have been achieved respectively. Although this laser-cooled ion sources can deliver high brightness ion beams (mainly rubidium, chromium and lithium [172]), they are not designed to produce high brightness proton beams due to the short wavelength required to ionize hydrogen gas (13.6 eV [162], [163]).

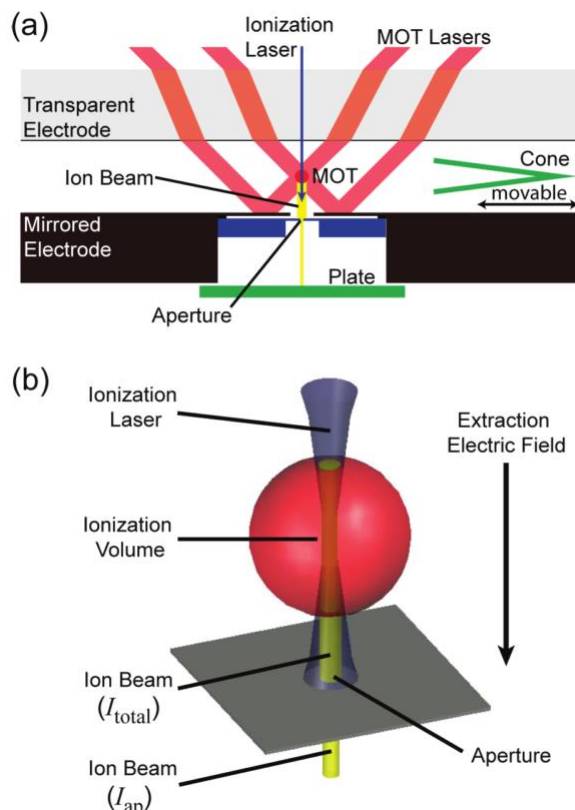


Figure. 1-13 Schematics of Laser-cooled ion source [178].

1.4 Scope of this thesis

A summary of the different high brightness positively charged ion sources is shown in Table. 1-1. As discussed in the previous part, a high brightness ion source can be achieved via two approaches. One is to reduce the source emitting area with high emitting beam current density, while the other is to lower the operational temperature for a small intrinsic angular spread. For high helicon RF and multicusp ion sources, the reported high brightness is achieved by reducing the source size to few 10s μm . LMIS and GFIS both employ small source size (5nm and 0.3 nm respectively) to achieve high brightness. Laser-cooled ion source adopts super low operational temperature to obtain small intrinsic angular spread beam, resulting in high brightness. However, no high brightness hydrogen ion source ($> 10^4 \text{ A}/(\text{m}^2\text{srV})$) is available. This thesis aims to develop a high brightness ion source, with reduced source emitting size down to sub-micrometer featuring a low energy spread.

Table. 1- 1 Summary of characteristics for different kinds of ion source.

	Capacitively coupled RF	Helicon RF	Multicusp	LMIS	GFIS	Laser-cooled	Ideal source characteristics
Ionization mechanism	RF	RF	RF	Field evaporation	Gas field	Laser	
Ion species	Gaseous ions	Gaseous ions	Gaseous ions	Ga, Al, In, Be, Sn, Cs, Bi, Au	He, Ne	Rb, Li, Cr	H
Extracted current	~10 – 100s μA	~100s μA	~100s μA	~few μA	~10 – 100s pA	100s pA	
Probe current*	~10 fA	few pA, with a resolution of 10s nm		few pA	20 pA	few pA	> pA
Virtual source size	~mm	Typical ~100 μm to mm, smallest is ~10 μm	Typical ~100 μm to mm	5 nm	0.3 nm	~10s μm to few mm	
Reduced brightness (A/(m²srV))	~10s (< 74 for H ⁺)	Typical ~100, highest is 9100 for Xe ⁺ , ~10 ³ for H ₃ ⁺	Typical ~10 – 100, highest is 2200 for He ⁺	10 ⁶	10 ⁹	Theoretical 10 ⁷ , achieved 10 ⁶	10 ⁴ – 10 ⁷
Energy spread (eV)**	20 – 100***	~10	< 3	5	< 1	< 0.5	< 1

* At high-resolution mode (sub-10 nm).

** Here the energy spread ΔE is defined by $E_0 - \Delta E$, double as the energy spread $E \pm \Delta E$ described in Chapter 1.1.3.

*** Energy stability of the current PBW system at 1- 2 MeV is ~20 eV.

The thesis is organized as follows:

Chapter 2 discusses a potential high brightness nano-aperture ion source (NAIS), which utilizes electrons to ionize gas within a sub-micron ionization chamber. The concept and configuration of this NAIS are introduced. The theoretical evaluation of this NAIS are studied using conventional scanning electron microscope (SEM) as electron injector. In Chapter 3, NAIS simulations are performed based on the tested geometries. First, the gas distribution in the sub-micron ionization chamber is analyzed. The gas distribution and injected electron distribution determine the ion beam emission profile. Second, the electric field generated inside NAIS is calculated. Results from these simulations are used to simulate the performance of NAIS. The influence from Coulomb effects for NAIS are investigated. Chapter 4 describes the NAIS ionization chambers that have been fabricated and subsequently tested inside SEMs. Based on the test performances, a NAIS with internal electrodes is proposed to achieve high brightness and low energy spread. Chapter 5 proposes a low energy proton microscope based on miniaturized Einzel lens, and a 200 keV compact-PBW (c-PBW) system for high resolution fast writing applications featuring NAIS. In chapter 6, the summary of this thesis is discussed.

References

- [1] R. J. Goldston and P. H. Rutherford, *Introduction to plasma physics*. CRC Press, 1995.
- [2] I. G. Brown, *The physics and technology of ion sources*. John Wiley & Sons, 2004.
- [3] D. C. Faircloth, “Ion sources for high-power hadron accelerators,” *Cern Accel. Sch. CAS 2011 High Power Hadron Machines*, pp. 369–407, 2011.
- [4] Z. H. Shun, *Ion sources*. Springer, 1999.
- [5] F. Watt, M. B. H. Breese, A. A. Bettoli, and J. A. van Kan, “Proton beam writing,” *Mater. Today*, vol. 10, no. 6, pp. 20–29, 2007.
- [6] J. A. van Kan, A. A. Bettoli, and F. Watt, “Three-dimensional nanolithography using proton beam writing,” *Appl. Phys. Lett.*, vol. 83, no. 8, pp. 1629–1631, 2003.
- [7] J. A. Van Kan, A. A. Bettoli, K. Ansari, E. J. Teo, T. C. Sum, and F. Watt, “Proton beam writing: a progress review,” *Int. J. Nanotechnol.*, vol. 1, no. 4, p. 464, 2004.
- [8] C. D. Moak, H. Reese, and W. M. Good, “Design and operation of a radio-frequency ion source for particle accelerators,” *Nucleonics*, vol. 9, no. 3, pp. 18–23, 1951.
- [9] R. Szymanski and D. N. Jamieson, “Ion source brightness and nuclear microprobe applications,” *Nucl. Instruments Methods Phys. Res. Sect. B Beam Interact. with Mater. Atoms*, vol. 130, no. 1, pp. 80–85, 1997.
- [10] J. A. Van Kan, P. Malar, and A. B. De Vera, “The second generation Singapore high resolution proton beam writing facility,” *Rev. Sci. Instrum.*, vol. 83, no. 2, p. 02B902, 2012.
- [11] P. W. H. De Jager and L. J. Vijgen, “Beam interactions in a focused ion beam system with a liquid metal ion source,” *Microelectron. Eng.*, vol. 23, no. 1–4, pp. 107–110, 1994.
- [12] M. Reiser, *Theory and design of charged particle beams*. John Wiley & Sons, 2008.
- [13] J. Orloff, *Handbook of charged particle optics*. CRC press, 2008.
- [14] I. M. Kapchinskij and V. V. Vladimirovskij, “Limitations of proton beam current in a strong focusing linear accelerator associated with the beam space charge,” in *Proceedings of the International Conference on High Energy Accelerators and Instrumentation*, 1959, p. 274.
- [15] C. A. Brau, “What brightness means,” in *The Physics and Applications of High Brightness Electron Beams*, 2003, vol. 1, pp. 20–27.
- [16] P. M. Lapostolle, “Possible emittance increase through filamentation due to space charge in continuous beams,” *IEEE Trans. Nucl. Sci.*, vol. 18, no. 3, pp. 1101–1104, 1971.
- [17] F. J. Sacherer, “RMS envelope equations with space charge,” *IEEE Trans. Nucl. Sci.*, vol. 18, no. 3, pp. 1105–1107, 1971.
- [18] D. B. Langmuir, “Theoretical limitations of cathode-ray tubes,” *Proc. Inst. Radio Eng.*, vol. 25, no. 8, pp. 977–991, 1937.
- [19] J. R. Pierce, “Limiting current densities in electron beams,” *J. Appl. Phys.*, vol. 10, no. 10, pp. 715–724, 1939.
- [20] J. Worster, “The brightness of electron emission systems,” *J. Phys. D. Appl. Phys.*, vol. 2, no. 6, p. 889, 1969.
- [21] M. Born and E. Wolf, *Principles of Optics: Electromagnetic Theory of Propagation, Interference and Diffraction of Light*. Pergamon Press, 1959.

- [22] J. D. Lawson and J. P. Blewett, “The Physics of Charged-Particle Beams.” AIP, 1978.
- [23] P. W. Hawkes and E. Kasper, “Principles of Electron Optics, Vol. 2: Applied Geometrical Optics, Chap. 47, Brightness.” Academic Press, New York, 1989.
- [24] J. Struckmeier, J. Klabunde, and M. Reiser, “On the stability and emittance growth of different particle phase-space distributions in a long magnetic quadrupole channel,” *Part. Accel.*, vol. 15, no. 1, pp. 47–65, 1984.
- [25] H. Boersch, “Experimentelle Bestimmung der Energieverteilung in thermisch ausgelösten Elektronenstrahlen,” *Zeitschrift für Phys.*, vol. 139, no. 2, pp. 115–146, 1954.
- [26] G. H. Jansen, “Coulomb Interactions in Particle Beams (Advances in Electronics and Electron Physics Supplement 21).” Academic Press, 1990.
- [27] J. P. Freidberg, *Plasma physics and fusion energy*. Cambridge University Press, 2007.
- [28] I. Langmuir, “The effect of space charge and initial velocities on the potential distribution and thermionic current between parallel plane electrodes,” *Phys. Rev.*, vol. 21, no. 4, p. 419, 1923.
- [29] C. D. Child, “Discharge from hot CaO,” *Phys. Rev. (Series I)*, vol. 32, no. 5, p. 492, 1911.
- [30] Y. Y. Lau, “Simple theory for the two-dimensional Child-Langmuir law,” *Phys. Rev. Lett.*, vol. 87, no. 27, p. 278301, 2001.
- [31] I. H. Hutchinson, “Principles of plasma diagnostics.,” *Princ. plasma diagnostics., by Hutchinson, IH. Cambridge Univ. Press. Cambridge (UK), 1990, 379 p., ISBN 0-521-32622-2, Price£ 55.00 (cloth). ISBN 0-521-38583-0, Price£ 14.95 (paper).*, vol. 1, 1990.
- [32] W. Knauer, “Energy broadening in field emitted electron and ion beams,” *Optik (Stuttgart)*, vol. 59, no. 4, pp. 335–354, 1981.
- [33] S. Beck, E. Plies, and B. Schiebel, “Low-voltage probe forming columns for electrons,” *Nucl. Instruments Methods Phys. Res. Sect. A Accel. Spectrometers, Detect. Assoc. Equip.*, vol. 363, no. 1–2, pp. 31–42, 1995.
- [34] M. G. R. Thomson, “Electron-electron scattering in microcolumns,” *J. Vac. Sci. Technol. B Microelectron. Nanom. Struct. Process. Meas. Phenom.*, vol. 12, no. 6, pp. 3498–3502, 1994.
- [35] W. D. Meisburger, A. D. Brodie, and A. A. Desai, “Low-voltage electron-optical system for the high-speed inspection of integrated circuits,” *J. Vac. Sci. Technol. B Microelectron. Nanom. Struct. Process. Meas. Phenom.*, vol. 10, no. 6, pp. 2804–2808, 1992.
- [36] R. L. Seliger, R. L. Kubena, R. D. Olney, J. W. Ward, and V. Wang, “High-resolution, ion-beam processes for microstructure fabrication,” *J. Vac. Sci. Technol.*, vol. 16, no. 6, pp. 1610–1612, 1979.
- [37] I. Adesida, “Fine line lithography using ion beams,” *Nucl. Instruments Methods Phys. Res. Sect. B Beam Interact. with Mater. Atoms*, vol. 7, pp. 923–928, 1985.
- [38] K.-H. Brenner, M. Frank, M. Kufner, and S. Kufner, “H⁺ lithography for 3-D integration of optical circuits,” *Appl. Opt.*, vol. 29, no. 26, pp. 3723–3724, 1990.
- [39] Y. H. Wang, P. Malar, and J. A. van Kan, “Resist evaluation for proton beam writing, Ni mold fabrication and nano-replication,” *Microsyst. Technol.*, vol. 20, no. 10–11, pp. 2079–2088, 2014.
- [40] J. A. Van Kan, P. Malar, and Y. H. Wang, “Resist materials for proton beam writing: A review,” *Appl. Surf. Sci.*, vol. 310, pp. 100–111, 2014.
- [41] M. B. H. Breese, G. W. Grime, F. Watt, and D. Williams, “MeV ion beam lithography of PMMA,” *Nucl. Instruments Methods Phys. Res. Sect. B Beam Interact. with Mater. Atoms*, vol. 77, no. 1–4, pp. 169–174, 1993.

- [42] F. Menzel, D. Spemann, S. Petriconi, J. Lenzner, and T. Butz, “Proton beam writing of submicrometer structures at LIPSION,” *Nucl. Instruments Methods Phys. Res. Sect. B Beam Interact. with Mater. Atoms*, vol. 260, no. 1, pp. 419–425, 2007.
- [43] V. Auzelyte *et al.*, “Exposure parameters for MeV proton beam writing on SU-8,” *Microelectron. Eng.*, vol. 83, no. 10, pp. 2015–2020, 2006.
- [44] J. Simčič *et al.*, “3D micromachining of SU-8 polymer with proton microbeam,” *Nucl. Instruments Methods Phys. Res. Sect. B Beam Interact. with Mater. Atoms*, vol. 241, no. 1, pp. 479–485, 2005.
- [45] I. Rajta, I. Gomez-Morilla, M. H. Abraham, and A. Z. Kiss, “Proton beam micromachining on PMMA, Foturan and CR-39 materials,” *Nucl. Instruments Methods Phys. Res. Sect. B Beam Interact. with Mater. Atoms*, vol. 210, pp. 260–265, 2003.
- [46] P. Mistry *et al.*, “Proton beam lithography at the University of Surrey’s Ion Beam Centre,” *Nucl. Instruments Methods Phys. Res. Sect. B Beam Interact. with Mater. Atoms*, vol. 242, no. 1, pp. 387–389, 2006.
- [47] M. Cutroneo, V. Havranek, A. Mackova, V. Semian, L. Torrisi, and L. Calcagno, “Micro-patterns fabrication using focused proton beam lithography,” *Nucl. Instruments Methods Phys. Res. Sect. B Beam Interact. with Mater. Atoms*, vol. 371, pp. 344–349, 2016.
- [48] N. Uchiya *et al.*, “Micro-machining of resists on silicon by proton beam writing,” *Nucl. Instruments Methods Phys. Res. Sect. B Beam Interact. with Mater. Atoms*, vol. 260, no. 1, pp. 405–408, 2007.
- [49] R. Tsuchiya and H. Nishikawa, “Fabrication of silica-based three-dimensional structures by changing fluence using proton beam writing,” *Trans. Mater. Res. Soc. Japan*, vol. 36, no. 3, pp. 325–328, 2011.
- [50] D. J. W. Mous, R. G. Haitsma, T. Butz, R.-H. Flagmeyer, D. Lehmann, and J. Vogt, “The novel ultrastable HVEE 3.5 MV Singletron™ accelerator for nanoprobe applications,” *Nucl. Instruments Methods Phys. Res. Sect. B Beam Interact. with Mater. Atoms*, vol. 130, no. 1–4, pp. 31–36, 1997.
- [51] F. Watt *et al.*, “The National University of Singapore high energy ion nano-probe facility: Performance tests,” *Nucl. Instruments Methods Phys. Res. Sect. B Beam Interact. with Mater. Atoms*, vol. 210, pp. 14–20, 2003.
- [52] Y. Yao and J. A. van Kan, “Automatic beam focusing in the 2nd generation PBW line at sub-10nm line resolution,” *Nucl. Instruments Methods Phys. Res. Sect. B Beam Interact. with Mater. Atoms*, vol. 348, pp. 203–208, 2015.
- [53] P. Marmier and E. Sheldon, “PHYSICS OF NUCLEI AND PARTICLES. VOLUME I.,” 1969.
- [54] R. D. Evans and A. Noyau, “The atomic nucleus,” 1955.
- [55] F. Watt, A. A. Bettoli, J. A. Van Kan, E. J. Teo, and M. B. H. Breese, “Ion beam lithography and nanofabrication: a review,” *Int. J. Nanosci.*, vol. 4, no. 3, pp. 269–286, 2005.
- [56] D. P. Shoemaker, C. W. Garland, and J. I. Steinfeld, *Experiments in physical chemistry*. McGraw-Hill New York, 1962.
- [57] M. N. Hedhili, P. Cloutier, A. D. Bass, T. E. Madey, and L. Sanche, “Electron stimulated desorption of anionic fragments from films of pure and electron-irradiated thiophene,” *J. Chem. Phys.*, vol. 125, no. 9, p. 94704, 2006.
- [58] M. P. Seah and W. A. Dench, “Quantitative electron spectroscopy of surfaces: a standard data base for electron inelastic mean free paths in solids,” *Surf. interface Anal.*, vol. 1, no. 1, pp. 2–11, 1979.
- [59] T. H. P. Chang, “Proximity effect in electron-beam lithography,” *J. Vac. Sci. Technol.*, vol. 12, no. 6, pp. 1271–1275, 1975.

- [60] C. Udalagama, A. A. Bettoli, and F. Watt, "Stochastic spatial energy deposition profiles for MeV protons and keV electrons," *Phys. Rev. B*, vol. 80, no. 22, p. 224107, 2009.
- [61] C. G. Willson, L. F. Thompson, and M. J. Bowden, "Introduction to microlithography," in *ACS Symposium Series*, 1994, vol. 219, pp. 123–126.
- [62] X. Chen, T. Zhang, V. Constantoudis, S.-L. Zhang, and Z. Zhang, "Aged hydrogen silsesquioxane for sub-10nm line patterns," *Microelectron. Eng.*, vol. 163, pp. 105–109, 2016.
- [63] A. E. Grigorescu and C. W. Hagen, "Resists for sub-20-nm electron beam lithography with a focus on HSQ: state of the art," *Nanotechnology*, vol. 20, no. 29, p. 292001, 2009.
- [64] J. K. W. Yang *et al.*, "Understanding of hydrogen silsesquioxane electron resist for sub-5-nm-half-pitch lithography," 2009.
- [65] V. R. Manfrinato *et al.*, "Resolution limits of electron-beam lithography toward the atomic scale," *Nano Lett.*, vol. 13, no. 4, 2013.
- [66] W. W. Hu, K. Sarveswaran, M. Lieberman, and G. H. Bernstein, "Sub-10 nm electron beam lithography using cold development of poly (methylmethacrylate)," *J. Vac. Sci. Technol. B*, vol. 22, no. 4, pp. 1711–1716, 2004.
- [67] V. R. Manfrinato *et al.*, "Aberration-Corrected Electron Beam Lithography at the One Nanometer Length Scale," *Nano Lett.*, p. acs.nanolett.7b00514, 2017.
- [68] J. F. Ziegler and J. P. Biersack, "The stopping and range of ions in matter," in *Treatise on Heavy-Ion Science*, Springer, 1985, pp. 93–129.
- [69] J. Morgan, J. Notte, R. Hill, and B. Ward, "An introduction to the helium ion microscope," *Microsc. Today*, vol. 14, no. 4, pp. 24–31, 2006.
- [70] Y. V Petrov, O. F. Vyvenko, and A. S. Bondarenko, "Scanning helium ion microscope: distribution of secondary electrons and ion channeling," *J. Surf. Investig. X-ray, Synchrotron Neutron Tech.*, vol. 4, no. 5, pp. 792–795, 2010.
- [71] K. Ohya, T. Yamanaka, K. Inai, and T. Ishitani, "Comparison of secondary electron emission in helium ion microscope with gallium ion and electron microscopes," *Nucl. Instruments Methods Phys. Res. Sect. B Beam Interact. with Mater. Atoms*, vol. 267, no. 4, pp. 584–589, 2009.
- [72] R. Ramachandra, B. Griffin, and D. Joy, "A model of secondary electron imaging in the helium ion scanning microscope," *Ultramicroscopy*, vol. 109, no. 6, pp. 748–757, 2009.
- [73] Y. Petrov and O. Vyvenko, "Secondary electron emission spectra and energy selective imaging in helium ion microscope," 2011, vol. 8036, p. 80360O–80360O–10.
- [74] D. R. Medeiros *et al.*, "High resolution patterning in chemically amplified resists : the effect of film thickness," *Processing*, vol. 4345, no. 845, pp. 241–250, 2001.
- [75] S. Regonda, M. Aryal, and W. (Walter) Hu, "Stability of HSQ nanolines defined by e-beam lithography for Si nanowire field effect transistors," *J. Vac. Sci. Technol. B Microelectron. Nanom. Struct.*, vol. 26, no. December, p. 2247, 2008.
- [76] M. Yan, S. Choi, K. R. V. Subramanian, and I. Adesida, "The effects of molecular weight on the exposure characteristics of poly(methylmethacrylate) developed at low temperatures," *J. Vac. Sci. Technol. B Microelectron. Nanom. Struct.*, vol. 26, no. 6, p. 2306, 2008.
- [77] A. E. Grigorescu, M. C. van der Krog, C. W. Hagen, and P. Kruit, "10 nm lines and spaces written in HSQ, using electron beam lithography," *Microelectron. Eng.*, vol. 84, no. 5–8, pp. 822–824, 2007.
- [78] J. K. W. Yang *et al.*, "Understanding of hydrogen silsesquioxane electron resist for sub-5-nm-half-pitch lithography," *J. Vac. Sci. Technol. B Microelectron. Nanom. Struct.*, vol. 27, no. 6, pp. 2622–2627, 2009.

- [79] V. Sidorkin, A. Grigorescu, H. Salemink, and E. van der Drift, "Resist thickness effects on ultra thin HSQ patterning capabilities," *Microelectron. Eng.*, vol. 86, no. 4–6, pp. 749–751, 2009.
- [80] V. Sidorkin, A. van Run, A. van Langen-Suurling, A. Grigorescu, and E. van der Drift, "Towards 2-10 nm electron-beam lithography: A quantitative approach," *Microelectron. Eng.*, vol. 85, no. 5–6, pp. 805–809, 2008.
- [81] A. S. Gangnaik, Y. M. Georgiev, and J. D. Holmes, "New Generation Electron Beam Resists: A Review," 2017.
- [82] J. A. van Kan *et al.*, "New resists for proton beam writing," *Nucl. Instruments Methods Phys. Res. Sect. B Beam Interact. with Mater. Atoms*, vol. 260, no. 1, pp. 460–463, 2007.
- [83] J. A. van Kan, A. A. Bettiol, and F. Watt, "Hydrogen silsesquioxane a next generation resist for proton beam writing at the 20 nm level," *Nucl. Instruments Methods Phys. Res. Sect. B Beam Interact. with Mater. Atoms*, vol. 260, no. 1, pp. 396–399, 2007.
- [84] N. Puttaraksa, R. Norarat, M. Laitinen, T. Sajavaara, S. Singkarat, and H. J. Whitlow, "Lithography exposure characteristics of poly(methyl methacrylate) (PMMA) for carbon, helium and hydrogen ions," *Nucl. Instruments Methods Phys. Res. Sect. B Beam Interact. with Mater. Atoms*, vol. 272, pp. 162–164, 2012.
- [85] V. Sidorkin, E. van Veldhoven, E. van der Drift, P. Alkemade, H. Salemink, and D. Maas, "Sub-10-nm nanolithography with a scanning helium beam," *J. Vac. Sci. Technol. B Microelectron. Nanom. Struct.*, vol. 27, no. 2009, p. L18, 2009.
- [86] J. A. Van Kan, P. Malar, and Y. H. Wang, "Resist materials for proton beam writing: A review," *Appl. Surf. Sci.*, vol. 310, pp. 100–111, 2014.
- [87] National Institute of Standards and Technology, "How New Helium Ion Microscope Measures Up," 2008. [Online]. Available: <https://www.sciencedaily.com/releases/2008/09/080904115132.htm>.
- [88] V. N. Tondare, "Quest for high brightness, monochromatic noble gas ion sources," *J. Vac. Sci. Technol. A*, vol. 23, no. 6, pp. 1498–1508, 2005.
- [89] V. Veligura, G. Hlawacek, R. P. Berkelaar, R. van Gastel, H. J. W. Zandvliet, and B. Poelsema, "Digging gold: keV He⁺ ion interaction with Au," *Beilstein J. Nanotechnol.*, vol. 4, no. 1, pp. 453–460, 2013.
- [90] T. C. Pekin, F. I. Allen, and A. M. Minor, "Evaluation of neon focused ion beam milling for TEM sample preparation," *J. Microsc.*, vol. 264, no. 1, pp. 59–63, 2016.
- [91] J. A. van Kan, A. A. Bettiol, and F. Watt, "Proton beam writing of three-dimensional nanostructures in hydrogen silsesquioxane," *Nano Lett.*, vol. 6, no. 3, pp. 579–582, 2006.
- [92] S. Y. Chou, P. R. Krauss, and P. J. Renstrom, "Imprint of sub-25 nm vias and trenches in polymers," *Appl. Phys. Lett.*, vol. 67, no. 1995, p. 3114, 1995.
- [93] K. Ansari, P. G. Shao, J. A. Van Kan, A. A. Bettiol, and F. Watt, "Proton beam fabrication of nickel stamps for nanoimprint lithography," *Nucl. Instruments Methods Phys. Res. Sect. B Beam Interact. with Mater. Atoms*, vol. 231, no. 1–4, pp. 407–412, 2005.
- [94] K. Ansari, J. A. Van Kan, A. A. Bettiol, and F. Watt, "Fabrication of high aspect ratio 100 nm metallic stamps for nanoimprint lithography using proton beam writing," *Appl. Phys. Lett.*, vol. 85, no. 3, pp. 476–478, 2004.
- [95] K. Ansari, J. A. Van Kan, A. A. Bettiol, and F. Watt, "Stamps for nanoimprint lithography fabricated by proton beam writing and nickel electroplating," *J. Micromechanics Microengineering*, vol. 16, no. 10, pp. 1967–1974, 2006.
- [96] F. Liu, Y. Yao, and J. A. van Kan, "OrmoStamp mold fabrication via PBW for NIL," *Nucl. Instruments Methods Phys. Res. Sect. B Beam Interact. with Mater.*

- Atoms*, vol. 348, pp. 229–232, 2015.
- [97] P. Abgrall, A. Bancaud, and P. Joseph, “Nanofluidic Devices and Their Potential Applications,” *Microfluid. Devices Nanotechnol. Fundam. Concepts*, vol. 80, no. 7, pp. 155–214, 2010.
 - [98] K. A. Mahabadi, I. Rodriguez, S. C. Haur, J. A. van Kan, A. A. Bettoli, and F. Watt, “Fabrication of PMMA micro- and nanofluidic channels by proton beam writing: electrokinetic and morphological characterization,” *J. Micromechanics Microengineering*, vol. 16, no. 7, pp. 1170–1180, 2006.
 - [99] C. Udalagama, E. J. Teo, S. F. Chan, V. S. Kumar, A. A. Bettoli, and F. Watt, “Proton beam writing of long, arbitrary structures for micro/nano photonics and fluidics applications,” *Nucl. Instruments Methods Phys. Res. Sect. B Beam Interact. with Mater. Atoms*, vol. 269, no. 20, pp. 2417–2421, 2011.
 - [100] T. C. Sum, A. A. Bettoli, J. A. Van Kan, F. Watt, E. Y. B. Pun, and K. K. Tung, “Proton beam writing of low-loss polymer optical waveguides,” *Appl. Phys. Lett.*, vol. 83, no. 9, pp. 1707–1709, 2003.
 - [101] A. A. Bettoli *et al.*, “A progress review of proton beam writing applications in microphotonics,” *Nucl. Instruments Methods Phys. Res. Sect. B Beam Interact. with Mater. Atoms*, vol. 231, no. 1–4, pp. 364–371, 2005.
 - [102] A. Roberts and M. L. Von Bibra, “Fabrication of buried channel waveguides in fused silica using focused MeV proton beam irradiation,” *J. Light. Technol.*, vol. 14, no. 11, pp. 2554–2557, 1996.
 - [103] T. C. Sum, A. A. Bettoli, H. L. Seng, I. Rajta, J. A. Van Kan, and F. Watt, “Proton beam writing of passive waveguides in PMMA,” *Nucl. Instruments Methods Phys. Res. Sect. B Beam Interact. with Mater. Atoms*, vol. 210, pp. 266–271, 2003.
 - [104] M. P. Blencowe, “Nanoelectromechanical systems,” *Contemp. Phys.*, vol. 46, no. 4, pp. 249–264, 2005.
 - [105] E. J. Teo *et al.*, “Three-dimensional microfabrication in bulk silicon using high-energy protons,” *Appl. Phys. Lett.*, vol. 84, no. 16, pp. 3202–3204, 2004.
 - [106] M. B. H. Breese, E. J. Teo, D. Mangaiyarkarasi, F. Champeaux, A. A. Bettoli, and D. Blackwood, “Proton beam writing of microstructures in silicon,” *Nucl. Instruments Methods Phys. Res. Sect. B Beam Interact. with Mater. Atoms*, vol. 231, no. 1–4, pp. 357–363, 2005.
 - [107] a. N. Cleland and M. L. Roukes, “Fabrication of high frequency nanometer scale mechanical resonators from bulk Si crystals,” *Appl. Phys. Lett.*, vol. 69, no. 18, pp. 2653–2655, 1996.
 - [108] D. Mangaiyarkarasi, E. J. Teo, M. B. H. Breese, A. A. Bettoli, and D. J. Blackwood, “Controlled shift in emission wavelength from patterned porous silicon using focused ion beam irradiation,” *J. Electrochem. Soc.*, vol. 152, no. 10, pp. D173–D176, 2005.
 - [109] D. Mangaiyarkarasi, M. B. H. Breese, Y. S. Ow, and C. Vijila, “Controlled blueshift of the resonant wavelength in porous silicon microcavities using ion irradiation,” *Appl. Phys. Lett.*, vol. 89, no. 2, pp. 1–4, 2006.
 - [110] E. J. Teo *et al.*, “Multicolor photoluminescence from porous silicon using focused, high-energy helium ions,” *Adv. Mater.*, vol. 18, no. 1, pp. 51–55, 2006.
 - [111] A. A. Bettoli, Z. Mi, and F. Watt, “High-resolution fast ion microscopy of single whole biological cells,” *Appl. Phys. Rev.*, vol. 3, no. 4, p. 41102, 2016.
 - [112] M. D. Ynsa *et al.*, “Zinc mapping and density imaging of rabbit pancreas endocrine tissue sections using nuclear microscopy,” *Microsc. Microanal.*, vol. 15, no. 4, pp. 345–352, 2009.
 - [113] Y. A. Getting, “Preliminary results on two new ion sources,” *Phys. Rev.*, vol. 59, p. 467, 1941.
 - [114] P. C. Thonemann, “High-Frequency Discharge as an Ion Source,” *Nature*, vol.

- 158, p. 61, 1946.
- [115] P. C. Thonemann, J. Moffatt, D. Roaf, and J. H. Sanders, “The performance of a new radio-frequency ion source,” *Proc. Phys. Soc.*, vol. 61, no. 5, p. 483, 1948.
- [116] R. N. Hall, “High Frequency Proton Source,” *Rev. Sci. Instrum.*, vol. 19, no. 12, pp. 905–910, 1948.
- [117] High Voltage Engineering Europa, “RF Ion Source Model SO-173 (short bottle).” [Online]. Available: <http://www.highvolteng.com/media/Leaflets/RFS-3.pdf>.
- [118] P. Pelicon *et al.*, “A high brightness proton injector for the Tandetron accelerator at Jožef Stefan Institute,” *Nucl. Instruments Methods Phys. Res. Sect. B Beam Interact. with Mater. Atoms*, vol. 332, pp. 229–233, 2014.
- [119] R. B. Piejak, V. A. Godyak, and B. M. Alexandrovich, “A simple analysis of an inductive RF discharge,” *Plasma sources Sci. Technol.*, vol. 1, no. 3, p. 179, 1992.
- [120] V. Miroshnichenko, S. Mordyk, D. Shulha, V. Storizhko, and V. Voznyy, “Development of the RF ion source for use in accelerator-based microprobes,” *Nucl. Instruments Methods Phys. Res. Sect. B Beam Interact. with Mater. Atoms*, vol. 260, no. 1, pp. 39–44, 2007.
- [121] A. J. Perry, D. Vender, and R. W. Boswell, “The application of the helicon source to plasma processing,” *J. Vac. Sci. Technol. B Microelectron. Nanom. Struct. Process. Meas. Phenom.*, vol. 9, no. 2, pp. 310–317, 1991.
- [122] V. P. Katukha, G. S. Kirichenko, A. V. Rusavskii, V. B. Taranov, and K. P. Shamrai, “Helicon ion source for plasma processing,” *Rev. Sci. Instrum.*, vol. 65, no. 4, pp. 1368–1370, 1994.
- [123] V. I. Miroshnichenko, S. M. Mordyk, V. E. Storizhko, B. Sulkio-Cleff, and V. I. Voznyy, “Development of a dedicated ion injector for accelerator-based nanoprobe facilities,” *Vacuum*, vol. 73, no. 2, pp. 237–242, 2004.
- [124] S. M. Mordyk, V. I. Voznyy, V. I. Miroshnichenko, V. E. Storizhko, B. Sulkio-Cleff, and D. P. Shulha, “Hydrogen/helium ion injector for accelerator-based microprobe facilities,” *Nucl. Instruments Methods Phys. Res. Sect. B Beam Interact. with Mater. Atoms*, vol. 231, no. 1–4, pp. 37–42, 2005.
- [125] S. N. Mordyk, V. I. Voznyy, V. I. Miroshnichenko, A. G. Ponomarev, V. E. Storizhko, and B. Sulkio-Cleff, “High brightness rf ion source for accelerator-based microprobe facilities,” *Rev. Sci. Instrum.*, vol. 75, no. 5 PART II, pp. 1922–1924, 2004.
- [126] N. S. Smith *et al.*, “High brightness inductively coupled plasma source for high current focused ion beam applications,” *J. Vac. Sci. Technol. B Microelectron. Nanom. Struct.*, vol. 24, no. 6, p. 2902, 2006.
- [127] FEI, “Vion Plasma Focused Ion Beam.” [Online]. Available: <https://www.fei.com/products/fib/vion/>.
- [128] T. Hrnčíř *et al.*, “Novel plasma FIB/SEM for high speed failure analysis, 3D tomography and other applications,” in *Proceedings of the 15th European Microscopy Congress Manchester, UK (Sept. 2012)*, pp. 16–21.
- [129] P. Tesch, N. Smith, N. Martin, and D. Kinion, “High current focused ion beam instrument for destructive physical analysis applications,” in *Proceedings from the 34th International Symposium for Testing and Failure Analysis (ISTFA), 2008*, pp. 7–13.
- [130] N. S. Smith, P. P. Tesch, N. P. Martin, and R. W. Boswell, “New Ion Probe for Next Generation FIB, SIMS, and Nano-Ion Implantation,” *Microsc. Today*, vol. 17, no. 5, pp. 18–23, 2009.
- [131] O. Physics, “Hyperion I Positive Ion Source.” [Online]. Available: <http://www.oregon-physics.com/hyperion1.php>.
- [132] N. Smith, P. Tesch, N. Martin, and R. Boswell, “The Hyperion™ Ion Probe for Next Generation FIB, SIMS and Nano-Ion, Implantation,” *Microsc. Microanal.*,

- vol. 15, no. S2, pp. 312–313, 2009.
- [133] P. C. Thonemann, “Progress in nuclear physics,” *Pergamon Press. London*, vol. 53, p. 219, 1953.
- [134] P. C. Thonemann and E. R. Harrison, “Unclassified Report AERE GP.” R, 1955.
- [135] K. N. Leung, T. K. Samec, and A. Lamm, “Optimization of permanent magnet plasma confinement,” *Phys. Lett. A*, vol. 51, no. 8, pp. 490–492, 1975.
- [136] K. N. Leung, D. A. Bachman, P. R. Herz, and D. S. McDonald, “Rf driven multicusp ion source for pulsed or steady-state ion beam production,” *Nucl. Inst. Methods Phys. Res. B*, vol. 74, no. 1–2, pp. 291–294, 1993.
- [137] D. Wutte *et al.*, “Development of an rf driven multicusp ion source for nuclear science experiments,” *Nucl. Instruments Methods Phys. Res.*, vol. 142, pp. 409–416, 1998.
- [138] Y. Lee *et al.*, “Production of low energy spread ion beams with multicusp sources,” *Nucl. Instruments Methods Phys. Res. Sect. A Accel. Spectrometers, Detect. Assoc. Equip.*, vol. 374, no. 1, pp. 1–6, 1996.
- [139] Y. Lee *et al.*, “A compact filament-driven multicusp ion source,” *Nucl. Instruments Methods Phys. Res. Sect. B Beam Interact. with Mater. Atoms*, vol. 119, no. 4, pp. 543–548, 1996.
- [140] K. L. Scott, T.-J. King, K.-N. Leung, and R. F. Pease, “Characterization of multicusp-plasma ion source brightness using micron-scale apertures,” *J. Vac. Sci. Technol. B Microelectron. Nanom. Struct.*, vol. 19, no. 6, p. 2602, 2001.
- [141] M. Moser *et al.*, “High brilliance multicusp ion source for hydrogen microscopy at SNAKE,” *Nucl. Instruments Methods Phys. Res. Sect. B Beam Interact. with Mater. Atoms*, vol. 273, pp. 226–230, 2012.
- [142] J. Visser, D. J. W. Mous, A. Gottdang, and R. G. Haitsma, “Considerations on accelerator systems requirements and limitations for μ -probe applications,” *Nucl. Instruments Methods Phys. Res. Sect. B Beam Interact. with Mater. Atoms*, vol. 231, no. 1, pp. 32–36, 2005.
- [143] N. C. Podaru, A. Gottdang, D. J. W. Mous, and F. Group, “On the performance of the HVE high-current light-ion 3MV TandetronTM accelerator system,” *Nucl. Instruments Methods Phys. Res. Sect. B Beam Interact. with Mater. Atoms*, vol. 273, pp. 231–233, 2012.
- [144] Q. Ji, X. Jiang, T.-J. King, K.-N. Leung, K. Standiford, and S. B. Wilde, “Improvement in brightness of multicusp-plasma ion source,” *J. Vac. Sci. Technol. B Microelectron. Nanom. Struct. Process. Meas. Phenom.*, vol. 20, no. 6, pp. 2717–2720, 2002.
- [145] Case Technology Inc, “Ion Source Technology,” 2014. [Online]. Available: <http://www.casetechnology.com/implanter/source.html>.
- [146] J. Orloff, M. Utlaut, and L. Swanson, *High Resolution Focused Ion Beams: FIB and Its Applications : The Physics of Liquid Metal Ion Sources and Ion Optics and Their Application to Focused Ion Beam Technology*. Springer Science & Business Media, 2003.
- [147] L. W. Swanson, “Liquid metal ion sources: Mechanism and applications,” *Nucl. Instruments Methods Phys. Res.*, vol. 218, no. 1–3, pp. 347–353, 1983.
- [148] R. G. Forbest, “Understanding how the liquid-metal ion source works,” *Vacuum*, vol. 48, no. 1, pp. 85–97, 1997.
- [149] P. D. Prewett and G. L. R. Mair, *Focused ion beams from liquid metal ion sources*, vol. 1. Research Studies PressLtd, 1991.
- [150] G. Taylor, “Disintegration of water drops in an electric field,” in *Proceedings of the Royal Society of London A: Mathematical, Physical and Engineering Sciences*, 1964, vol. 280, no. 1382, pp. 383–397.
- [151] R. E. Honig, *Vapor pressure data for the more common elements*. David Sarnoff

- Research Center, 1957.
- [152] C. W. Hagen, E. Fokkema, and P. Kruit, “Brightness measurements of a gallium liquid metal ion source,” *J. Vac. Sci. Technol. B*, vol. 26, no. 6, pp. 2091–2096, 2008.
 - [153] G. L. R. Mair and T. Mulvey, “Some aspects of liquid metal ion sources,” *J. Microsc.*, vol. 142, no. 2, pp. 191–200, 1986.
 - [154] Applied Beams LLC, “Ion Sources,” 2017. [Online]. Available: <https://www.appliedbeams.com/product-category/consumables/ion-sources/>.
 - [155] G. Hlawacek, V. Veligura, R. van Gastel, and B. Poelsema, “Helium ion microscopy,” *J. Vac. Sci. Technol. B Microelectron. Nanom. Struct.*, vol. 32, no. 2, p. 20801, 2014.
 - [156] N. P. Economou, J. A. Notte, and W. B. Thompson, “The history and development of the helium ion microscope,” *Scanning*, vol. 34, no. 2, pp. 83–89, 2012.
 - [157] B. W. Ward, J. A. Notte, and N. P. Economou, “Helium ion microscope: A new tool for nanoscale microscopy and metrology,” *J. Vac. Sci. Technol. B Microelectron. Nanom. Struct.*, vol. 24, no. 6, p. 2871, 2006.
 - [158] E. W. Müller, “Das feldionenmikroskop,” *Zeitschrift für Phys.*, vol. 131, no. 1, pp. 136–142, 1951.
 - [159] E. W. Müller and K. Bahadur, “Field ionization of gases at a metal surface and the resolution of the field ion microscope,” *Phys. Rev.*, vol. 102, no. 3, p. 624, 1956.
 - [160] E. W. Müller, “Study of atomic structure of metal surfaces in the field ion microscope,” *J. Appl. Phys.*, vol. 28, no. 1, pp. 1–6, 1957.
 - [161] F. H. M. Rahman, S. McVey, L. Farkas, J. A. Notte, S. Tan, and R. H. Livengood, “The prospects of a subnanometer focused neon ion beam,” *Scanning*, vol. 34, no. 2, pp. 129–134, 2012.
 - [162] J. E. Sansonetti and W. C. Martin, “Handbook of basic atomic spectroscopic data,” *J. Phys. Chem. Ref. Data*, vol. 34, no. 4, pp. 1559–2259, 2005.
 - [163] W. M. Haynes, *CRC handbook of chemistry and physics*. CRC press, 2014.
 - [164] R. Börret, K. Böhringer, and S. Kalbitzer, “Current-voltage characteristics of a gas field ion source with a supertip,” *J. Phys. D. Appl. Phys.*, vol. 23, no. 10, pp. 1271–1277, 1990.
 - [165] R. Hill, J. Notte, and B. Ward, “The ALIS He ion source and its application to high resolution microscopy,” *Phys. Procedia*, vol. 1, no. 1, pp. 135–141, 2008.
 - [166] J. Notte *et al.*, “An introduction to the helium ion microscope,” in *AIP Conference Proceedings*, 2007, vol. 931, no. 1, pp. 489–496.
 - [167] R. H. Livengood, S. Tan, R. Hallstein, J. Notte, S. McVey, and F. H. M. F. Rahman, “The neon gas field ion source—a first characterization of neon nanomachining properties,” *Nucl. Instruments Methods Phys. Res. Sect. A Accel. Spectrometers, Detect. Assoc. Equip.*, vol. 645, no. 1, pp. 136–140, 2011.
 - [168] J. Notte, F. H. M. F. Rahman, S. McVey, S. Tan, and R. H. Livengood, “Neon gas field ion source—stability and lifetime,” *Microsc. Microanal.*, vol. 16, no. 2, pp. 28–29, 2010.
 - [169] H. J. Metcalf and P. Van der Straten, *Laser cooling and trapping*. Springer Science & Business Media, 2012.
 - [170] J. L. Hanssen, J. J. McClelland, E. A. Dakin, and M. Jacka, “Laser-cooled atoms as a focused ion-beam source,” *Phys. Rev. A*, vol. 74, no. 6, p. 63416, 2006.
 - [171] K. A. Twedt, L. Chen, and J. J. McClelland, “Scanning ion microscopy with low energy lithium ions,” *Ultramicroscopy*, vol. 142, pp. 24–31, 2014.
 - [172] J. J. McClelland, A. V Steele, B. Knuffman, K. A. Twedt, A. Schwarzkopf, and T. M. Wilson, “Bright focused ion beam sources based on laser-cooled atoms,”

- Appl. Phys. Rev.*, vol. 3, no. 1, p. 11302, 2016.
- [173] B. Knuffman, A. V Steele, and J. J. McClelland, “Cold atomic beam ion source for focused ion beam applications,” *J. Appl. Phys.*, vol. 114, no. 4, p. 44303, 2013.
 - [174] S. B. Van der Geer, M. P. Reijnders, M. J. de Loos, E. J. D. Vredenbregt, P. H. A. Mutsaers, and O. J. Luiten, “Simulated performance of an ultracold ion source,” *J. Appl. Phys.*, vol. 102, no. 9, p. 94312, 2007.
 - [175] L. Kime *et al.*, “High-flux monochromatic ion and electron beams based on laser-cooled atoms,” *Phys. Rev. A*, vol. 88, no. 3, p. 33424, 2013.
 - [176] J. L. Hanssen, S. B. Hill, J. Orloff, and J. J. McClelland, “Magneto-optical-trap-based, high brightness ion source for use as a nanoscale probe,” *Nano Lett.*, vol. 8, no. 9, pp. 2844–2850, 2008.
 - [177] G. Ten Haaf *et al.*, “Direct Magneto-Optical Compression of an Effusive Atomic Beam for Application in a High-Resolution Focused Ion Beam,” *Phys. Rev. Appl.*, vol. 7, no. 5, pp. 1–12, 2017.
 - [178] A. V Steele, B. Knuffman, and J. J. McClelland, “Inter-ion coulomb interactions in a magneto-optical trap ion source,” *J. Appl. Phys.*, vol. 109, no. 10, p. 104308, 2011.

Chapter 2. Nano-aperture ion source (NAIS)

In order to realize the full potential of keV to MeV PBW system, a high brightness hydrogen ion source featuring low energy spread is desired. However, as discussed in Chapter 1, there is no such high brightness hydrogen ion source available, thus limiting the resolution and throughput of PBW. Nano-aperture ion source (NAIS) [1] is a potential candidate to be as an integral part of sub-10 nm keV to MeV PBW system. NAIS is based on electron impact ionization, where ions are generated by electron-gas collisions, within a sub-micron ionization chamber, and further extracted from a small aperture. In this chapter, the principle of NAIS will be described along with its conceptual design and different theoretical evaluation of the same.

2.1 The Concept of NAIS

2.1.1 Electron ionization process

Electron ionization (EI, formally electron impact/bombardment ionization [2], [3]), as the name implies, is an ionization mechanism in which energetic electrons are employed to ionize atoms or molecules through inelastic interaction [4], [5]. The electron impact ion source was first developed and widely used for mass spectrometry [6]. The electron impact ionization process can ionize the atoms/molecules into different charge states, based on the prevailing impact parameters and the chemical/physical nature of atoms/molecules. The most common ionization process is to remove the loosely bound electron, which requires a minimum ionization energy E_i . This process can be expressed as: $e^- + X \rightarrow X^+ + e^- + e^-$, where X and X^+ are the atom/molecule and its ion, respectively, as shown in Figure. 2-1. Energy conservation requires that the energy of impact electrons must exceed the ionization energy E_i to trigger the ionization process. Table. 2-1 presents the first ionization energies E_i for different gases, whose values are in 10s eV range.

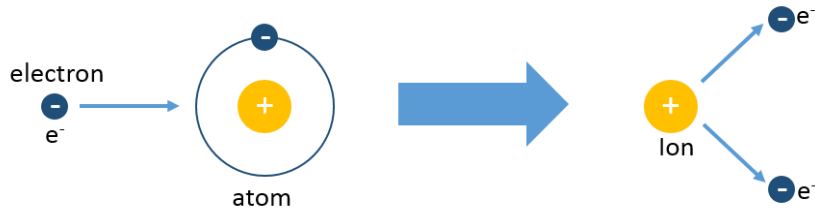


Figure. 2- 1 Electron ionization process to generate ions.

Table. 2- 1 First ionization energy E_i for different gases [7], [8].

	H ₂	He	Ar
Ionization Energy E_i (eV)	13.6	24.6	15.8

In the electron impact ionization process, not all collisions result in ionizing gas atoms/molecules. Electron ionization cross section [2], [5], [9] gives the probability

that an electron of a certain energy ionizes an atom/molecule. The cross section for creation of multi-charged states ions, in the other words n th electron ionization process ($n > 1$), are usually very small, when compared to first election ionization process [10]. H₂ molecular gas is different to monoatomic gas. The electron ionization process from hydrogen has two products, H₂⁺ and H⁺. The H⁺ ionization process requires an additional 4.5 eV energy to dissociate H-H bonds at room temperature 293 K. Figure. 2-2 shows the experimentally measured ionization cross sections of different ions as a function of incident electron energies.

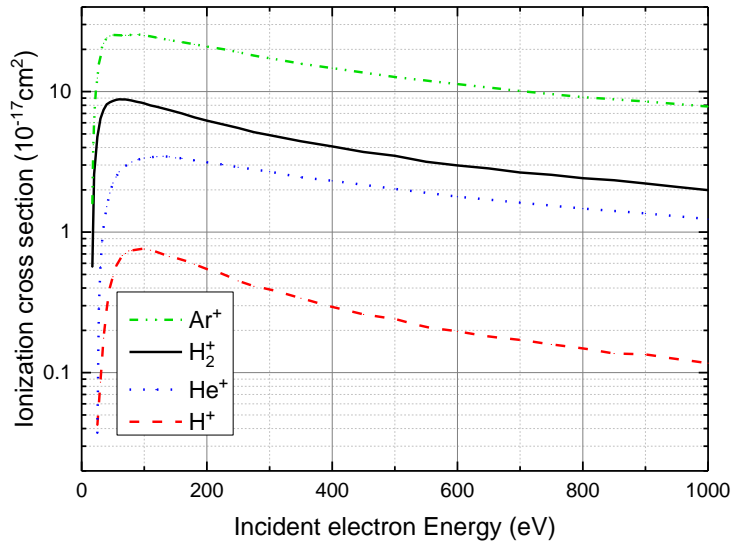


Figure. 2- 2 Experimentally measured ionization cross sections of different ions as a function of incident electron energies. Data is extracted from Ref [10], [11].

2.1.2 The configuration of NAIS

As discussed in Chapter 1, the typical reduced brightness for Helicon RF ion source and multicusp ion source is $\sim 100 \text{ A}/(\text{m}^2\text{srV})$, whereas a higher brightness of around $10^3 - 10^4 \text{ A}/(\text{m}^2\text{srV})$ was achieved in these ion sources by reducing its emitting area. The same strategy is adopted for electron impact ion source; in which a sub-micron source emitting size is chosen, which is referred to as nano-aperture ion source (NAIS). The attempt of electron impact ion source for high brightness and low energy spread was

made by Barth and his colleagues in 1985 [12]. The key point of this ion source is to maintain the ionization region at micron size, and inject a high density electron beam into the ionization region. The micron size gas cluster was created by effusing gas through a small aperture, where the thermal electrons were introduced via a magnetic mirror system from 2π electron emitter [12]. The experimental reduced brightness from this ion source was $100 \text{ A}/(\text{m}^2\text{srV})$, which was limited by the low injected electron current. It was estimated potentially to deliver up to $10^4 \text{ A}/(\text{m}^2\text{srV})$ of brightness if more electron current was injected [12]. The idea to emit ions from a small sized chamber coupled with high brightness and low energy spread is very promising due to semiconductor industrial history for achieving dedicated and small structures. Following the trend of miniaturization, a nano-aperture ion source comprised of sub-micron emitting size was invented by Kruit and Tondare based on microelectromechanical systems (MEMS) technology in 2006 [13], [14]. NAIS relies on a sub-micron ionization chamber to which the gas of interest is constrained. The schematic of NAIS configuration and its dimensions is shown in Figure. 2-3. An electron beam is injected into the double-aperture ($0.1 - 1 \mu\text{m}$) to ionize gas by electron impact ionization process. A strong electric field ($\sim 10^7 \text{ V/m}$) is maintained by applying a small bias voltage across the sub-micron NAIS ionization chamber. The ionization chamber is electrically isolated between these two electrodes. The generated ions are extracted from the double-aperture due to this electric field and further accelerated downstream by an extractor. The extractor must be kept at a more negative potential than the injected electron energy to prevent the transmission of electrons. The small opening size of the double-aperture not only reduces the ion emitting size, but also helps to reduce gas escaping from the ionization chamber into the vacuum. On the flip side, the reduced double-aperture size will greatly affect the total output of the ion current. Thus, the selection of double-aperture size is a trade-off between the output ion current and required brightness.

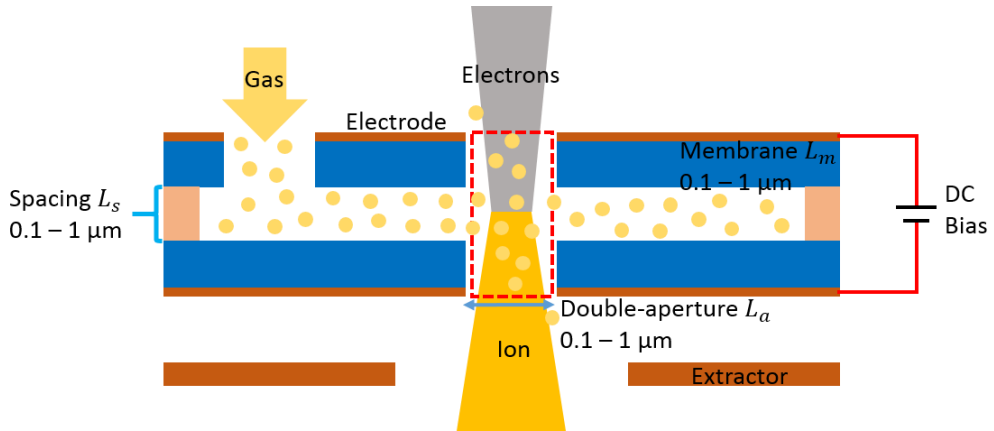


Figure. 2- 3 Schematic of NAIS configuration and its dimensions.

2.1.3 Operational condition of NAIS

In NAIS, ion-gas and ion-ion interactions will degrade the quality of beam, thus, resulting in low brightness and high energy spread. This scenario could be avoided by choosing an optimal working pressure at the ionization chamber. Knudsen number K_n as illustrated in Figure. 2-4, is a dimensionless number, and is expressed as

$$K_n = \frac{\lambda}{L} \quad (2.46)$$

where λ is the mean free path of a particle in the gas, and L is the characteristic length where such gas is constrained. To prevent ion-gas and ion-ion interactions, NAIS should be operated in free-molecule flow or transition regime, where non-collective effect (no collision between gas molecules) becomes more significant [15]. Under this condition, gas is either moderately or highly rarefied, with Knudsen number being more than 0.1.

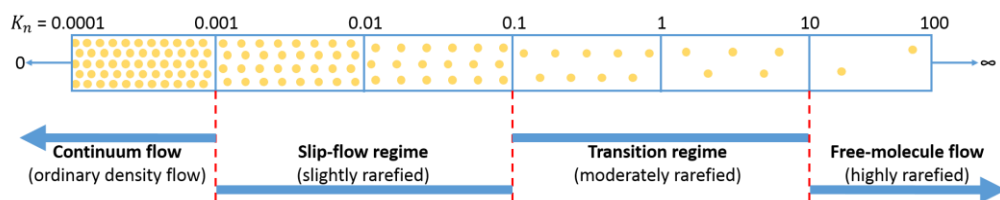


Figure. 2- 4 Knudsen number K_n regimes.

Figure. 2-5 shows Knudsen number K_n for hydrogen, helium, and argon as a function of characteristic length L for various gas pressures, at room temperature (293 K). For more than 1 bar of gas pressure, sub-1 μm characteristic length satisfies the required operational condition for NAIS. On the other hand, sub-100 mm characteristic length can hold gas pressure more than 10 bar. Clearly, the characteristic length is determined by maximum gas operational pressure. Sub μm characteristic length at or below 1 bar will ensure $K_n < 0.1$, therefore meeting the requirement of most operational conditions. The characteristic length of NAIS is aimed to 100 nm to 1 μm , where the operational gas pressure can reach up to 10 to 1 bar respectively.

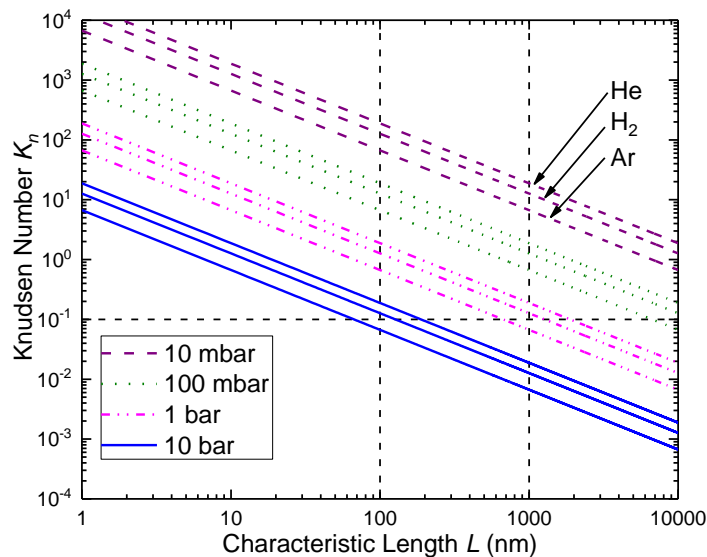


Figure. 2- 5 Knudsen number K_n for hydrogen, helium, and argon as a function of characteristic length L for various gas pressures at room temperature (293 K).

From the definition of reduced brightness, high ion current density is crucial for high brightness. From the perspective of ionization cross section, injected electrons with an energy of 50 – 200 eV are optimal, seen Figure. 2-2. Other than the cross section, the injected electron current density needs to be taken into consideration. Generally speaking, attainable electron current density from scanning electron microscopes (SEMs) is inversely proportional to the electron energy. The most commonly available

minimal electron energy is 1 keV in conventional SEMs, therefore, the energy of injected electrons is chosen to be 1 keV, as a tradeoff between available electron beam current density and optimal ionization cross section. The attainable electron probe current as a function of probe size is described in Appendix-2.

2.2 Theoretical NAIS source performance

2.2.1 Theoretical NAIS reduced brightness

The gas that needs to be ionized is fed into the ionization chamber of NAIS, and was found to reside in the double-aperture region with negligible leakage to the vacuum [16]. In the transverse plane of NAIS, gas pressure (and correspondingly its density) drops from the double-aperture edge to the center, while the injected electron current density has a Gaussian spatial distribution [17], [18]. Therefore, the initial ion beam is quasi-uniformly distributed along the radial distance. Along the longitudinal direction, gas pressure drops dramatically from the double-aperture to the vacuum, assuming a quasi-Gaussian distribution [16] of standard deviation σ equal to half channel gap (spacing) $\frac{1}{2}L_s$ for approximation, seen in Figure. 2-3. The number of ions generated by electron impact inside the chamber is given by

$$I_i = \int dI_i = \int I_e \rho(z)\sigma(g)dz = \sqrt{\frac{\pi}{2}} I_e \rho_0 \sigma(g) L_s \quad (2.47)$$

in which I_i and I_e are the ion and electron currents. $\rho(z)$ is the gas density with a Gaussian distribution in the longitudinal direction, represented in the form of $\rho_0 \exp(-\frac{z^2}{2(L_s/2)^2})$. $\sigma(g)$ is the partial ionization cross section of gas. In this equation, the injected electron current is considered as constant because the cross section is relatively small, which implies that only a few electrons will collide with gas molecules. The ionization efficiency η for NAIS is expressed as

$$\eta = \frac{I_i}{I_e} = \frac{J_i}{J_e} = \sqrt{\frac{\pi}{2}} \rho_0 \sigma(g) L_s \quad (2.48)$$

where J_e and J_i are the injected electron and generated ion current densities. The injected electron current density J_e can be derived from Appendix-1, and is as shown in Figure. 2-6. The ionization efficiency η is proportional to the gas density (pressure) and the channel height. However, as mentioned in the preceding discussion, the gas

pressure and channel height should satisfy the requirement of gas operational condition, i.e. K_n should be more than 0.1. For Schottky (thermal field emission) SEM [19], obtaining an electron probe current of more than μA is not available [20], therefore, as seen from Figure. 2-6, a probe size of less than 100 nm is the optimal choice. Whereas for LaB_6 and tungsten SEMs, the electron probe size can be chosen up to 1 μm . However, the choice of using too small electron probe size is not desirable, as this will lead to a reduced injected electron current resulting in a lower ion brightness.

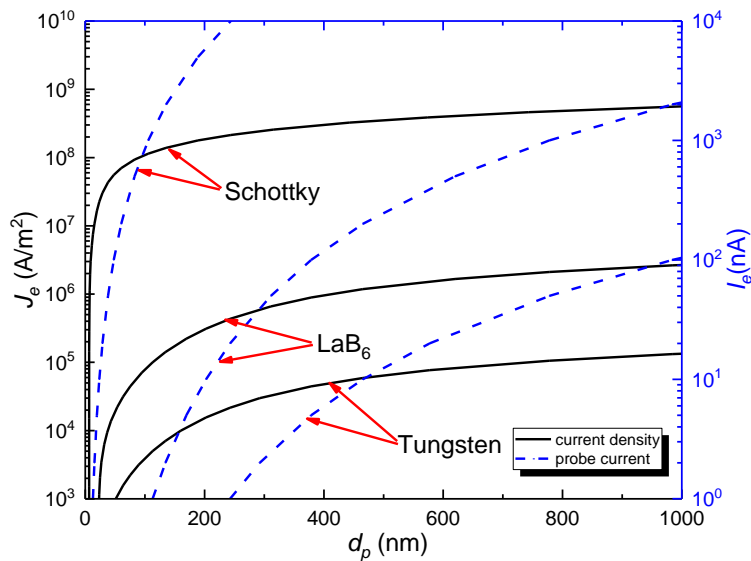


Figure. 2- 6 Electron probe current density J_e and current I_e as a function of electron probe size d_p for tungsten, LaB_6 and Schottky emitters for 1 keV electron.

The resulting reduced brightness, assuming a thermionic source, derived from Eq. 1.26, is

$$B_r = \frac{e\rho_0\sigma(g)L_S J_e}{\sqrt{2\pi}kT} \quad (2.49)$$

The reduced brightness is proportional to the NAIS channel length L_S , injected electron current density, and gas density (pressure). However, the achievable reduced brightness is strongly limited by the practical operational pressure of NIAS and attainable electron beam current density.

For obtaining the achievable maximum reduced brightness, under the NAIS operational limits as explained earlier from conventional SEMs, the operational gas pressure for Schottky SEM is 10 bar with less than 100 nm characteristic length. Whereas for LaB₆ and tungsten SEMs, it is 1 bar of gas pressure with less than 1 μm characteristic length. The injected electron beam size, double-aperture size, and channel length were all kept equal to the characteristic length. Using the above assumption, Figure. 2-7, Figure. 2-8, and Figure. 2-9 describe ion current I_i and reduced brightness B_r as a function of characteristic length L for tungsten, LaB₆, and Schottky SEMs, respectively, with 1 keV injected electron beam. The tungsten SEM has the ability to deliver reduced brightness up to $10^5 \text{ A}/(\text{m}^2\text{srV})$ for H₂⁺ while $5 \times 10^3 \text{ A}/(\text{m}^2\text{srV})$ for H⁺ with ion beam emitting size of 1 μm . Ion currents are 100 nA for H₂⁺ and less than 1 nA for H⁺. For Ar⁺, due to the high ionization cross section, the reduced brightness can reach few $10^5 \text{ A}/(\text{m}^2\text{srV})$. As expressed by Eq. 2.4, a higher injected electron current density is capable of generating higher ion reduced brightness. Schottky SEM is an ideal choice for an electron injector, since it can supply more than $10^8 \text{ A}/\text{m}^2$ electron beam at large probe size (as seen from Figure. 2-6). From Figure. 2-9, when using schottky SEM delivering 100 nm electron spot size: the highest estimated ion reduced brightness is around $10^7 \text{ A}/(\text{m}^2\text{srV})$ for H₂⁺, and a few $10^6 \text{ A}/(\text{m}^2\text{srV})$ for H⁺ while having up to 100 nA of ion beam current. Whereas the maximum reduced brightness for Ar⁺ is estimated to be about $10^8 \text{ A}/(\text{m}^2\text{srV})$.

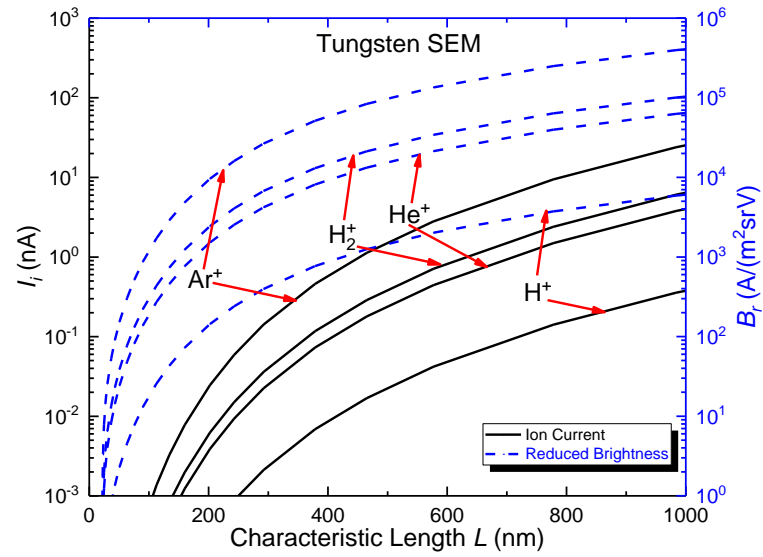


Figure. 2- 7 Ion current I_i and reduced brightness B_r as a function of characteristic length L for tungsten SEM with 1 keV injected electron beam.

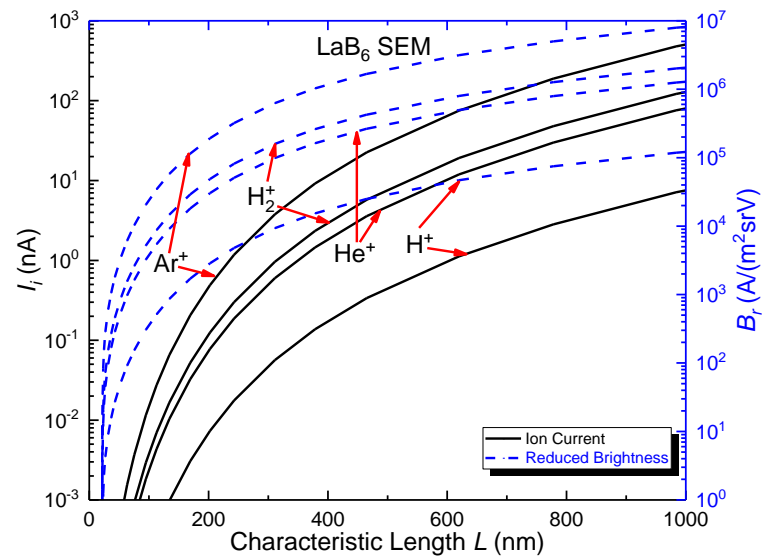


Figure. 2- 8 Ion current I_i and reduced brightness B_r as a function of characteristic length L for LaB₆ SEM with 1 keV injected electron beam.

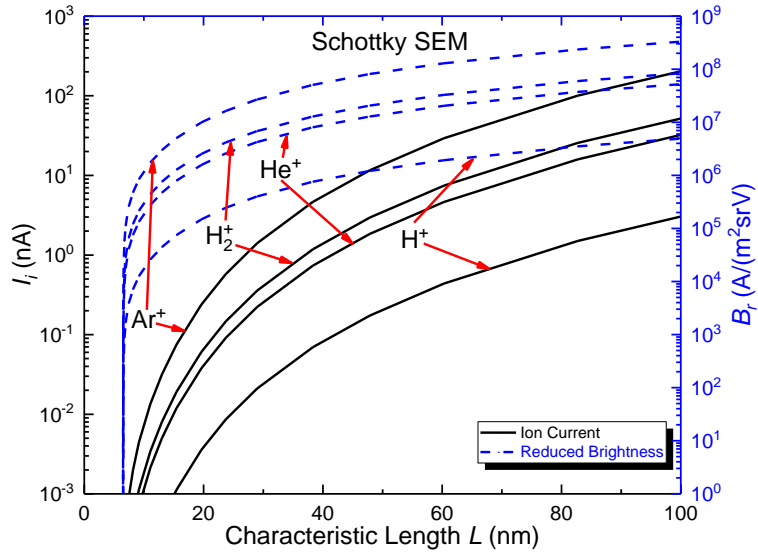


Figure. 2- 9 Ion current I_i and reduced brightness B_r as a function of characteristic length L for Schottky SEM with 1 keV injected electron beam.

In the above estimation, the operational condition of gas pressure is near the upper limit: 1 bar for tungsten and LaB_6 SEMs, and 10 bar for Schottky SEM. Additionally, SEM electron probe is assumed to be perfectly tuned with maximum electron current density for desired probe size. However, the maximum estimated reduced brightness is based on conventional SEMs, therefore this maximum value is still a conservative estimate.

2.2.2 Energy spread

As discussed in Chapter 1.1.3, there are three different contributions to the overall longitudinal energy spread. First, the intrinsic energy spread originates from the thermal energy following a Maxwell-Boltzmann distribution. Thus during the ionization process, ions will inherit the original gas thermal energy (~0.038 eV at room temperature 293 K) with a portion towards longitudinal energy spread of ~0.026 eV.

The second contribution to the longitudinal energy spread is due to the variation of local electric potential across the ionization volume (created by the DC bias across the ionization chamber), where a particular ion is generated in NAIS, shown in the red

dotted box in Figure. 2-3. The electric field in the NAIS is preferred to be as high as possible in order to reduce the ion extraction time, so that the statistical Coulomb effects (i.e. Boersch effect and trajectory displacement effect) can be reduced. However, the electric field cannot exceed the breakdown field of the insulating materials. Additionally, a larger DC bias will contribute to larger energy spread. The electric field is chosen to be $\sim 10^7$ V/m, lower than the threshold of silicon breakdown field ($\sim 3 \times 10^7$ V/m [21]). Using Schottky SEM as electron injector, the ionization chamber height is the same as characteristic length of 100 nm. Therefore the DC bias is required to be ~ 3 V, while it is ~ 30 V for tungsten SEM with 1 μm characteristic length. The *rms* energy spread calculated from this effect is ~ 1 eV and ~ 10 eV for Schottky and tungsten SEMs, respectively. For further reduction of the energy spread, electrodes can be integrated inside the NAIS ionization chamber. The *rms* energy spread will be ~ 0.3 eV and ~ 3 eV for Schottky and tungsten SEMs, respectively.

Coulomb effects among ions, including Boersch effect [22] and trajectory displacement effect [23] are the 3rd contribution to the energy spread. Due to the non-equilibrium state of energy spread between transverse plane and longitudinal direction, the “hot” temperature in transverse plane tends to transfer to longitudinal direction for a 3D thermodynamic equilibrium state, according to Coulomb collision and other processes, as detailed in Chapter 1.1.4 and in the following part. This contribution to energy spread can be neglected as the dominant factor comes from the DC bias across the NAIS ionization chamber.

2.3 The influence of Coulomb effect

The important factor to clarify the influence of Coulomb effects is Debye length λ_D . In the NAIS, there exists three different kinds of charged particles: injected electrons (1 keV), secondary electrons generated from ionization process, and generated ions. For simplification, the first two kinds of electrons can be classed as a same kind. The electron temperature is related to the electron beam energy. The generated ions inherit the thermal energy of the gas, with an ion temperature of room temperature 273 K. In the following sub-section, the Debye length λ_D is calculated when maximum reduced brightness is reached for both tungsten and Schottky SEMs for H_2^+ and H^+ . It serves as the upper limit for the operation for NAIS.

2.3.1 Space charge effect

As described in Chapter 1.1.4, Debye length λ_D is given by the combination of electron and ion Debye lengths λ_{D_e} and λ_{D_i} [24],

$$\frac{1}{\lambda_D^2} = \frac{1}{\lambda_{D_e}^2} + \frac{1}{\lambda_{D_i}^2} = \frac{q_e^2 n_e}{\epsilon_0 k T_e} + \frac{q_i^2 n_i}{\epsilon_0 k T_i} \quad (2.50)$$

where q_e and q_i are the electron and ion charges, n_e and n_i are the electron and ion densities, T_e and T_i are the temperatures of the electrons and ions, respectively, ϵ_0 is the electric constant. When beam dimension is much larger than Debye length λ_D , the Debye shielding will affect the maximum beam current density, caused by the collective effect of self-generated the field. For electrons, the Debye length is much larger than that for ions, therefore the Debye length of entire plasma (electrons and ions) can be approximated as ion Debye length.

The spaced charge limited (SCL) current inside NAIS is calculated based on the 2D Child-Langmuir Law, as described in Chapter 1.1.4 [25],

$$J(2) \cong J(1) \left(1 + \frac{D}{\pi L_a}\right) = \frac{4\epsilon_0}{9D^2} \left(\frac{2e}{m}\right)^{1/2} V^{3/2} \left(1 + \frac{D}{\pi L_a}\right) \quad (2.51)$$

In Table. 2-2, for tungsten SEM, we can find that Debye lengths for different ion species are $> 10^{-5}$ m, which is at least one order of magnitude larger than the beam size of 1 μm . The noticeable point is that H^+ and H_2^+ are generated simultaneously, so both of them should be considered together as to estimate space charge effects. However it is reasonable to consider only H_2^+ because H_2^+ is the dominant portion (H^+ 5.6%, H_2^+ 94.4% [11]). As a cross check, the SCL current density and current (calculated from Eq. 2.6) are much higher than the maximum obtainable beam current density and current for NAIS. Therefore, the space charge effect is not important or crucial for NAIS in this operational condition equipped with tungsten SEM.

Table. 2- 2 Debye length λ_D and SCL beam current density J and current I for different ion species, at 1 μm characteristic length equipped with 1 keV tungsten SEM.

	Theoretical upper limit				SCL	
	Debye length λ_D (m)	Ionization efficiency η (%)	Current density J (A/m ²)	Current I (nA)	Current density J (A/m ²)	Current I (nA)
e^-	9.3×10^{-4}		1.3×10^5	100		
H^+	9.6×10^{-5}	0.4	4.6×10^2	0.4	2.3×10^6	1800
H_2^+	2.3×10^{-5}	6.1	7.8×10^3	6.1	1.6×10^6	1300
He^+	3.0×10^{-5}	3.8	4.8×10^3	3.8	1.1×10^6	900
Ar^+	1.2×10^{-5}	24	3.1×10^4	24	3.6×10^5	300

For Schottky SEM, as shown in Table. 2-3, it differs from its tungsten SEM counterpart by its high injected electron current density and smaller characteristic length (5×10^{-7} – 3×10^{-6} m), which is slightly larger compared to the characteristic length of 100 nm. In this situation, the space charge effect will pose a practical limit to the maximum beam current, above which space charge effect starts to play a role. To mitigate these effects one approach is to reduce the operational gas pressure, or use smaller injected electron current.

Table. 2- 3 Debye length λ_D and SCL beam current density J and current I for different ion pieces, at 100 nm characteristic length equipped with 1 keV Schottky SEM.

	Theoretical upper limit				SCL	
	Debye length λ_D (m)	Ionization efficiency η (%)	Current density J (A/m ²)	Current I (nA)	Current density J (A/m ²)	Current I (nA)
e ⁻	3.0×10^{-5}		1.3×10^8	1000		
H ⁺	3.0×10^{-6}	0.4	4.8×10^5	4	7.2×10^6	60
H ₂ ⁺	7.1×10^{-7}	6.5	8.3×10^6	65	5.2×10^6	40
He ⁺	9.1×10^{-7}	4.0	5.1×10^6	40	3.6×10^6	30
Ar ⁺	3.6×10^{-7}	25	3.2×10^7	250	1.1×10^6	10

To operate the NAIS equipped with Schottky SEM unaffected by space charge effect, the desired ion beam current is utilized to check the performance of NAIS. Although the reduced brightness will decrease due to the low emitting current density, we could still obtain more than 10^6 A/(m²srV) for all ion species, as shown in Table. 2-4. This value of reduced brightness can satisfy the requirement for high brightness ion source.

Table. 2- 4 Reduced brightness calculated, where space charge effect is negligible for NAIS equipped with Schottky SEM with a characteristic length of 100 nm.

Ion	Desired current density J (A/m ²)	Desired Current I (nA)	Reduced brightness (A/(m ² srV))
H ⁺	1.5×10^5	1.2	2×10^6
H ₂ ⁺	2.6×10^6	20	2×10^7
He ⁺ , Ar ⁺	6.4×10^5	5	7×10^6

In the above scenario, the maximum current density from Child-Langmuir's limit is derived from the situation where all ions are generated from one electrode plane. Whereas in NAIS, ions are generated in the entire ionization chamber, which results in a reduction of estimated space charge effect. Additionally, in NAIS, the injected electrons have the ability to compensate the space charge effect. Therefore, it is reasonable to neglect the space charge effect for the tungsten SEM and Schottky SEM

with low desired ion beam current, as indicated in Table. 2-4. In addition, such space charge effect can be compensated by external focus lens for a uniformly distributed ion beam.

2.3.2 Statistical Coulomb effects

The statistical Coulomb effects consist of Boersch effect and trajectory displacement effect, originating from the individual pairs of particle-particle interaction [26]. The high current density of slow moving beam (usually in a beam crossover or source emitting area) will usually be affected more by Coulomb effects. For NAIS, this is located inside the NAIS ionization chamber. When the beam is extracted from the NAIS, it will get broadened and accelerated, which is considered as “collision free”, where the Coulomb effects can be neglected.

Boersch effect causes a cooling effect across the transverse and longitudinal directions to reach a 3D thermodynamic equilibrium state. The effective transverse-longitudinal temperature relaxation time τ_{eff} to reach the equilibrium state is shown in Table. 2-5 and Table. 2-6. The ion flight time through NAIS is much shorter than the effective temperature relaxation time, meaning Boersch effect doesn't have enough time to reach thermodynamic equilibrium. Even if the equilibrium state is reached within the NAIS, the *rms* energy spreads are 0.4 eV and 0.1 eV for tungsten SEM and Schottky SEM, respectively. These energies only account to a fraction of the total energy spread.

Table. 2- 5 Effective transverse-longitudinal temperature relaxation time τ_{eff} and the ion flight time in NAIS, equipped with tungsten SEM with a characteristic length of 1 μm .

Ion	Current I (nA)	τ_{eff} (s)	Flight time in NAIS (s)	Maximum current* (nA)
H⁺	0.4	2.6×10^{-4}	2.3×10^{-11}	7.0
H₂⁺	6.1	2.1×10^{-5}	3.2×10^{-11}	5.0
He⁺	3.8	4.9×10^{-5}	4.6×10^{-11}	3.5
Ar⁺	24	2.5×10^{-5}	1.4×10^{-10}	1.1

* Beam current when only one ion exists inside NAIS at a time.

Table. 2- 6 Effective transverse-longitudinal temperature relaxation time τ_{eff} and the ion flight time in NAIS, equipped with Schottky SEM with a characteristic length of 100 nm.

Ion	Current I (nA)	τ_{eff} (s)	Flight time in NAIS (s)	Maximum current* (nA)
H⁺	1.2	4.0×10^{-6}	7.2×10^{-12}	22.2
H₂⁺	20	3.3×10^{-7}	1.0×10^{-11}	15.9
He⁺	5.0	1.9×10^{-6}	1.4×10^{-11}	11.1
Ar⁺	5.0	6.0×10^{-6}	4.6×10^{-11}	3.5

* Beam current when only one ion exists inside NAIS at a time.

The transverse trajectory effect broadens the virtual source size, causing the reduction of beam reduced brightness. The broadening effect is proportional to the beam current density. The strong electric field across the NAIS ionization chamber can shorten the interaction time and reduce the trajectory displacement effect. Table. 2-5 and Table. 2-6 show the effective transverse-longitudinal temperature relaxation time τ_{eff} , and ion flight time when only one ion exists inside NAIS at a time with the corresponding maximum ion beam current, equipped with tungsten SEM at 1 μm and Schottky SEM at 100 nm, respectively. Although this is a very conservative estimate, relaxation time τ_{eff} is already several orders of magnitude lower than the flight time. Therefore, Boersch effect can be neglected. This also implies that there will be no ion-ion collision inside the NIAS ionization chamber, therefore the transverse trajectory effect is insignificant. For Ar⁺ with tungsten SEM and Schottky SEM respectively, more than one ion exist inside the NAIS ionization chamber simultaneously. Nevertheless, this is a very rough estimate to judge the influence of Coulomb effects. It maybe worthwhile to have a more elaborate simulation to gain more information and details regarding Coulomb effects.

2.4 Summary

In this chapter, the concept and configuration of NAIS ion source have been described. Consequently, the operational condition of NAIS is discussed, suggesting that a 100 nm characteristic length with 1 bar gas pressure, and a 1 μm characteristic length with 10 bar gas pressure can meet the requirement of a more than 0.1 Knudsen number. For a 1 keV electron injector, is proposed to use a conventional SEM column to generate ions in the NAIS. Tungsten SEM and Schottky SEM were theoretically evaluated with characteristic lengths of 1 μm and 100 nm, separately. Subsequently, the current and current density regime where Coulomb effects, including space charge effect and statistical effects, degrade the beam quality, were discussed. The tungsten SEM has the ability to deliver ion beams with a reduced brightness of up to $10^5 \text{ A}/(\text{m}^2\text{srV})$ for H_2^+ and $5 \times 10^3 \text{ A}/(\text{m}^2\text{srV})$ for H^+ , while the Schottky SEM can deliver up to $10^7 \text{ A}/(\text{m}^2\text{srV})$ for H_2^+ and $10^6 \text{ A}/(\text{m}^2\text{srV})$ for H^+ . The energy spreads are 10 eV and 1 eV with external electrodes, and 3 eV and 0.3 eV with internal electrodes, for tungsten and Schottky SEMs respectively. The NAIS equipped with Schottky is a promising hydrogen ion source for high brightness and low energy spread, with $> \text{nA}$ H_2^+ current. According to our knowledge, the results obtained from the theoretical performance is better than any existing hydrogen ion source would produce.

Reference

- [1] D. S. Jun, V. G. Kutchoukov, and P. Kruit, “Ion beams in SEM: An experiment towards a high brightness low energy spread electron impact gas ion source,” *J. Vac. Sci. Technol. B*, vol. 29, no. 6, p. 06F603, 2011.
- [2] T. D. Märk and G. H. Dunn, *Electron impact ionization*. Springer Science & Business Media, 2013.
- [3] H. R. Kaufman, U. S. N. A. and S. Administration, and L. R. Center, *Performance Correlation for Electron-bombardment Ion Sources*. National Aeronautics and Space Administration, 1965.
- [4] A. D. McNaught and A. D. McNaught, *Compendium of chemical terminology*, vol. 1669. Blackwell Science Oxford, 1997.
- [5] L. Vályi, *Atom and ion sources*. Akadémiai Kiado, 1977.
- [6] J. Griffiths, “A brief history of mass spectrometry,” *Anal. Chem.*, vol. 80, no. 15, pp. 5678–5683, 2008.
- [7] J. E. Sansonetti and W. C. Martin, “Handbook of basic atomic spectroscopic data,” *J. Phys. Chem. Ref. Data*, vol. 34, no. 4, pp. 1559–2259, 2005.
- [8] W. M. Haynes, *CRC handbook of chemistry and physics*. CRC press, 2014.
- [9] H. S. W. Massey, E. H. S. Burhop, and H. B. Gilbody, “Electronic and ionic impact phenomena,” 1969.
- [10] R. Rejoub, B. G. Lindsay, and R. F. Stebbings, “Determination of the absolute partial and total cross sections for electron-impact ionization of the rare gases,” *Phys. Rev. A*, vol. 65, no. 4, p. 42713, 2002.
- [11] H. C. Straub, P. Renault, B. G. Lindsay, K. A. Smith, and R. F. Stebbings, “Absolute partial cross sections for electron-impact ionization of H₂, N₂, and O₂ from threshold to 1000 eV,” *Phys. Rev. A*, vol. 54, no. 3, p. 2146, 1996.
- [12] J. E. Barth *et al.*, “Gas ion source for focused beams,” *Microelectron. Eng.*, vol. 3, no. 1, pp. 147–152, 1985.
- [13] V. N. Tondare, “Towards a high brightness, monochromatic electron impact gas ion source,” TU Delft, Delft University of Technology, 2006.
- [14] P. Kruit and V. N. Tondare, “Particle-optical apparatus equipped with a gas ion source,” European Patent 06220357.0, 2006.
- [15] M. Gad-el-Hak, “The fluid mechanics of microdevices—the Freeman scholar lecture,” *J. Fluids Eng.*, vol. 121, no. 1, pp. 5–33, 1999.
- [16] J. Peatross and D. D. Meyerhofer, “Novel gas target for use in laser harmonic generation,” *Rev. Sci. Instrum.*, vol. 64, no. 11, pp. 3066–3071, 1993.
- [17] M. S. Bronsgeest, J. E. Barth, L. W. Swanson, and P. Kruit, “Probe current, probe size, and the practical brightness for probe forming systems,” *J. Vac. Sci. Technol. B*, vol. 26, no. 3, pp. 949–955, 2008.
- [18] J. R. Michael and D. B. Williams, “A consistent definition of probe size and spatial resolution in the analytical electron microscope,” *J. Microsc.*, vol. 147, no. 3, pp. 289–303, 1987.
- [19] J. Orloff, *Handbook of charged particle optics*. CRC press, 2008.
- [20] G. Dehm, J. M. Howe, and J. Zweck, *In-situ electron microscopy: applications in physics, chemistry and materials science*. John Wiley & Sons, 2012.
- [21] V. Siklitsky, “New semiconductor materials. characteristics and properties,” *Online]. Available <http://www.ioffe.rssi.ru/SVA/NSM>, 2001.*
- [22] H. Boersch, “Experimentelle Bestimmung der Energieverteilung in thermisch ausgelösten Elektronenstrahlen,” *Zeitschrift für Phys.*, vol. 139, no. 2, pp. 115–146, 1954.
- [23] G. H. Jansen, “Coulomb Interactions in Particle Beams (Advances in Electronics and Electron Physics Supplement 21).” Academic Press, 1990.

- [24] J. P. Freidberg, *Plasma physics and fusion energy*. Cambridge University Press, 2007.
- [25] Y. Y. Lau, “Simple theory for the two-dimensional Child-Langmuir law,” *Phys. Rev. Lett.*, vol. 87, no. 27, p. 278301, 2001.
- [26] M. Reiser, *Theory and design of charged particle beams*. John Wiley & Sons, 2008.

Chapter 3. Simulated performance of nano-aperture ion source (NAIS)

3.1 Introduction

The nano-aperture ion source (NAIS) employs a dedicated sub-micron ionization chamber to constrain the gas within it. A focused electron beam is then injected into this ionization chamber, which generates desired ions through electron impact processes. In the previous chapter, the reduced brightness of the NAIS was evaluated theoretically with several assumptions. The gas distribution was taken to be a Gaussian distribution [1] along the optical axis. Ions were assumed to originate from different planes across the NAIS ionization chamber with the same emitting area, and with no ions being generated outside the ionization chamber. In addition, all generated ions were assumed to be extracted from the ionization chamber with no collisions occurring with NAIS chamber membranes, and no ions escaping through the electron injecting aperture. Also, the theoretical reduced brightness estimation does not consider an influence from the NAIS chip bias where a constant electric field (10^7 V/m) was used to evaluate the energy spread. Furthermore, the deterioration of reduced brightness from Coulomb effects was ignored.

In this chapter, the beam parameters for an ideal NAIS performance are simulated and evaluated in the following procedures, and shown in Figure. 3-1. First, the gas distribution (within the sub-micron ionization chamber) is analyzed using COMSOL Multiphysics® [2], a finite element analysis software. The gas distribution and the spatial distribution of injected electrons determine the ion emission profile. Second, Poisson Superfish code [3] is applied to calculate the electric field generated in z-axis symmetric cylindrical coordinates. The results from these simulations are fed into the General Particle Tracer (GPT) package [4] to simulate beam trajectories and beam

emittance from the NAIS. The following parameters were used in GPT simulation: The injected electron energy is fixed at 1 keV as a trade-off between the ionization cross section and practical performance of available electron guns (as seen in Appendix 2). The extractor plate is biased to -1 kV and is placed 1 mm away from the NAIS, so as to extract the ion beam and at the same time prevent the injected electrons from entering downstream of the setup. In the GPT simulation, Coulomb effects were included to check their influence on the reduced brightness. The virtual source size was computed by tracing back the slopes of beam trajectory rays, to a point where they form the smallest crossover.

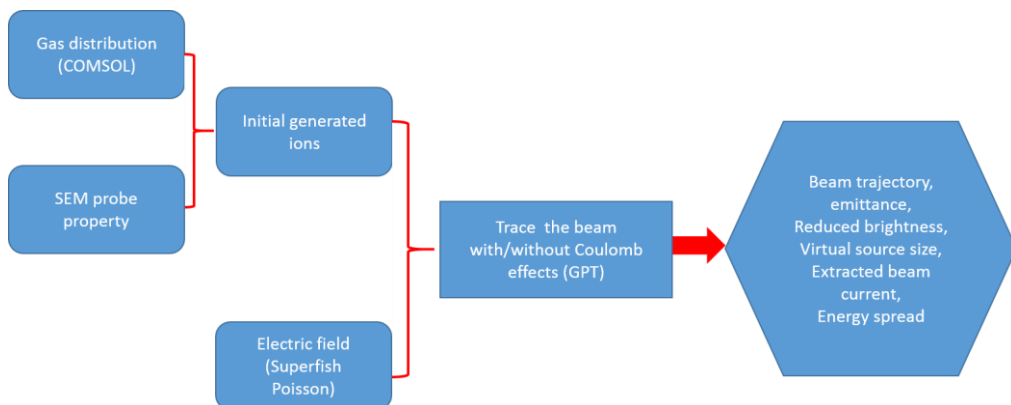


Figure. 3- 1 NAIS simulation flow chart.

3.2 Gas distributions

Inside the NAIS ionization chamber, ions are not generated from a single point or plane but from a sub-micrometer volume. Since the ionization probability is directly dependent on the availability of gas molecules, it is important to identify the gas distribution inside the ionization region. Knowing the spatial distribution of gas molecules, where individual ions are generated, will provide information about the initial energy distribution of the ion beam originating from the NAIS. COMSOL simulations were performed using a laminar flow model, although the operating condition of the NAIS is under a transitional or molecular flow. The upper limit of the gas pressure with Knudsen number $K_n \approx 0.1$ is solved via conventional continuum equations [5]. The Knudsen number can meet the requirement of molecular flow or transitional flow only in the double-aperture region of NAIS. Within the gas feed channel, gas is in the continuum (laminar) flow regime. Therefore, it is reasonable to simulate the gas distribution under a laminar flow model within NAIS.

3.2.1 Consideration of the NAIS geometry relationship

For a NAIS ionization chamber, there are three critical parameters, i.e. double-aperture size L_a , spacing height L_s , and membrane thickness L_m that determine the performance of the NAIS. L_m and L_s are maintained at equal dimensions, so that thick membranes can confine more gas inside the chip since the chamber spacing is higher. Now, the relationship between L_a and L_s has to be carefully investigated.

The design of the NAIS ionization chamber is a cuboid channel with concentric apertures as described in Chapter 2. L_a is kept very small in comparison to the cuboid channel (few mm \times few mm of length and width). Gas is fed through one side of the ionization chamber with few mm distance from the double-aperture. In the simulation, the gas pressure in the ionization chamber inlet was set at 1 bar at room temperature of

293 K. Gas can fill the entire ionization chamber with a symmetric leakage from the double-aperture, as shown in Figure. 3-2.

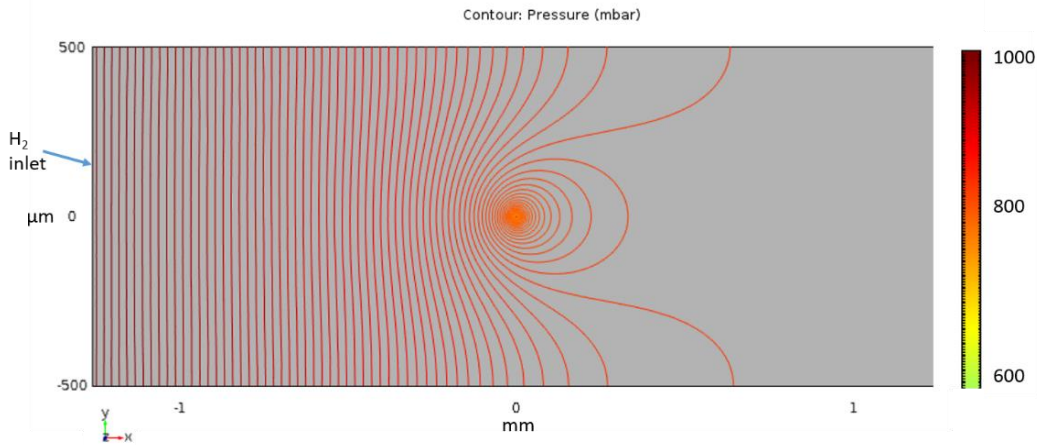


Figure. 3- 2 Gas pressure contour of the ionization chamber, simulated by COMSOL.

The primary region of interest for gas distribution is within the double-aperture region, where the gas gets ionized. From Figure. 3-2, it is reasonable to simplify the simulation of gas distribution based on a rotationally symmetric model near the double-aperture region (within 100 μm radius). The configuration of simplified ionization chamber used to evaluate relative gas density distribution in the double-aperture region for different geometries is shown in Figure. 3-3.

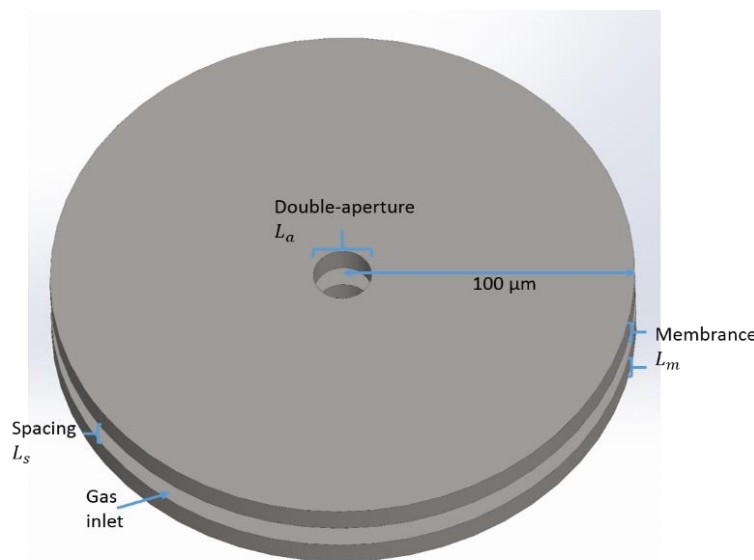


Figure. 3- 3 A rotationally symmetric simplified ionization chamber model for COMSOL simulation.

As discussed in Chapter 2, the maximum gas pressure for a 100 nm characteristic length is 10 bar. The hydrogen gas distribution for a 100 nm L_a and a 100 nm L_s configuration of the NAIS is shown in Figure. 3-4. According to COMSOL simulation, the inlet gas pressure and its corresponding gas pressure distribution scales linearly, within NAIS.

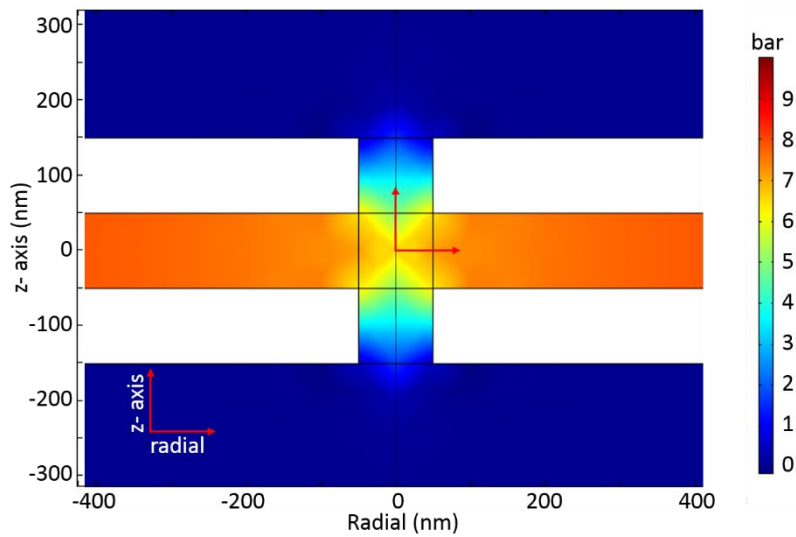


Figure. 3- 4 Hydrogen gas pressure distribution (simulated by COMSOL) for 100 nm spacing, 100 nm membranes, and 100 nm double-aperture configuration at 10 bar inlet gas pressure.

The influences of L_a and L_s on the gas pressure distribution are related to the gas pressure reduction of the inlet gas pressure. The axial gas distribution through the center of double-aperture was examined as a function of L_a for its corresponding various spacing (L_s from 100 nm to 1 μm). As seen from Figure. 3-5, for L_a equal to L_s , the axial peak hydrogen gas pressure is about 65% to 75%. For these openings, a reasonable gas pressure is maintained in the double-aperture region when compared with its corresponding inlet gas pressure. However, when L_a is larger than L_s , axial peak gas pressure drops significantly as compared with inlet gas pressure, thus resulting in a dramatic loss of gas in the ionization volume. It is impractical to increase the inlet gas pressure to compensate for this. It is clear that an efficient containment of gas can happen when L_a is smaller than L_s due to the small gas leak area. Therefore, it is reasonable to consider for a NAIS design with L_a , L_s , and L_m to be of equal dimensions in the simulation. Considering the probe focus ability of Schottky SEM and

tungsten SEM, the characteristic lengths of the NAIS are designed as 100 nm and 1 μm , respectively.

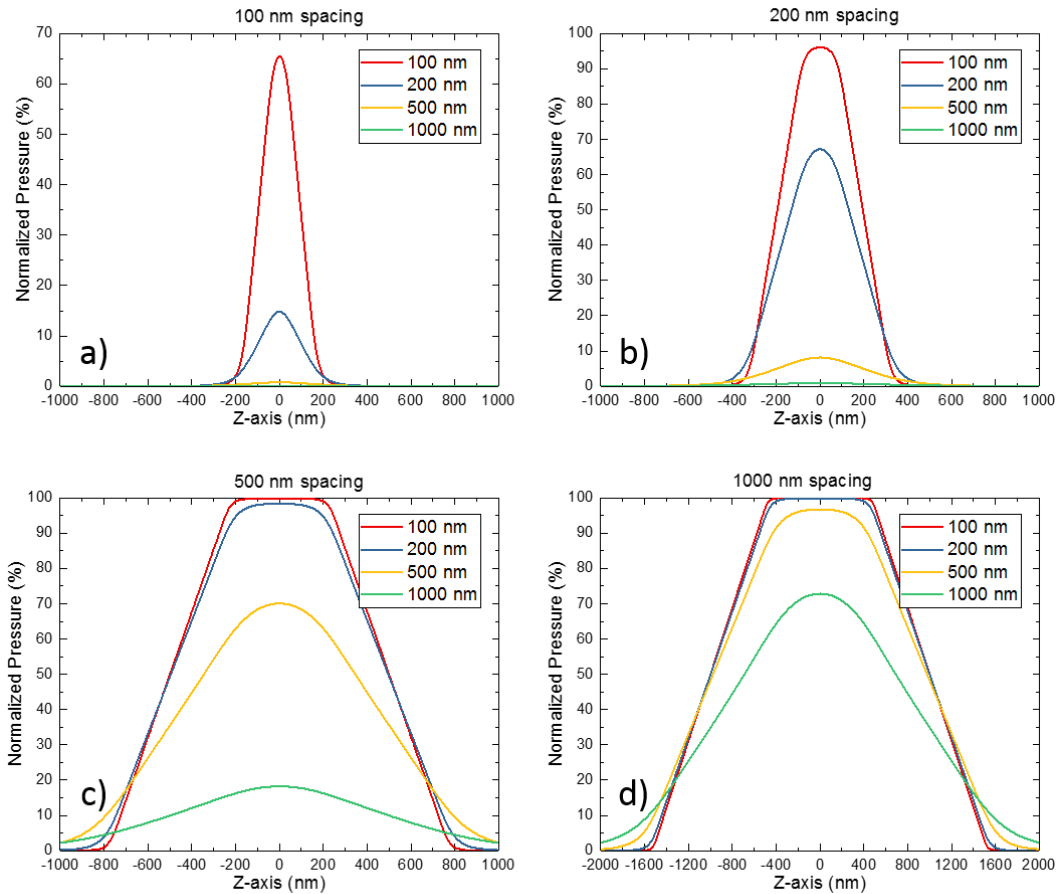


Figure. 3- 5 Axial normalized hydrogen gas pressure distributions (normalized to the inlet hydrogen gas pressure, data extracted from COMSOL) for various L_a corresponding to a fixed spacing, L_s , of a) 100 nm, b) 200 nm, c) 500 nm, and d) 1 μm . In all above simulations $L_m = L_s$.

3.2.2 Gas distributions of desired NAIS geometries

For 100 nm characteristic length, the maximum gas pressure in the double-aperture region can be up to 10 bar. Here, we set the inlet gas pressure as 10 bar to obtain the normalized gas pressure distribution, which can be used to scale up/down the gas pressure in the double-aperture region. As seen from Figure. 3-6, gas pressure in the double-aperture region is comparable to the inlet gas pressure. In the spacing, radial gas density reduces from the gas inlet to the center of the chip. The radial gas pressure

reduction from the edge of double-aperture to the center of chip is ~5%. While the injected electron current density is taken to be a Gaussian spatial distribution [6], [7], we simplify the generated beam to be quasi-uniformly distributed in the radial plane of the NAIS. Considering that the electron beam along the z-axis is continuous and uniform, the generated beam closely matches with the z-axis gas distribution. The z-axis normalized gas distribution is very consistent with Gaussian distribution with a standard deviation of 84.5 nm. The axial gas pressure drops rapidly to the background vacuum level outside the NAIS, resulting in a well constrained build-up of gas pressure in the ionization region with minimal gas leakage to the vacuum.

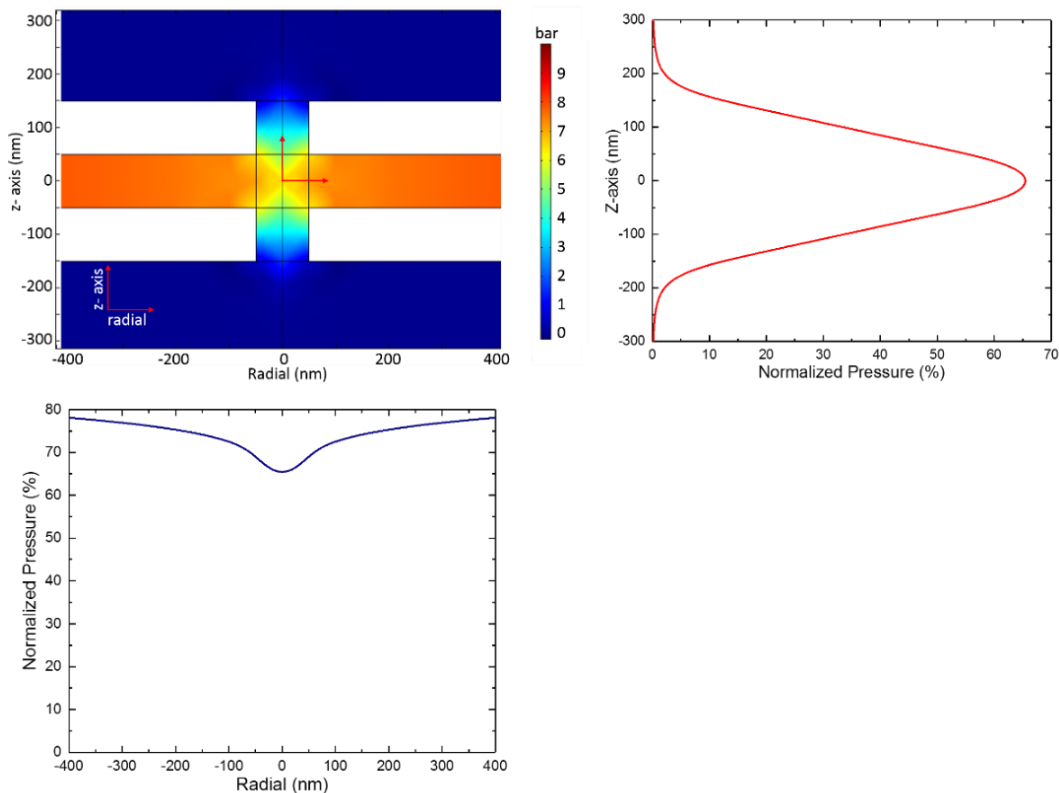


Figure. 3- 6 Hydrogen gas pressure distribution (simulated by COMSOL) for 100 nm spacing, 100 nm membranes, and 100 nm double-aperture configuration at 10 bar inlet gas pressure. Right top: Axial normalized hydrogen gas pressure distribution. Left bottom: Radial normalized hydrogen gas pressure distribution.

In an ionization process, protons inherit the original hydrogen gas thermal energy (~0.038 eV) with Maxwell-Boltzmann distribution at room temperature. In addition,

because gas escapes from the NAIS, hydrogen will gain extra energy. This extra energy will be transferred to protons after hydrogen gas molecules were ionized. Hydrogen gas flow rates vary according to different inlet gas pressures as shown in Figure. 3-7. Nevertheless, the relative gas flow velocities inside the ionization chamber of NAIS are the same. Absolute gas flow velocities are linear with respect to the inlet gas pressure. For 10 bar inlet gas pressure, the highest gas flow velocity is ~300 m/s, contributing up to ~0.001 eV extra energy to the hydrogen gas molecules. This extra energy is negligible when compared to the thermal energy of ~0.038 eV. More importantly, as shown in Figure. 3-7, at the center of the NAIS ionization chamber where most ions are generated, the gas flow velocity is even smaller. Therefore, it is quite reasonable to neglect the effect of gas flow to the gas molecule velocities in this configuration.

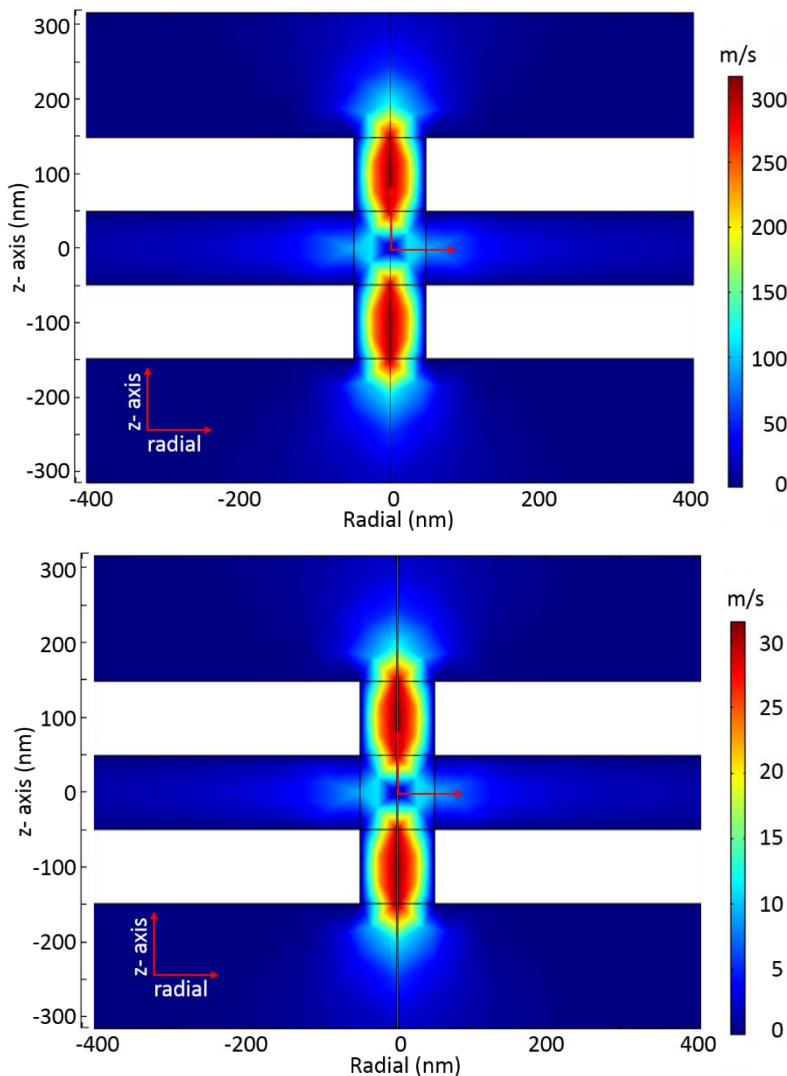


Figure. 3- 7 Hydrogen gas flow velocity (simulated by COMSOL) for 100 nm spacing, 100 nm membranes, and 100 nm double-aperture configuration. Top: hydrogen inlet gas pressure at 10 bar. Bottom: hydrogen inlet gas pressure at 1 bar.

The other desired configuration of the NAIS is with a 1 μm characteristic length for tungsten SEM. Here L_a , L_s , and L_m are 1 μm respectively. As discussed in Chapter 2, the upper operational limit for this configuration is 1 bar gas pressure in the center of the NAIS ionization chamber. As seen from Figure. 3-8, gas pressure in the center of the NAIS ionization chamber drops to $\sim 73\%$ of the inlet gas pressure, similar to the amount for 100 nm characteristic length. In the spacing, radial gas pressure reduction from the edge of double-aperture to the center of chip is $\sim 4\%$. As discussed for the 100 nm characteristic length, we can make a reasonable simplification so that the generated

beam is quasi-uniformly distributed in the radial plane of the NAIS with the assumption that the injected electron beam has a Gaussian spatial distribution [6], [7]. The z-axis normalized gas distribution is consistent with a Gaussian distribution with a standard deviation of ~820 nm.

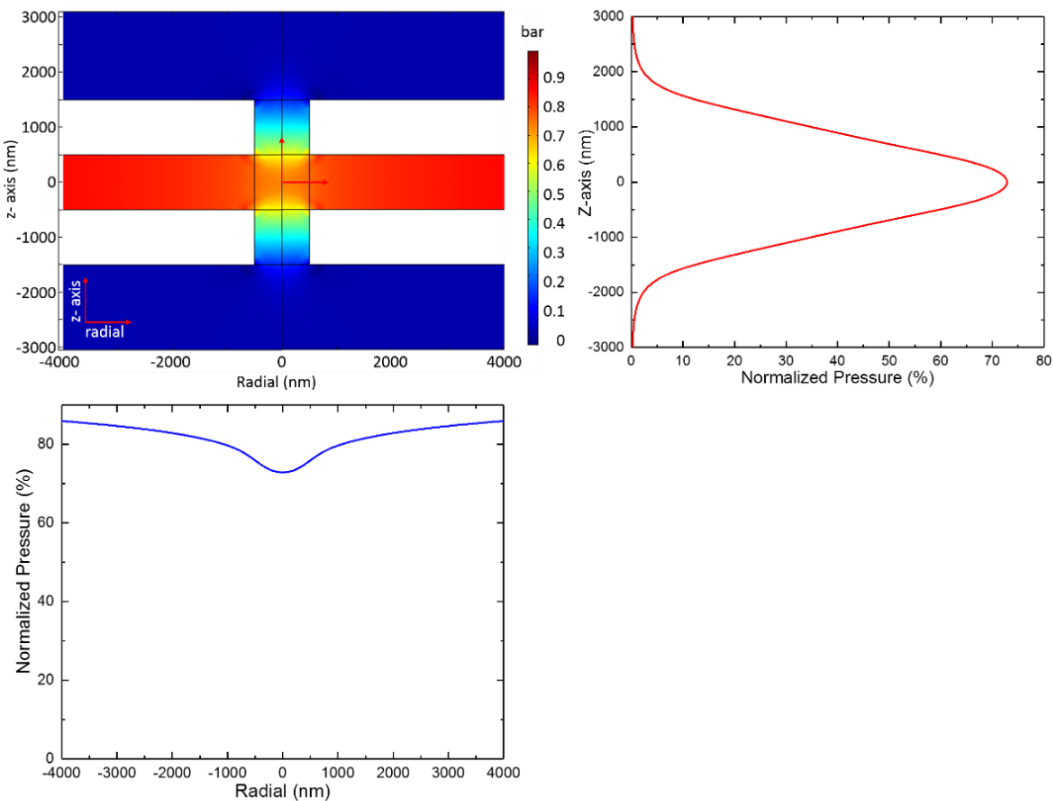


Figure. 3- 8 Hydrogen gas pressure distribution (simulated by COMSOL) for 1 μm spacing, 1 μm membranes, and 1 μm double-aperture configuration at 10 bar inlet gas pressure. Right top: Axial normalized hydrogen gas pressure distribution. Left bottom: Radial normalized hydrogen gas pressure distribution.

The maximum extra energy of hydrogen molecules gained by the gas flow inside the NAIS for a 1 bar inlet gas pressure is ~0.001 eV, from Figure. 3-9. When compared with the characteristic length of 100 nm, for 1 bar inlet gas pressure, the gas flow rate is ~10 times higher due to the larger opening. In this configuration, the gas flow rate is directly proportional to the inlet gas pressure. Under the upper operational limit, where the pressure in the center of the double-aperture region is 1 bar, a maximum extra energy of ~0.002 eV has no influence on the thermal energy (~0.038eV).

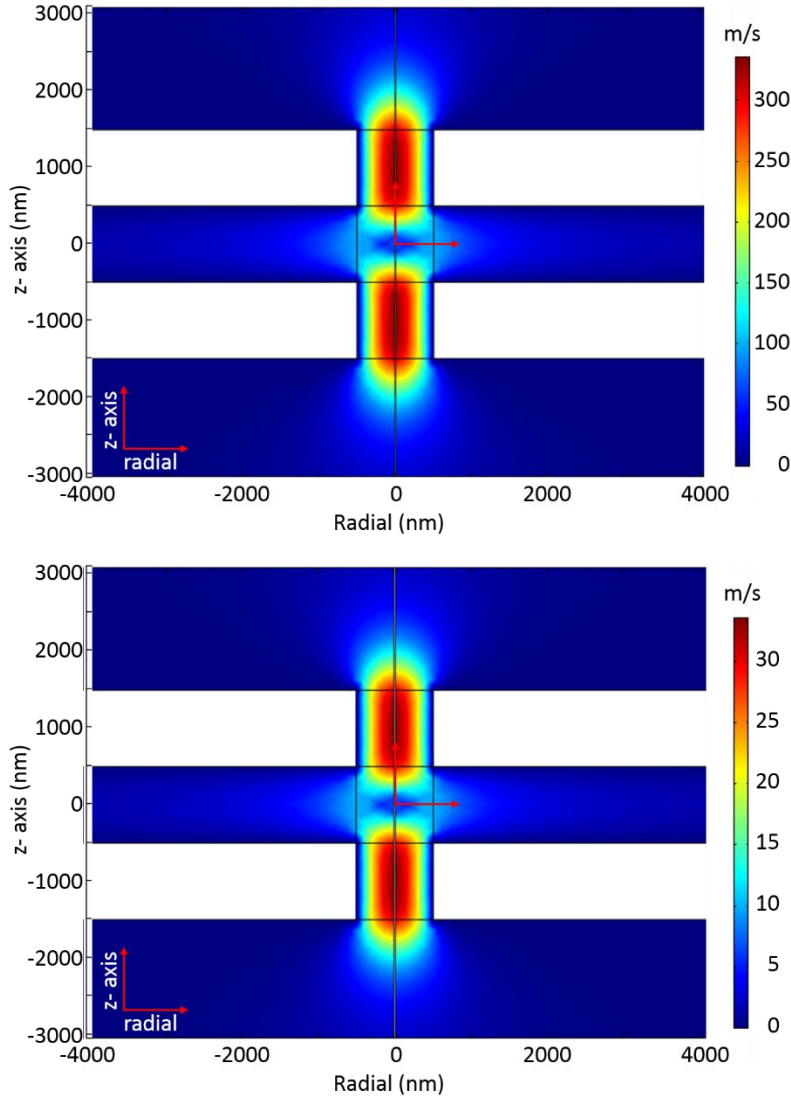


Figure. 3- 9 Hydrogen gas flow velocity (simulated by COMSOL) for 1 μm spacing, 1 μm membranes, and 1 μm double-aperture configuration. Top: hydrogen inlet gas pressure at 1 bar. Bottom: hydrogen inlet gas pressure at 0.1 bar.

The simulation results of gas distributions suggest that it is desirable to have all L_a , L_s , and L_m to be equal. Under this condition, the gas in the double-aperture region can hold a relatively high pressure as compared to the inlet gas pressure. It is impractical to have L_a larger than L_s due to the significant loss of gas. For the configuration that leads to the condition of $L_a = L_s = L_m$, the radial gas pressure drops about 5% from the edge of double-aperture to the center of double-aperture. Therefore, the generated radial ion distribution can be assumed to be uniform when combined with the injected electron beam. The gas distribution in the z -axis direction is found to be in good agreement with

a Gaussian distribution. The standard deviation of axial gas distribution is ~0.8 times to the characteristic lengths, resulting in a good containment of gas within the NAIS ionization chamber. The contribution to ion energy from gas flow rate is much smaller than the gas molecule thermal velocity.

3.3 Simulated performance of NAIS

3.3.1 Initial condition of NAIS

Gas distribution from the COMSOL simulation shows that a negligible portion of gas resides outside of the double-aperture region, indicating good containment of gas for these NAIS configurations. The injected electrons are used to ionize the gas molecules inside the NAIS ionization chamber. Due to the high mass difference between gas molecules and injected electrons, ions will effectively only inherit the original gas thermal energy (~0.038 eV) with Maxwell-Boltzmann distribution at room temperature of 293 K. Once ions are generated inside the NAIS ionization chamber, an electric field created by chip bias will manipulate the beam trajectory. The chip bias can accelerate and extract the beam out of the NAIS ionization chamber. An extractor plate is biased to -1 kV, which is placed 1 mm away from the end of the double-aperture, so as to extract the ion beam and at the same time prevent the injected electrons from entering the downstream of the setup, as shown in Figure. 3-10.

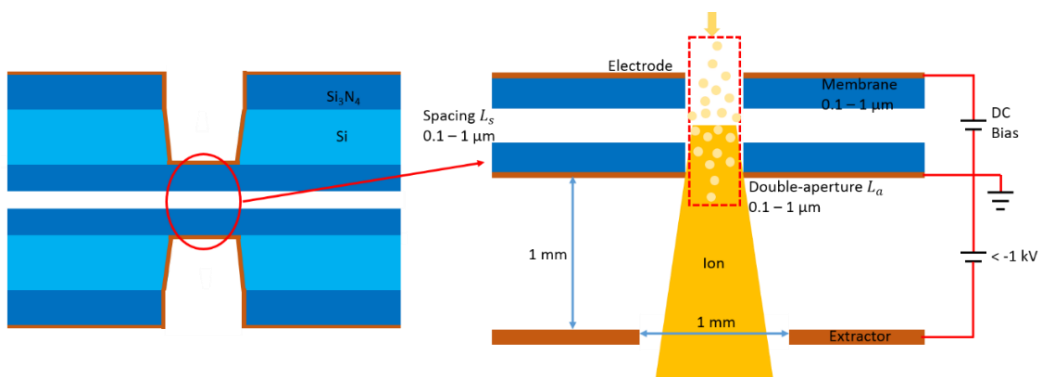


Figure. 3- 10 Schematic of the NAIS setup to simulate its performance. Initial proton beam is represented by light yellow circles. Ionization only happens at the double-aperture region, with a well confined gas distribution. The initial ion beam in NAIS is uniform in radial direction, and has a Gaussian distribution along the z-axis.

Electric field in the NAIS has a cylindrical symmetry as shown in Figure. 3-11, simulated by Poisson/ Superfish code [3]. At the double-aperture exit where the electric field has an ability to converge the ion beam, the double-aperture will act as a focus

lens and shape the beam. Electric field in the NAIS is fed into the General Particle Tracer (GPT) package [4], to simulate beam performance.

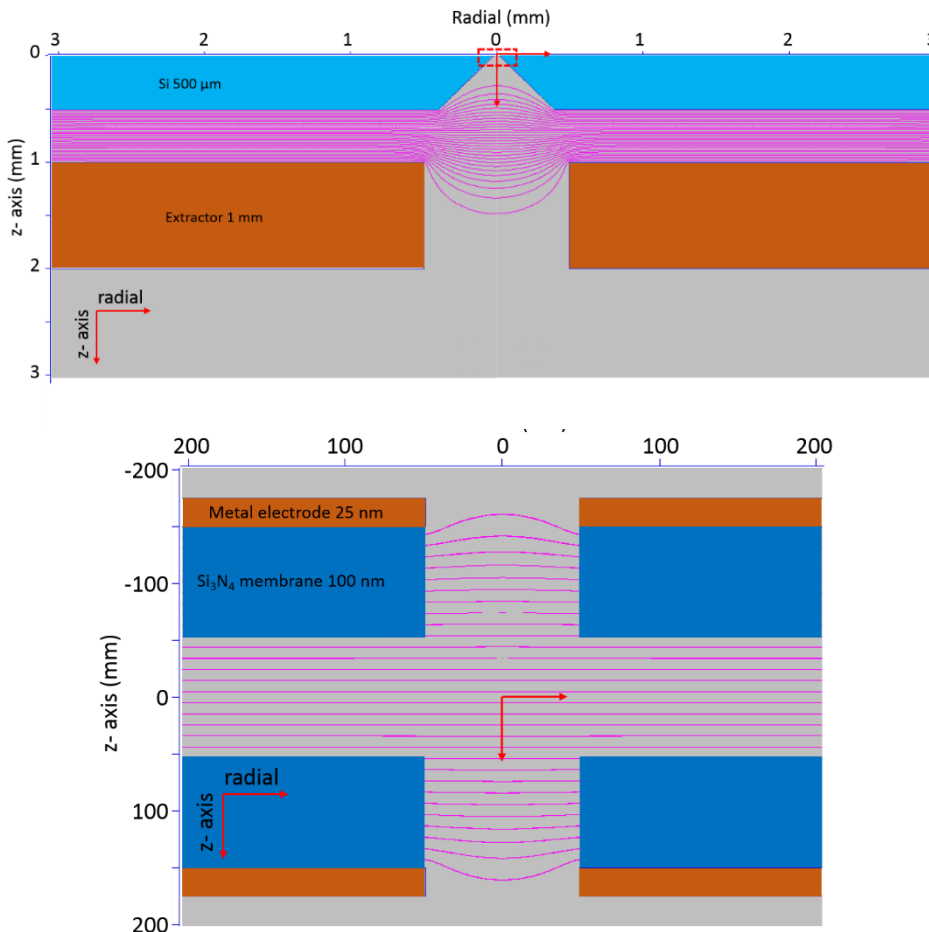


Figure. 3- 11 Electric field distributions with cylindrical symmetry (simulated by Poisson/Superfish code). Top: For the NAIS chip with an extractor having an electric field of 10^6 V/m (Si_3N_4 membranes and metal electrodes are not visible due to the small size). Bottom: Close view of the double-aperture region with an electric field of 10^7 V/m.

The initial beam is uniform in the transverse plane, and has a Gaussian distribution in the z-axis direction, as shown in Figure. 3-12 for the characteristic length of 100 nm. Along the z-axis, three standard deviations are considered for the beam optics simulation which includes 97.7% initial generated beam. The initial beam has a Maxwell-Boltzmann energy distribution at room temperature with a mean kinetic energy of 0.038 eV.

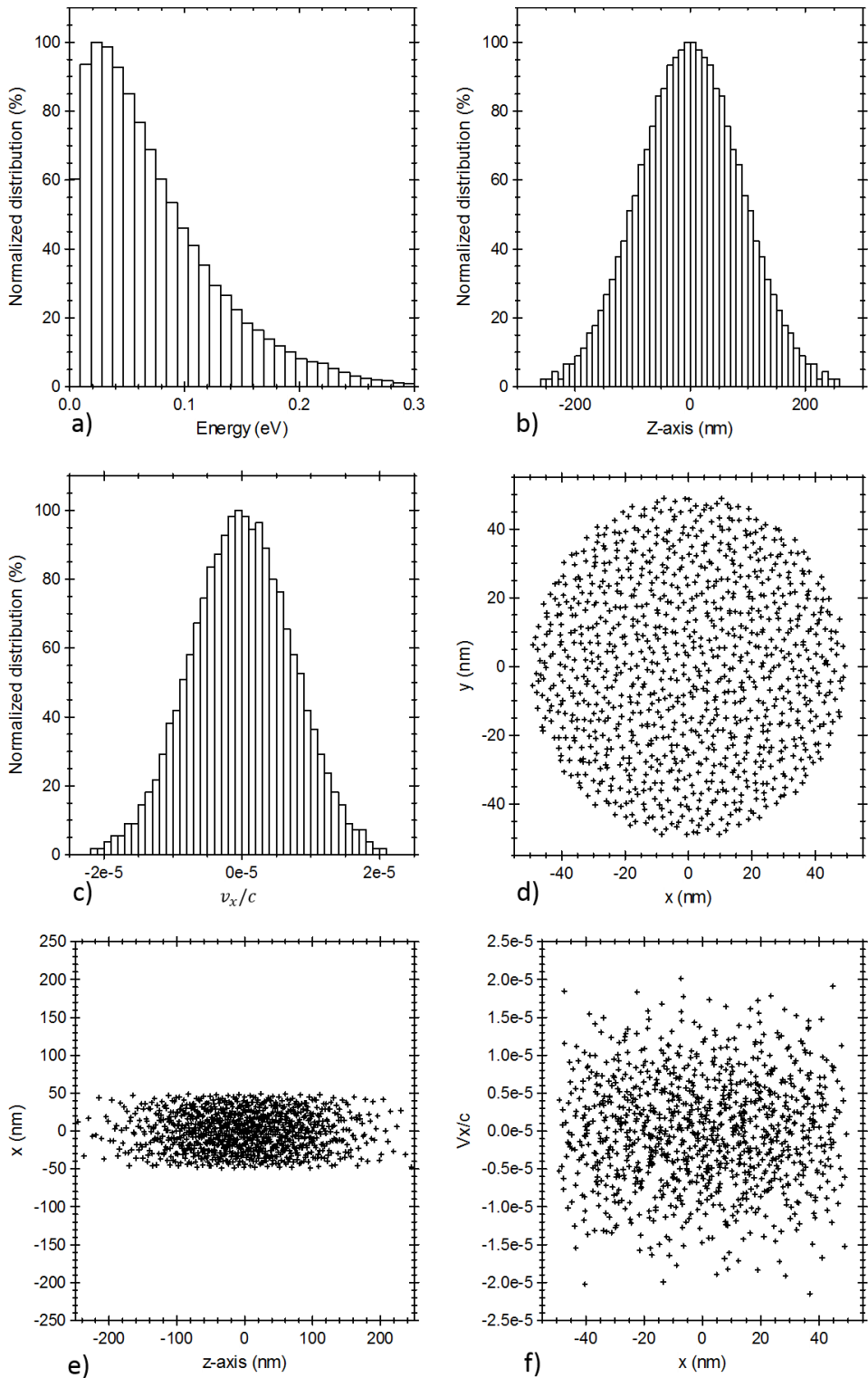


Figure. 3- 12 Initial beam parameters for characteristic lengths of 100 nm. a) Normalized energy distribution, satisfying the Maxwell-Boltzmann distribution at room temperature. b) Normalized z-axis distribution. c) Normalized velocity distribution in the transverse plane, satisfying a Gaussian distribution (where c is the speed of light). d) Beam in the transverse plane with a uniform distribution. e) Beam distribution at the z-x plane. f) Phase space with a Gaussian distribution of velocity in the transverse plane, where c is speed of light.

3.3.2 Emittance, reduced brightness and energy spread

For a characteristic length of 100 nm with a Schottky SEM, the trajectory of generated proton beam is shown in Figure. 3-13, where the electric field inside NAIS is 10^7 V/m and the extraction field is 10^6 V/m, corresponding to a chip bias of 3 V and an extraction voltage of -1 kV, respectively. As shown in Figure. 3-13 a) and c), parts of generated proton beam collide with the membrane or escape from the electron injecting aperture. This collision effect reduces the total extracted proton beam current, but helps in lowering the beam emittance due to the removal and stopping further transport of high-angle scattered beam. Under this condition, about 37.5% of generated proton beam can be extracted, resulting in an extracted proton beam current of ~950 pA for a maximum input electron current from a Schottky SEM of ~1000 nA. Figure. 3-13 d) shows that the *rms* emittance in transverse plane increases significantly when ion beam is extracted. After extraction, beam emittance reaches a constant value according to Liouville's theorem, as discussed in Chapter 1. The proton beam characteristics at the test plane ($z = 4$ mm) where an equipotential surface is maintained at -1 kV are plotted and shown in Figure. 3-14. The proton beam has a symmetric circular distribution with a higher density toward to the center, as shown in Fig. 3-14 a). It is seen that the proton beam energy spread satisfies a Gaussian distribution with a standard deviation of 1.1 eV. However, from Figure. 3-14 c), two small secondary peaks appear on the left (low-energy end) and right (high-energy end) shoulder of the primary peak. In the most significant low-energy end, a secondary peak indicates that protons closer to the ion exit aperture are extracted more than those at the electron injecting aperture because protons generated near the electron injecting aperture have a higher probability to collide with membranes. With the increase of chip bias, the high-energy end secondary peak will become more apparent. This can be attributed to the lens effect of the NAIS, where high chip bias converges (focuses) more protons generated near the electron injecting aperture.

The reduced brightness derived from emittance (more details in Chapter 1.1.2) can be approximated as

$$B_r = \frac{2I}{\pi^2 \epsilon_x \epsilon_y U} \approx \frac{2I}{16\pi^2 \epsilon_{x rms} \epsilon_{y rms} U} \quad (3.52)$$

where I is the total beam current, ϵ_x and ϵ_y are the edge emittances along the transverse plane, and $\epsilon_{x rms}$ and $\epsilon_{y rms}$ are the *rms* emittances.

On substituting the values obtained from GPT simulations into Eq. (3.1), the reduced brightness is calculated to be $\sim 8 \times 10^6$ A/(m²srV). The reduced brightness calculated here is slightly higher than the theoretical estimation ($\sim 5 \times 10^6$ A/(m²srV) in Chapter 2.2.1) because the high angle scattered beam collides with the NAIS membrane wall or escapes from the electron injecting aperture, thereby reducing the beam current to ~ 1.9 nA.

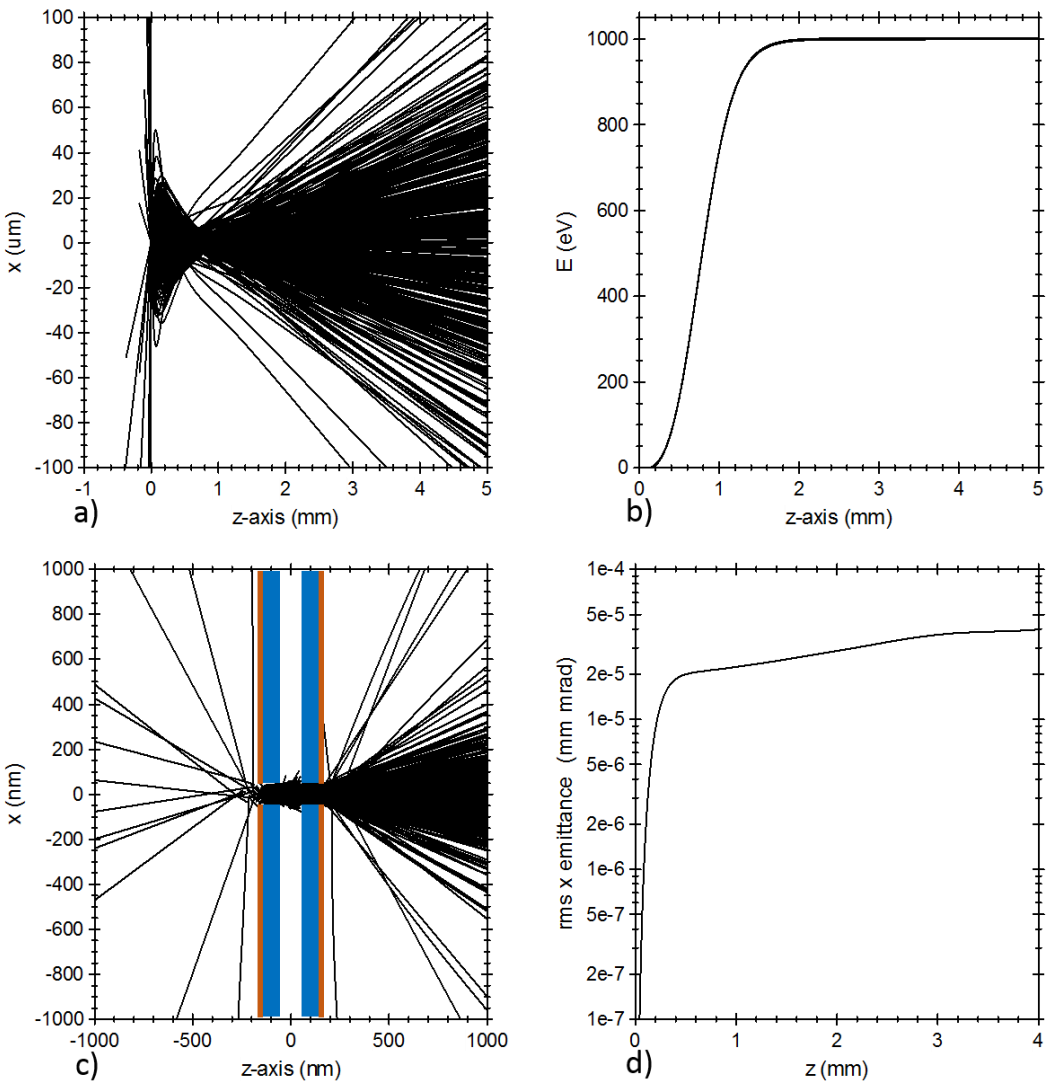


Figure. 3- 13 Proton beam trajectory simulation for characteristic lengths of 100 nm (simulated by GPT) a) Proton beam trajectory in large scale. b) Proton beam energy as a function of beam path z. c) Proton beam trajectory in NAIS region. d) Proton beam rms emittance in x direction as a function of beam path z.

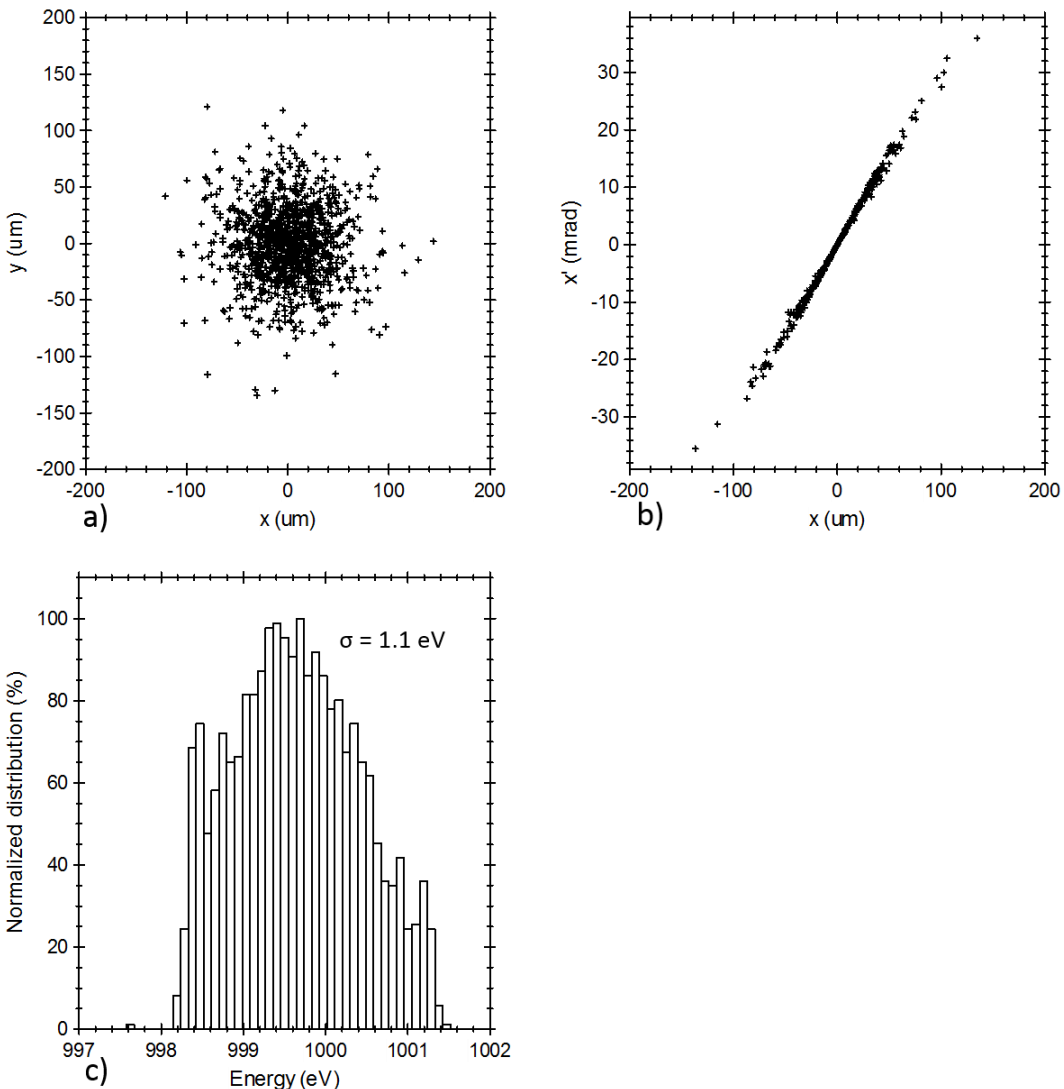


Figure. 3- 14 Proton beam characteristics at $z = 4 \text{ mm}$ plane for a characteristic length of 100 nm (simulated by GPT) a) Transverse beam distribution. b) Transverse phase space distribution. c) Beam energy spread distribution, satisfying a Gaussian distribution with a standard deviation of 1.1 eV .

Once the initial beam parameters and the NAIS geometry configuration are fixed, NAIS chip bias and extractor potential are the two essential factors that can alter beam reduced emittance, reduced brightness, and extracted beam current. The extractor potential modulates extraction field, resulting in different beam trajectories. Figure. 3-15 shows normalized emittance has a decreasing tendency with an increase in extraction field. This is because the extraction field has a convergence effect on protons that are generated after the ion exit aperture region. However, the modulation of the extraction field cannot alter the extracted beam current because it has insignificant

influence on the beam trajectory inside the NAIS. However, as seen in Figure. 3-15, the increase in reduced brightness is not significantly high, but rather brings an operational complexity due to high voltage. Therefore, a -1 kV extractor voltage is reasonable to repel the injected electron beam, while maintaining a reasonable reduced brightness.

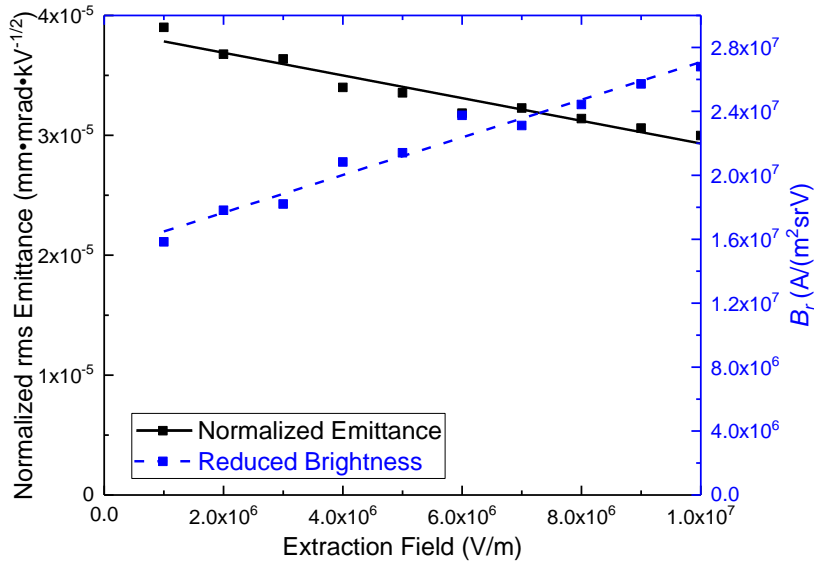


Figure. 3- 15 Normalized rms emittance and reduced brightness as a function of extraction field. Emittance is normalized to extractor potential for comparison.

The NAIS electric field is varied to examine its influence on the performance, with a fixed extractor potential of -1kV, as shown in Figure. 3-16. With the increase of the NAIS electric field, more beam is extracted out of the NAIS chip, as illustrated in Figure. 3-16 b), because a stronger field converges more beam inside the NAIS chip preventing beam collision with membranes. Simultaneously, this effect makes it possible to extract more of the high spread angle beam causing an increase in the emittance, as shown in Figure. 3-16 a). These two competing effects give rise to a relatively constant reduced brightness when the NAIS electric field is smaller than $\sim 5 \times 10^7$ V/m as shown Figure. 3-16 c). However, a strong NAIS electric field will introduce a large energy spread thereby deteriorating beam quality. Since the NAIS

electric field has a significant influence on virtual source size, as shown in Figure. 3-16 e), for a weak NAIS electric field most of the generated proton beam is lost due to collision with the membranes. Only the paraxial beam is unaffected and can be extracted downstream, which then behaves like a point ion source. The virtual source size in this condition is \sim 10 nm, smaller than the injected electron beam size of 100 nm. But, with an increase of the NAIS field, more high-angle spread beam is extracted, where the beam mimics as if originating from a plane instead of a point source. Hence the virtual source size will exceed the injected electron beam size with a strong NAIS electric field. Thus the simulation suggests that an electric field of 10^7 V/m in NAIS is a reasonable option that corresponds well with the theoretical assumption. Moreover, a lower energy spread and slightly higher reduced brightness can be achieved using a lower NAIS electric field, compromising the beam current (down to hundreds of pA).

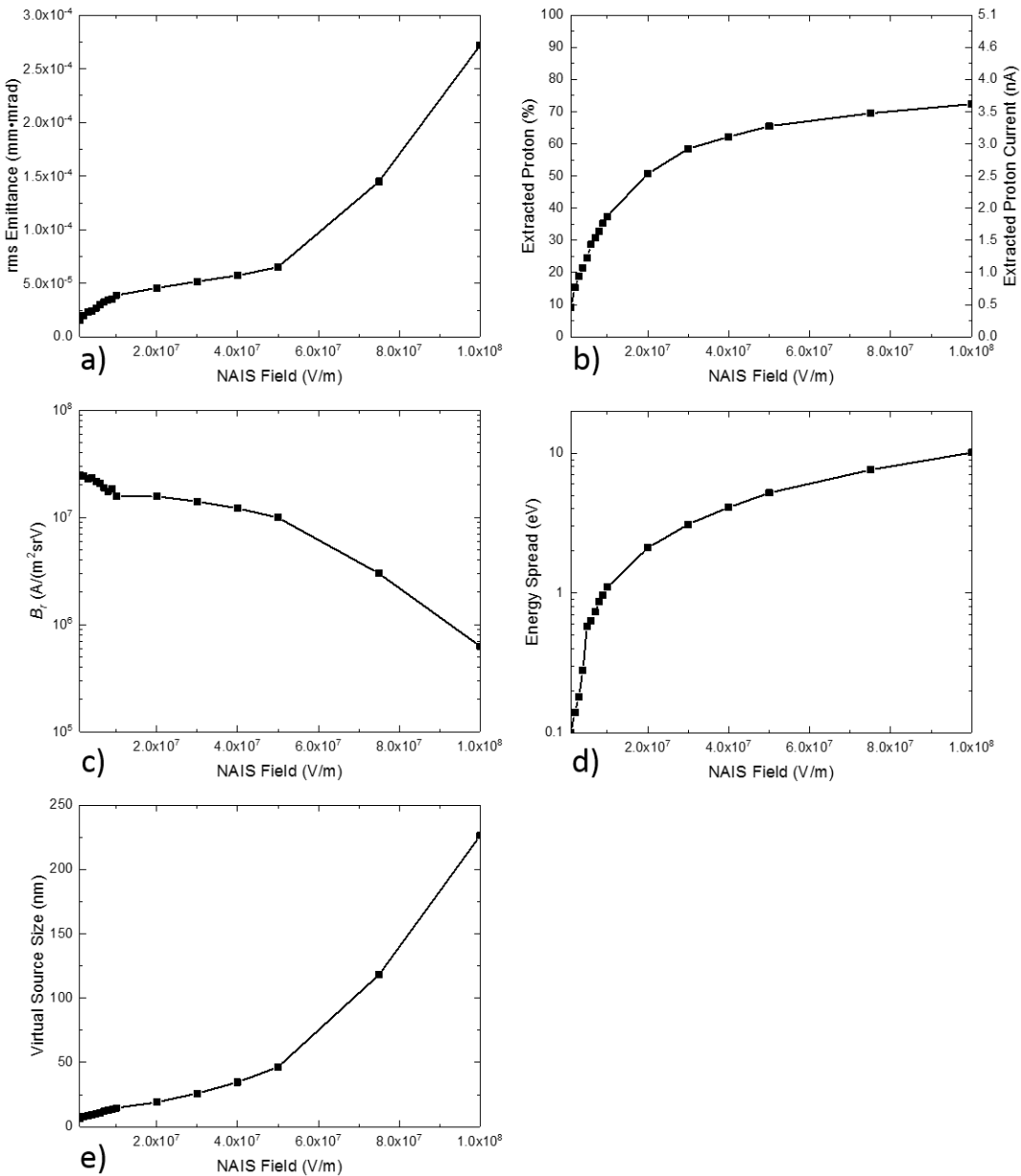


Figure. 3- 16 NAIS source performances as a function of the NAIS electric field at a fixed extractor potential of -1 keV for a characteristic length of 100 nm. a) rms emittance vs NAIS electric field. b) Extracted proton current vs NAIS field. c) Reduced brightness vs NAIS field. d) Energy spread vs NAIS field. e) Virtual source size vs NAIS field.

The other geometry of consideration for the NAIS is characteristic length of 1 μm equipped with a tungsten SEM.

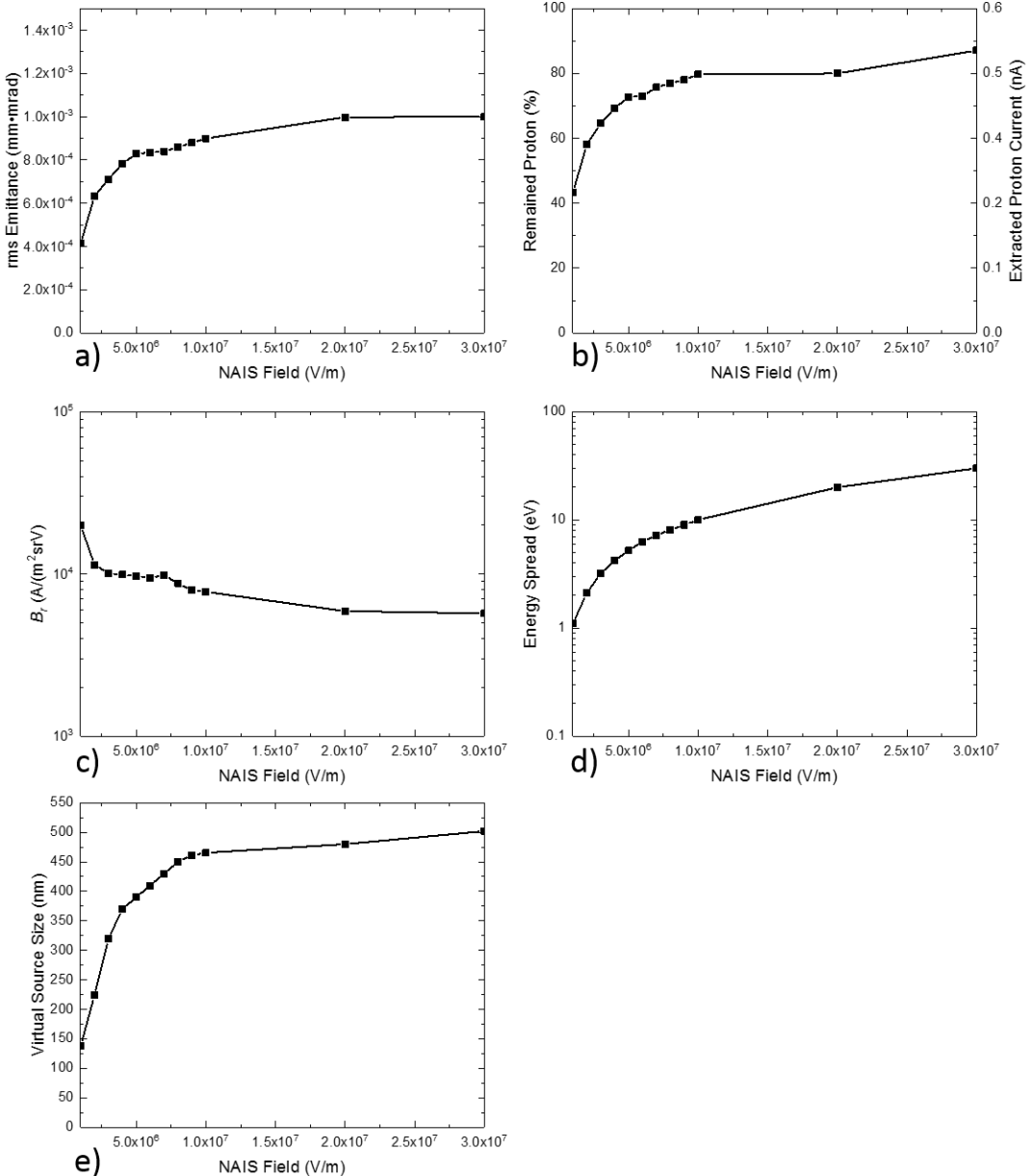


Figure. 3- 17 NAIS source performances as a function of the NAIS electric field at a fixed extractor potential of -1 keV for a characteristic length of 1 μ m. a) rms emittance vs NAIS electric field. b) Extracted proton current vs NAIS field. c) Reduced brightness vs NAIS field. d) Energy vs NAIS field. e) Virtual source size vs NAIS field.

As shown in Figure. 3-17, for a weak NAIS electric field, rms emittance varies little, because the amount of protons extracted due to the large opening of double-aperture does not change significantly (within 0.2 – 0.4 nA). Reduced brightness in this configuration also has a relatively steady value of $\sim 10^4$ A/(m²srV). However, energy spread in this configuration is very high due to the large distance (3 μ m) between the

NAIS chip bias electrodes. Nevertheless, this does not mean that this configuration can be ignored. A low energy spread (~ 1 eV) is still achievable with the NAIS electric field of 10^6 V/m.

In the above simulation, the incoming electron beam covers the entire area of the double-aperture. This can cause clogging of the double-aperture. To prevent this effect, another set of GPT simulation was carried out with the injected electron beam being illuminated to only half the diameter of the double-aperture. The corresponding proton beam performance with the NAIS electric field of 10^7 V/m and 10^6 V/m for characteristic length of 100 nm with Schottky SEM and 1 μ m with tungsten SEM at a fixed extractor potential of -1 keV is shown in Table. 3-1, respectively. In this case, due to the extra distance between the generated proton beam and membrane walls, fewer protons collide with the ionization chamber, and therefore a higher percentage of the generated proton beam can be extracted. However, this increased extracted beam will contain a higher fraction of high-angle scattered protons. On the other hand, with the decrease of the proton emitting area, the emittance increases slightly. It is evident that reducing the injected electron beam size results in a significant decrease in beam current (due to a small emitting area and low electron beam current at small probe size), and a slight change in beam emittance, giving a lower reduced brightness. The value of the electron beam diameter is thus chosen such that there is a tradeoff between the competing effects of higher ion brightness output and double-aperture clogging. Hence a preferred electron beam size would be slightly smaller than L_a , without lowering the beam brightness significantly.

H_2^+ beam performance is also shown in Table. 3-1. Due to the higher cross section for the production of H_2^+ [8], the NAIS generates a higher current and brighter H_2^+ beam as compared to protons.

As discussed in Chapter 2, electrodes of NAIS can be mounted internally which will reduce the *rms* energy spread to ~0.4 eV. In addition, some part of the beam collides with the membrane. If the electrodes are embedded inside NAIS, the collided beam can be conducted away instead of accumulating in Si₃N₄ membranes.

Table. 3- 1 NAIS performance for hydrogen gas with different injected electron beam diameters at characteristic length of 100 nm equipped with a Schottky SEM, and characteristic length of 1 μ m equipped with a tungsten SEM, respectively.

Ion species	Injected electron covering diameter (%)	Reduced brightness (A/(m ² srV))		Energy spread (eV)		Extracted current (nA)	
		100 nm	1 μ m	External electrodes	Internal electrodes	100 nm	1 μ m
H ⁺	100	1.6 \times 10 ⁷	2.0 \times 10 ⁴	1.1	0.4	1.90	0.27
H ⁺	50	1.5 \times 10 ⁶	1.0 \times 10 ⁴	1.1	0.4	0.16	0.02
H ₂ ⁺	100	5.6 \times 10 ⁸	7.4 \times 10 ⁵	1.1	0.4	33.6	4.7
H ₂ ⁺	50	5.1 \times 10 ⁷	4.3 \times 10 ⁴	1.1	0.4	2.8	0.3

3.4 Coulomb effects of the NAIS

Simulated results in the preceding part reveal the influence of the extraction field and the NAIS electric field on the source performance. However, Coulomb effects on these simulations were not considered. GPT simulations were performed considering all pairwise Coulomb interactions between ions. The Coulomb interactions for each and every ion i occurring from the rest of the ions j are solved from first principles as given in [4], [9]

$$m\ddot{\mathbf{r}}_i = \sum_{j \neq i} \frac{q_i q_j}{4\pi\epsilon_0} \frac{\mathbf{r}_j - \mathbf{r}_i}{|\mathbf{r}_j - \mathbf{r}_i|^3} + q_i \mathbf{E}_E(\mathbf{r}_i) \quad (3.53)$$

where \mathbf{E}_E is the external electric field. Here all the Coulomb effects are calculated including collective effect (space charge effect) and statistical effects (Boersch effect and trajectory displacement effect).

For a hydrogen NAIS, both H_2^+ (94.4%) and H^+ (5.6%) are generated simultaneously in the ionization process by a 1 keV injected electron beam. Therefore, pairwise Coulomb interactions that degrade beam quality for H_2^+ are mostly between H_2^+ - H_2^+ pairs, and those for protons are mostly between H_2^+ - H^+ pairs.

In the absence of Coulomb effects, the emittance is constant when the NAIS configuration and electric field are fixed and independent of ion beam current. However, when Coulomb effects are considered, the emittance depends on ion beam current due to the pairwise interactions between ions, as illustrated in Eq. 3.2. The Coulomb effects mainly deteriorate the beam quality within the NAIS ionization chamber because of low moving speed and relatively high beam current density. However, after the ions are extracted from the NAIS ionization chamber they are accelerated to a high energy and divergence, resulting in negligible pairwise interactions.

To incorporate Coulomb effects within GPT simulations, a NAIS electric field of 10^7 V/m and 10^6 V/m was used for characteristic lengths of 100 nm and 1 μm , respectively,

while maintaining an equal extractor potential of -1 kV for both characteristic lengths. This was done to keep a low energy spread while having a comparable extracted beam current as discussed in the previous section. The NAIS performance as a function of the extracted ion beam is evaluated and illustrated in Figure. 3-18, Figure. 3-19, and Figure. 3-20. As shown in Figure. 3-18, *rms* emittance increases with the extracted beam current. However, the Coulomb effects do not significantly decrease the beam brightness. The *rms* energy spread increases only by a few 0.1's eV (see Figure. 3-19) due to Coulomb effects, because the energy spread results mostly from ions generated at different electric potentials. The reduced brightness (derived from Eq. 3.1) primarily depends on the extracted ion beam current rather than on to a minimal change in the emittance, as seen Figure. 3-20.

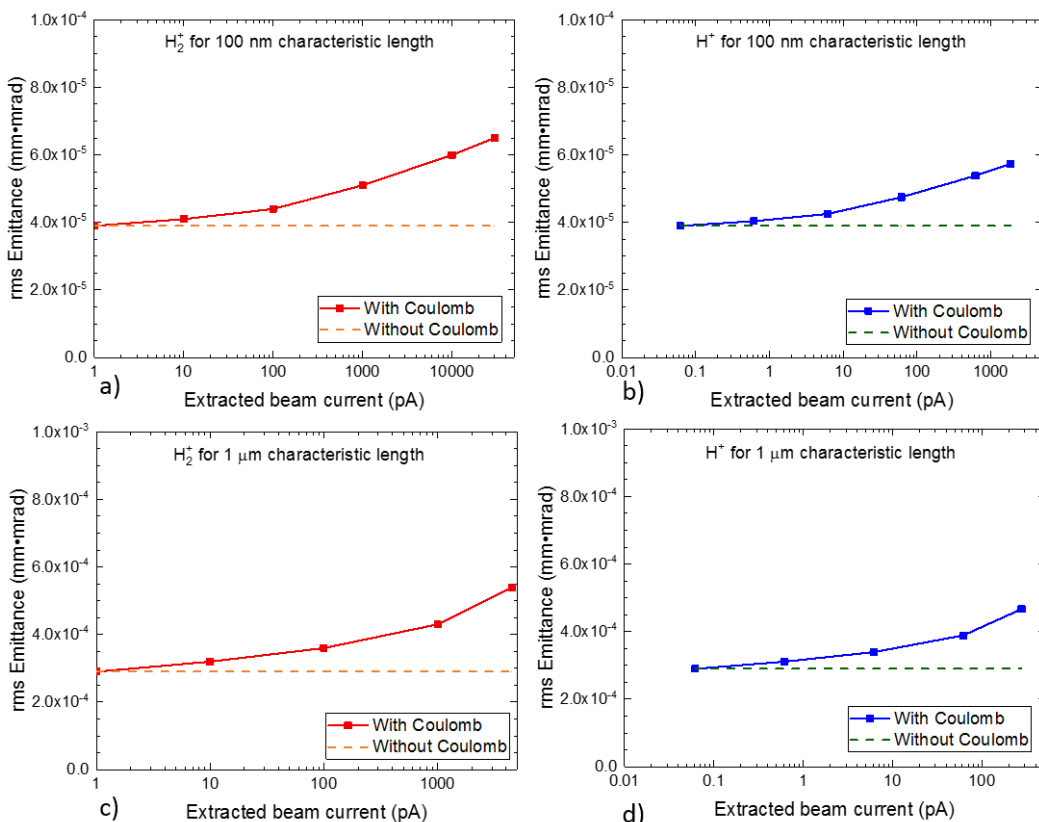


Figure. 3- 18 NAIS emittance as a function of extracted beam current at a fixed extractor potential of -1 keV. NAIS electric fields are 10^7 V/m and 10^6 V/m for characteristic length of 100 nm and 1 μ m, respectively. a) For H_2^+ with 100 nm. b) For H^+ with 100 nm. c) For H_2^+ with 1 μ m. d) For H^+ with 1 μ m.

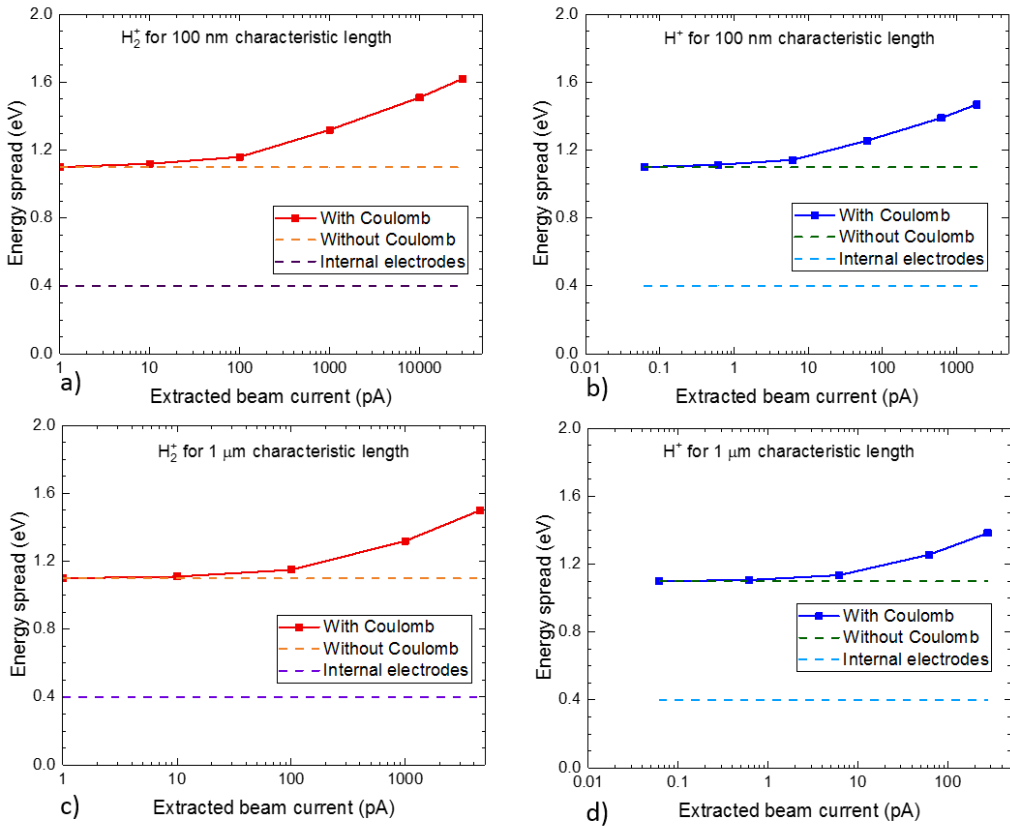


Figure. 3- 19 NAIS rms energy spread as a function of extracted beam current at a fixed extractor potential of -1 keV. NAIS electric fields are 10^7 V/m and 10^6 V/m for characteristic length of 100 nm and 1 μm . a) For H_2^+ with 100 nm. b) For H^+ with 100 nm. c) For H_2^+ with 1 μm . d) For H^+ with 1 μm .

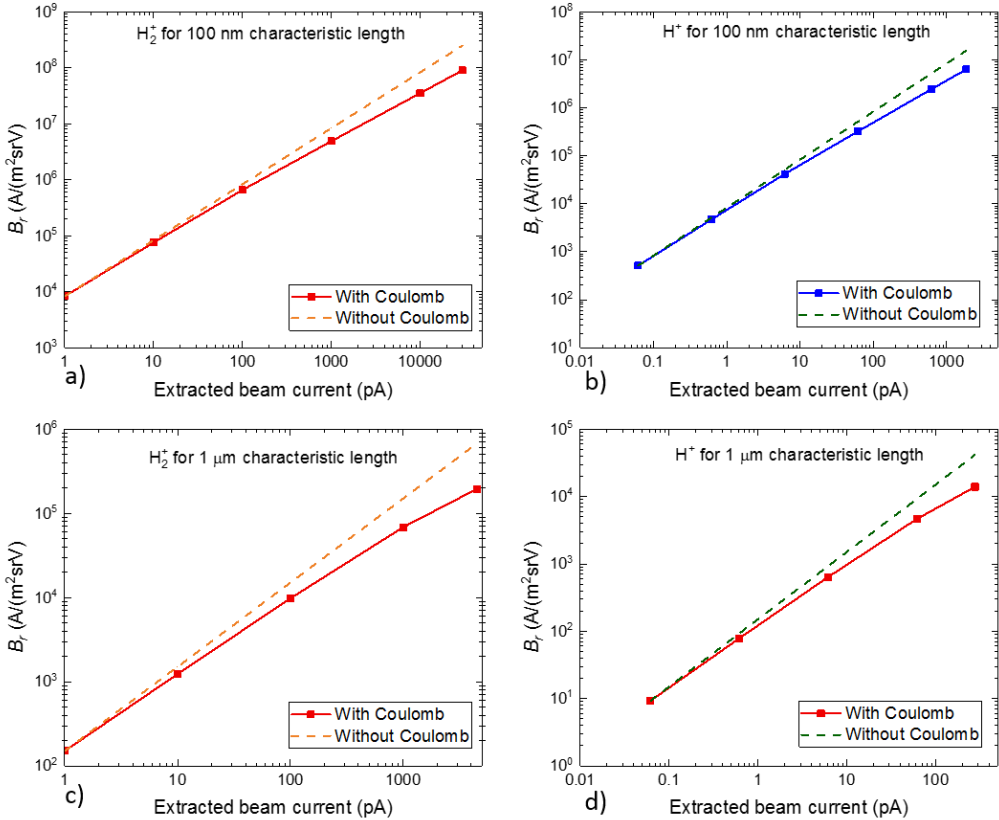


Figure. 3- 20 NAIS reduced brightness as a function of extracted beam current at a fixed extractor potential of -1 keV. NAIS electric fields are 10^7 V/m and 10^6 V/m for characteristic length of 100 nm and 1 μ m, respectively. a) For H_2^+ with 100 nm. b) For H^+ with 100 nm. c) For H_2^+ with 1 μ m. d) For H^+ with 1 μ m.

The simulated result illustrates Coulomb effects degrading the reduced brightness and increasing the energy spread, towards high extracted beam current. However, the reduced brightness still maintains to be in the same order of magnitude even when operating at the upper limit of the NAIS (maximum injected electron current with 10 bar and 1 bar gas pressure for Schottky and tungsten SEMs, respectively). More importantly, the injected electrons have the ability to compensate the space charge effect. It is therefore reasonable to neglect Coulomb effects here and still achieve a very high brightness through the NAIS. For a characteristic length of 100 nm equipped with a Schottky SEM, the NAIS is capable of achieving more than 10^7 A/(m²srV) reduced brightness for H_2^+ . For the same NAIS configuration, a reduced brightness of 10^6 A/(m²srV) can be obtained for protons. Whereas for a 1 μ m characteristic length

equipped with a tungsten SEM, more than 10^5 A/(m²srV) of reduced brightness for H₂⁺ and protons can be achieved.

3.5 Summary

To investigate the feasibility of the NAIS an extensive set of simulations with the GPT code have been performed in this work. Different configurations of the NAIS equipped with different SEMs as the electron beam injector have been examined. Source design parameters including gas distribution, NAIS electric field, extractor field, and Coulomb effects have been looked into. The simulations indicate that the axial gas distribution is a crucial parameter to be considered in designing a chip that can confine the gas for ionization and achieve low energy spread. L_a is preferred to be the same size as ionization chamber height, L_a , in order to obtain a reasonable gas pressure compared to the inlet gas pressure. Coulomb effects were also investigated, and found to have minimal effect on the performance of NAIS, in our desired operating conditions. Calculations indicate that a high brightness hydrogen beam can be obtained using a Schottky SEM, employing a 100 nm thick membrane having a 100 nm thick spacer with a 100 nm double-aperture configuration, in a Schottky SEM. This configuration can deliver a proton beam with a reduced brightness of $10^7 \text{ A}/(\text{m}^2\text{srV})$ having an *rms* energy spread of $\sim 1 \text{ eV}$. With the internal electrodes, *rms* energy spread can be further reduced to $\sim 0.4 \text{ eV}$.

References

- [1] J. Peatross and D. D. Meyerhofer, “Novel gas target for use in laser harmonic generation,” *Rev. Sci. Instrum.*, vol. 64, no. 11, pp. 3066–3071, 1993.
- [2] COMSOL Inc., “COMSOL Multiphysics®.” [Online]. Available: <https://www.comsol.com/>.
- [3] The Los Alamos Accelerator Code Group, “Poisson Superfish.” [Online]. Available: <http://laacg.lanl.gov/>.
- [4] Pulsar Physics, “General Particle Tracer.” [Online]. Available: <http://www.pulsar.nl/gpt/>.
- [5] J. Nassios, “Kinetic Theory an the BGK equation: Gas Dynamics for the Nanoscale,” *Univ. Melb. Math. Dep.*, 2008.
- [6] M. S. Brongsgeest, J. E. Barth, L. W. Swanson, and P. Kruit, “Probe current, probe size, and the practical brightness for probe forming systems,” *J. Vac. Sci. Technol. B*, vol. 26, no. 3, pp. 949–955, 2008.
- [7] J. R. Michael and D. B. Williams, “A consistent definition of probe size and spatial resolution in the analytical electron microscope,” *J. Microsc.*, vol. 147, no. 3, pp. 289–303, 1987.
- [8] H. C. Straub, P. Renault, B. G. Lindsay, K. A. Smith, and R. F. Stebbings, “Absolute partial cross sections for electron-impact ionization of H₂, N₂, and O₂ from threshold to 1000 eV,” *Phys. Rev. A*, vol. 54, no. 3, p. 2146, 1996.
- [9] S. B. Van der Geer, M. P. Reijnders, M. J. de Loos, E. J. D. Vredenbregt, P. H. A. Mutsaers, and O. J. Luiten, “Simulated performance of an ultracold ion source,” *J. Appl. Phys.*, vol. 102, no. 9, p. 94312, 2007.

Chapter 4. NAIS fabrication and performance

4.1 Introduction

The NAIS is a high brightness, low energy spread electron impact ion source. High brightness and low energy spread ions are generated by injecting electrons into a sub-micron ionization chamber. This sub-micron ionization chamber is essential in achieving a small virtual source size, with a low energy spread. The primary step in developing the NAIS is to fabricate NAIS ionization chamber in a feasible and reliable manner. Hence, the focus of this chapter will be on the fabrication and performance of the NAIS ionization chamber. The fabrication of the chamber will be carried out using the well documented microelectromechanical systems (MEMS) techniques [1]–[3], involving semiconductor process techniques. Moreover, these techniques also provide low cost and are capable of batch fabrication. The performance of the NAIS will be carried out using SEM as a source for electron injector.

The sub-micron ionization chamber mainly consists of two separate parallel membranes with a spacing of $0.1 - 1 \mu\text{m}$ to form a gas constrained channel, as shown in Figure. 2-3. A gas inlet window and concentric double-apertures are included in the ionization chamber for feeding gas, to inject electrons, and to extract ions. Two electrically insulated electrodes are used to generate electric field to extract ions.

This chapter discusses the fabrication of two kinds of NAIS ionization chambers (chip), namely, a NAIS with metal spacer and a NAIS with recessed Si_3N_4 . These two NAIS ionization chambers have a different geometry following different fabrication methods, resulting in different outputs of reduced brightness. These NAIS chips are mounted inside commercial SEMs to examine their performance.

In addition to these two type of NAISs, this work will also discuss a new kind of NAIS with internal electrodes that avoids membrane bulge aiming for a lower energy spread.

4.2 Performance test of the NAIS with metal spacer¹

The NAIS chip is fabricated from a 530 μm thick 4" $<100>$ silicon wafer with 1 μm thick double-side coated Si_3N_4 (single side polished). A good quality Si_3N_4 film, with uniformity ($\pm 7\%$) and homogeneity, is deposited by low-pressure chemical vapor deposition (LPCVD) [4]–[6]. To enable batch production, the top and bottom chips are designed to be identical to each other. Fabrication details of the NAIS with metal spacer can be found in Ref [7]. The completed NAIS chip has an overall dimension of 11 mm \times 11 mm \times 1.06 mm and consists of a gas inlet and a double-aperture window of 300 $\mu\text{m} \times 300 \mu\text{m}$ and 50 $\mu\text{m} \times 50 \mu\text{m}$ respectively. Several double-apertures ranging from 1.5 μm to 3.5 μm were milled within the double-aperture window. The spacing height for the double-apertures was 600 nm.

To evaluate the performance of this NAIS with metal spacer, preliminary brightness measurements were conducted at the Centre for Integrated Circuit Failure Analysis and Reliability (CICFAR), NUS. A Philips XL30 Environmental Scanning Electron Microscope (ESEM) consisting of a Schottky emitter, as shown in Figure. 4-1, was used as an electron injector. As discussed in Chapter 2, a more practical choice of the electron beam energy need to be a trade-off between ionization cross section and electron beam properties, which is 1 keV. Therefore, the characteristics of the SEM at 1 keV were examined here experimentally.

The electron beam brightness was $\sim 900 \text{ A}/(\text{m}^2\text{srV})$ with a probe beam current density of 10^3 A/m^2 . However, the ideal Schottky SEM has a 10^8 A/m^2 probe beam current density and has a reduced brightness of more than $10^7 \text{ A}/(\text{m}^2\text{srV})$, as seen in Appendix 2. The measured reduced brightness of the ESEM at CICFAR is much lower than the ideal Schottky SEM. This is because of the aging Schottky emitter, resulting in a broadened source size.

¹ This work was done with Liu Nannan (NUS PhD thesis: Development of an Electron Impact Gas Ion Source for Proton Beam Writing Applications, 2015). Data was re-analyzed based on the simulation in Chapter 3.

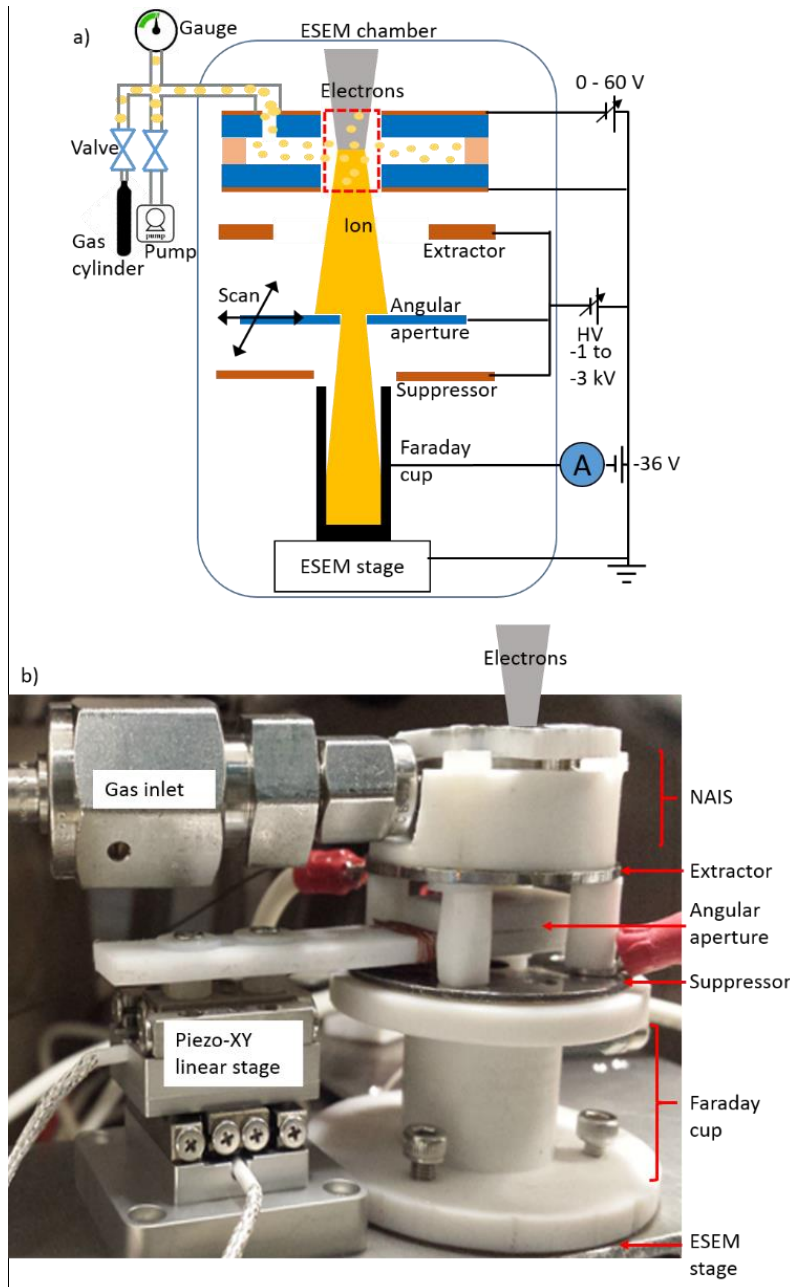


Figure. 4- 1 NAIS reduced brightness measurement, carried out inside a Philips XL30 ESEM.
a) Schematic. b) The actual setup inside the ESME.

To evaluate the performance of the NAIS with metal spacer, a reduced brightness measurement setup was designed and installed inside the ESEM chamber, as shown in Figure. 4-1. This setup consists of a gas inlet line, the NAIS chip holder with chip, extractor, angular aperture, Piezo-XY linear stage (SmarAct® SLC-1720-S-HV), suppressor, and Faraday cup. Each component was electrically isolated through Teflon. The NAIS chip was biased by a DC power supply (0 – 60 V). The extractor was varied

in the range of -1 kV to -3 kV to extract and accelerate ions, and repel the injected electrons. An angular aperture mounted on a piezo-XY stage was used to find the peak axial ion beam current through scanning. The angular aperture had an opening of ~95 $\mu\text{m} \times 95 \mu\text{m}$ and was placed 10 mm away from the NAIS chip. To create a field-free region for ions, a suppressor with the same potential as the extractor was placed downstream of the angular aperture. A Faraday cup to measure the ion beam current was biased at -36 V to aid ion beam-landing. In addition, the potential difference between the suppressor and Faraday cup can constrain secondary electrons inside the Faraday cup. Gas pressure within the NAIS chip was varied from 0.1 mbar to 1 bar.

In order to examine the NAIS, argon gas was used because of its high ionization cross section [8], [9] and chemical inertness, resulting in a larger ion beam current output. Additionally, argon gas produces 95% Ar^+ and 5% Ar^{n+} ($n = 2$ to 4) [8] for 1 keV injected electrons. Therefore, the measured ion beam current was predominantly Ar^+ .

The influence of the total beam current $I_{i-total}$ from extraction voltage is shown in Figure. 4-2. The inlet argon gas pressure was maintained at 700 mbar and chip bias was fixed at 9 V. In chapter 3, the simulation shows that extraction voltage doesn't have a significant influence on the performance of the NAIS. The experimental result here is in general agreement with the simulated result, although a slight downward trend is seen with an increase of extraction voltage. This unexpected downward trend may be caused by two possible reasons. First, the higher suppressor potential (equal to extraction potential) generates a stronger electric field gradient between the suppressor and Faraday cup, resulting in a more broadened beam before entering the Faraday cup, due to a strong defocusing effect. Additionally, a misalignment between the NAIS chip and extractor can cause the beam to deviate from the optical axis. This deviation results in a larger beam broadening, especially at higher suppressor potentials. The misalignment also results in an off-axis aberration that can cause a negative influence

on ion current measurement at high extraction potentials [10]. Because of these two combined effects, part of the beam is lost and does not reach the Faraday cup at high extraction voltages. In order to eliminate these unexpected influences, a more accurate alignment between the NAIS chip and extractor is under construction. It is also preferred to operate the extractor at lower voltages, to reduce the degradation from beam broadening before it lands into the Faraday cup.

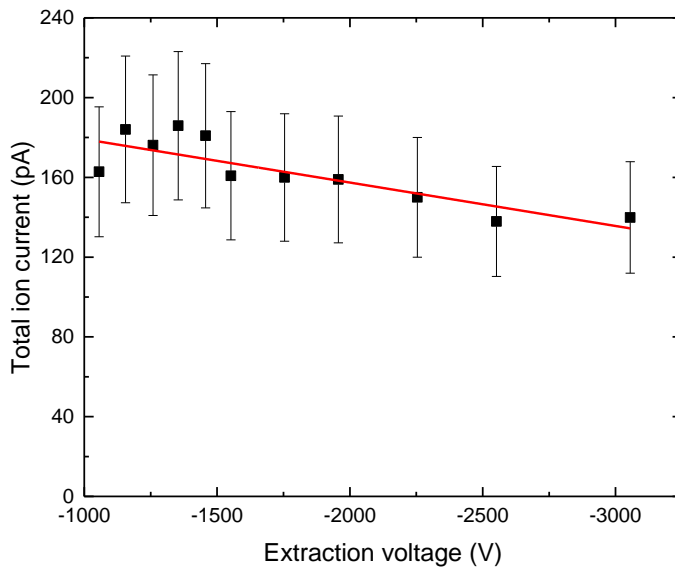


Figure. 4- 2 Total Ar ion current as a function of extraction voltage. The inlet argon gas pressure was maintained at 700 mbar and chip bias was fixed at 9 V. Reproduced from Ref. [7].

To investigate the influence of chip bias, the total argon beam current $I_{i-total}$ as a function of chip bias is experimentally examined, as shown in Figure. 4-3. A 700 mbar inlet argon gas pressure and -1.55 kV extraction voltage were used. The total ion current increases gradually with the chip bias, as predicted in Chapter 3. A higher chip bias has more focusing effect within the NAIS chip, resulting in a lower loss of ions due to collision with the membrane walls. With an increase of chip bias, the ions will emit from a plane instead of a point. Moreover, higher chip bias gives a larger energy spread that deteriorates the beam quality. As seen from Figure. 4-3, the chip bias can

therefore be reduced to satisfy the lower requirement on energy spread without losing too much beam current.

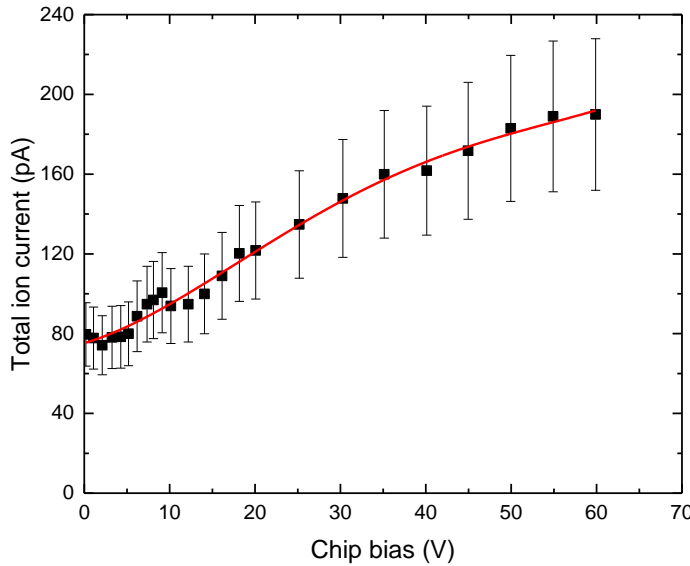


Figure. 4- 3 Total Ar ion current as a function of chip bias. A 700 mbar inlet argon gas pressure and -1.55 kV extraction voltage were used. Reproduced from Ref. [7].

The experimental reduced brightness B_r for ion beam is expressed as [11], [12]

$$B_r = \frac{I_{i\text{-axial}}}{A_s \Omega V} = \frac{I_{i\text{-axial}}}{A_s \frac{A_a}{L^2} V} \quad (4.54)$$

where $I_{i\text{-axial}}$ is the axial ion beam current, A_s is the virtual source area, Ω is the solid angle which defines the beam divergence, V is the beam acceleration potential, A_a is the angular aperture area, and L is the distance between virtual source and the angular aperture.

The angular aperture was scanned using a piezo-XY linear stage to find the maximum axial ion current. The axial Ar ion current $I_{i\text{-axial}}$ as a function of chip bias was measured and is shown in Figure. 4-4. With an increase of chip bias, axial ion current increases rapidly eventually reaching a plateau at about 50 pA. The rapid increase in ion current is due to a higher extracted ion current from the NAIS. This is because a higher chip bias converges more large-angle scattered ions within the NAIS chip,

causing less collision between ions and membrane walls. However, the angular aperture has a limit on the maximum divergence of the extracted ion beam. At higher chip bias, although more ions can be extracted, as shown in Figure. 4-3, the increased extracted ions are from large-angle scattered ions that are collimated by the angular aperture. Additionally, the misalignment between NAIS and extractor will enhance extracted beam angle. Therefore, the axial beam current shows a saturation behavior at high chip bias.

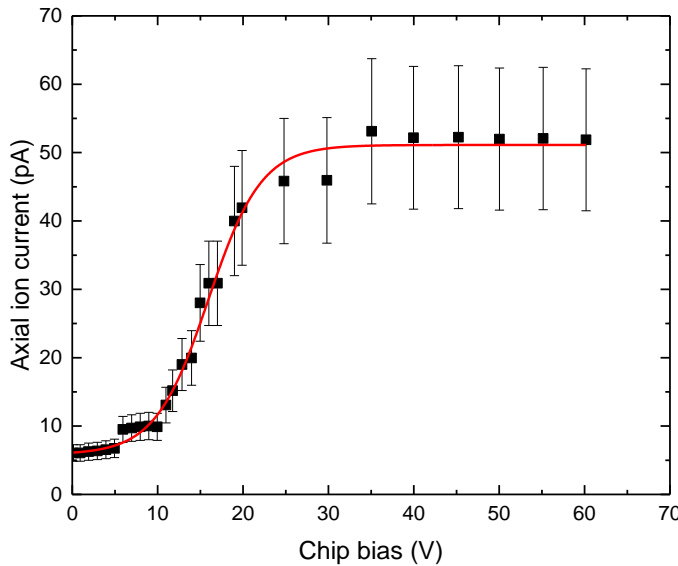


Figure. 4- 4 Total Ar ion current as a function of chip bias. A 700 mbar inlet argon gas pressure and -1.55 kV extraction voltage were used. Reproduced from Figure. 4-25(b) in Ref. [7].

To estimate the experimental reduced brightness, the virtual source size as a function of chip bias is illustrated in Figure. 4-5. Here, a spacing height of 1000 – 1400 nm was assumed, instead of the actual height of 600 nm, to account for the membrane deformation (200 – 400 nm). In Ref. [7], only the initial beam with $\pm 10^\circ$ emission angles originating at 5 different transverse planes was used to determine the virtual source size, by back ray tracing from angular aperture using Lorentz - 2EM [13], [14]. This approximation causes inaccuracy in calculation of the virtual source size, especially with low chip bias. To obtain a more accurate virtual source size, initial beam with full emission angle within entire NAIS and the gas pressure distribution was taken

into consideration. As seen from Figure. 4-5 and Eq. 4.1, the virtual source size changes less at high chip bias resulting in a more accurate evaluation of the reduced brightness because of a higher axial beam current.

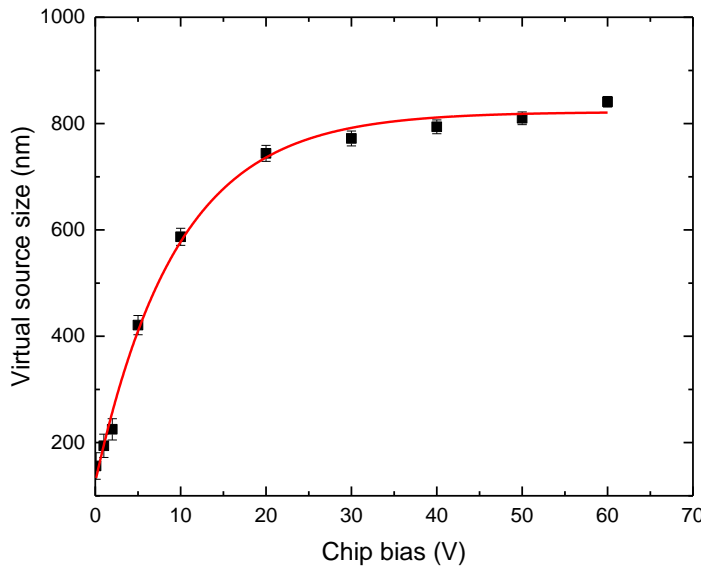


Figure. 4- 5 Simulated virtual source size as a function of chip bias by GPT.

The reduced brightness B_r as a function of chip bias was calculated from Eq. 4.1, see Figure. 4-6. As predicted by the simulation in Chapter 3, the reduced brightness declines rapidly when the chip bias starts to increase. After chip bias reaches ~ 20 V, the reduced brightness starts to level off. However, as seen in Figure. 4-6, a sharp drop appears around a chip bias of 10 V that does not match the simulated result. This mainly comes from the simulated virtual source size. As shown in Figure. 4-5, simulated virtual source size varies significantly with chip bias at low voltages. This suggests that the estimated reduced brightness cannot be precisely obtained from the calculation at low chip bias and is therefore more reliable at high chip bias. A reduced brightness of $8_{-1}^{+6} \times 10^2$ A/(m²srV) is obtained. The observed relatively low brightness of this NAIS with metal spacer originates from a low reduced brightness of the electron injector (~ 900 A/(m²srV)), low input gas pressure (700 mbar), large double-aperture size (1.5 μ m), thick membranes (1 μ m), and a large spacer of 600 nm (including

membrane deformation of 200 – 400 nm). Also, the misalignment between the NAIS and extractor contributes to the degradation of reduced brightness. Due to the relatively large chip bias, a larger energy spread is expected in this experiment.

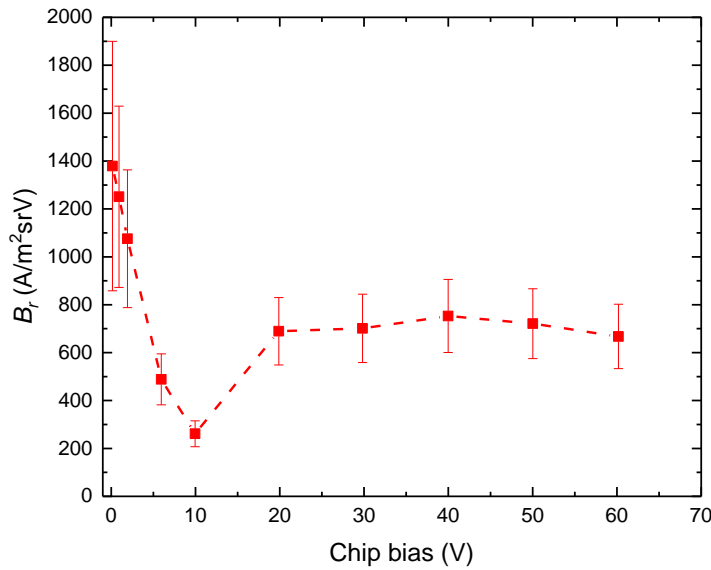


Figure. 4- 6 Reduced brightness as a function of chip bias.

4.3 NAIS with recessed Si₃N₄

4.3.1 Fabrication of NAIS with recessed Si₃N₄

Here a modified ionization chamber named as NAIS with recessed Si₃N₄ is fabricated to further improve the performance of the NAIS. A 7 mm × 1 mm × 300 nm NAIS ionization chamber has been fabricated by gluing two silicon nitride membranes together, using a microelectromechanical system (MEMS) technique. The step-by-step fabrication procedure is shown in Figure. 4-7. The ionization chamber was formed in the top and bottom Si₃N₄ layer of two Si chips (400 μm thick <100> Si). The silicon wafer was double-side-polished with a 280 nm, LPCVD, silicon nitride on both sides. To enable batch production, the top and bottom chips were designed to be identical to each other. In order to create the gas inlet, the electron beam inlet, and the ion beam outlet (referred as double-aperture) windows, the front side of the wafer was spin-coated with 2.5 μm thick AZ 1518 photoresist followed by a 50 s soft bake at 100 °C. Subsequently, the photoresist was exposed with a 405 nm laser to pattern the windows. The exposed windows were developed in AZ 400k developer diluted to 1:4 with deionized water (DI water) for 1 min. The patterned windows were then transferred to silicon nitride through deep reactive ion etching (DRIE) (Oxford PlasmaPro Cobra 100) with process parameters of 48 sccm CHF₃, 5 sccm O₂, 15 Pa pressure, and 250 W RF power. The DRIE processed chip is shown schematically in Figure. 4-7 a). This was followed by stripping of the residual AZ 1518 resist in acetone, opening up access holes by etching the exposed Si in Potassium hydroxide (KOH) solution (Figure. 4-7 b)) and creating a free-standing silicon nitride membrane. Later, the electrode was formed by depositing a conductive layer (10 nm Cr and 20 nm Au) via magnetron sputtering on the processed side of the wafers (Figure. 4-7 c)). Next, the ionization chamber was created at the back side of the wafer. For the back side, the wafer was spin-coated with 5 μm thick AR-P 3250 photoresist followed by 2 min soft bake at 95 °C. The ionization

channel pattern was exposed using a 365 nm ultraviolet (UV) and developed in AR 300-26 developer diluted to 3:2 in DI water for 1.5 min. The back side of silicon nitride membrane was dry-etched down to ~150 nm depth in a selected window (DRIE step, see Figure. 4-7 d)). The two chips were then bonded face to face (see Figure. 4-7e)) to create a gas handling chamber with a dimension of 7 mm × 1 mm × 300 nm. The gas inlet aperture and the double-aperture were created with the aid of gallium focused ion beam (FIB) milling (FEI Quanta Dual Beam, operated with ~1 nA at 30 keV Ga⁺). The double-aperture size was set to be $L_a = 500$ nm, $L_s = 300$ nm, $L_m = 130$ nm. Here L_a is larger than the membrane due to the limited stability in the SEM. Finally, the larger opening at the bottom side of the NAIS chip was sealed off using a vacuum glue, for holding a better gas pressure within.

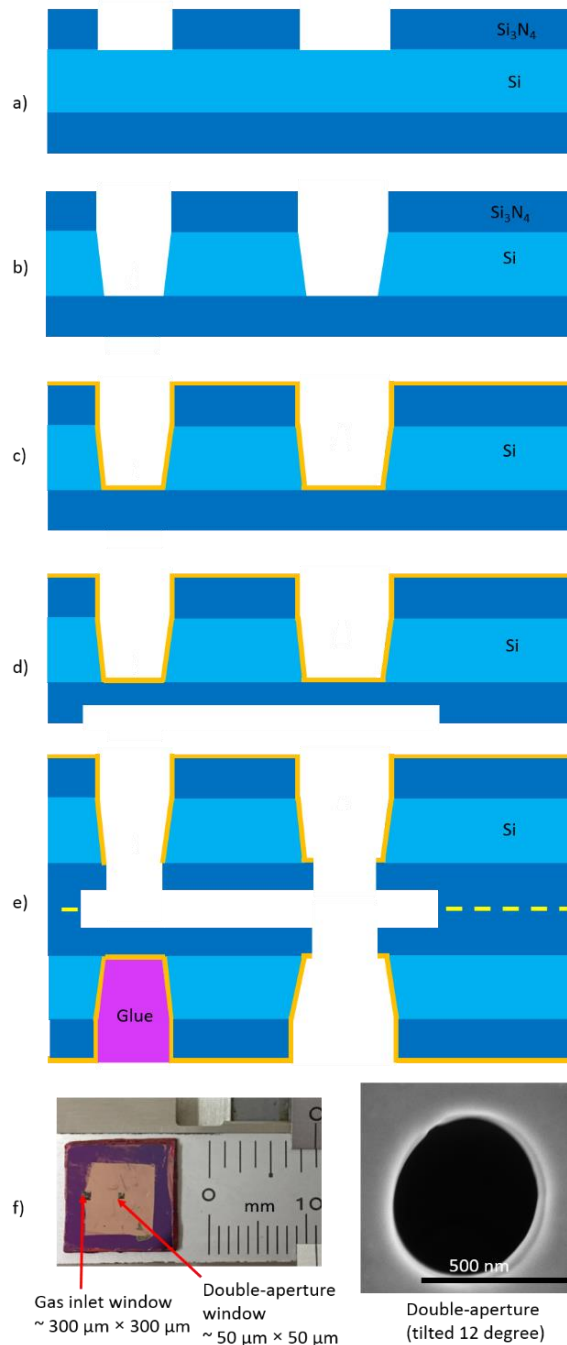


Figure. 4-7 Depiction of NAIS with recessed Si_3N_4 chip fabrication process: a) DRIE to create gas inlet and double-aperture windows on silicon nitride. b) KOH etching to reach the bottom side of silicon nitride membrane. c) 10 nm Cr + 20 nm Au deposited by magnetron sputtering for electrode. d) 150 nm depth ionization spacer created by DRIE. e) NAIS chip bonded with two individual chips and FIB-milled for creating gas inlet aperture and double-aperture. The diameter of the double-aperture is 500 nm. (f) A fabricated NAIS chip with a 300 $\mu\text{m} \times$ 300 μm gas inlet and 50 $\mu\text{m} \times$ 50 μm double-aperture windows, the double-aperture is ~500 nm diameter.

A chip holder, to mount NAIS chip, which can aid the detection of secondary electrons, was designed and manufactured, as shown in Figure. 4-8. This chip holder was designed to host NAIS chip, and deliver gas to it. Vacuum seal, between gas feed line and SEM chamber, was achieved using four Viton® O-rings. These O-rings also insulate one side of NAIS chip from chip holder. The NAIS chip is biased using a spring electrode.

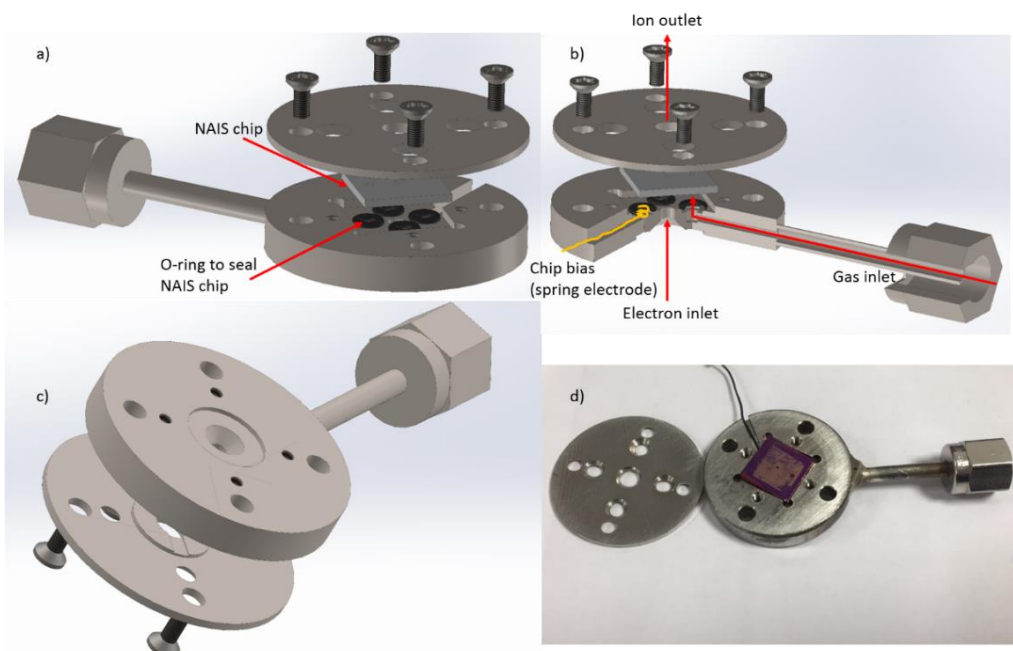


Figure. 4- 8 Schematics of NAIS chip holder. a) 3D view of NAIS chip holder. b) Sectional view of NAIS chip holder. c) Reverse 3D view of NAIS chip holder. d) Real image of modified NAIS chip holder.

The setup of NAIS chip holder with chip was placed inside a test chamber of helium leak detector (Adixen ASM 142 helium leak detector [15]). An external gas feed line was connected to the gas inlet fitting of NAIS chip holder. Helium gas was fed into NAIS chip, with varying pressure from 1 mbar to 1 bar, using a regulated all-metal gas-dosing valve (Agilent Varian) with a resolution of 10^{-11} mbar l/s. First, the chip holder was tested with a NAIS with recessed Si_3N_4 chip (and without double-aperture in it). Here a leak rate of 2×10^{-10} mbar l/s (with the base leak rate of 1×10^{-10} mbar l/s) was detected, with chamber's base pressure of $\sim 10^6$ mbar. Hence, NAIS with recessed Si_3N_4

with \sim 100 nm to 200 nm Si_3N_4 membrane is capable of constraining at least 1 bar gas pressure. Next, a NAIS with recessed Si_3N_4 with three double-apertures (\sim 500 μm opening) was tested to have a leakage rate of $\sim 10^{-7}$ mbar l/s at helium inlet gas pressure up to 1 bar.

4.3.2 Brightness measurement of NAIS with recessed Si_3N_4

We have customized a tungsten (W) SEM (JEOL JSM-5600) at Department of Physics, NUS, to suit for testing the NAIS chip, as shown in Figure. 4-9.

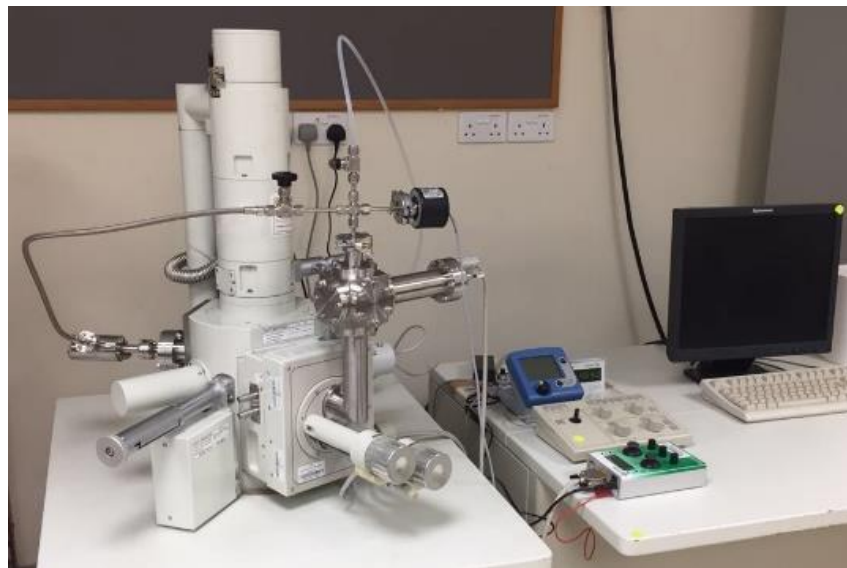


Figure. 4- 9 JEOL JSM-5600 W SEM at Department of Physics, NUS

The essential factor for testing NAIS is the injected electron beam current density. Electron probe currents were measured to be around 5 – 15 nA for 1 keV, under various operational conditions. The probe current density is found to be few 10^3 A/m².

In preliminary test of NAIS with recessed Si_3N_4 , the double-apertures got clogged during the experiment after several minutes. As shown from the measurement, the injected electron beam, used to ionize Ar gas molecules, has a relatively large spot size with respect to the double-aperture and is operated at a relatively high pressure environment. The injected electron beam size was larger than the double-aperture size (500 nm) due to the limit of W SEM at low energy and the mechanical instability of

the system, resulting in carbon deposition, causing clogging effect of the double apertures. The poor chamber vacuum pressure (few $10^{-5} - 10^{-4}$ mbar) is a second reason for the clogging [16]. Figure. 4-10 shows a clogged aperture after a typical brightness measurement. Predictably, this clogging effect will become very critical for smaller double-aperture sizes.

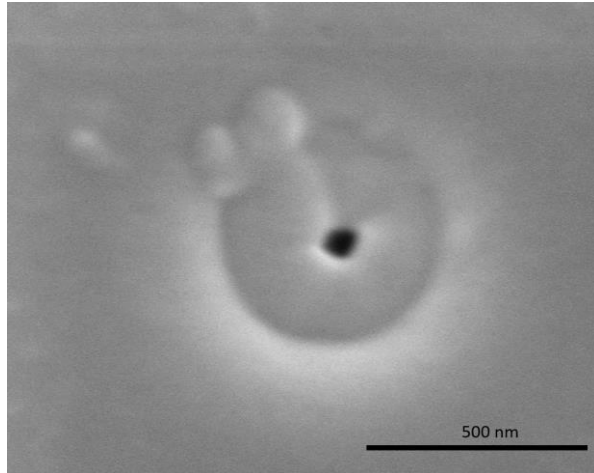


Figure. 4- 10 SEM image (taken by field emission SEM, FEI Verios 460) of the double-aperture after being used.

The brightness measurement setup was positioned inside the W SEM chamber as shown in Figure. 4-11. The extractor voltage was fixed at -1.2 kV during the brightness measurement of NAIS with recessed Si_3N_4 to repel the 1 keV electrons and to minimize the off-axis aberration originating due to the misalignment between NAIS chip and extractor. Meanwhile, to further reduce the influence from misalignment, the Faraday cup was biased at -90 V to enhance the ion beam-landing.

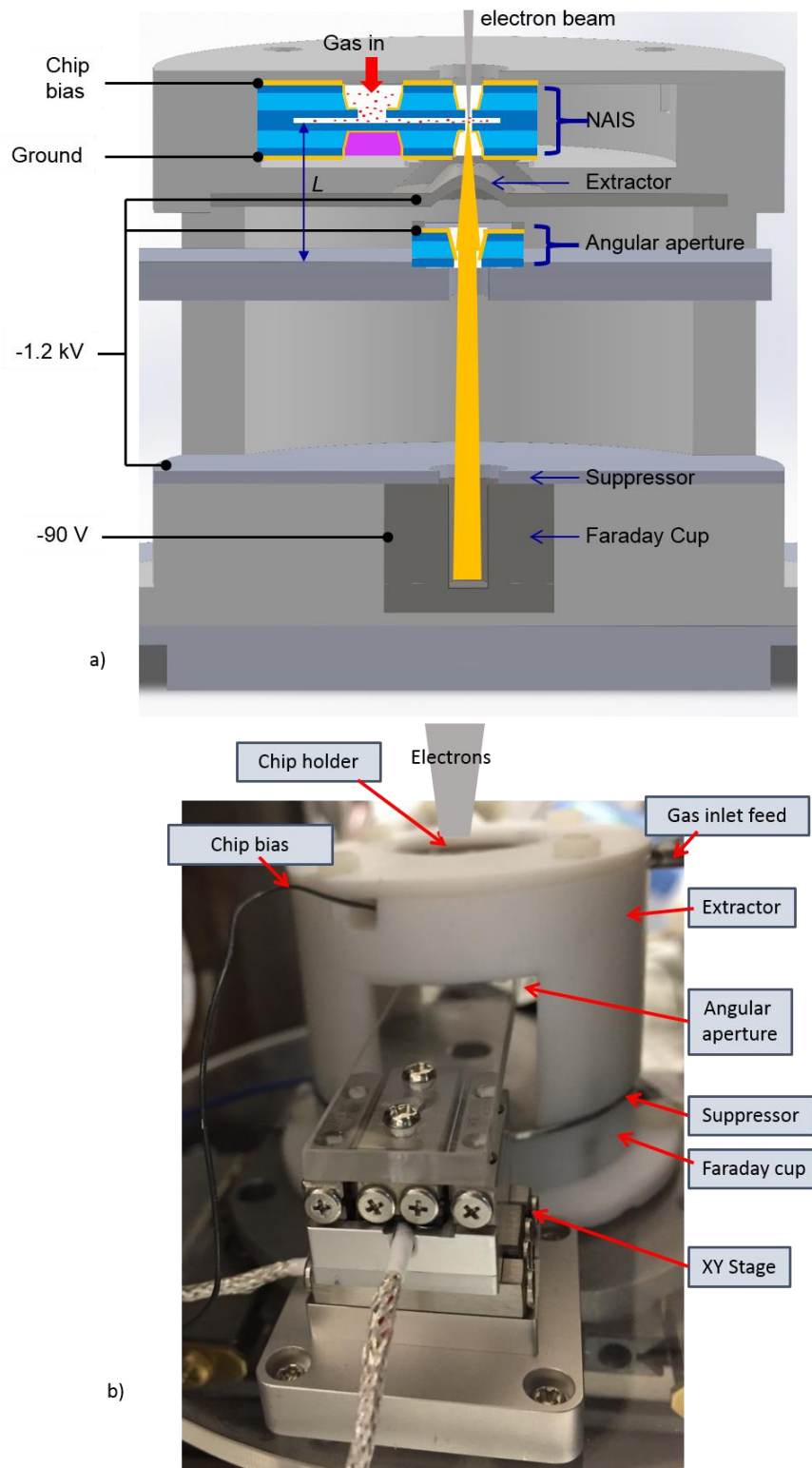


Figure. 4- 11 Reduced brightness measurement of NAIS with recessed Si_3N_4 , carried out inside a JEOL JSM-5600 W SEM. a) Schematic of brightness measurement set-up. b) The actual setup inside the W SME.

A regulator valve was used to control inlet gas pressure between 1 mbar and 1 bar. The reduced brightness measurement was performed with argon ions (Ar^+ 95%, the rest are Ar^{n+} , $n = 2$ to 4) [8] to examine the performance of this NAIS with recessed Si_3N_4 . The electric field inside the NAIS chamber was varied by tuning the bias across the NAIS chip from 0 to 100 V. An angular aperture ($95 \mu\text{m} \times 112 \mu\text{m}$, 10 mm downstream from the NAIS chip), used to define the solid angle, was kept at the same potential as the extractor. The angular aperture was fabricated by a similar process as adopted for the NAIS chip's double aperture. This angular aperture was mounted on a piezo-XY linear stage (SmarAct® SLC-1720-S-HV) and scanned through the beam to find the peak axial beam current as measured in a Faraday cup. Downstream of the angular aperture, a suppressor electrode (at equipotential with the extractor) was used to maintain a field-free region for ions.

In the current experiment the inlet Ar gas pressure was set to be 860 mbar. The Knudsen number K_n , under the current condition is around 0.2 when the pressure in double-aperture region is same as inlet gas pressure. Further increase in the inlet gas pressure is feasible as long as the Knudsen number K_n remains larger than 0.1. Chip bias is used to guide ions out of NAIS chamber. The schematic of the experimental details for reduced brightness B_r measurement is shown in Figure. 4-12. The reduced brightness was measured and recorded when an axial peak current was obtained, by tuning the chip bias, before the clogging effect starts to deteriorate the measurement.

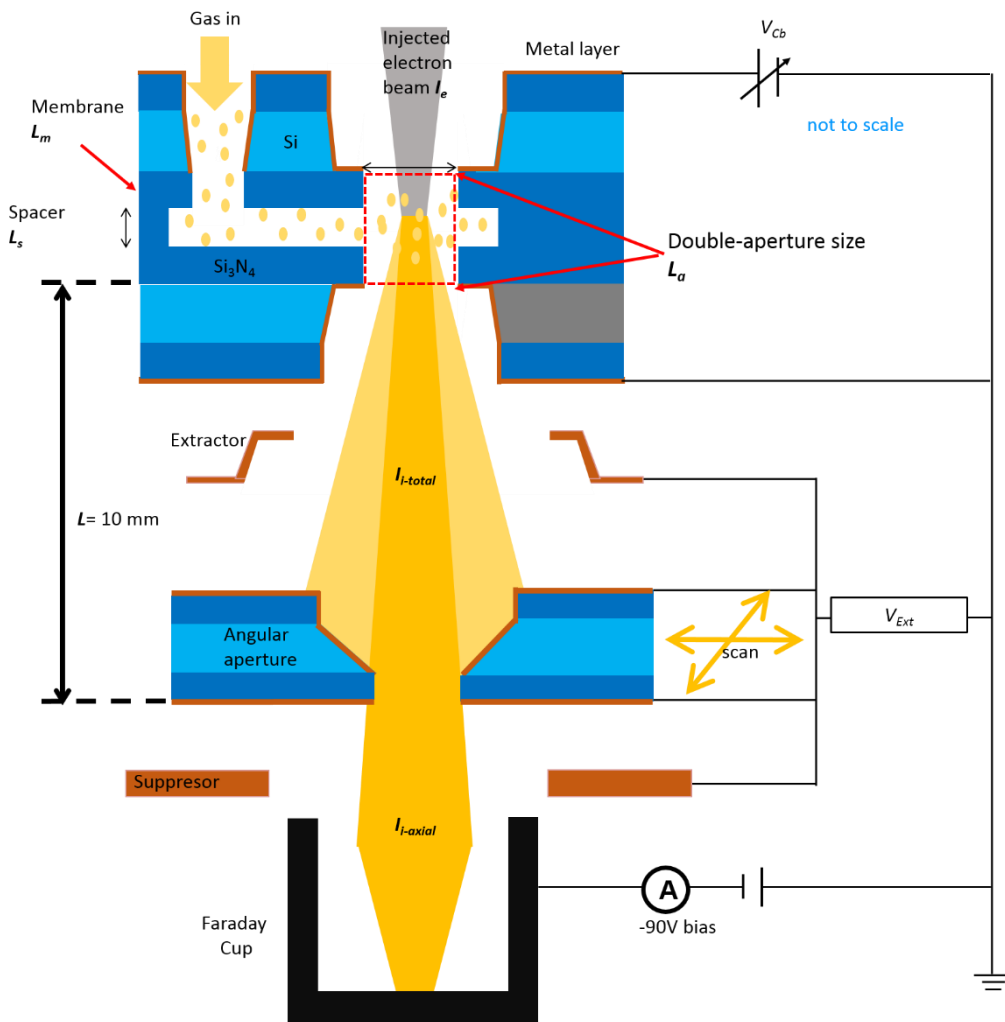


Figure. 4- 12 Detailed schematic setup of NAIS and the brightness measurement.

With the following parameters: inlet gas pressure of 860 mbar, chip bias of 23 V, and an extractor potential of -1.2 kV, an axial peak current of 230 pA has been observed.

On substituting these values in Eq. 4.1, a reduced brightness for Ar⁺ is found to be $9.1 \times 10^3 \text{ A}/(\text{m}^2\text{srV})$. Here, the value of virtual source size was considered to be the same as the double-aperture size (500 nm). This is a conservative evaluation, since the virtual source size of NAIS is expected to be smaller than the real source size. The GPT simulated virtual source size is ~350 nm based on the experimental geometry. Therefore, the reduced brightness for Ar⁺ is $0.9_{-0.1}^{+1.0} \times 10^4 \text{ A}/(\text{m}^2\text{srV})$, which is an order higher than the NAIS with metal spacer and 3 orders higher than the RF source in the existing PBW system [17].

4.4 Second-generation NAIS

4.4.1 Approach to high brightness NAIS

NAISs with metal spacer and recessed Si₃N₄ have been tested and show promising performances, which match simulated prediction. With the increase of gas pressure in the vicinity of double-aperture region, the reduced brightness can be much higher than currently measured values. However, the chip bias of both NAISs (~20 V) was found to be larger than the required (as predicted from simulation) NAIS electric field of ~10⁷ V/m. This implies that the actual distance, during experiment, between the two electrodes is 2 – 3 μm, rather than the fabricated 2.6 μm and 560 nm. For NAIS with metal spacer, this distance roughly matches the experimental design of ~2.6 μm. However, for NAISs with recessed Si₃N₄ there is a huge discrepancy from experimental design (~560 nm). It is believed that the discrepancy comes from the increased flexibility due to the reduction of Si₃N₄ membranes from 1 μm of NAIS with metal spacer to ~130 nm (280 nm Si₃N₄ membrane with 150 nm recessed gas channel) of modified NAIS.

To evaluate the deflection of the free-standing Si₃N₄ membranes in the region of double-aperture window, coupled fluid flow model and solid structural deformation model were employed. The differential gas pressure will lead to the deformation of Si₃N₄, which will in turns affect the gas flow. Here, COMSOL Multiphysics® [18] with Fluid-Structure Interaction (FSI) module will be used to analyze this coupled interaction.

As for the NAIS configuration, only the free standing Si₃N₄ double-aperture window will be studied, as shown in Figure. 4-13. Outside this region the NAIS is constrained by a thick layer of silicon, where deformation can be neglected in the simulations. The

boundary of the free standing Si_3N_4 membranes are constrained due to reinforced from thick layer of silicon.

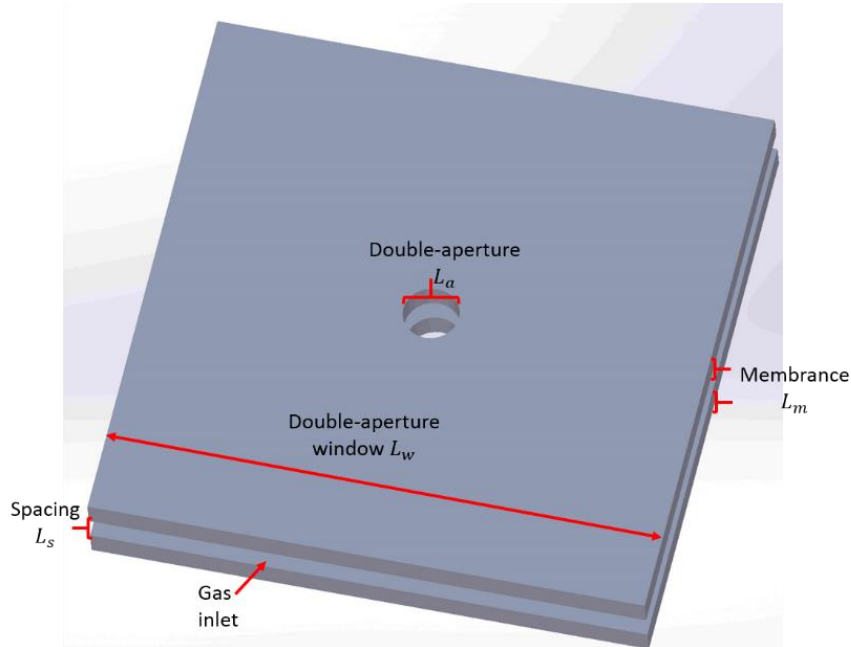


Figure. 4-13 Double-aperture window model (not at scale) for COMSOL simulation. The gray slab represents the silicon nitride with the double aperture in the middle.

For NAIS with a characteristic length of 1 μm and inlet gas pressure of 1 bar, the deformation along the middle of the double-aperture window is simulated for different areas of the free-standing Si_3N_4 window, as shown in Figure. 4-14. From the simulation, the gas species don't have significant influence to the deformation because the differential pressure is the dominant factor here. The maximum deformation for 100 $\mu\text{m} \times 100 \mu\text{m}$ window is $\sim 400 \text{ nm}$, and for 50 $\mu\text{m} \times 50 \mu\text{m}$ window is $\sim 30 \text{ nm}$. By decreasing the area of the window, the deformation of Si_3N_4 reduces dramatically. Therefore, for 1 μm thick Si_3N_4 membrane, a less than 50 $\mu\text{m} \times 50 \mu\text{m}$ window has relatively small deformation ($< 30 \text{ nm}$, i.e. 3%).

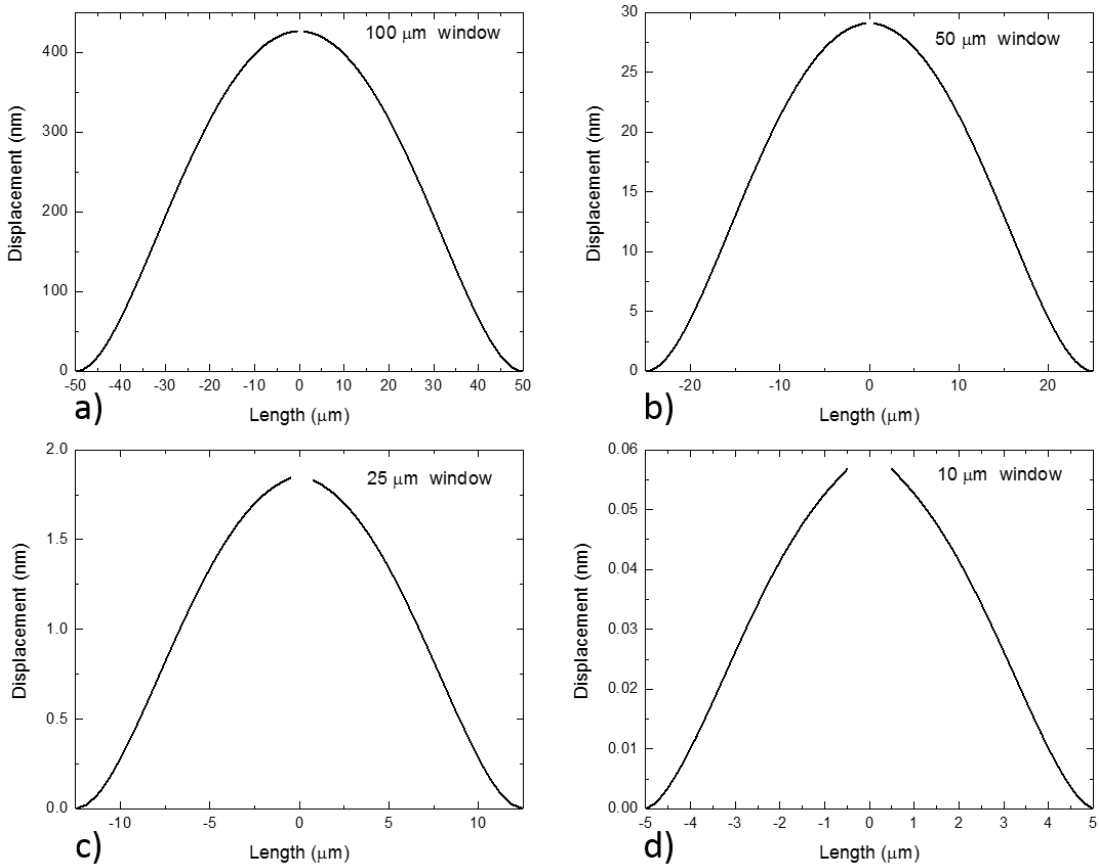


Figure. 4- 14 Deformation of the Si₃N₄ membranes for different areas of double-aperture window for characteristic length of 1 μm. The gap between lines is the double-aperture window's diameter.

For NAIS with characteristic length of 100 nm, as predicted in chapter 2, the maximum inlet gas pressure can be as high as 10 bar. The maximum deformation of 100 nm thick Si₃N₄ of different window area with inlet gas pressure of 1 bar and 10 bar are simulated, and shown in Figure. 4-15. For a 10 μm × 10 μm window, 10 bar inlet gas pressure introduces a deformation more than the thickness of Si₃N₄ membrane (100 nm) (i.e. > 100%), which is undesirable. In order to maintain up to 10 bar differential pressure with deformation of less than the thickness of Si₃N₄ membrane, a 5 μm x 5 μm is recommended, which has ~30 nm (30 %) deformation. However, a large size of double-aperture window can be used when the operational inlet gas pressure is below 10 bar.

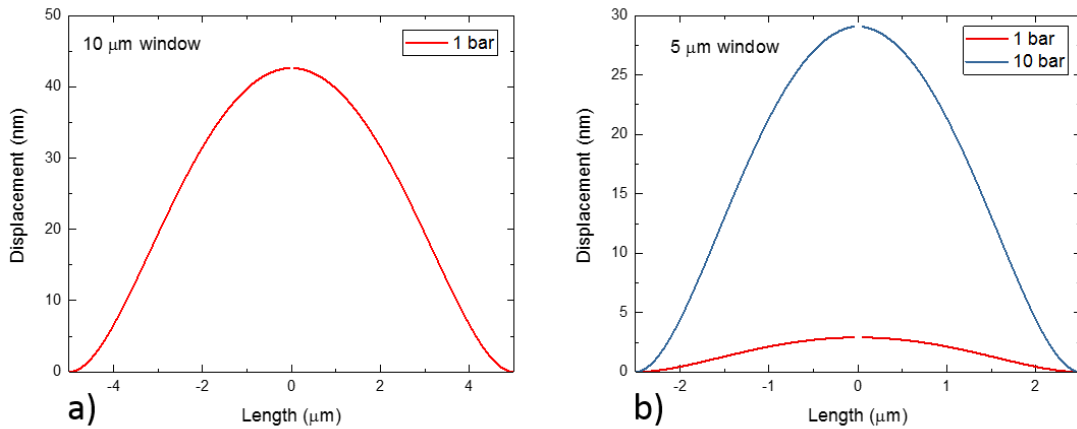


Figure. 4- 15 Deformation of the Si_3N_4 membranes for different sizes of double-aperture window for characteristic length of 100 nm. The gap between lines is the double-aperture.

NAISs with metal spacer and recessed Si_3N_4 were simulated here based on the experimental configuration. For NAIS with metal spacer, Si_3N_4 membranes of double-aperture window were $100 \mu\text{m} \times 100 \mu\text{m} \times 1 \mu\text{m}$, with a $1.5 \mu\text{m}$ diameter double-aperture in the middle. In between the two Si_3N_4 membranes, a spacing of 600 nm height was used. The boundary gas pressure along the double-aperture was simplified to be the same as experimental input gas pressure of 700 mbar for argon. The maximum deformation is $\sim 360 \text{ nm}$ from the simulation. For NAIS with recessed Si_3N_4 , a $100 \mu\text{m} \times 100 \mu\text{m} \times 130 \text{ nm}$ double-aperture window with 300 nm spacing and 500 nm diameter double-aperture was used. The maximum simulated deformation is $\sim 1.2 \mu\text{m}$. Therefore, it is necessary to reduce the deformation of Si_3N_4 membranes so that the energy spread could be reduced.

To reduce the deformation of Si_3N_4 membranes, we can reduce the double-aperture window size to $\sim 5 - 10 \mu\text{m}$. However, when we adopt this approach, multiple double-apertures can't be fabricated within the same NAIS chip. An alternative approach is to reinforce the Si_3N_4 membranes with a silicon grid structure. The addition of the silicon grids divides the large area of Si_3N_4 into many evenly distributed small areas of free-standing Si_3N_4 membranes of $5 - 10 \mu\text{m}$, hence increasing the stiffness. Figure. 4-16

illustrates this proposal of creating a silicon grid structure to reinforce the silicon nitride membrane in the NAIS.

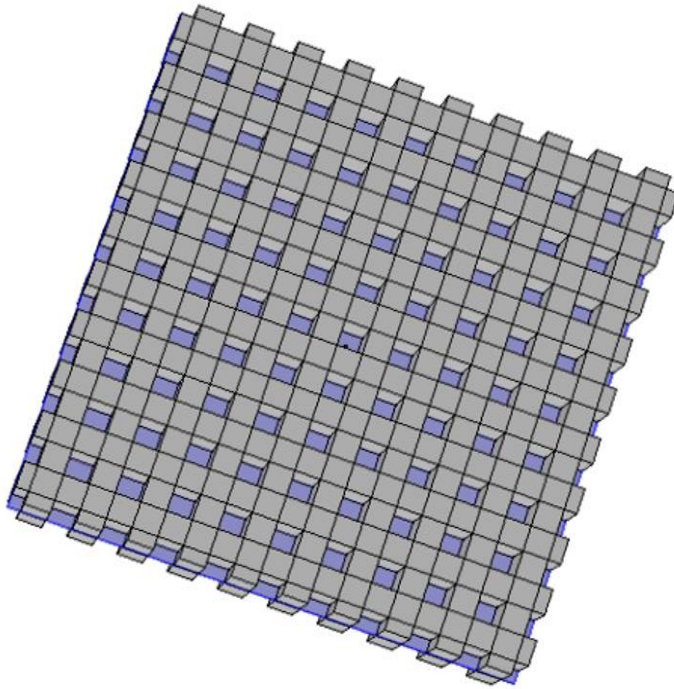


Figure. 4- 16 Schematic for a general geometry for the proposed NAIS used for COMSOL Multiphysics simulation. The blue slab represents the silicon nitride with the double aperture in the middle, and the supporting silicon grid structure, on the silicon nitride, is shown in grey.

A $100 \mu\text{m} \times 100 \mu\text{m} \times 100 \text{ nm}$ silicon nitride membrane with additional silicon supporting grid with cross section of $5 \mu\text{m}$ long and $10 \mu\text{m}$ high was evaluated. The addition of the silicon supporting grid greatly reduces the maximum deflection experienced by the silicon nitride, down to about tens of nanometers, as against a few μm deflection in a conventional NAIS design. For inlet gas pressure of 1 bar, the combined deformation of both silicon grids and silicon nitride is less than 5 nm (< 5 %). If the inlet gas pressure is increased to 10 bar, more deformation is expected as shown in Figure. 4-17. The main deformation is attributed to the $5 \mu\text{m} \times 10 \mu\text{m}$ supporting grid. The ripples superimposed on the main curve originate from the evenly distributed $5 \mu\text{m} \times 5 \mu\text{m}$ silicon nitride windows in between the silicon supporting grids. The maximum deformation is $\sim 60 \text{ nm}$ for an inlet gas pressure of 10 bar. To achieve a minimum energy spread, either the height of the ionization chamber has been reduced,

or the double-aperture should be shifted towards the edge of the overall window, as indicated in Figure. 4-17. Alternatively, reducing the grid spacing can dramatically reduce the deformation.

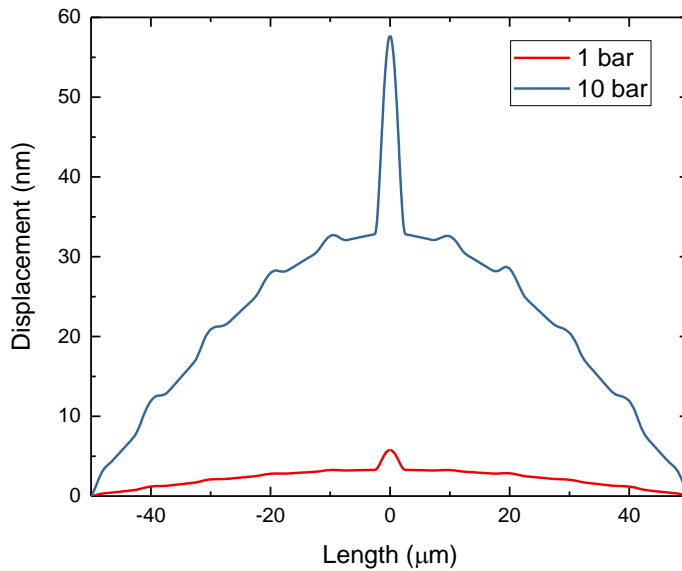


Figure. 4- 17 Deflection of the Si_3N_4 membrane with silicon supporting grid structure.

4.4.2 NAIS with internal electrodes

The NAIS developed in this thesis has the ability to deliver Ar^+ ion current of ~few 100s pA with a reduced brightness as high as $0.9_{-0.1}^{+1.0} \times 10^4 \text{ A}/(\text{m}^2\text{srV})$. The higher reduced brightness can be achieved with the improvement of electron probe current density and better alignment as well as improved mechanical stability. However, the currently developed NAISs are limited by their large energy spread, which comes mainly from the deformation of membranes and high chip bias across the NAIS ionization chamber (used to maintain an electric field of $\sim 10^7 \text{ V/m}$). Here we present a design and fabrication method for a NAIS chip with internal electrodes which can achieve both high brightness and low energy spread ($< 1 \text{ eV}$).

Figure. 4-18 shows a chip which can be integrated as NAIS. The gas inlet window and electron inlet/ ion outlet window are formed in a $<100>$ silicon wafer with 50-500 nm

double side coated silicon nitride. The bottom side silicon nitride serves as the ionization chamber wall to constrain the gas and holds the pressure difference between gas (up to 10 bar) and vacuum. The top side silicon nitride acts as a mask for desired pattern following by RIE. The pyramid shape in the silicon can be formed in the potassium hydroxide (KOH) solution and accurately control the etching depth for a ~10 μm thick residual silicon. The residual silicon is milled by FIB to create supporting beams/ grids. Since the silicon nitride is very thin, the milling process must stop before reaching the silicon nitride membrane, with thin μm protective silicon layer left. This protective silicon layer can be removed by RIE or KOH etching. The supporting grids are orthogonally distributed with ~5 – 10 μm spacing arrangement depending on the operating gas pressure.

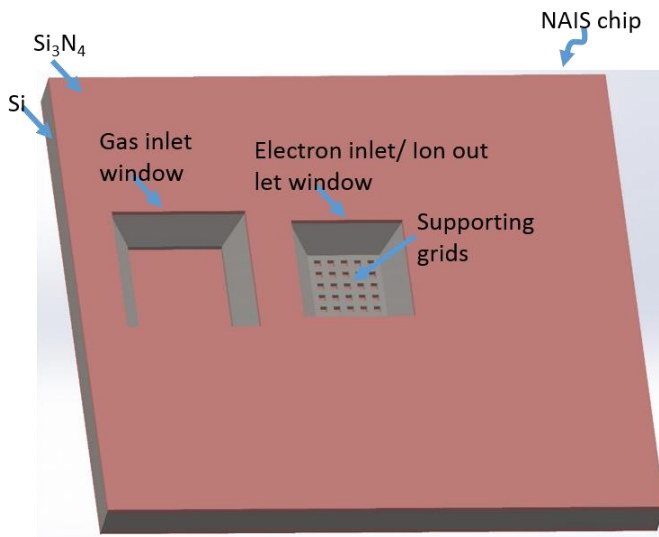


Figure. 4- 18 A top view of NAIS chip with internal electrodes.

Next, the fabrication process is carried out on the back side of the wafer to create the ionization chamber. The ionization chamber is created by RIE for 50 – 200 nm depth, subsequently followed by ~10 nm gold electrode deposition to create the electrodes, A ~5 nm chromium serves as an adhesion layer between gold and silicon nitride. Electrodes are chosen to have no-contact to each other when bonding two chips together. Once the chips are fabricated, two chips are bonded. These two chips can be

precisely aligned according to the supporting grids. The electron inlet apertures and ion outlet apertures are milled by FIB resulting in well aligned sub-micron size apertures.

4.5 Summary

In this chapter, the successful fabrication, through MEMS technique, of NAISs with metal spacer and recessed Si_3N_4 were discussed. Both of the fabrication processes were designed for batch production. These NAIS chips are vacuum compatible with good sealing property. The performance of both NAIS chips were tested using SEM as an electron injector. The performance of NAIS was examined as a function of inlet gas pressure, extraction voltage and chip bias, and shows a good agreement with the simulated result. Table 4-1 shows the experimentally achieved reduced brightness for the different configurations used, reaching up to 3 orders higher reduced brightness compared to the RF source in the existing PBW system [17]. Better mechanical alignment of NAIS chip and extractor, higher electron beam current density, determination of more appropriate virtual source size, higher gas pressure and fine tuning of other parameters will result in enhanced reduced brightness.

Table. 4-1 Experimentally measured reduced brightness and energy spread of NAISs with metal spacer and recessed Si_3N_4 , with comparison to the predicted NAIS with internal electrodes.

	NAIS with metal spacer	NAIS with recessed Si_3N_4	Future NAIS with internal electrodes*
Reduced brightness (A/(m²srV))	$8_{-1}^{+6} \times 10^2$	$0.9_{-0.1}^{+1.0} \times 10^4$	> 10^6 for proton
Injected electron current density (A/m²)	10^3	$1.5 - 5 \times 10^3$	10^8
Energy spread* (eV)	~20	~23	< 1

* Energy spread ΔE is defined by $E_0 - \Delta E$

** With an ideal Schottky electron injector system

However, the energy spread from both NAISs with metal spacer and recessed Si_3N_4 were relatively larger due to the bulging effect of Si_3N_4 membranes. The effect of double-aperture window size of characteristic length of 1 μm and 100 nm were simulated. The result shows that a 5 μm double-aperture window is capable of reducing the energy spread, due to the small bulging effect. To achieve high reduced brightness

and low energy spread NAIS, NAIS with internal electrodes is proposed. The deformation issue of the ionization chamber can be solved by integrating silicon supporting grids to the silicon nitride membranes. The orthogonally distributed rigid and thick ($\sim 10 \mu\text{m}$) silicon grids can reduce silicon nitride membranes' bulge. Additionally, the embedded electrodes inside the ionization chamber should give lower energy spread. The NAIS with internal electrodes is predicted to deliver ions with a reduced-brightness of $10^6 \text{ A}/(\text{m}^2\text{srV})$ and energy spread of $< 1 \text{ eV}$.

References

- [1] S. E. Lyshevski, *MEMS and NEMS: systems, devices, and structures*. CRC press, 2002.
- [2] V. Choudhary and K. Iniewski, *MEMS: Fundamental technology and applications*. CRC Press, 2013.
- [3] M. Gad-el-Hak, *The MEMS handbook*, vol. 2. CRC/Taylor & Francis Florida, 2006.
- [4] University Wafer, “Nitride Silicon Wafer.” [Online]. Available: <http://www.universitywafer.com/silicon-nitride.html>.
- [5] M. J. Cooke, “A review of LPCVD metallization for semiconductor devices,” *Vacuum*, vol. 35, no. 2, pp. 67–73, 1985.
- [6] K. Seshan, *Handbook of thin film deposition*. William Andrew, 2012.
- [7] L. Nannan, “Development of an Electron Impact Gas Ion Source for Proton Beam Writing Application,” National University of Singapore, 2015.
- [8] R. Rejoub, B. G. Lindsay, and R. F. Stebbings, “Determination of the absolute partial and total cross sections for electron-impact ionization of the rare gases,” *Phys. Rev. A*, vol. 65, no. 4, p. 42713, 2002.
- [9] H. C. Straub, P. Renault, B. G. Lindsay, K. A. Smith, and R. F. Stebbings, “Absolute partial cross sections for electron-impact ionization of H₂, N₂, and O₂ from threshold to 1000 eV,” *Phys. Rev. A*, vol. 54, no. 3, p. 2146, 1996.
- [10] D. W. O. Heddle, *Electrostatic lens systems*. CRC Press, 2000.
- [11] L. Reimer, *Scanning electron microscopy: physics of image formation and microanalysis*, 2nd ed. Springer-Verlag Berlin Heidelberg, 1998.
- [12] M. B. H. Breese, D. N. Jamieson, and P. J. C. King, “Materials analysis with a nuclear microprobe,” *Wiley, New York*, 1996.
- [13] Intergrated Engineering Software, “Lorentz - 2EM.” [Online]. Available: <https://www.integratedsoft.com/>.
- [14] N. Liu, X. Xu, R. Pang, P. S. Raman, A. Khursheed, and J. A. Van Kan, “Brightness measurement of an electron impact gas ion source for proton beam writing applications,” *Rev. Sci. Instrum.*, vol. 87, no. 2, 2016.
- [15] Pfeiffer Vacuum, “Leak Detectors.” [Online]. Available: <https://www.pfeiffer-vacuum.com/en/products/leak-detectors/>.
- [16] G. Blondiaux, M. Valladon, L. Quaglia, G. Robaye, G. Weber, and J. L. Debrun, “Study of the growth of carbon on targets during ion bombardment,” *Nucl. Instruments Methods Phys. Res. Sect. A Accel. Spectrometers, Detect. Assoc. Equip.*, vol. 227, no. 1, pp. 19–23, 1984.
- [17] J. A. Van Kan, P. Malar, and A. B. De Vera, “The second generation Singapore high resolution proton beam writing facility,” *Rev. Sci. Instrum.*, vol. 83, no. 2, p. 02B902, 2012.
- [18] COMSOL Inc., “COMSOL Multiphysics®.” [Online]. Available: <https://www.comsol.com/>.

Chapter 5. Evaluation and design for a low energy proton microscope and a compact PBW (c-PBW) system

Microscopy has spurred development in many fields and has been an integral part of scientific development for more than a hundred years. Any form of microscopy is limited by the wavelength of the probe used. Microscopy using protons with the wavelength below nanometer range has several advantages over traditional forms of microscopy. In addition to diffraction being negligible, due to the mass mismatch between protons and electrons, a proton beam will follow a practically straight path in materials. During proton-electron collisions the secondary electrons just get enough energy to break chemical bonds within a range of ~1 nm of the original proton track [1]. The small interaction volume means a good resolution for both imaging and lithography. Low mass ions are the ideal tools for imaging and lithography where the sputtering effect is insignificant, especially for the lightest ion: proton, with negligible sputtering effect, as described in Chapter 1. Scanning ion microscopy like conventional gallium focused ion beam (FIB) [2] and helium ion microscope (HIM) [3] has shown merits in good surface sensitivity and distinct contrast compared to scanning electron microscope (SEM). Current proton microscopes are typically very large, not user-friendly and have an ion source brightness which is typically several million times less compared to competitive beam sources like gallium and helium ion sources. NAIS is a high brightness and low energy spread electron impact ion source, with the potential to expand applications in high-resolution imaging and single digital nanometer lithography. In this chapter, the evaluation and design of a low energy proton microscope and a compact PBW (c-PBW) system will be discussed.

5.1 Low energy proton microscopy

5.1.1 Introduction

Low energy microscopy is advantageous in surface analysis for both electrons and ions due to a small interaction volume, high secondary electron yield and high backscattering yield. This microscopy is surface-sensitive and composition-sensitive only to the topmost layer. These characteristics have been widely exploited in low energy electron microscopy (LEEM), and in low energy ion scattering (LEIS) experiments (also called ion scattering spectroscopy (ISS)) [4]–[9]. Because chromatic aberration limits the resolution in the low energy range (as discussed in Appendix 2), generally LEEM uses high energy electron beam to focus and subsequently retards the focused electron beam to low energy through biasing the sample. Another version of LEEM adopts aberration correctors and energy filters to improve the lateral resolution down to the nm range [10], [11]. While typical LEIS instruments directly guide a low energy ion beam to the sample with 100 μm lateral resolution, they are not capable of imaging. Based on a laser-cooled lithium ion source, Jabez McCelland and his team at National Institute of Standards and Technology (NIST), US, have unveiled first low energy FIB microscope with beam energy ranging from 500 eV to 5 keV [12], [13]. The exciting results have achieved < 100 nm resolution with a beam energy of 700 eV, while the best resolution is 26.7 nm with beam current of 1 pA at beam energy of 2 keV [12], [13]. The advantage of low energy ion microscopy is due to the high cross sections for ion-atom interactions. Although the achieved resolution is not yet as good as SEM or HIM, the merits of low energy microscopy is to acquire images of nonconductive samples and distinguishable chemical composition at topmost layer of materials. The detection of backscattered ions can not only illustrate the chemical difference of adjacent materials, but also analyze the elemental composition. Low energy ion microscopy is a new high resolution technique with good surface sensitivity

and elemental sensitivity. Light ions can be used for imaging with the absence of sample damage due to the low sputter yield, especially for proton. On the other hand, heavy ions are well suited for milling because of relatively high sputter yield.

NAIS, as a high brightness and low energy spread ion source, offers compelling advantages over other ion sources. In principle, any gas that can be ionized is compatible with NAIS, enabling the generation of ion beams spanning different gaseous ion species with a simple and convenient way to switch among different gas species. Here, we will concentrate on the design consideration of proton microscope equipped with hydrogen NAIS.

5.1.2 Advantage of low energy proton microscopy

When ions strike a target, electronic stopping (generating secondary electrons) and nuclear stopping (generating backscattered ions, sputtered target atoms and/or defects) are the main interaction mechanisms, as discussed in Chapter 1.

When secondary electrons are generated along the incident ions path, some secondary electrons near the surface can escape. Compared to electron-induced secondary electrons, ion-induced secondary electrons have lower energy and higher yield due to the larger mass difference between ions and electrons [1], [14]. Additionally, ions have a smaller interaction volume than electrons with the same energy. The interaction volume can be referred to as effective probe size. These secondary electrons generated by low energy ions are advantageous and sensitive in the topmost surface of a target with a high signal to noise ratio and small interaction volume. Therefore, low energy ion microscopy (including proton) is suitable to image topographic contrast with high surface sensitivity.

Other than inelastic collisions generating secondary electrons, elastic collision with target nuclei also happens which can generate backscattered ions for low mass incident

ion beam. This effect is referred as Rutherford scattering with a differential cross section $\frac{d\sigma}{d\Omega}$ in laboratory system of [15],

$$\frac{d\sigma}{d\Omega} = \left(\frac{Z_1 Z_2 e^2}{2E_0} \right)^2 \frac{\left[\cos \theta + \sqrt{1 - (\sin \theta M_1/M_2)^2} \right]^2}{\sin^4 \theta \sqrt{1 - (\sin \theta M_1/M_2)^2}} \quad (5.55)$$

E , the energy of the backscattered ion is given by [15]

$$E = E_0 \left[\frac{\cos \theta \pm \sqrt{(M_2/M_1)^2 - \sin^2 \theta}}{1 + M_2/M_1} \right]^2 \quad (5.56)$$

Where Z_1 and Z_2 are the atomic number of incident ion with mass M_1 and target nucleus with mass M_2 . E_0 is the energy of incident ion. θ is the scattered angle in laboratory system.

The backscattered ions can be employed to image the sample. As seen from Eq. 5.1 and Figure. 5-1, the differential cross section σ increases with decreasing incident ion energy E_0 and the decreasing mass M_1 at a fixed angle θ . The nuclear stopping happens more at low incident ion energy, meaning more signal can be acquired. Also, with the decrease of incident ion energy, the effective probe size decreases, meaning a better imaging resolution can be achieved.

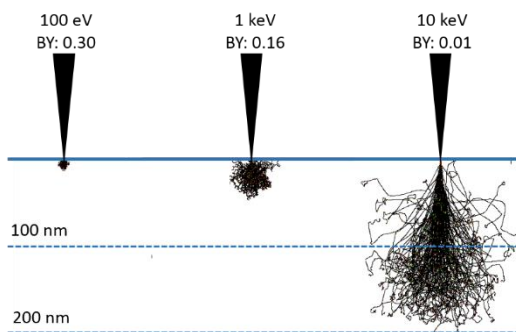


Figure. 5- 1 Trajectories and backscattered yield (BY) of protons (200 protons) for different incident energies (100 eV, 1 keV and 10 keV) in silicon. Simulated using Monte Carlo simulation program SRIM [16].

In fact, backscattered ions may be used for composition analysis. As seen from Eq. 5.1, the backscattered yield depends on the target atomic number. Meanwhile, the energy

of backscattered ions is related to the target atoms, which can be used for quantitative composition analysis by detecting the energy spectrum. Both the mass and concentration of the surface atoms can be obtained due to the small penetration of the probe. Another advantage of backscattered ions, as compared to secondary electrons, is that backscattered ions can be employed to analyze non-conducting samples, because the accumulated charge from incident ions can be compensated by electron beam flood exposure. Therefore, a low energy ion microscope with low mass ion species and good resolution would be an attractive option, due to surface sensitivity and composition contrast.

However, for ion microscopy, the ion probe size generally shrinks with the increase of ion energy. At low energy, ion probe size is typically limited by chromatic aberration, if diffraction aberration is absent (more detail about SEM can be seen in Appendix-2). Therefore, a high brightness and low energy spread ion source is clearly needed. NAIS is a potential candidate to be part of low energy proton microscope for any gaseous ions.

5.1.3 Miniaturized Einzel lens

Contributions to final focused probe size are dominated by the demagnified virtual source size at imaging plane, contributions from chromatic aberration and spherical aberration, with the absence of diffraction aberration (Airy disk) due to the extreme short ion wavelength. At low energy range, a high brightness ion source's probe size is mainly limited by its chromatic aberration (as seen Appendix-2). Since NAIS is a promising high brightness and low energy spread ion source, it will be a competitive candidate to be a part of a low energy proton microscope. Therefore, the key part of this microscope is to equip it with a low chromatic aberration focus lens.

An Einzel lens is an electrostatic lens which can focus a charged particle beam without changing its beam energy. Generally, it consists of three symmetrical apertures or tubes

with the same electric potential at the first (entrance) and third (exit) apertures. The electric potential at the middle aperture is varied to focus the beam either by acceleration-deceleration or deceleration-acceleration mode. For an Einzel consisting of three apertures (as shown in Figure. 5-2), typically the size of apertures and distance between apertures are about the same as the working distance of the lens. The advantage of the Einzel lens is its simplicity, compactness and no dissipation of external power. Generally, the chromatic aberration of the lens relies on its design, geometry and operating condition. The coefficient of chromatic aberration is approximately equal to the focal length (similar order of magnitude compared to working distance), as discussed in Appendix-1.

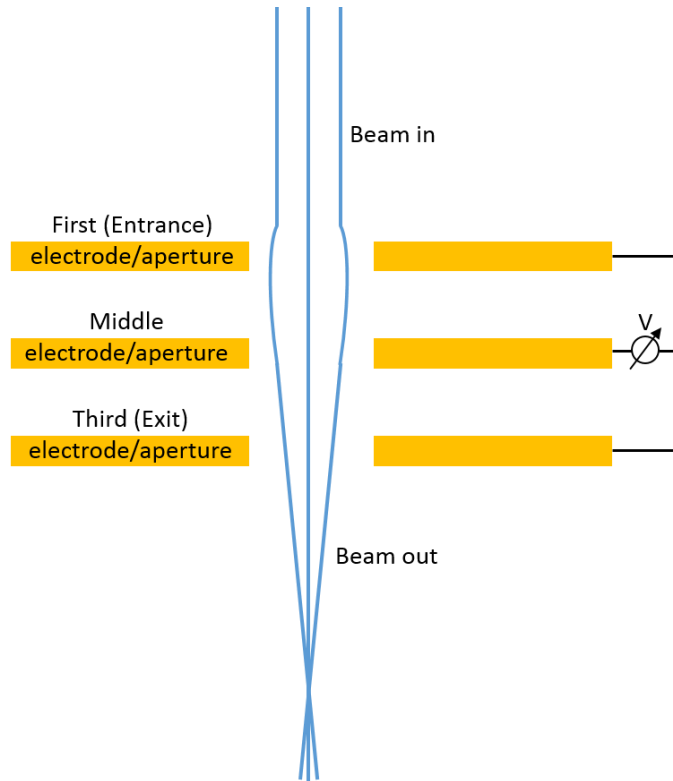


Figure. 5- 2 Schematic of three-aperture Einzel lens. It consists of three apertures with first (entrance) and third (exit) apertures at same electric potential. The potential of the middle aperture is used to adjust the focus of the beam.

Miniaturization of the lens will help to obtain smaller chromatic aberration for low energy ion beams. When an Einzel lens is scaled down to microscopic dimension by a

scaling factor ($k < 1$), a reduction of aberrations can be achieved [17]. Table. 5-1 illustrates the scaling down effect to the Einzel lens with constant field and constant potential. The constant potential mode maintains the same potential as a macroscopic lens configuration at the same beam energy which reduces both chromatic aberration and spherical aberration by the scaling factor k . Since the potential is not scaled down, the field will increase which may cause breakdown between apertures.

Table. 5- 1 Scaling down of lens for constant field and constant potential modes ($k < 1$).

	Constant field	Constant potential
Lengths	k	k
Potential	k	1
Field	1	$1/k$
Chromatic aberration	1	k
Spherical aberration	k	k

Realizing a scaled down Einzel lens, utilizing MEMS technique is chosen to be part of a low energy proton microscope, as shown in Figure. 5-3.

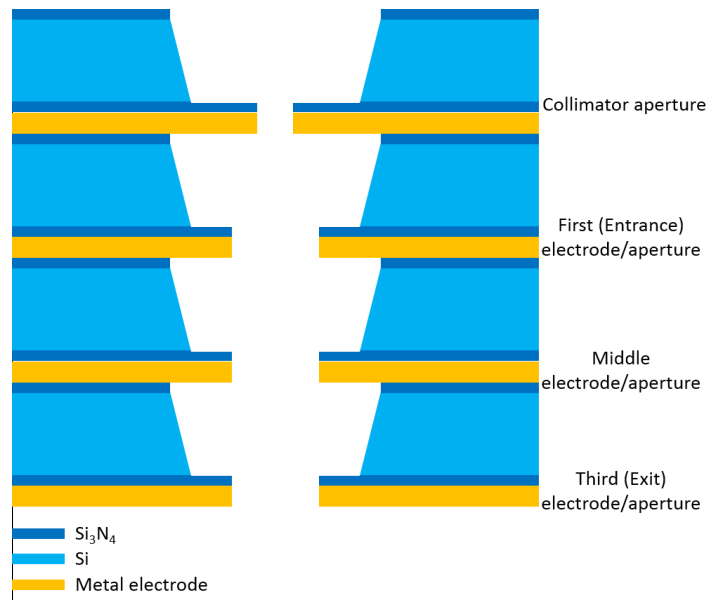


Figure. 5- 3 Illustration of miniaturized Einzel lens, consisting of a collimator aperture (top aperture) and three-aperture focus lens.

An Einzel lens has two different modes of operation. For deceleration-acceleration mode, a high focus power (short focal length) is reachable with the lower electric field as compared with an acceleration-deceleration mode where a higher field is required. The high focusing power is due to the longer interaction time of the beam during beam deceleration. On the other hand, acceleration-deceleration mode has the following advantages. The spherical and chromatic aberrations are smaller compared to deceleration-acceleration mode. Because the beam travels closer to the optical axis, and faster through the Einzel lens, where smaller third order aberration effect contributes to spherical aberration (see Appendix-1) and less influenced by chromatic aberration.

For the miniaturized Einzel lens, the beam envelope is comparable to the aperture size in contrast to a macroscopic Einzel lens. Constant values for chromatic and spherical aberration coefficients cannot be maintained while operational conditions are being changed (e.g. electric potential of middle aperture and collimator aperture size), even for a fixed geometry of the Einzel lens. The final focused probe size, for a low energy proton microscope, is mainly limited by the demagnified virtual source size at imaging plane, chromatic aberration and spherical aberration. SIMION® 8.1 [18] is capable of simulating the performance of a low energy proton microscope equipped with NAIS and miniaturized Einzel lens. Simulations will primarily be used to calculate the electric fields and the trajectories of charged particles in those fields, including contributions to probe size from virtual source size, chromatic aberration, and spherical aberration.

A NAIS with $10^6 \text{ A}/(\text{m}^2\text{srV})$ reduced brightness, 500 pA current, 1 eV energy spread, and 60 nm virtual source size is adopted for this evaluation. Protons are generated by electron-gas collisions, in NAIS, and extracted with a tunable extraction voltage. The miniaturized Einzel lens is positioned 5 mm downstream. The thickness of electrodes is 2 μm , and are separated from each other by a distance of 0.53 mm (silicon with

double-side coated silicon nitride). The imaging plane is fixed 1 mm away from the exit of the Einzel lens. The first and third electrodes are grounded. The middle electrode is varied to focus the beam. For this low energy proton microscopy, proton beam energy is set as 100 eV and 1 keV to evaluate the performance through varying the size of the three-apertures for different probe beam current in both deceleration-acceleration mode and acceleration-deceleration mode. Since the threshold of the silicon breakdown field is $\sim 3 \times 10^7$ V/m [19], the electric field between different electrodes is limited to 2×10^7 V/m. For both 100 eV and 1 keV protons, the electric field is less than 10^7 V/m when the lens is operated to focus the beam.

Figure. 5-4 and Figure. 5-5 show proton probe size as a function of probe current for different three-aperture sizes for acceleration-declaration and deceleration-acceleration modes with 100 eV and 1 keV protons, respectively. The deceleration-acceleration mode has a larger spot size because the beam travels slower and off-centered from the optical axis, resulting in larger chromatic and spherical aberrations. This miniaturized Einzel has the ability to focus \sim pA proton beam down to \sim 30 nm with three-aperture sizes in between 200 μ m and 500 μ m. For such low energy (100 eV) protons, chromatic aberration dominates the focused probe size. The three-aperture size has a dramatic effect on spherical aberration, but contributing less to probe size. However, the large three-aperture allows more proton beam to pass through the miniaturized Einzel lens. From a practical standpoint, large three-aperture size is more ideal due to the high tolerance in fabrication and can yield large probe beam current. For 1 keV proton, as the beam current increasing, small probe size still can be achieved with large three-aperture. With a three-aperture size of 200 μ m, 10 nm probe size can be obtained. In this energy range, spherical aberration starts to affect the probe size. Therefore, three-aperture size should be considered more seriously. 200 μ m three-aperture is a preferred, which can be used both for 100 eV and 1 keV protons.

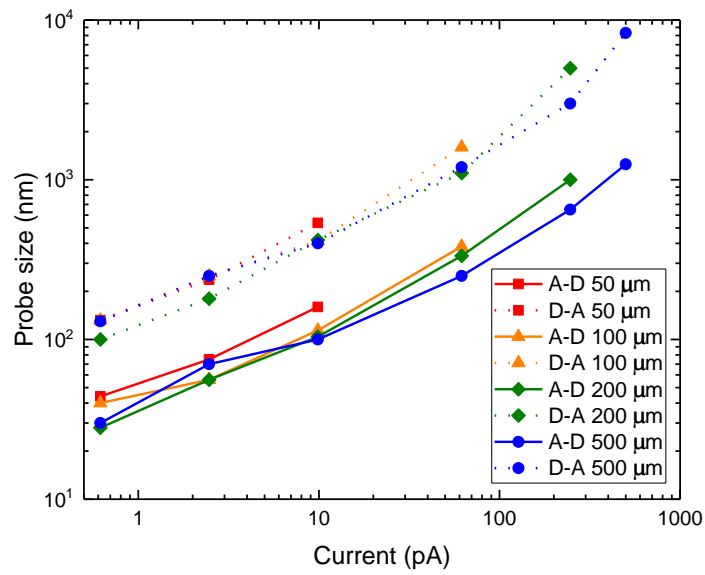


Figure. 5- 4 Proton probe size as function of probe current for different three-aperture sizes for acceleration-declaration (A-D) and deceleration-acceleration (D-A) modes with 100 eV protons.

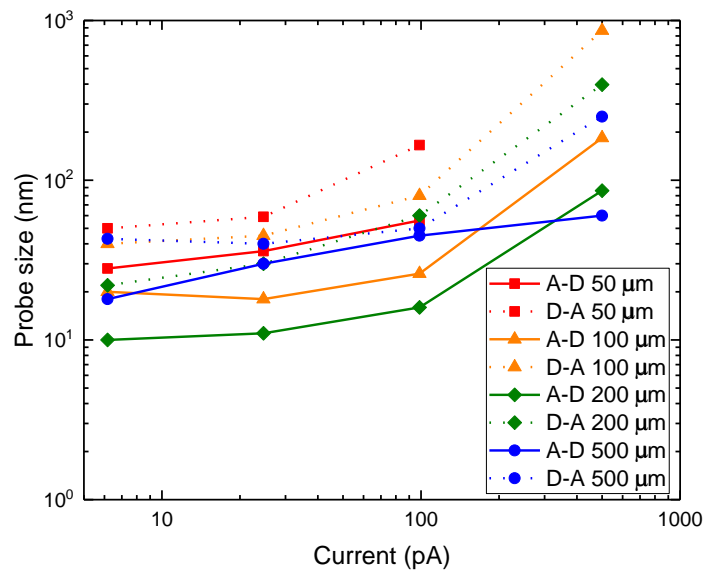


Figure. 5- 5 Proton probe size as function of probe current for different three-aperture sizes for acceleration-declaration (A-D) and deceleration-acceleration (D-A) modes with 1 keV protons.

5.2 Design of c-PBW system

5.2.1 Introduction

The objective of the proposed c-PBW system is to fabricate sub-10 nm structures in 200 nm thick photoresists. For finer patterns, the response of photoresists is very important and hence the choice of resists becomes critical. Pattern dimensions are determined by the response of photoresist, the beam lateral spread, the beam spot size, and the energy transferred to secondary electrons. Protons with an energy range of a few 10s keV – 100s keV will transfer very low energy to secondary electrons (< 10 eV) [14], [20]–[22], which is just enough to alter the chemical property of photoresists [23], [24], resulting in negligible proximity effects. The energy deposited to photoresists by secondary electrons will induce chemical chain-scission/ cross-linking, and eventually forms the desired pattern.

Photoresists play a vital role in forming ultimate resolution transferred from the focused beam. Photoresists are generally polymeric materials which can be formed on the surface of the substrate to pattern structures by exposing to the photon, X-ray or charged particles [25]. Both organic and inorganic polymers are well-established for high resolution applications. To achieve high resolution, especially for sub- 10 nm, low sensitivity and high contrast photoresists are more suitable [25], [26]. Back/forward-scattered electrons will broaden the energy deposition to a volume larger than the exposed feature size. For a low sensitive photoresist, the influence of broadened energy deposition is less pronounced, however, such photoresists require high doses for complete exposure. For protons, due to the low transferred energy to secondary electrons as compared with EBL process, a higher contrast of photoresists at high resolution can be expected.

Positive tones of polymethyl methacrylate (PMMA), SML and ZEP 520A, and negative tone of hydrogen silsesquioxane (HSQ) are the most commonly used photoresists for high resolution. PMMA, SML, ZEP 520 and HSQ have demonstrated with sub-10 nm structuring capability. 4-5 nm structures were successfully patterned in PMMA by EBL [27], [28]. Unprecedented resolution of isolated 1.7 nm feature size has been produced in PMMA through aberration-corrected EBL with 200 keV energy [29]. 2-3 nm wide isolated features were written in HSQ through EBL [30]. 8.6 nm and 7 nm linewidths were achieved in SML and ZEP 520A through EBL [31]. For helium ion beam (HIM) lithography, 6 nm dots were successfully fabricated in HSQ [32]. Non-conventional resist like fullerene molecular resist with 7.3 nm line widths has also been achieved using HIM [33]. All these structures show that the property of photoresists is not a limitation for charged particles to create sub-10 nm feature sizes.

Protons are more suitable for fabricating nanostructures in thicker resists. The lateral spread radii of a proton beam for different beam energies within PMMA were simulated using Monte Carlo simulation program SRIM [16], and are shown in Figure. 5-6. Plots in Figure. 5-6 were obtained by accounting for 90% of the total incoming protons. As seen from Figure. 5-6, for 100 keV protons, the beam spot size is broadened to 10 nm after passing through 200 nm of PMMA. However, the lateral beam diameter broadening within 200 nm of PMMA is 5 nm for 200 keV protons and 2 nm for 500 keV protons. Taking secondary electrons into account, for 500 keV protons, 90% of energy deposited due to secondary electrons are within 1 nm radial distance from the original proton track [1]. Furthermore, for lower energy protons, secondary electrons will travel even shorter distance due to the reduced energy transferred from protons. Therefore, from a system design perspective, 200 keV protons with a sub-5 nm beam spot size are well suited to fabricate sub-10 nm structures in 200 nm thick PMMA. For thinner PMMA, beam lateral spread and secondary electrons play a less crucial role in beam broadening, and hence the pattern dimensions are dictated by the beam spot size.

Therefore, for the c-PBW, a sub-10 nm beam spot size is sufficient to meet the objective of achieving sub-10 nm structures in 200 nm thick photoresists.

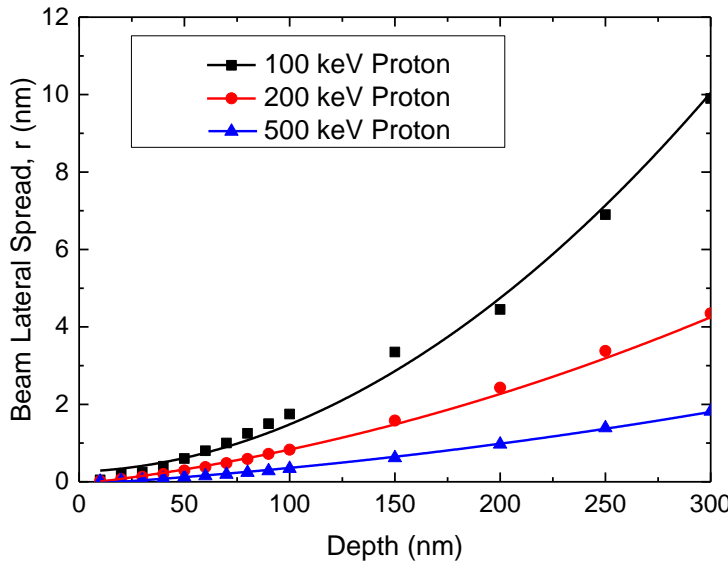


Figure. 5- 6 Proton beam lateral spread radii in PMMA for 100 keV, 200 keV and 500 keV, calculated from SRIM. These plots were obtained by accounting for 90 % of the total incoming protons.

Although a sub-10 nm spot size in one direction has been achieved with the current PBW system [34], the primary limitation of this system is its low reduced brightness resulting in a slow writing speed. This restricts the sub-10 nm focusing capability and also ends up having a low beam current (~ 0.01 fA) resulting in a low throughput [34]. For EBL, the typical beam current at the image plane is around tens of pA [35], which is 6 orders of magnitude higher than the current PBW system. But the typical dose required for protons in PMMA is $80\text{-}150$ nC/mm 2 [36], [37], which is 100 times lower than in EBL [38]. For sub-10 nm feature size, statistical dose fluctuations, so-called shot-noise, will cause variations in exposure dose. This effect is more significant for ion beam exposure because of highly localized stopping distance [32]. Thus in order to make the proposed c-PBW comparable to the EBL in its performance, a high brightness ion source is required that can deliver \sim pA beam current at the image plane.

5.2.2 Layout of the c-PBW system

Here we propose a c-PBW system that will employ a promising high brightness NAIS for sub-10 nm lithography. As discussed in Chapter 2 and 3, a NAIS with $10^6 \text{ A}/(\text{m}^2\text{srV})$ reduced brightness, 500 pA current, and 60 nm virtual source size is adopted to evaluate the c-PBW system performance. The layout of the proposed c-PBW system is shown in Figure. 5-7. Protons are generated by electron-gas collisions, in NAIS, and extracted with a tunable extraction voltage in the range of -5 kV to -10 kV. Subsequently, a condenser lens is used to shape the beam. The converged beam is then passed through an acceleration column, where it gains a final energy of 200 keV. A collimator aperture is used to prevent further transmission of high angular scattered ions, while mostly allowing less divergent ions to enter into the focusing lenses. An electrostatic scanner is used, before the focusing lens system, to scan the beam after it is collimated. Three or four electromagnetic quadrupole lenses are employed to focus the beam into the end-station with sub-10 nm resolution. Considering a 200 nm inaccuracy in sample positioning (at image plane), with a preset upper limit of the beam half angle α to 2.5 mrad, will ensure that the beam broadening is not more than 1 nm. The reduced brightness is given as [39]

$$B_r = \frac{I_P}{A_0 \Omega V} \approx \frac{I_P}{\frac{\pi}{4} d_P^2 \pi \alpha^2 V} \quad (5.57)$$

where I_P (1 pA) is the proton beam current, A_0 is the beam area, d_P (< 10 nm) is the beam diameter at the focal plane, Ω is the solid angle, α (< 2.5 mrad) is the beam half-angle divergence, and V (200 kV) is electric potential related to beam energy. In order to achieve fast writing speed using the c-PBW system, with the limitation explained above, we require an ion source with a reduced brightness of more than $3 \times 10^3 \text{ A}/(\text{m}^2\text{srV})$, which NAIS can deliver.

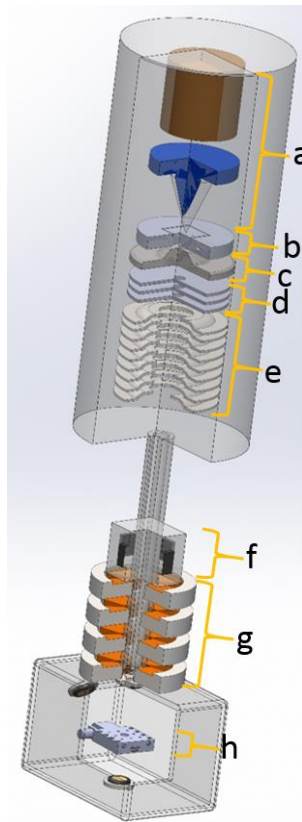


Figure. 5- 7 Schematic of a proposed c-PBW system for sub-10 nm lithography with 200 kV terminal voltage, integrated with a NAIS. (a) Electron injector, (b) NAIS, (c) Extractor, (d) Condenser lens, (e) Acceleration tube, (f) Electrostatic scanner, (g) Focusing lenses, (h) Sample stage.

Apart from the need for a high source reduced brightness, different lens configurations play a critical role in determining the capability to reach sub-10 nm proton beam resolution. Particle Beam Optics Laboratory 3.0 (PBO Lab) [40] is used to study the focusing capability of different lens configurations. The two commonly used lens configurations are the low excitation Russian quadruplet [41] and the spaced Oxford triplet [42] configurations, shown in Figure. 5-8. The Russian quadruplet configuration has the same demagnification in both X and Y, while the spaced Oxford triplet configuration has different demagnifications in X and Y. Four electromagnetic lenses make up the Russian quadruplet configuration, where the separation between all lenses is fixed at 25 mm. For the spaced Oxford triplet configuration, three electromagnetic lenses were used with a fixed separation of 25 mm between lens 2 and 3. The distance

between lens 1 and 2 is 105 mm. These two lens configurations can be installed in the same beamline due to the similar physical layouts. In the c-PBW system, protons are extracted and accelerated to 200 keV to reach the object plane. In our simulations, we have considered the object beam size (d_v) to be the same as virtual source size for simplicity. The distance between object plane and focusing lens 1, L_1 , is set to be 2 m for this c-PBW system. The working distance L_2 is fixed at 30 mm for both lens configurations. A 200 keV proton beam is considered to have 2.5 eV beam energy spread, caused by the combined effect of the NAIS source energy spread (< 1 eV) and < 10 ppm acceleration power instability (< 2 V for 200 kV). The instability of the magnetic field from the focus lens is 1 ppm.

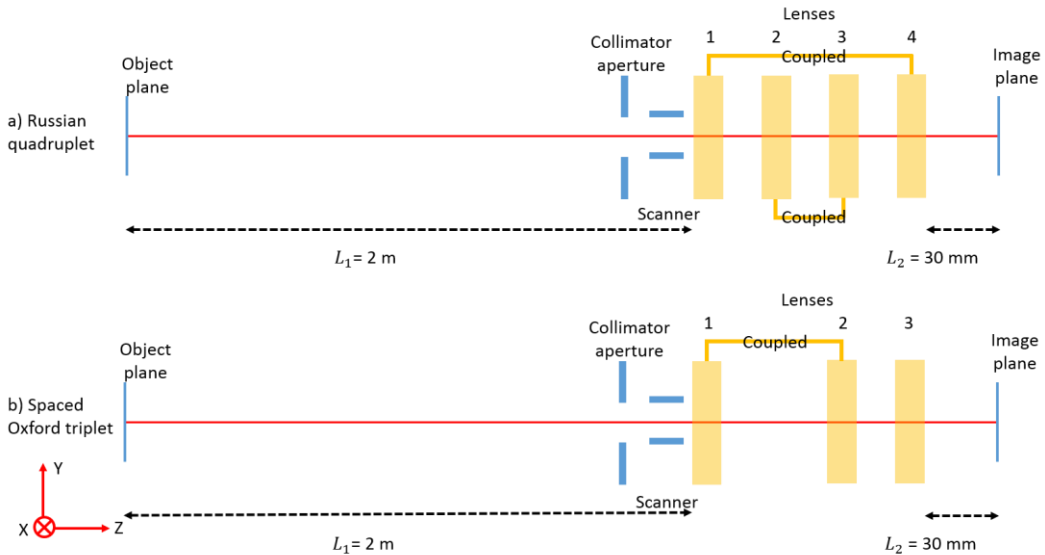


Figure. 5- 8 Layout of focusing lens configurations. (a) Russian quadruplet configuration with 4 lenses and (b) Spaced Oxford triplet configuration with 3 lenses.

5.2.3 Evaluation of c-PBW system

A systematic approximation by root-power-sum algorithm for full width 50% (FW50, the width including 50% of beam current, which is commonly used to define EBL spot size) proton beam diameter d_p at image plane is described as [43]

$$d_p = \{[d_I^{1.3} + (d_A^4 + d_C^4)^{1.3/4}]^{2/1.3} + d_s^2\}^{1/2} \quad (5.58)$$

Where d_I is the demagnified virtual source size, and is given by

$$d_I = \frac{d_v}{Dem} = \frac{2}{\pi} \sqrt{\frac{I_p}{B_r V}} \frac{1}{\alpha} \quad (5.59)$$

(where d_v is the proton virtual source diameter, Dem is the demagnification of the focusing lens) d_A , d_S , and d_C are the contributions from diffraction aberration, spherical aberration, and chromatic aberration, respectively. The contribution from spherical, chromatic, and diffraction aberrations are

$$d_S = 0.18 C_S \alpha_e^3 \quad (5.60)$$

$$d_C = 0.6 C_C \frac{\delta U}{V} \alpha_e \quad (5.61)$$

$$d_A = 0.54 \frac{\lambda}{\alpha} \quad (5.62)$$

α_e is the proton beam half angle before entering the focusing lens, C_S and C_C are the spherical and chromatic aberrations, δU is the beam energy spread, and λ is the de Broglie wavelength (~ 64 fm) of 200 keV proton.

PBO Lab calculates the lens demagnification (Dem), chromatic (C_C), and spherical (C_S) aberrations. These parameters are expressed in two orthogonal directions (X and Y directions) for this astigmatic lens system. The characteristic values obtained from PBO Lab for Russian quadruplet configuration and Oxford triplet are summarized in Table. 5-2. Russian quadruplet configuration has same demagnification in both X and Y directions, resulting in a symmetric focus ability. While Oxford triplet has different demagnifications in X and Y direction with a very large demagnification in one direction which can focus beam to extremely small size. However, both chromatic and spherical aberrations are significant for Oxford triplet configuration. Therefore, Oxford triplet configuration is more suitable to operate with low beam current to achieve small beam size where both aberrations are not dominant.

Table. 5- 2 Parameters obtained from PBO Lab with the Russian quadruplet and Oxford triplet configurations.

		Russian quadruplet	Spaced Oxford triplet
Proton beam energy (keV)		200	200
Object plane to lens distance (m)		2	2
Demagnification, <i>D_{em}</i>	$1/\langle x x \rangle$	-10.5	125.6
	$1/\langle y y \rangle$	-10.5	-22.0
Chromatic aberration, <i>C_C (μm/mrad)</i>	$\langle x x'l' \rangle$	2872.5	-8819.0
	$\langle y y'l' \rangle$	5765.6	27055.0
Spherical aberration, <i>C_S (μm/mrad³)</i>	$\langle x x'^3 \rangle$	-1.414	8.107
	$\langle x x'y'^2 \rangle$	-8.801	5.777
	$\langle y y'^3 \rangle$	-8.689	-230.434
	$\langle y x'^2y' \rangle$	-8.801	-329.484

The final probe beam widths and divergences at the image plane are examined according to different beam currents, as shown in Figure. 5-9 a), b), c), and d). From Figure. 5-9 a), we can see that the beam spot size remains sub-10 nm up to 20 pA for Russian quadruplet lens configuration. The beam width only increases dramatically for high proton beam current (>20 pA), because chromatic and spherical aberrations are relatively small for this lens configuration, as shown in Table. 5-2. The different beam currents are obtained by changing the collimator aperture, resulting in the change of beam half angle α . From Figure. 5-9 b), it is clear that in order not to exceed the preset upper limit of beam half angle α (2.5 mrad), the beam current of 20 pA for the Russian quadruplet lens configuration can meet this requirement.

Spaced Oxford triplet configuration has different demagnification in X and Y directions, the beam spot size remains sub-10 nm in both directions with beam current up to 2.4 pA. However, from Figure. 5-9 d), the beam half angle in X direction α_x exceeds the upper limit (2.5 mrad). Whereas due to the high demagnification in X

direction, the upper limit of α_x can be increased whereby it can still maintain a sub-10 nm focus in X direction, see Figure. 5-9 c). For beam current less than 0.2 pA, a sub-1 nm in X direction is achievable.

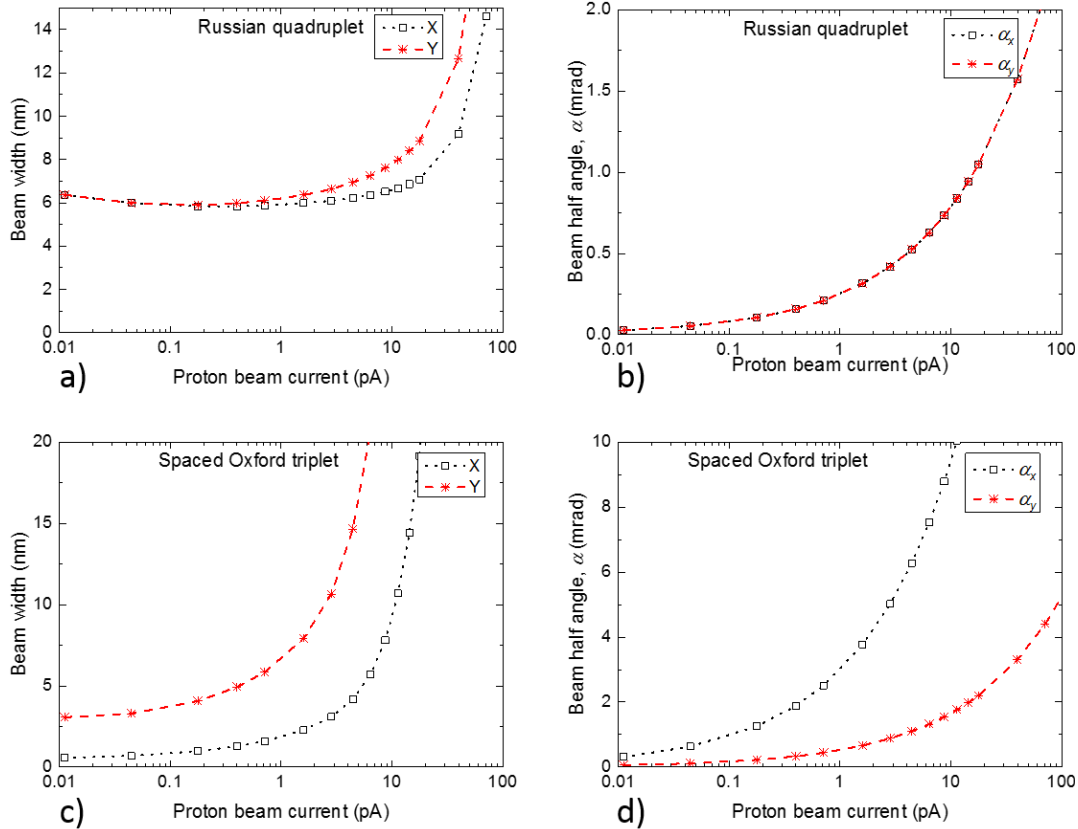


Figure. 5-9 Proton beam FW50 widths in X and Y directions for (a) proton beam widths in X and Y directions with the variation of beam current and (b) proton beam divergence α with the variation of beam current, for Russian quadruplet lens configuration, (c) proton beam widths in X and Y directions with the variation of beam current and (d) proton beam divergence α with the variation of beam current, for spaced Oxford triplet lens configuration.

To exam the achievable smallest beam size with > 0.2 pA proton beam current, smallest beam width as a function of overall system energy spread is shown in Figure. 5-10. For Russian quadruplet lens configuration, energy spread doesn't have a significant influence on beam size due to the low chromatic aberration in both X and Y directions. The achievable smallest proton beam size is less than 10 nm even with an energy spread of 20 eV. However, for spaced Oxford triplet configuration, chromatic aberration in Y

direction is relatively large, resulting in a large beam width at Y direction for high energy spread. Therefore, energy spread is more critical for Spaced Oxford triplet lens configuration to achieve small beam size.

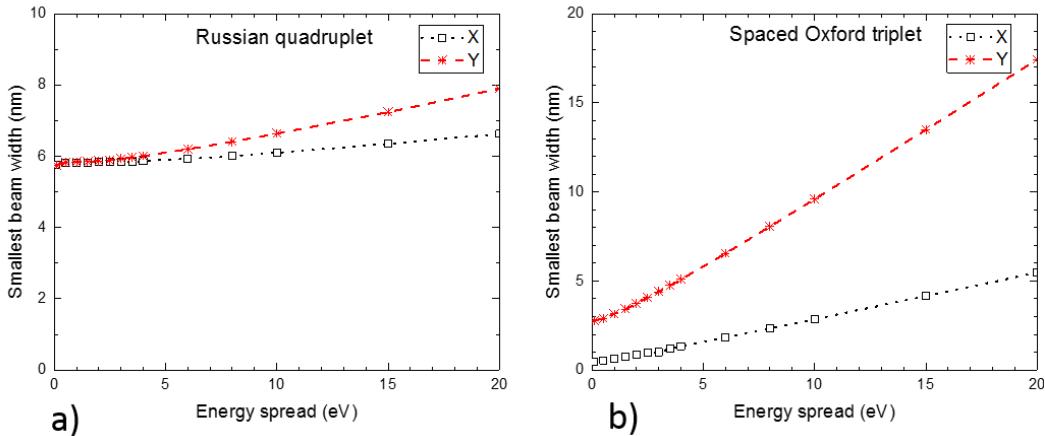


Figure. 5- 10 Achievable smallest proton beam FW50 widths in X and Y directions as a function of overall system energy spread with > 0.2 pA beam current for (a) Russian quadruplet lens configuration, and (b) spaced Oxford triplet lens configuration.

In lithography, the possibility of having a large scan size (~ 10 's μm) in the image plane is desirable. The current PBW in CIBA employs an electrostatic scanning system with X and Y scanning plates [44]. The off-axis aberration caused by spherical aberration can deteriorate the final beam quality, and enlarge the beam size. In the PBO simulation, a scanner is located 20 mm upstream from the first lens for both lens configurations. In this case, energy spread is 2.5 eV. As shown in Figure. 5-11, the Russian quadruplet lens configuration can achieve sub-10 nm beam size with a $500 \times 500 \mu\text{m}^2$ scan size, while the spaced Oxford triplet lens configuration can only have a $20 \times 20 \mu\text{m}^2$ scan size, which is limited by the larger off-axis aberration (all simulations were performed with 0.4 pA).

Table. 5-3 summarizes the performance of these two lens configurations for the c-PBW system, compared with the current PBW and EBL. It shows a promising high-throughput for the c-PBW system in the sub-10 nm regime that is faster than in EBL.

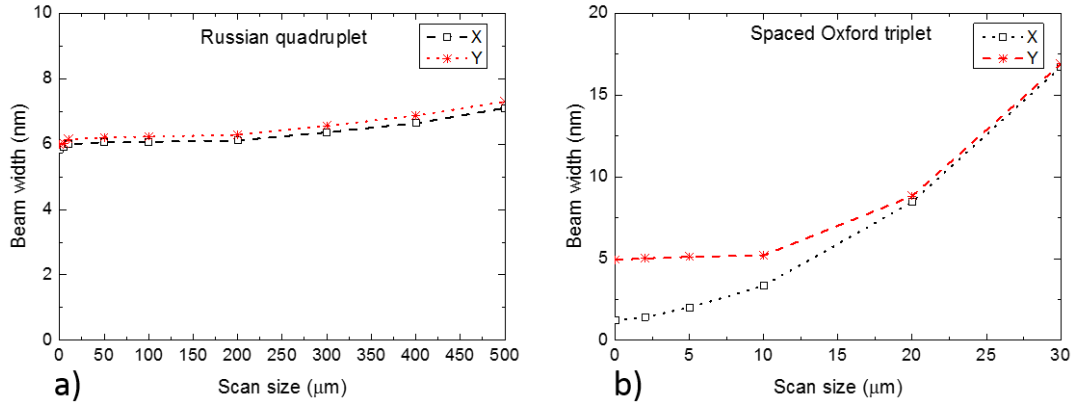


Figure. 5-11 Proton beam widths in X and Y directions as a function of scan size, (a) Russian quadruplet lens configuration, (b) Spaced Oxford triplet lens configuration.

Table. 5-3 Summary of 200 kV c-PBW with different lens configurations, to write a $10 \mu\text{m} \times 10 \mu\text{m}$ square on PMMA, comparing with current PBW and EBL. (Required doses for proton and electron are $10 \mu\text{C}/\text{cm}^2$ [37] and $1000 \mu\text{C}/\text{cm}^2$ [38], respectively).

Lithographic probe	c-PBW		Current PBW [34]	EBL [35]
	Russian quadruplet	Spaced Oxford triplet		
Beam virtual source diameter (nm)	60	60	$\sim 2 \text{ mm}$	
Extracted beam current (pA)	500	500	$\sim \mu\text{A}$	
Beam energy (keV)	200	200	2000	$\sim 10's$
Beam size at image plane (nm^2)	7.4×9.4	2.9×9.7	9.3×32	5×5
Beam current at image plane (pA)	20	2.4	0.013	20
Beam half angle at image plane (mrad)	1×1	4.6×0.8	1.7×0.3	
Beam reduced brightness ($\text{A}/(\text{m}^2\text{srV})$)	$\sim 1 \times 10^6$	$\sim 1 \times 10^6$	~ 10	$\sim 1 \times 10^7$
Writing time (second)	0.5	4	~ 800	50

5.3 Summary

Equipping with NAIS, a low energy proton microscope was proposed for surface-sensitive and composition-sensitive analysis. This microscope is proposed to employ a miniaturized Einzel lens to reduce the chromatic aberration in low energy range. The miniaturized Einzel lens can be fabricated using MEMS technique, as a similar process as NAIS. The performance of this miniaturized Einzel lens was simulated, and shown to achieve 30 and 10 nm beam spot size for 100 eV to 1 keV protons, respectively.

The schematic of developing a compact sub-10 nm level PBW system has been briefly discussed. The c-PBW is designed for 200 kV, which is capable of patterning sub-10 nm structures in 200 nm thick PMMA. For obtaining fast writing speed comparable to EBL, a NAIS is employed in this c-PBW system. The NAIS has the potential to deliver protons with $> 10^6 \text{ A}/(\text{m}^2\text{srV})$ brightness, which is 5 orders of magnitude larger than current PBW system and can dramatically increase the throughput. With this ideal NAIS, Russian quadruplet and spaced Oxford triplet lens configurations are capable of focusing the beam down to a sub-10 nm spot size, with fast writing speeds. The Russian quadruplet lens configuration has the ability to deliver 15 pA probe current with $7.0 \times 8.5 \text{ nm}^2$ spot size, whereas spaced Oxford triplet can deliver 2.4 pA with $2.9 \times 9.7 \text{ nm}^2$ spot size. Spaced Oxford triplet configuration is capable of achieving sub-1 nm beam spot size at one direction with less than 0.2 pA beam current. Both configurations can match the writing speed to that of an EBL system, with sub-10 nm beam spot size. Calculation shows that a sub-10 nm focused beam can be scanned over an area of $500 \times 500 \mu\text{m}^2$ with the Russian quadruplet lens configuration and $20 \times 20 \mu\text{m}^2$ with the spaced Oxford triplet lens configuration. The typical beam scan size for EBL is a few 10's μm^2 [45], [46]. Both lens configurations for the c-PBW system can provide comparative scan area as in EBL at high resolution writing mode. For writing a large area, a high-precision stage can be employed in stitching mode. While these design

considerations of a c-PBW system are a conservative estimate, they already suggest a competitive writing speed coupled with minimal proximity effects.

References

- [1] C. Udalagama, A. A. Bettoli, and F. Watt, "Stochastic spatial energy deposition profiles for MeV protons and keV electrons," *Phys. Rev. B*, vol. 80, no. 22, p. 224107, 2009.
- [2] J. Orloff, M. Utlaut, and L. Swanson, *High Resolution Focused Ion Beams: FIB and Its Applications : The Physics of Liquid Metal Ion Sources and Ion Optics and Their Application to Focused Ion Beam Technology*. Springer Science & Business Media, 2003.
- [3] B. W. Ward, J. A. Notte, and N. P. Economou, "Helium ion microscope: A new tool for nanoscale microscopy and metrology," *J. Vac. Sci. Technol. B Microelectron. Nanom. Struct.*, vol. 24, no. 6, p. 2871, 2006.
- [4] H. H. Brongersma, "Low- Energy Ion Scattering," *Charact. Mater.*, 2012.
- [5] H. Niehus, W. Heiland, and E. Taglauer, "Low-energy ion scattering at surfaces," *Surf. Sci. Rep.*, vol. 17, no. 4–5, pp. 213–303, 1993.
- [6] H. H. Brongersma, M. Draxler, M. De Ridder, and P. Bauer, "Surface composition analysis by low-energy ion scattering," *Surf. Sci. Rep.*, vol. 62, no. 3, pp. 63–109, 2007.
- [7] I. B. M. Journal, "Low-energy electron microscopy," 2000.
- [8] E. Bauer, "Low energy electron microscopy," vol. 57, no. December 1993, pp. 895–938, 1994.
- [9] H. Niehus, W. Heiland, and E. Taglauer, "Low-energy ion scattering at surfaces," *Surf. Sci. Rep.*, vol. 17, no. 4–5, pp. 213–303, 1993.
- [10] R. M. Tromp, J. B. Hannon, W. Wan, A. Berghaus, and O. Schaff, "A new aberration-corrected, energy-filtered LEEM/PEEM instrument II. Operation and results," *Ultramicroscopy*, vol. 127, pp. 25–39, 2013.
- [11] R. M. Tromp, J. B. Hannon, A. W. Ellis, W. Wan, A. Berghaus, and O. Schaff, "A new aberration-corrected, energy-filtered LEEM/PEEM instrument. I. Principles and design," *Ultramicroscopy*, vol. 110, no. 7, pp. 852–861, 2010.
- [12] B. Knuffman, A. V Steele, J. Orloff, and J. J. McClelland, "Nanoscale focused ion beam from laser-cooled lithium atoms," *New J. Phys.*, vol. 13, no. 10, p. 103035, 2011.
- [13] K. A. Twedt, L. Chen, and J. J. McClelland, "Scanning ion microscopy with low energy lithium ions," *Ultramicroscopy*, vol. 142, pp. 24–31, 2014.
- [14] R. Ramachandra, B. Griffin, and D. Joy, "A model of secondary electron imaging in the helium ion scanning microscope," *Ultramicroscopy*, vol. 109, no. 6, pp. 748–757, 2009.
- [15] W.-K. Chu, *Backscattering spectrometry*. Elsevier, 2012.
- [16] J. F. Ziegler and J. P. Biersack, "The stopping and range of ions in matter," in *Treatise on Heavy-Ion Science*, Springer, 1985, pp. 93–129.
- [17] T. H. P. Chang, D. P. Kern, and L. P. Muray, "Microminiaturization of electron optical systems," *J. Vac. Sci. Technol. B*, vol. 8, no. 6, pp. 1698–1705, 1990.
- [18] I. (SIS) Scientific Instrument Services, "SIMION® Version 8.1." [Online]. Available: <http://simion.com/>.
- [19] V. Siklitsky, "New semiconductor materials. characteristics and properties," *OnlineJ. Available http://www. ioffe. rssi. ru/SVA/NSM*, 2001.
- [20] Y. V Petrov, O. F. Vyvenko, and A. S. Bondarenko, "Scanning helium ion microscope: distribution of secondary electrons and ion channeling," *J. Surf. Investig. X-ray, Synchrotron Neutron Tech.*, vol. 4, no. 5, pp. 792–795, 2010.
- [21] K. Ohya, T. Yamanaka, K. Inai, and T. Ishitani, "Comparison of secondary electron emission in helium ion microscope with gallium ion and electron microscopes," *Nucl. Instruments Methods Phys. Res. Sect. B Beam Interact. with*

- Mater. Atoms*, vol. 267, no. 4, pp. 584–589, 2009.
- [22] Y. Petrov and O. Vyvenko, “Secondary electron emission spectra and energy selective imaging in helium ion microscope,” 2011, vol. 8036, p. 80360O–80360O–10.
- [23] M. N. Heddili, P. Cloutier, A. D. Bass, T. E. Madey, and L. Sanche, “Electron stimulated desorption of anionic fragments from films of pure and electron-irradiated thiophene,” *J. Chem. Phys.*, vol. 125, no. 9, p. 94704, 2006.
- [24] D. P. Shoemaker, C. W. Garland, and J. I. Steinfeld, *Experiments in physical chemistry*. McGraw-Hill New York, 1962.
- [25] A. S. Gangnaik, Y. M. Georgiev, and J. D. Holmes, “New Generation Electron Beam Resists: A Review,” 2017.
- [26] C. Zheng, “Nanofabrication: principles, capabilities and limits,” *Springer, Ger.*, 2008.
- [27] W. W. Hu, K. Sarveswaran, M. Lieberman, and G. H. Bernstein, “Sub-10 nm electron beam lithography using cold development of poly (methylmethacrylate),” *J. Vac. Sci. Technol. B*, vol. 22, no. 4, pp. 1711–1716, 2004.
- [28] S. Yasin, D. G. Hasko, and H. Ahmed, “Fabrication of <5 nm width lines in poly(methylmethacrylate) resist using a water:isopropyl alcohol developer and ultrasonically-assisted development,” *Appl. Phys. Lett.*, vol. 78, no. 18, pp. 2760–2762, 2001.
- [29] V. R. Manfrinato *et al.*, “Aberration-Corrected Electron Beam Lithography at the One Nanometer Length Scale,” *Nano Lett.*, p. acs.nanolett.7b00514, 2017.
- [30] V. R. Manfrinato *et al.*, “Resolution limits of electron-beam lithography toward the atomic scale,” *Nano Lett.*, vol. 13, no. 4, 2013.
- [31] A. Gangnaik, Y. M. Georgiev, B. McCarthy, N. Petkov, V. Djara, and J. D. Holmes, “Characterisation of a novel electron beam lithography resist, SML and its comparison to PMMA and ZEP resists,” *Microelectron. Eng.*, vol. 123, pp. 126–130, 2014.
- [32] V. Sidorkin, E. van Veldhoven, E. van der Drift, P. Alkemade, H. Salemink, and D. Maas, “Sub-10-nm nanolithography with a scanning helium beam,” *J. Vac. Sci. Technol. B Microelectron. Nanom. Struct.*, vol. 27, no. 2009, p. L18, 2009.
- [33] X. Shi, P. Prewett, E. Huq, D. M. Bagnall, A. P. G. Robinson, and S. A. Boden, “Helium ion beam lithography on fullerene molecular resists for sub-10 nm patterning,” *Microelectron. Eng.*, vol. 155, pp. 74–78, 2016.
- [34] Y. Yao and J. A. van Kan, “Automatic beam focusing in the 2 nd generation PBW line at sub-10nm line resolution,” *Nucl. Instruments Methods Phys. Res. Sect. B Beam Interact. with Mater. Atoms*, vol. 348, pp. 203–208, 2015.
- [35] J. Orloff, *Handbook of charged particle optics*. CRC press, 2008.
- [36] J. A. van Kan *et al.*, “New resists for proton beam writing,” *Nucl. Instruments Methods Phys. Res. Sect. B Beam Interact. with Mater. Atoms*, vol. 260, no. 1, pp. 460–463, 2007.
- [37] J. A. Van Kan, P. Malar, and Y. H. Wang, “Resist materials for proton beam writing: A review,” *Appl. Surf. Sci.*, vol. 310, pp. 100–111, 2014.
- [38] M. Yan, S. Choi, K. R. V. Subramanian, and I. Adesida, “The effects of molecular weight on the exposure characteristics of poly(methylmethacrylate) developed at low temperatures,” *J. Vac. Sci. Technol. B Microelectron. Nanom. Struct.*, vol. 26, no. 6, p. 2306, 2008.
- [39] A. V Crewe, “Optimization of small electron probes,” *Ultramicroscopy*, vol. 23, no. 2, pp. 159–167, 1987.
- [40] A. Inc., “Particle Beam Optics Laboratory 3.0 (PBO Lab).” [Online]. Available: <http://www.ghga.com/accelsoft/pbolab.html>.
- [41] F. Watt and G. W. Grime, “Principles and applications of high-energy ion

- microbeams,” 1987.
- [42] G. W. Grime and F. Watt, *Beam Optics of Quadrupole Probe-Forming Systems*. Hilger, 1984.
- [43] J. E. Barth and P. Kruit, “Addition of different contributions to the charged particle probe size,” *Optik (Stuttg.)*, vol. 101, no. 3, pp. 101–109, 1996.
- [44] J. A. Van Kan, P. Malar, and A. B. De Vera, “The second generation Singapore high resolution proton beam writing facility,” *Rev. Sci. Instrum.*, vol. 83, no. 2, p. 02B902, 2012.
- [45] C. Vieu *et al.*, “Electron beam lithography: resolution limits and applications,” *Appl. Surf. Sci.*, vol. 164, no. 1, pp. 111–117, 2000.
- [46] Centre for Advanced 2D Materials and Graphene Research Centre National University of Singapore, “Jeol JBX-6300FS Electron Beam Lithographer Specifications.” [Online]. Available: <https://graphene.nus.edu.sg/content/jeol-electron-beam-lithographer-specifications>.

Chapter 6. Conclusion

The goal of this PhD thesis was to develop a high brightness and low energy spread ion source. An electron-impact ionization based nano-aperture ion source (NAIS) is a potential candidate to be part of compact-proton beam writing (c-PBW) system, which could deliver sub-10 nm features. Theoretical and computer simulations were carried out to examine the performance of NAIS under different configurations. The calculations suggest that a high brightness proton beam can be obtained by employing 100 nm thick membranes having a 100 nm thick spacer with a 100 nm double-aperture configuration. This configuration can deliver a proton beam with a reduced brightness of $> 10^6 \text{ A}/(\text{m}^2\text{srV})$, and less than 1 eV energy spread.

Based on MEMS technique, two different types of NAIS have been successfully fabricated. The performance of these NAISs were tested using conventional SEMs as electron injectors, showing a good agreement with the simulated result, see Table. 6-1. Better mechanical alignment of NAIS chip and extractor, higher electron beam current density, determination of more appropriate virtual source size, and fine tuning of other parameters will result in yielding an enhanced reduced brightness. To further improve the performance of NAIS, a NAIS with internal electrodes was proposed to eliminate the membrane bulge, thereby reducing the energy spread, by integrating silicon supporting grids and embedded electrodes.

Table. 6- 1 Experimentally measured reduced brightness and energy spread of NAISs with metal spacer and recessed Si_3N_4 .

	NAIS with metal spacer	NAIS with recessed Si_3N_4
Reduced brightness ($\text{A}/(\text{m}^2\text{srV})$)	$8_{-1}^{+6} \times 10^2$	$0.9_{-0.1}^{+1.0} \times 10^4$
Energy spread* (eV)	~20	~23

* Energy spread ΔE is defined by $E_0 - \Delta E$

Equipped with NAIS, a low energy proton microscope with integration of miniaturized Einzel lens for low lens aberrations was examined through simulation. Such system has an ability to achieve sub-100 nm beam spot size for 100 eV to 1 keV protons. On the other hand, to realize a fast sub-10 nm direct proton beam writing (PBW) system, a 200 keV compact-PBW (c-PBW) system was discussed by employing a dedicate NAIS as proton source. Two different lens configurations were evaluated. Both configurations can satisfy fast writing and sub-10 nm resolution with a reasonable beam scan area. This c-PBW is expected to have a comparable writing speed to electron beam lithography for more than 200 nm thick photoresist with minimal proximity effects.

Appendix 1. Lens aberrations

1.1 Ideal lens optics

A lens that has the ability to focus a parallel beam to a focal point and vice versa is considered as an ideal lens. An ideal lens presumes that the beam is deflected by an angle $\Delta\alpha$ proportional (linear) to the beam distance r_o from the optical axis, but is independent of the beam passing angle α_o , as shown in Figure. A1-1, and expressed mathematically as

$$\Delta\alpha = r_o/z_o + r_i/z_i = (1/z_o + 1/z_i)r_o = a_1r_o \quad (\text{A1.63})$$

where z_o and z_i are the distances from the object to lens and lens to image, r_o and r_i are the distance from beam entrance to optical axis and beam exit to optical axis, respectively.

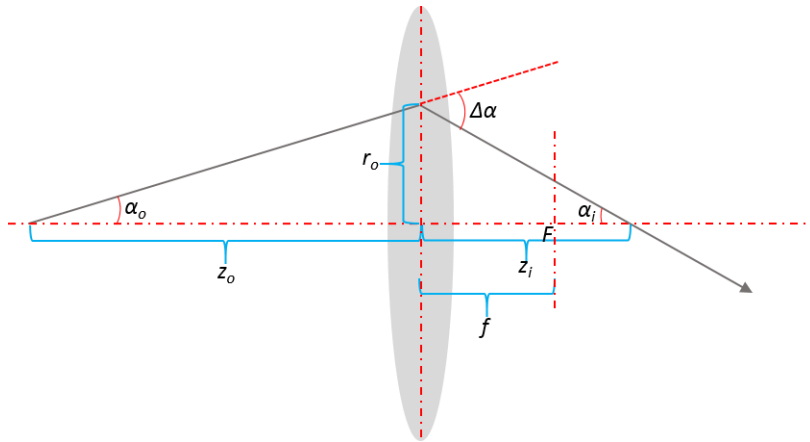


Figure. A1- 1 Ideal lens: A beam passing the lens at distance r_o from the optical axis is deflected by an angle $\Delta\alpha = a_1r_o$.

For a thin ideal lens, a Thin Lens Formula with focal length f is used to describe its focus ability as

$$\frac{1}{z_o} + \frac{1}{z_i} = \frac{1}{f} \quad (\text{A1.64})$$

As shown in Figure. A1-2, the lateral (transverse or linear) magnification M is

$$M = \frac{d_i}{d_o} = \frac{z_i}{z_o} \quad (\text{A1.65})$$

where d_o and d_i are objective and imaging sizes, respectively.

The angular magnification M_A is

$$M_A = \frac{\alpha_i}{\alpha_o} \quad (\text{A1.66})$$

The relationship between lateral magnification M and angular magnification M_A is illustrated by the Helmholtz-Lagrange law as

$$MM_A = \left(\frac{E_o}{E_i}\right)^{1/2} \quad (\text{A1.67})$$

Here E_o and E_i are the beam energy in the object and image sides respectively. For most electrostatic lenses, the beam energy on the object and image sides is the same, which implies that the lateral magnification and angular magnification are inversely proportional to each other ($M_A = 1/M$).

The longitudinal (axial) magnification M_L is expressed as

$$M_L = \frac{l_i}{l_o} = \frac{M}{M_A} = M^2 \quad (\text{A1.68})$$

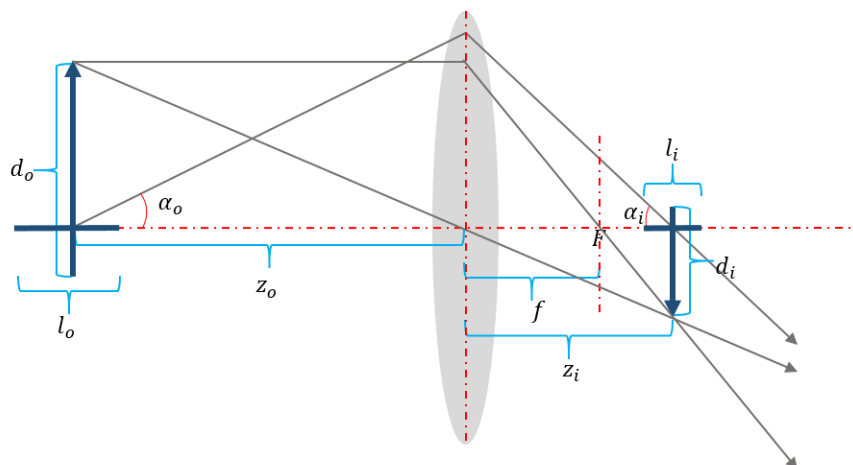


Figure. A1- 2 An image d_i of an object d_o in an ideal lens.

1.2 Chromatic aberration

A charged particle beam having different energies and originating from same point that passes through a lens will converge in a different focal point on the image side of the lens.

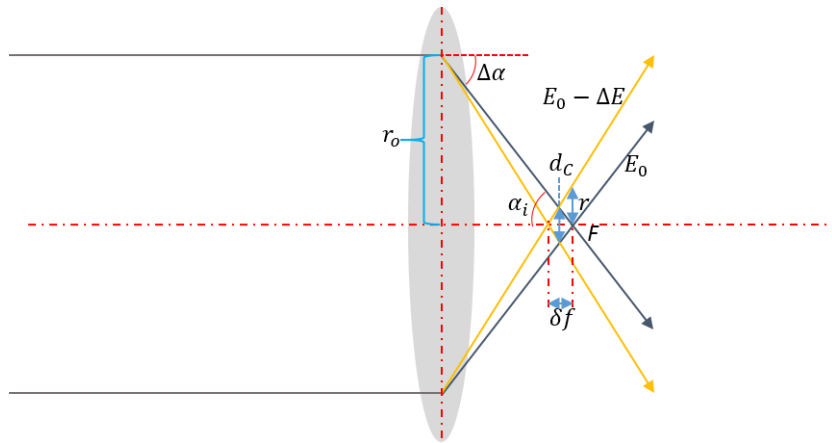


Figure. A1- 3 Chromatic aberration showing parallel beam having different energies are focused at two different points. F is the focal point for beam with energy E_0 .

The focal length for electrostatic lens is directly proportional to beam energy [1], [2]

$$\frac{\delta f}{f} \approx \frac{\Delta E}{E_0} \quad (\text{A1.69})$$

The disc radius r due to the energy spread in the image plane is

$$r = \Delta \alpha \delta f = a_1 r_o f \frac{\Delta E}{E_0} \quad (\text{A1.70})$$

The chromatic aberration $C_C(\infty)$ (∞ is the object angle) for the incident parallel beam is defined as

$$r = C_C(\infty) \alpha_i \frac{\Delta E}{E_0} \quad (\text{A1.71})$$

From Eq. A1.8 and Eq. A1.9, chromatic aberration $C_C(\infty)$ is

$$C_C(\infty) = \frac{\Delta \alpha f}{\alpha_i} = \frac{a_1 r_o f}{\alpha_i} \quad (\text{A1.72})$$

For the indecent parallel beam, $\alpha_i = \Delta\alpha = a_1 r_o$. Therefore, the chromatic aberration $C_C(\infty)$ has the same value as that of the focal length f . For a more elaborate and practical consideration, the chromatic aberration depends on the lens design, geometry, and the operating conditions. However, it is still within the same order of magnitude as the focal length [1], [3]. Generally, in a high-resolution mode the working distance (image distance) is kept small to have a lower chromatic aberration. As seen from Figure. A1-3, the plane of least confusion is located near the image plane, where $d_C \approx r$ due to the small angle and low value of $\frac{\Delta E}{E_0}$, and therefore the chromatic aberration is expressed as

$$d_C = C_C(\infty) \alpha_i \frac{\Delta E}{E_0} \quad (\text{A1.73})$$

For a real object formed on the image side with a magnification of M , as shown in Figure. A1-2, the chromatic aberration $C_C(M)$ is expressed as

$$C_C(M) = \frac{\Delta\alpha z_i}{\alpha_i} = \frac{a_1 r_o z_i}{\alpha_i} \quad (\text{A1.74})$$

From Eq. A1.4 and $\Delta\alpha = \alpha_i + \alpha_o$, we get $\Delta\alpha = (1 + M)\alpha_i$.

With $z_i = (1 + M)f$, we then have

$$C_C(M) = \frac{\Delta\alpha z_i}{\alpha_i} = (1 + M)^2 f \quad (\text{A1.75})$$

As a result, $C_C(M) = (1 + M)^2 C_C(\infty)$. For most electrostatic lenses, the magnification $M \ll 1$, therefore $C_C(M) \approx C_C(\infty)$.

For chromatic aberration with a larger beam angle, a wider beam energy spread, and a lower beam energy, the contribution of d_C will be greater. In the low energy range, usually the contribution from chromatic aberration is the main limitations to achieve small probe size.

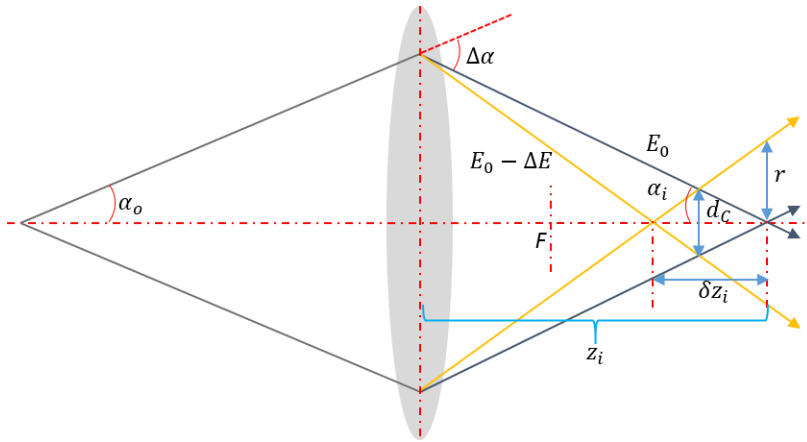


Figure. A1- 4 Chromatic aberration with magnification M . Different energy beams are focused onto different points. F is the focal point for parallel beam with energy E_0 .

It has to be noted that the other commonly used definition of chromatic aberration adopts the object angle instead of an image angle. The chromatic aberration coefficient on the object side is equal to the coefficient on the image side multiplied by $1/M$, because $\frac{\alpha_i}{\alpha_o} = \frac{1}{M}$. Additionally, some authors define the energy spread as $E_0 \pm \Delta E$. This energy spread should be doubled so as to be consistent with the preceding discussion with $E_0 - \Delta E$.

1.3 Spherical aberration

The ideal lens has a first-order (linear) focusing property as described in Eq. A1.1. However, all lenses will deviate from an ideal lens due to lens aberrations. These aberrations will introduce higher order terms into Eq. A1.1, as given by [1]

$$\Delta\alpha = a_1 r_o + a_3 r_o^3 + a_5 r_o^5 + \dots \quad (\text{A1.76})$$

Only odd orders occur here since the sign of $\Delta\alpha$ is that of r_o itself in the rotationally symmetric lens system. Coefficient of a_1 comes from the ideal lens as the first-order term. The third-order term is the spherical aberration that causes a disk of least confusion instead of a point at a Gaussian image plane for parallel beam as shown in Figure. A-2. The position away from the optical axis has a stronger spatial focusing ability since the potential extremum exists at boundaries in the lens system [4].

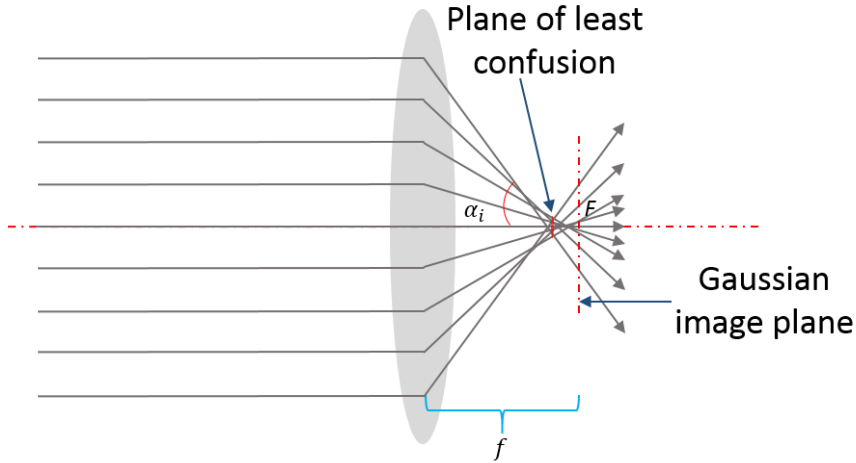


Figure. A1- 5 Schematic showing spherical aberration. The parallel beams far away from optical axis are deflected more strongly, creating a disc in the Gaussian image plane. F is the focal point.

To consider a more realistic situation, the beam is considered to originate from a point with a semi-angle α_o and focused in the Gaussian image plane, with a magnification of M , and a convergence angle of α_i , forming a disc of radius r , caused by third-order term $a_3 r_o^3$, as shown in Figure. A1-6,

$$r = a_3 r_o^3 z_i \quad (\text{A1.77})$$

Spherical aberration $C_S(M)$ is defined similar to the chromatic aberration as

$$r = C_S(M) a_i^3 \quad (\text{A1.78})$$

From Eq. A1.15, Eq. A1.16, and $r_o = z_i \alpha_i$, the spherical aberration $C_S(M)$ can be written as

$$C_S(M) = a_3 z_i^4 = a_3 (1 + M)^4 f^4 \quad (\text{A1.79})$$

In a charged particle beam transportation system, a small beam size is used rather than the disc in the Gaussian image plane. The beam size d_S in the plane of least confusion is given by

$$d_S = \frac{1}{2} C_S(M) a_i^3 \quad (\text{A1.80})$$

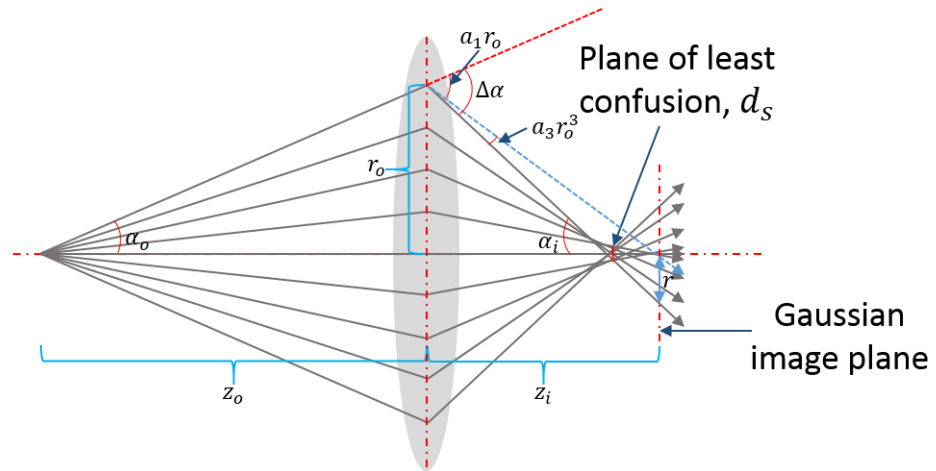


Figure. A1- 6 Schematic showing spherical aberration with magnification of M . The blue dash line represents the beam ray for ideal lens.

Here, similar to the preceding discussion on chromatic aberration, spherical aberration for incident parallel beam has the relationship of $C_S(M) = (1 + M)^4 C_S(\infty)$. Since the magnification $M \ll 1$, we get $C_S(M) \approx C_S(\infty)$.

Similar to chromatic aberration, if object angle is used to define the spherical aberration, the spherical aberration coefficient on the object side is equal to the coefficient on the image side multiplied by $1/M^3$.

Contribution of d_s from spherical aberration is proportional to the third power of angle, resulting in an enlarged probe size in the large angular aperture opening. Therefore, under a high beam current, contribution of spherical aberration is one of the primary parameters to restrict the probe size. In addition, for a large working distance, as seen from Eq. A1.17, the spherical aberration coefficient will increase dramatically to a point where a small probe size cannot be achieved.

1.4 Diffraction aberration

For a small convergence angle probe, diffraction aberration will play a role due to the wave nature of charged particle beam. An Airy disc is formed rather than a point by an ideal lens system in the Gaussian image plane, as shown in Figure. A1-7. The

contribution from the diffraction to the probe size is taken as one-half of the Airy disc as [5]

$$d_d = 0.61 \lambda / \alpha_i \quad (\text{A1.81})$$

where λ is the wavelength of charged particle beam, as governed by de Broglie equation, and α_i is the beam convergence semi-angle.

$$\lambda = \frac{h}{\sqrt{2m_0 E_0}} \frac{1}{\sqrt{1 + \frac{E_0}{2m_0 c^2}}} \quad (\text{A1.82})$$

in which, m_0 and E_0 are the rest mass and beam energy of charged particle respectively, c is the speed of light.

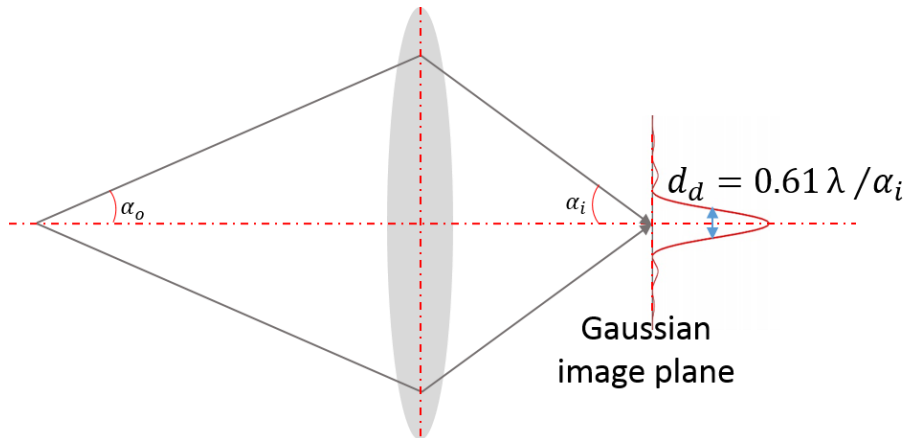


Figure. A1- 7 Schematic showing diffraction aberration, where a point is blurred to an Airy disc in the Gaussian image plane with a small convergence semi-angle α_i .

The diffraction aberration contributes to d_d with a smaller convergence angle and low beam energy. This means that, considering the probe size alone, the size of the final aperture to limit the beam angle should not be kept relatively small.

1.5 Other aberrations

Other than those of the above-mentioned aberrations, the other common aberration is astigmatism. Asymmetry in the field, caused by machining inaccuracy, misalignment, or charging effect in the apertures or polepieces, will give rise to astigmatism. The charged particle beam originating from the same point will have two different focal

points at an orthogonal angle to each other instead of the same focal point. This can be corrected by using astigmatism corrector known as a stigmator.

In summary, chromatic, spherical, and diffraction aberrations are the three major aberrations that degrade the focusing property and limit the probe size. Additionally, there exists other aberrations such as coma, pincushion and barrel distortion, and field curvature. But these will have a negligible effect on the focusing property and probe size, and hence can be neglected in this work.

References

- [1] J. T. L. Thong, *Electron beam testing technology*. Springer Science & Business Media, 2013.
- [2] L. Reimer, “Scanning electron microscopy: physics of image formation and microanalysis.” IOP Publishing, 2000.
- [3] J. Goldstein *et al.*, *Scanning electron microscopy and X-ray microanalysis: a text for biologists, materials scientists, and geologists*. Springer Science & Business Media, 2012.
- [4] H. H. Rose, “Optics of high-performance electron microscopes,” *Sci. Technol. Adv. Mater.*, vol. 9, no. 1, p. 14107, 2008.
- [5] O. C. Wells, *Scanning Electron Microscopy*. McGraw-Hill, New York, 1974.

Appendix 2. Relationship between electron probe current and probe size for different electron emitters

The performance of a scanning electron microscope (SEM) is determined by the electron emitter and the characteristics of the lens. Table. A2-1 is the comparison between different source emitter's performances.

Table. A2- 1 Comparison of different electron emitter characteristics [1]–[6].

	Tungsten	LaB ₆	Schottky	Cold Field
Emitting mechanism	Thermionic	Thermionic	Field emission	Field emission
Cathode	W	LaB ₆	ZrO/W (100)	W (310)
Operating temperature (K)	2500-2900	1800	1800	300
Cathode size (nm)	120,000	20,000	< 2,000	< 200
Virtual source size (nm)	50,000	10,000	30	5
Emission current density (A/m²)	10^4	10^6	10^7	10^9
Total emitting current (μA)	200	80	200	5
Reduced brightness (A/(m²srV))	5×10^4	10^6	5×10^7	10^8
Energy spread (eV)	1 - 3	1 - 3	0.3 - 1	0.2 – 0.3

For a SEM, the final probe size d_p is governed by the demagnified virtual source size d_I at the image plane, contributions from chromatic aberration d_C , spherical aberration d_S , and diffraction aberration (Airy disk) d_A , as discussed in Appendix 1. All these contributions to the final probe size are combined in a quadrature sum (root-power-sum), and given as [7]–[10],

$$d_p = (d_I^2 + d_C^2 + d_S^2 + d_A^2)^{1/2} \quad (\text{A2.83})$$

where,

$$d_I = \left(\frac{4I_p}{B_r V \pi^2 \alpha_p^2} \right)^{1/2} \quad (\text{A2.84})$$

$$d_C = C_c \frac{\Delta E}{E} \alpha_p \quad (\text{A2.85})$$

$$d_S = \frac{1}{2} C_s \alpha_p^3 \quad (\text{A2.86})$$

$$d_A = 0.61 \frac{\lambda}{\alpha_p} \quad (\text{A2.87})$$

Substituting into Eq. A2.1,

$$d_p = \left[\frac{4I_p}{B_r V \pi^2 \alpha_p^2} + \left(C_c \frac{\Delta E}{E} \alpha_p \right)^2 + \left(\frac{1}{2} C_s \alpha_p^3 \right)^2 + \left(0.61 \frac{\lambda}{\alpha_p} \right)^2 \right]^{1/2} \quad (\text{A2.88})$$

For each desired probe current I_p , a different optimal probe convergence angle α_{opt} can be obtained that minimizes the probe size d_p . The minimal probe size d_p as a function of probe current I_p for different electron emitters and lens conditions are presented in Figure. A2-1 and Figure. A2-2. In an SEM system, a pinhole lens is a common objective lens used for tungsten and LaB₆ emitters, while a snorkel lens is employed for Schottky and cold field emitters for obtaining high-resolution probe due to the higher brightness and lower aberration. Meanwhile, an immersion lens is also highly adopted for ultra-high resolution in an SEM system, similar to a transmission electron microscope, but only for a small specimen that is placed within the lens. Here we only consider the pinhole lens and snorkel lens for a more practical and convenient approach, along with the conservative values of chromatic C_c and spherical C_s aberrations [1], [3], [5], [11]–[14]. Four configurations are examined:

- a) Tungsten emitter ($\Delta E = 1$ eV) with a pinhole lens ($C_c = 10$ mm, $C_s = 20$ mm).

Appendix 2. Relationship between electron probe current and probe size for different electron emitters

- b) LaB₆ emitter ($\Delta E = 1$ eV) with a pinhole lens ($C_c = 10$ mm, $C_s = 20$ mm).
- c) Schottky emitter ($\Delta E = 0.3$ eV) with a snorkel lens ($C_c = 3$ mm, $C_s = 3$ mm).
- d) Cold field emitter ($\Delta E = 0.2$ eV) with a snorkel lens ($C_c = 3$ mm, $C_s = 3$ mm).

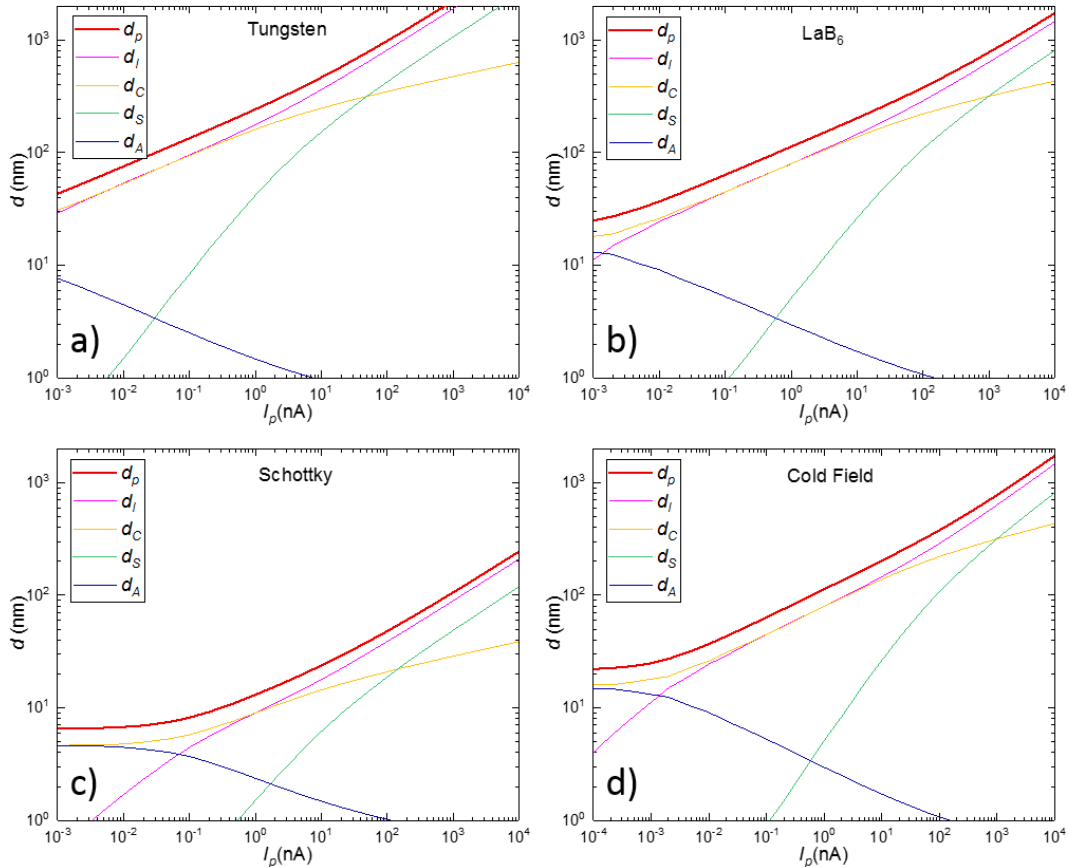


Figure. A2- 1 Minimal probe size d_p as a function of probe current I_p for different electron emitters and lens conditions for 1 keV electron beam. The individual contributions to the total probe size from a demagnified virtual source size d_l at image plane, chromatic aberration d_C , spherical aberration d_S , and diffraction aberration d_A are shown. a) Tungsten emitter ($\Delta E = 1$ eV) with a pinhole lens ($C_c = 10$ mm, $C_s = 20$ mm). b) LaB₆ emitter ($\Delta E = 1$ eV) with a pinhole lens ($C_c = 10$ mm, $C_s = 20$ mm). c) Schottky emitter ($\Delta E = 0.3$ eV) with a snorkel lens ($C_c = 3$ mm, $C_s = 3$ mm). d) Cold field emitter ($\Delta E = 0.2$ eV) with a snorkel lens ($C_c = 3$ mm, $C_s = 3$ mm).

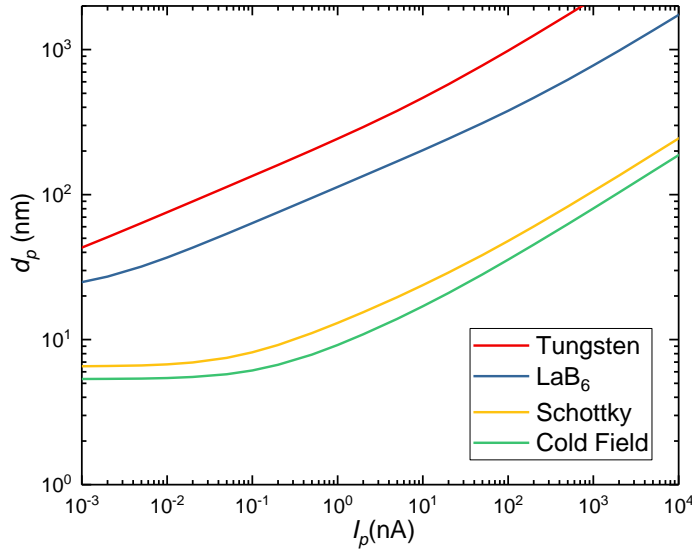


Figure. A2- 2 Minimal probe size d_p as a function of probe current I_p for tungsten, LaB_6 , Schottky, and cold field emitters for 1 keV electron beam, data compiled from Figure. A2-1.

As seen from Eq. A2.6, at low energy, the contributions from chromatic aberration d_C and diffraction aberration d_A dominates the probe size d_p at low current condition (low convergence semi-angle α_p). Due to an opposite trend between d_C vs α_p and d_A vs α_p , the smallest probe size d_{ps} is obtained under the condition of $d_C = d_A$ (at high energy, $d_S = d_A$ because the chromatic aberration is negligible), as

$$d_{ps} = C_C \frac{\Delta E}{E} \alpha_{opt} = 0.61 \frac{\lambda}{\alpha_{opt}}, \quad \alpha_{opt} = \left(\frac{0.61 \lambda E}{C_C \Delta E} \right)^{1/2} \quad (\text{A2.89})$$

Figure. A 2-1c) and Figure. A2-1d) clearly illustrate the attainable smallest probe size and their condition. In fact, Figure. A2-1a) and Figure. A2-1c) can also show this phenomenon if the graphs are extrapolated to the lower probe current range. However, it is not practical to do this because the probe current is too low (< 1 pA) in this condition, limited by low reduced brightness. Therefore, the resolution for thermionic SEMs is generally beam current limited, while for field emission SEMs it is generally aberration limited.

Appendix 2. Relationship between electron probe current and probe size for different electron emitters

The required injected electron beam current, for NAIS, should be more than 100 nA.

Although for cold field SEM, the estimated probe current in Figure. A2-2 can be very high, the obtainable probe current is usually limited to about 1 nA. Therefore, the cold field SEM is an impractical choice for using as an electron injector for NAIS. The Schottky SEM is an ideal injector with a high probe current for a given probe size.

References

- [1] J. Orloff, *Handbook of charged particle optics*. CRC press, 2008.
- [2] G. Dehm, J. M. Howe, and J. Zweck, *In-situ electron microscopy: applications in physics, chemistry and materials science*. John Wiley & Sons, 2012.
- [3] A. Khursheed, *Scanning electron microscope optics and spectrometers*. World scientific, 2011.
- [4] R. F. Egerton, *Physical principles of electron microscopy: An Introduction to TEM, SEM, and AEM*, 2nd ed. Springer International Publishing, 2016.
- [5] J. Goldstein *et al.*, *Scanning electron microscopy and X-ray microanalysis: a text for biologists, materials scientists, and geologists*. Springer Science & Business Media, 2012.
- [6] B. Fultz and J. M. Howe, *Transmission electron microscopy and diffractometry of materials*. Springer Science & Business Media, 2012.
- [7] C. W. Oatley, W. c. Nixon, and R. F. W. Pease, “Scanning Electron Microscopy,” *Adv. Electron. Electron Phys.*, vol. 21, pp. 181–247, 1966.
- [8] V. E. Cosslett, “Probe Size And Probe Current In Scanning Transmission Electron-Microscope,” *Optik (Stuttg.)*, vol. 36, no. 1, p. 85, 1972.
- [9] J. XIMEN, Z. SHAO, and P. S. D. LIN, “Theoretical calculation of probe size of low-voltage scanning electron microscopes,” *J. Microsc.*, vol. 170, no. 2, pp. 119–124, 1993.
- [10] K. C. A. Smith, “The scanning electron microscope and its fields of application,” PhD Dissertation, University of Cambridge, 1956.
- [11] R. F. W. Pease and W. C. Nixon, “High resolution scanning electron microscopy,” *J. Sci. Instrum.*, vol. 42, pp. 2–7, 1965.
- [12] J. Goldstein, *Practical scanning electron microscopy: electron and ion microprobe analysis*. Springer Science & Business Media, 2012.
- [13] L. Reimer, *Scanning electron microscopy: physics of image formation and microanalysis*, 2nd ed. Springer-Verlag Berlin Heidelberg, 1998.
- [14] L. Reimer, *Transmission electron microscopy: physics of image formation and microanalysis*, vol. 36. Springer, 2013.

List of Publications

1. “An ionization chamber chip for a nano-aperture ion source and method of fabrication thereof, for forming an integral part in a compact proton beam writing system” was submitted to apply for patent, J. A. van Kan, X. Xu, R. Pang, P. S. Raman, filled on 28 July 2017.
2. “Fabrication and development of high brightness nano-aperture ion source”, X. Xu, R. Pang, P. S. Raman, R. Mariappan, A. Khursheed, and J. A. van Kan, *Microelectronic Engineering*, 174, 20-23, 2017.
3. “Performance test of high brightness nano-aperture ion source”, X. Xu, P. S. Raman, R. Pang, N. Liu, A. Khursheed, and J. A. van Kan, *Nuclear Instruments and Methods in Physics Research Section B: Beam Interactions with Materials and Atoms*, In Press, 2017.
4. “Design considerations for a compact proton beam writing system aiming for fast sub-10 nm direct write lithography”, X. Xu, N. Liu, P. S. Raman, S. Qureshi, R. Pang, A. Khursheed, and J. A. van Kan, *Nuclear Instruments and Methods in Physics Research Section B: Beam Interactions with Materials and Atoms*, In Press, 2016.
5. “Brightness measurement of an electron impact gas ion source for proton beam writing applications”, N. Liu, X. Xu, R. Pang, P. S. Raman, A. Khursheed, and J. A. van Kan, *Review of Scientific Instruments*, 87(2), 02A903, 2016.
6. “Development of ion sources: Towards high brightness for proton beam writing applications”, N. Liu, P. S. Raman, X. Xu, H. M. Tan, A. Khursheed, and J. A. van Kan, *Nuclear Instruments and Methods in Physics Research Section B: Beam Interactions with Materials and Atoms*, 348, 23-28, 2015.